MULTISCALE NUMERICAL STUDY OF TURBULENT FLOW AND BUBBLE ENTRAINMENT IN THE SURF ZONE

BY

GANGFENG MA, JAMES T. KIRBY AND FENGYAN SHI

RESEARCH REPORT NO. CACR-12-08
JUNE 2012

This study was supported by the Office of Naval Research
Award No. N00014-10-1-0088

CENTER FOR APPLIED COASTAL RESEARCH

Ocean Engineering Laboratory
University of Delaware
Newark, Delaware 19716

TABLE OF CONTENTS

LIST OF FIGURES

ABSTRACT

Wave breaking in the surf zone entrains large volumes of air bubbles into the water column. These bubbles are involved in intense interactions with mean flow and turbulence, producing a complex two-phase bubbly flow field. Many studies have revealed that the turbulent bubbly flow under surf zone breaking waves is characterized by large-scale, organized flow structures, which play a significant role on the bubble entrainment and transport. On the other hand, it is well known that the presence of bubbles can suppress liquid phase turbulence and alter the local vorticity field. Therefore, it is necessary to describe the dynamics of breaking waves as a two-phase flow with air bubbles of appropriate size distribution. In this thesis, a polydisperse two-fluid model is developed to study the bubble plume dynamics and void fraction evolution as well as large-scale coherent structures and their interactions with dispersed bubbles under surf-zone breaking waves. The bubble entrainment model is formulated by linearly correlating bubble entrainment rate with turbulent dissipation rate. The model is validated against laboratory measurements of oscillatory bubble plume as well as turbulence and void fraction evolution under surf zone breaking waves.

In order to better understand the turbulent bubbly flow field under breaking waves, both 2D and 3D simulations are performed. In 2D simulations, it is found that the void fraction has a linear growth and exponential decay in time. The vertical distribution of void fraction can be well described by an exponential function of distance to the free surface. At the early stage of wave breaking, the bubble plume follows the propagating breaking wave crest. At the later stage of wave breaking,

the bubble plume travels slower than the breaking wave, indicating that bubbles are spread behind the wave crest. In the 3D simulation, large-scale turbulent coherent structures such as obliquely descending eddies and downburst of turbulent fluid are captured by the model. These coherent structures play an important role in turbulent kinetic energy and momentum transport as well as bubble entrainment. High TKE and Reynolds stress are located at regions with strong downward velocities, which are found at the outer part of vortices. However, high void fraction is not only located at the outer core of vortices, but also found at the center of vortices due to the preferential accumulation of bubbles by the vorticity field. As the vortices move downward, bubbles are transported to the lower part of the water column. Therefore, the turbulent coherent structures tend to transport bubbles more deeply into the water column. Both 2D and 3D simulations show that the presence of bubbles suppress liquid phase turbulence and enstrophy. The mechanisms of the generation of obliquely descending eddies are also investigated. It was found that the obliquely descending eddies evolve from vertical vortices, which are initially generated due to bending of the primary spanwise vortices. The downburst of turbulent fluid plays a significant role in vortex evolution processes.

A Non-Hydrostatic WAVE model NHWAVE is developed to simulate dispersive surface wave processes, wave breaking, surf-zone turbulence and wave-driven circulation. A bubble transport model based on the mixture theory is incorporated into NHWAVE to study the bubble generation and transport in the large-scale surf zone. The model is applied to investigate the rip current systems and bubble transport in a rip current experiment (RCEX), which was conducted in the Sandy City beach, CA. The wave height distribution and rip currents are well reproduced by the model. The bubble transport is dominated by the vorticity field inside the surf zone. Bubbles can be transported to the outer surf zone by rip currents.

Chapter 1

INTRODUCTION

Wave breaking in the surf zone entrains large volumes of air bubbles that can extend $0.5m$ or more below the surface (Deane and Stokes, 2002), and have void fraction of air exceeding 20% (Cox and Shin, 2003). The bubbles may range in size from tens of microns to centimeters (Deane and Stokes, 2002). These bubbles have been shown to be important for a number of diverse phenomena, including the generation of sea-surface sound (Loewen and Melville, 1991, 1994; Deane, 1997), enhancement of gas exchange at the air-sea interface (Merlivat and Memery, 1983; Melville, 1996) and production of marine aerosols (Cipriano and Blanchard, 1981). In addition, it has been demonstrated that the presence of bubbles can significantly change the optical properties of the water column (Terrill et al, 2001), which may introduce large optics-based measurement errors. The concentration and size distribution of bubbles are two major factors determining the optical scattering in the water (Terrill et al., 2001). Therefore, there is a need to study bubble entrainment, transport and bubble size evolution in the surf zone.

Until now, bubble entrainment and transport in the surf zone is still not well studied. The problem is highly complicated with the involvement of a variety of physical processes that operate over a wide range of temporal and spatial scales. For example, bubble entrainment and fragmentation inside the breaking wave crest happens at the acoustically active phase (Deane and Stokes, 2002), which is on the order of $1s$. The length scale of interest is the bubble size scale ($\sim$100 microns).

However, bubble transport by the wave-induced circulation such as longshore current and rip current is in the nearshore scale ($\sim 100m$). A critical scientific challenge is to describe the physical mechanisms that operate at these various scales, and establish the interactions between different scale processes. A high-quality numerical model is the most appropriate and useful tool for this because it can incorporate scientific understanding and observations, and be applied to specific regions and problems.

In this study, two numerical models will be developed to study bubble entrainment and transport in the surf zone. One is based on the polydisperse two-fluid model developed by Carrica et al. (1999), which is employed to study bubble entrainment mechanism and bubble-turbulence interactions in the laboratory scale surf zone. The second model solves the non-hydrostatic Navier-Stokes equations in surface and terrain following coordinates, and can be used to simulate wave propagation, wave breaking, wave-induced circulation and turbulent transport at the nearshore scale. A bubble model is incorporated into the latter to study bubble transport by longshore and rip currents.

1.1 Turbulence under Surfzone Breaking Waves

Bubbles entrained by breaking waves are involved in intense interactions with mean flow and turbulence, producing a complex two-phase bubbly flow field. For example, turbulent coherent structures generated by breaking waves can significantly enhance the bubble entrainment. On the other hand, the presence of bubbles can suppress liquid phase turbulence (Wang et al., 1987; Kataoka and Serizawa, 1989; Serizawa and Kataoka, 1990; Lopez de Bertodano et al., 1994) and alter the local vorticity field and consequently deform or displace vortex structures (Sridhar and Katz, 1999; Watanabe et al., 2005). Therefore, to study bubble entrainment mechanism in the surf zone, it is necessary to understand turbulence under breaking waves.

Early research on breaking waves in the surf zone is mainly focused on the problem of finding where waves break on a beach, and on the breaking wave propagation and decay. These studies have been reviewed by Peregrine (1983) and Battjes (1988). Recently, more and more attention has been focused on the study of turbulence and turbulent coherent structures under the surf zone breaking waves. A number of laboratory experiments and numerical simulations have been conducted to study these issues. Modern optical techniques, namely Laser Doppler Velocimetry (LDV), sometimes referred to as Laser Doppler Anemometry (LDA), and Particle Image Velocimetry (PIV), have been employed to measure internal flow field and turbulence. Numerical methods such as Volume-of-Fluid (VOF) and smoothed-particle hydrodynamics (SPH) have been developed to reproduce wave breaking phenomenon with the assistance of various turbulent closures, for example k-ϵ model and large eddy simulation (LES).

1.1.1 Laboratory Experiments

Several studies based on laboratory experiments have revealed that turbulent bubbly flow in surf-zone breaking waves is characterized by large-scale, organized flow structures which occur intermittently in space and time (Ting, 2008). Nadaoka et al. (1989) studied regular breaking waves on a plane beach and found that wave breaking generates spanwise vortices with axes parallel to the crest line around the wave crest. The flow structure quickly becomes three-dimensional behind the wave crest, evolving into obliquely descending eddies. Kubo and Sunamura (2001) found another type of coherent structure, called downbursts, in their laboratory study of a spilling breaking wave. The downbursts show no significant vortical motion, but can carry a large amount of turbulent kinetic energy (TKE) into the water column. Ting (2006, 2008) systematically studied the forms and evolution of coherent structures. It was found that large-scale turbulence in the middle of the water column first arrived in the form of a downburst of turbulent fluid, which was accompanied by

two counter-rotating vortices. The turbulent kinetic energy and turbulence stresses showed episodic turbulent events near the free surface but more sporadic turbulence in the lower layer.

In addition to the above-mentioned studies, there are also other important laboratory investigations on the nature of breaking wave induced turbulence. For example, Ting and Kirby (1994, 1995, 1996) conducted comprehensive studies on the turbulence transport under different types of surf zone breaking waves, and found significant differences in the characteristics of turbulence transport in spilling and plunging breakers. Under plunging breakers, the turbulent kinetic energy is transported landward and dissipated within one wave cycle. In spilling breaking waves, turbulent kinetic energy is transported seaward and the dissipation rate is much slower. Chang and Liu (1998, 1999) applied PIV to investigate turbulence generated by breaking waves in water of intermediate depth. A TKE budget was analyzed to show that turbulence production and dissipation under the trough level were of the same order of magnitude, but not identical. The turbulence advection, production, and dissipation were equally important, while the turbulence diffusion was almost negligible. Cox and Kobayashi (2000) used LDV measurements to show the existence of intense, intermittent turbulence in the surf zone for spilling breaking waves. The intermittent turbulent events could extend into the bottom boundary layer, and account for a significant fraction of turbulent kinetic energy and shear stress at the boundary. Sou et al. (2010) used PIV to study evolution of turbulence structure in the surf and swash zone. They found that the large-scale turbulence structure is closely associated with the breaking wave and the bore-generated turbulence in the surf zone. Smaller-scale energy injection during the latter stage of the downwash phase is associated with the bed-generated turbulence, yielding a -1 slope in the upper inertial range in the spatial spectra. The TKE decay resembles the decay of grid turbulence during the latter stage of the uprush and the early

stage of the downwash.

1.1.2 Numerical Investigations

Besides laboratory experiments, a powerful tool to investigate the turbulent flow field in the surf zone and swash zone is solving the Navier-Stokes equations numerically with assistance of turbulence closure models. Early attempts to numerically study turbulent flow in the surf zone were based on 2-D RANS simulation coupled with a surface-capturing model, such as Volume-of-Fluid (VOF) model. For example, Lin and Liu (1998a,b) conducted 2-D RANS simulations to investigate the turbulence transport and vorticity dynamics under spilling and plunging breaking waves. They showed that the model could predict surface elevation and velocity well, but the predicted turbulence in the inner surf zone is generally 25% to 50% higher than the experimental measurements (Ting and Kirby, 1995, 1996). This overestimation of turbulence could be attributed to the k-ϵ turbulence closure model, which cannot accurately predict the initiation of turbulence in a rapidly distorted shear flow region such as in the initial stage of wave breaking (Shao and Ji, 2006). Ma et al. (2011) found that the overestimation of turbulence by a 2-D RANS simulation is partly induced by the neglect of dispersed bubble effects. Watanabe and Saeki (1999) investigated the vorticity evolution and the emergence of the spanwise velocity component during wave breaking using three-dimensional LES, with a sub-grid scale viscosity model based on the renormalization group theory. This work was extended by Watanabe et al. (2005) to investigate the vorticity and strain field for both plunging and spilling breakers. Their study reveals the possible generation mechanism of obliquely descending eddies during wave breaking. They argued that the obliquely descending eddies are essentially counter-rotating streamwise vortices, which are vortex loops produced by stretching and bending of perturbed vorticity in the saddle region between the rebounding jet and the primary spanwise vortex. Christensen and Deigaard (2001) developed a model for simulating wave breaking,

the large-scale water motions and turbulence. Their model consists of a free surface model using the surface marker method combined with a three-dimensional model that solves the flow equations. They successfully reproduced the obliquely descending eddies under different types of breakers. They also revealed that the turbulence in spilling breakers is generated in a series of eddies in the shear layer under the surface roller, while in strong plunging breakers, turbulence originates to a large degree from the topologically generated vorticity. The turbulence generated at the plunging point is almost immediately distributed over the entire water depth by large organized vortices. Christensen (2006) conducted another LES simulation based on VOF method to study wave setup, undertow and turbulence in breaking waves. He found that the results for wave height decay and undertow are satisfactory with a rather coarse resolution, but the turbulence levels tend to be over-predicted. Lubin et al. (2006) carried out a three-dimensional large eddy simulation of plunging breaking waves by solving the Navier-Stokes equations both in air and water. They discussed the physical processes of overturning, splash-up, vortex generation, air entrainment and energy dissipation. Lakehal and Liovic (2006, 2010) carried out large eddy simulations to investigate wave breaking on a steep beach. The free surface in their model was tracked by the VOF method featuring piecewise planar interface reconstructions on a twice-as-fine mesh. The Smagorinsky sub-grid scale model is coupled with a new scheme for turbulence decay treatment on the air-side of highly deformable free surfaces. They analyzed the energy transfer between the mean flow and the wave modes, and studied wave to turbulence interaction. They found that wave breaking is accompanied by intermittent generation of local vortices and increased surface wrinkling. The turbulent kinetic energy budget and the energy decay are linked to the localized incidence of coherent structures in the liquid. The energy spectra exhibit an undulation between two-dimensional turbulence with a -3 slope and fully developed three-dimensional with a -5/3 slope depending on the

position.

1.2 Bubble Entrainment and Transport in the Surf Zone

1.2.1 Laboratory Experiments

Early investigations of bubble entrainment and evolution under surf zone breaking waves mostly employ laboratory measurements. Deane and Stokes (1999, 2002) conducted photographic studies of the air entrainment mechanism and bubble size distribution under laboratory plunging breaking waves. They revealed that bubble creation is driven by two large-scale processes: the jet/wave-face interaction and the collapsing cavity. The first process is primarily responsible for the formation of small bubbles with radius less than Hinze scale ($\approx 1mm$), while the latter is mainly responsible for the generation of bubbles larger than Hinze scale. The bubble size spectrum of their measurements satisfies a -3/2 power law for small bubbles and a -10/3 power law for large bubbles. The latter is consistent with the analysis of Garrett et al. (2000). Cox and Shin (2003) carried out extensive laboratory studies on void fraction and turbulence in the bore region of surf zone waves. They showed that the temporal variation of void fraction, normalized respectively by the wave period and average void fraction, appears to be self-similar and can be modeled by an initial period of linear growth followed by exponential decay. Hoque and Aoki (2005) have measured spatial distributions of void fraction under breaking waves in the surf zone. They demonstrated that the void fraction decays exponentially with depth. Both the maximum void fraction and maximum penetration depth happen at the end of the roller. Mori et al. (2007) conducted a set of laboratory experiments to study the scale effects of air entrainment. They concluded that there are significant scale effects on void fraction, but the bubble size spectra are independent of the experimental scale. They also found that the relationship between time-averaged void fraction and total kinetic energy shows linear dependence. Blenkinsopp and Chaplin (2007) presented detailed measurements of the time-varying distribution of

void fraction in different breaking waves under laboratory conditions. They argued that the energy expended in entraining air and generating splash accounts for a minimum of between 6.5 and 14% of the total energy dissipated during wave breaking, depending on the breaker type.

1.2.2 Numerical Investigations

Compared with laboratory experiments, numerical studies of wave breaking induced two-phase bubbly flow field are still rare. Where they exist, they are mostly based on a simplified view of the circulation process of interest without involving detailed processes of bubble creation, interaction and evolution. For example, Thorpe (1982) developed a model to account for bubble dynamics and the gas flux across the surface of individual bubbles. Terrill et al. (2001) presented a numerical model based on an advection-diffusion equation to describe bubble lifetimes and transport in a rip current. Vagle et al. (2001) set up a similar model that includes bubble buoyancy and dissolution, rip current advection and the effects of a turbulent bottom boundary layer. Their models consider bubbles as passive scalars and are incapable of describing bubble effects on the mean flow field as well as bubble-bubble interactions. In reality, the bubbly flow under breaking waves is completely a two-phase flow phenomenon that involves intense interactions between bubbles, mean flow field and turbulence. These effects can only be modeled in a framework of two-fluid formulation (Drew, 1983).

Two-fluid models have been widely used to study gas-liquid flows in industrial applications (Sokolichin and Eigenberger, 1999; Delnoij et al., 1997, 1999; Mudde and Simonin, 1999; Deen et al, 2001; Buscaglia et al., 2002), but only a few applications exist on breaking wave induced bubbly flow. The main reason is perhaps due to the lack of robust and comprehensive bubble entrainment models. Carrica et al. (1999) developed a polydisperse two-fluid model to study the bubbly flow field

around a surface ship, but bubble entrainment processes in their model are not considered. Bubbles were introduced into the computation through measured data in plunging jet experiments. Moraga et al. (2008) proposed a sub-grid air entrainment model for breaking bow waves. Ma et al. (2010) used a similar sub-grid model to simulating the bubbly flow in a plunging jet. In their models, bubble entrainment was modeled through a volume source term in the bubble number density equation. The locations where bubbles are entrained is determined by the mean downward liquid velocity, which should be greater than 0.22 m/s. The bubble source intensity is specified to obtain a good comparison with measured data. Their models have no criterion to specify the bubble source intensity which is spatially and temporally variable. Additionally, the approach to determine bubble entrainment locations is questionable, considering that bubbles can also be entrained in regions where liquid velocity is not downward. Shi et al. (2008, 2010) presented a 2D polydisperse two-fluid bubbly flow model based on mixture theory. They formulated the air entrainment by connecting it with turbulence production at the air-water interface. Simulation results showed that the model can capture the evolution pattern of void fraction, but their air entrainment model results in a dimensional constant, which could limit its application to some other free surface flows. They argued that it is necessary to develop a more theoretically justifiable air entrainment formulation. Ma et al. (2010, 2011a,b) developed a 3D polydisperse two-fluid bubbly flow model to investigate bubble plume dynamics, turbulence coherent structures and their effects on bubble entrainment, and bubble-turbulence interactions under surfzone breaking waves. In their model, the bubble source due to entrainment is correlated with turbulent dissipation rate ϵ, which is found to be able to correctly predict when and where the bubbles are entrained. The model was validated by the laboratory experimental data by Cox and Shin (2003).

1.3 Scope of Present Study

In this study, we will present two numerical models that deal with bubble entrainment and transport phenomena in different spatial and time scales. One is based on the polydisperse two-fluid model developed by Carrica et al. (1999). The model is incorporated into a 3D VOF code TRUCHAS, which is improved to be capable of simulating wave propagation and wave breaking in the surf zone. The mathematical formulations of this model including governing equations, turbulence closure, bubble entrainment model, surface tracking algorithm and initial/boundary conditions are given in chapter 2. In chapter 3, the details of numerical implementation of the model is given and followed by a few numerical benchmarks. The model performance on simulating wave propagation, wave runup/rundown, turbulent flow under breaking waves and bubble plume dynamics is evaluated.

The mode is then applied to study the bubbly flow field under a surfzone spilling breaking wave in chapter 4. The numerical results are compared with the laboratory measurements by Cox and Shin (2003) in terms of wave height distribution and nonlinear characteristics, free surface elevation, mean velocity and void fraction. The void fraction evolution, bubble plume kinematics and dynamics are investigated. The bubble plume is parameterized by exponential laws. Finally, the buoyancy and bubble breakup effects on size distribution are discussed.

In chapter 5, the model is employed to study large-scale turbulence coherent structures and bubble entrainment under surfzone breaking waves. The turbulent coherent structures such as obliquely descending eddies and downbursts and their effects on turbulent kinetic energy and momentum transport are first investigated. Then the bubble-turbulence interactions including enhancement of bubble entrainment by turbulent coherent structures and turbulence suppression by the presence of bubbles are studied.

Chapter 6 presents a non-hydrostatic numerical model which can simulate

wave propagation, wave breaking, turbulence mixing and bubble transport in the nearshore-scale domain. First, the governing equations and numerical implementation are given. The model performance is then evaluated by seven benchmarks with analytical solutions and laboratory measurements. Finally, the model is applied to simulate a field rip current experiment (RCEX) and bubble transport by longshore and rip currents.

In the last chapter, the studies in this thesis are summarized. Possible future research is itemized.

Chapter 2

POLYDISPERSE TWO-FLUID MODEL

The dispersed bubbles entrained by wave breaking in the surf zone are involved in intense interactions with mean flow and turbulence, producing a complex two-phase bubbly flow field. The large-scale coherent structures under breaking waves can dramatically enhance bubble entrainment. Meanwhile, the presence of bubbles can suppress liquid phase turbulence (Wang et al., 1987; Kataoka and Serizawa, 1989; Serizawa and Kataoka, 1990; Lopez de Bertodano et al., 1994) and alter the local vorticity field and vortex structures (Sridhar and Katz, 1999; Watanabe et al., 2005). Therefore, in order to study the turbulent bubbly flow under breaking waves, it is necessary to describe the dynamics of breaking waves as two-phase (gas-liquid) flow with air bubbles of appropriate size distribution. In this chapter, we shall present a polydisperse two-fluid model, which accounts for momentum transfer between liquid phase and bubble phase, turbulence modulation induced by dispersed bubbles and bubble entrainment at the air-water interface.

2.1 Governing Equations

To simulate polydisperse two-fluid flow, the dispersed bubbles are separated into NG classes or groups. Each class has a characteristic bubble diameter d_{bi}, $i = 1, 2, \cdots, NG$, and a corresponding volume fraction $\alpha_{g,i}$. By definition, the volume fractions of all of the phases must sum to one:

$$\alpha_l + \sum_{i=1}^{NG} \alpha_{g,i} = 1 \tag{2.1}$$

where α_l is the volume fraction of liquid phase. The volume fraction of the ith bubble group is given by

$$\alpha_{g,i} = \frac{m_{g,i} N_{g,i}}{\rho_{g,i}} \tag{2.2}$$

where $m_{g,i}$ is the mass of an individual bubble in the ith group, $N_{g,i}$ is number density of bubble in the ith group, and $\rho_{g,i}$ is the bubble density.

The polydisperse bubbly flow model we employed is based on the analysis of Carrica et al. (1999), who neglected the inertia and shear stress tensors for the gas phase due to the relatively small gas volume and density. Compared to the model based on mixture theory (Buscaglia et al., 2002; Shi et al., 2010), the present model solves the momentum conservation equation for each bubble group to obtain the bubble velocity instead of using simplified formulas, which enables us to simulate more accurately the interactions between bubbles and large scale turbulence. Following Moraga et al. (2008), we neglect bubble coalescence and gas dissolution. Thus the governing equations are given by

Mass conservation for liquid phase:

$$\frac{\partial(\alpha_l \rho_l)}{\partial t} + \nabla \cdot (\alpha_l \rho_l \mathbf{u}_l) = 0 \tag{2.3}$$

Momentum conservation for liquid phase:

$$\frac{\partial(\alpha_l \rho_l \mathbf{u}_l)}{\partial t} + \nabla \cdot (\alpha_l \rho_l \mathbf{u}_l \mathbf{u}_l) = -\alpha_l \nabla p + \alpha_l \rho_l \mathbf{g} + \nabla \cdot \left[\alpha_l \mu_{eff,l} (\nabla \mathbf{u}_l + \nabla^T \mathbf{u}_l)\right] + \mathbf{M}_{gl} \tag{2.4}$$

Bubble number density equation:

$$\frac{\partial N_{g,i}}{\partial t} + \nabla \cdot (\mathbf{u}_{g,i} N_{g,i}) = B_{g,i} + S_{g,i} \tag{2.5}$$

Momentum conservation for bubble phase:

$$-\alpha_{g,i} \nabla p + \alpha_{g,i} \rho_{g,i} \mathbf{g} + \mathbf{M}_{lg,i} = 0 \tag{2.6}$$

where ρ_l is liquid density, $\mathbf{u}_l$ is liquid velocity, p is pressure which is identical in phases, $\mathbf{g}$ is gravity, $\mu_{eff,l}$ is the effective viscosity of liquid phase, $\mathbf{u}_{g,i}$ is bubble

velocity, $B_{g,i}$ is source for the ith group bubbles due to air entrainment, $S_{g,i}$ is the intergroup mass transfer which only accounts for bubble breakup in the present study, and $\mathbf{M}_{gl}$ and $\mathbf{M}_{lg,i}$ are the momentum transfers between phases, which satisfy the following relationship

$$\mathbf{M}_{gl} + \sum_{i=1}^{NG} \mathbf{M}_{lg,i} = 0 \tag{2.7}$$

2.2 Momentum Transfer

Due to relatively small bubble density, momentum transfer between different bubble groups are negligible. Therefore, the momentum transfer only accounts for the interactions between liquid and bubble phases, which includes virtual mass, lift force and drag force.

$$\mathbf{M}_{lg,i} = \mathbf{M}_{lg,i}^{VM} + \mathbf{M}_{lg,i}^{L} + \mathbf{M}_{lg,i}^{D} \tag{2.8}$$

The virtual mass force which accounts for the acceleration of liquid in the wake of bubbles is given by

$$\mathbf{M}_{lg,i}^{VM} = \alpha_{g,i}\rho_l C_{VM}\left(\frac{D\mathbf{u}_l}{Dt} - \frac{D\mathbf{u}_{g,i}}{Dt}\right) \tag{2.9}$$

where C_{VM} is the virtual mass coefficient with a constant value of 0.5. The D/Dt operators denote the substantial derivatives.

Bubble rotation with finite relative velocity, or fluid velocity gradients (shear motion), will induce a transverse component in the hydrodynamic force, which is known as the lift force. The effect of lift force is modeled as

$$\mathbf{M}_{lg,i}^{L} = \alpha_{g,i}\rho_l C_L(\mathbf{u}_l - \mathbf{u}_{g,i}) \times (\nabla \times \mathbf{u}_l) \tag{2.10}$$

where C_L is the lift force coefficient, which is set to 0.5.

The drag force is originally due to the resistance experienced by bubbles moving in the liquid. The momentum transfer by drag force is written as the following form (Clift et al, 1978)

$$\mathbf{M}_{lg,i}^{D} = \alpha_{g,i}\rho_l \frac{3}{4}\frac{C_D}{d_{bi}}(\mathbf{u}_l - \mathbf{u}_{g,i}) \mid \mathbf{u}_l - \mathbf{u}_{g,i} \mid \tag{2.11}$$

where C_D is drag coefficient depending on the flow regime and liquid properties. For rigid spheres the drag coefficient is usually approximated by the standard drag curve (Clift et al, 1978)

$$C_D = \frac{24}{Re_{g,i}}(1 + 0.15Re_{g,i}^{0.687}) \tag{2.12}$$

where $Re_{g,i}$ is bubble Reynolds number

$$Re_{g,i} = \frac{\alpha_l \rho_l \mid \mathbf{u}_l - \mathbf{u}_{g,i} \mid d_{bi}}{\mu_l} \tag{2.13}$$

According to Clift et al. (1978), the drag on bubbles in pure water is less than the drag predicted by the standard drag curve. In a contaminated system, on the other hand, the surfactant tends to collect at the rear of the bubble whereby the slip along the surface of the bubble is reduced (Delnoij et al., 1997). Therefore, bubbles behave more like rigid particles (Delnoij et al., 1997). In the wave flume, the water is more or less contaminated, therefore, it is decided to use the standard drag curve equation as an estimate for the drag coefficient of a spherical bubble.

2.3 Turbulence Models

Early attempts to model turbulent flow under breaking waves were based on 2-D RANS simulation, for example, Lin and Liu (1998a,b). Their simulations showed that the predicted turbulence in the inner surf zone is generally 25% to 50% higher than the measurements. They argued that this overestimation of turbulence is because the RANS simulation cannot accurately predict the initiation of turbulence in a rapidly distorted shear flow such as breaking wave. With this concern, more and more researchers start using large eddy simulation (LES) to study the turbulence flow structures in surf-zone breaking waves (Christensen and Deigaard, 2001; Watanabe et al., 2005; Lakehal and Liovic, 2011). Compared with RANS, LES models small eddies which tend to be more isotropic and problem independent, and directly resolves large-scale eddies. The computational cost of LES is normally more expensive.

In this section, both RANS and LES will be presented. In LES, the effective viscosity of the liquid phase $\mu_{eff,l}$ is composed of three contributions: the molecular viscosity $\mu_{L,l}$, the turbulent viscosity $\mu_{T,l}$ and an extra term due to bubble induced turbulence $\mu_{BIT,l}$ (Deen, 2001).

$$\mu_{eff,l} = \mu_{L,l} + \mu_{T,l} + \mu_{BIT,l} \tag{2.14}$$

The turbulent eddy viscosity is calculated by the Smagorinsky (1963) subgrid model.

$$\mu_{T,l} = \rho_l (C_s \Delta)^2 |\mathbf{S}| \tag{2.15}$$

where C_s is a model constant with a value of 0.1, $\mathbf{S} = \sqrt{2 S_{ij} S_{ij}}$ is the characteristic filtered rate of strain, S_{ij} is the resolved strain rate and $\Delta = (\Delta x \Delta y \Delta z)^{1/3}$ is the filter width.

The bubble induced turbulent viscosity is calculated by the model proposed by Sato and Sekoguchi (1975)

$$\mu_{BIT,l} = \rho_l C_{\mu,BIT} \sum_{i=1}^{NG} \alpha_{g,i} d_{bi} |\mathbf{u}_r| \tag{2.16}$$

where the model constant $C_{\mu,BIT}$ is equal to 0.6. $\mathbf{u}_r$ is the relative velocity between bubble phase and liquid phase.

The turbulent dissipation rate ϵ is used in both bubble entrainment model and bubble breakup model. Following van den Hengel et al. (2005), the turbulent dissipation rate is estimated on the basis of the turbulent viscosity.

$$\epsilon = \frac{2 \nu_{T,l}^3}{(C_s \Delta)^4} \tag{2.17}$$

in which $\nu_{T,l} = \mu_{T,l} / \rho_l$ is the turbulent kinematic eddy viscosity.

In the RANS model, the turbulent eddy viscosity is estimated as

$$\mu_{T,l} = \rho_l C_\mu \frac{k^2}{\epsilon} \tag{2.18}$$

The nonlinear $k-\epsilon$ model modified for two-phase bubbly flow (Troshko and Hassan, 2001) is used. The conservation equations of turbulent kinetic energy k and turbulent dissipation rate ϵ are formulated as

$$\frac{\partial(\alpha_l\rho_l k)}{\partial t} + \nabla\cdot(\alpha_l\rho_l\mathbf{u}_l k) = \nabla\cdot(\alpha_l\frac{\mu_{T,l}}{\sigma_k}\nabla k) + \alpha_l(P-\rho_l\epsilon) + S_{bk} \tag{2.19}$$

$$\frac{\partial(\alpha_l\rho_l \epsilon)}{\partial t} + \nabla\cdot(\alpha_l\rho_l\mathbf{u}_l \epsilon) = \nabla\cdot(\alpha_l\frac{\mu_{T,l}}{\sigma_\epsilon}\nabla \epsilon) + \alpha_l(C_{\epsilon 1}\frac{\epsilon}{k}P - C_{\epsilon 2}\rho_l\frac{\epsilon^2}{k}) + S_{b\epsilon} \tag{2.20}$$

where the standard constants for $k-\epsilon$ model are $\sigma_k = 1.0, \sigma_\epsilon = 1.3, C_{\epsilon 1} = 1.44, C_{\epsilon 2} = 1.92$. The term P is the production of turbulent kinetic energy and described as

$$P = -<u_i^{'}u_j^{'}>\frac{\partial<u_i>}{\partial x_j} \tag{2.21}$$

where $<>$ denotes Reynolds averaging. The Reynolds stress is calculated by the nonlinear eddy viscosity model proposed by Lin and Liu (1998a,b) for breaking waves, which is given by

$$\begin{aligned}
<u_i^{'}u_j^{'}> = &-C_d\frac{k^2}{\epsilon}\left(\frac{\partial<u_i>}{\partial x_j}+\frac{\partial<u_j>}{\partial x_i}\right)+\frac{2}{3}k\delta_{ij}\\
&-C_1\frac{k^3}{\epsilon^2}\left(\frac{\partial<u_i>}{\partial x_l}\frac{\partial<u_l>}{\partial x_j}+\frac{\partial<u_j>}{\partial x_l}\frac{\partial<u_l>}{\partial x_i}-\frac{2}{3}\frac{\partial<u_l>}{\partial x_k}\frac{\partial<u_k>}{\partial x_l}\delta_{ij}\right)\\
&-C_2\frac{k^3}{\epsilon^2}\left(\frac{\partial<u_i>}{\partial x_k}\frac{\partial<u_j>}{\partial x_k}-\frac{1}{3}\frac{\partial<u_l>}{\partial x_k}\frac{\partial<u_l>}{\partial x_k}\delta_{ij}\right)\\
&-C_3\frac{k^3}{\epsilon^2}\left(\frac{\partial<u_k>}{\partial x_i}\frac{\partial<u_k>}{\partial x_j}-\frac{1}{3}\frac{\partial<u_l>}{\partial x_k}\frac{\partial<u_l>}{\partial x_k}\delta_{ij}\right)
\end{aligned} \tag{2.22}$$

where C_d,C_1, C_2 and C_3 are empirical coefficients, which are given for breaking waves by (Lin and Liu, 1998a,b).

$$\begin{aligned}
C_d &= \frac{2}{3}\left(\frac{1}{7.4+2S_{max}}\right), \quad C_1 = \frac{1}{185.2+3D_{max}^2}\\
C_2 &= -\frac{1}{58.5+2D_{max}^2}, \quad C_3 = \frac{1}{370.4+3D_{max}^2}
\end{aligned} \tag{2.23}$$

where

$$S_{max} = \frac{k}{\epsilon} max \left\{ \left| \frac{\partial < u_i >}{\partial x_i} \right| \text{(indices not summed)} \right\}$$
$$D_{max} = \frac{k}{\epsilon} max \left\{ \left| \frac{\partial < u_i >}{\partial x_j} \right| \right\} \tag{2.24}$$

The above coefficients may ensure the non-negativity of turbulent velocities and bounded Reynolds stress, which have been successfully applied to simulate breaking waves in plane beaches (Lin and Liu, 1998a,b).

The last two terms S_{bk} and $S_{b\epsilon}$ are bubble induced turbulence production. Troshko and Hassan (2001) have proposed formulations for bubbly flow in a vertical duct

$$S_{bk} = \sum_{i=1}^{NG} \frac{3}{4} \frac{C_D}{d_{bi}} \alpha_{g,i} \rho_l |\mathbf{u}_r|^3 \tag{2.25}$$

$$S_{b\epsilon} = C_{\epsilon 3} \omega_b S_{bk} \tag{2.26}$$

where $\mathbf{u}_r$ is relative velocity. $C_{\epsilon 3}$ is a new constant which is found to be 0.45 (Troshko and Hassan, 2001). ω_b is the characteristic frequency of bubble-induced turbulence destruction originally given by Lopez de Bertodano et al. (1994).

$$\omega_b = (\frac{2 C_{VM} d_b}{3 C_D |\mathbf{u}_r|})^{-1} \tag{2.27}$$

where C_{VM} and C_D are virtual mass coefficient and drag coefficient.

2.4 Bubble Entrainment Model

Deane and Stokes (2002) divided the lifetime of wave-generated bubbles into two phases; the acoustic phase, where bubbles are entrained and fragmented inside the breaking wave crest, and the quiescent phase, where bubbles evolve under the influence of turbulent diffusion, advection, buoyant degassing, breakup, coalescence and dissolution. The acoustic phase is short lived and the time scale of bubble fragmentation is on the order of milliseconds. Given these features, direct simulations of the acoustic phase require high temporal and spatial resolution in order to capture

the details of the air entrainment process, making their applications on a surfzone-scale domain infeasible. A practical way to introduce bubbles into the computation is to prescribe air bubbles in a two-fluid model using a bubble entrainment formulation (Moraga et al., 2008; Shi et al., 2010; Ma et al., 2010, 2011). The model fed with the initially entrained bubbles simulates bubbly flows in the quiescent phase, thus requiring much less spatial and temporal resolution.

As mentioned by Moraga et al. (2008), there are two options to model air entrainment, namely a boundary condition at the interface or a volumetric source in a region close to the interface. The first option is problematic because we normally do not resolve small interfacial scales necessary for predicting bubble entrainment. Following Baldy (1993), we denote E_A as the characteristic turbulent energy available for the formation of bubbles under breaking waves, $E_b(a)$ as the energy required to entrain a single bubble with a radius of a, and η as the Kolmogorov dissipation length scale. In surf zone breaking waves, bubbles usually have sizes which satisfy $E_A \gg E_b(a)$ and $a \gg \eta$. In this range, the statistical state of the small-scale disturbances is self-similar and all the statistical parameters of such disturbances are self-preserving (Baldy, 1993). Therefore, bubble entrainment related to small-scale disturbances is also self-similar and independent of large-scale conditions (Baldy, 1993). According to the Kolmogorov hypothesis, these small-scale disturbances fall into the inertial subrange and are solely dependent on the dissipation rate ϵ. Thus, it is justified to assume that bubble creation under breaking waves is also determined by the turbulent dissipation rate ϵ.

Based on the above analysis, we can develop a quantitative bubble entrainment model. The energy required to entrain a single bubble with a radius of a is associated with surface tension, which is given by (Buckingham, 1997)

$$E_b(a) = 4\pi a^2 \sigma \tag{2.28}$$

where σ is the surface tension. If we assume that the energy required for bubble

creation per second is linearly proportional to ϵ, we get

$$E_b(a)B(a) = c_b\rho_l\alpha_l\epsilon \tag{2.29}$$

where $B(a)$ is the rate of bubble creation per cubic meter, and c_b is an air entrainment coefficient which has to be calibrated in the model. Thus, the bubble creation rate can be evaluated as

$$B(a) = \frac{c_b}{4\pi}(\frac{\sigma}{\rho_l})^{-1}\alpha_l a^{-2}\epsilon \tag{2.30}$$

Equation (2.30) is quite similar to the model developed by Baldy (1993) through dimensional consideration. It is derived based on the assumption that all entrained bubbles are the same size. In reality, bubbles under breaking waves are distributed over a range of sizes from microns to centimeters. The distribution of bubble sizes follows a power law and there appears to be a change in the value of the spectral slope separating the large and small bubble populations (Blenkinsopp and Chaplin, 2010). Deane and Stokes (2002) argued that it is the Hinze scale ($\approx 1mm$) that separates the large and small bubbles. This argument has been confirmed by various researchers (Leifer and de Leeuw, 2006; Blenkinsopp and Chaplin, 2010). Therefore, in the following analysis, the bubble size distribution is assumed to follow the laboratory measurements of Deane and Stokes (2002). The minimum bubble radius is taken as 0.1 mm, and the maximum is 10 mm. Since our studies will be focused on laboratory-scale breaking waves, the bubble size change due to the variation of pressure and temperature is negligible. Therefore, we separate bubbles into NG classes (or groups) with constant bubble radius. The characteristic bubble radius of each class is $a_1, a_2, \cdots, a_{NG}$. The width of each class is $a_{i+1/2} - a_{i-1/2}$, where $i = 1, 2, \cdots, NG$, $a_{i+1/2} = (a_i + a_{i+1})/2$. Thus we have $a_{1-1/2} = 0.1mm$ and $a_{NG+1/2} = 10mm$. According to Deane and Stokes (2002), bubbles larger than about 1 mm have a bubble density proportional to the bubble radius to the power

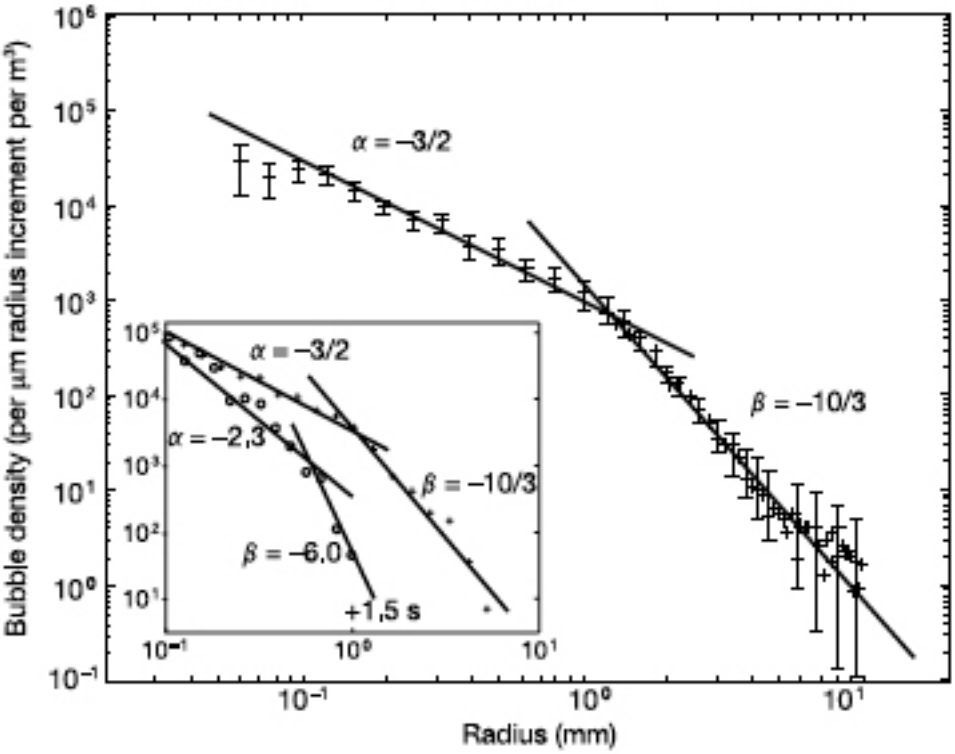

Figure 2.1: The average bubble size spectrum estimated from 14 breaking events during their acoustic phase (from Deane and Stokes, 2002).

of -10/3, while smaller bubbles have a -3/2 power-law scaling (figure 2.1).

$$\begin{aligned} f(a) &\propto a^{-10/3} \quad \text{if} \quad a \geq 1.0mm \\ f(a) &\propto a^{-3/2} \quad \text{if} \quad a \leq 1.0mm \end{aligned} \tag{2.31}$$

where $f(a)$ is the bubble size spectrum.

Then, the bubble entrainment rate per cubic meter for the ith group can be written as

$$B(a_i) = f_0 f(a_i) \Delta a_i \tag{2.32}$$

where f_0 is a coefficient and $B(a_i)$ is the entrainment rate for the ith group bubbles. We assume that the total energy required for bubble entrainment is linearly

proportional to turbulent dissipation rate, then

$$\sum_{i=1}^{NG} 4\pi a_i^2 \sigma B(a_i) = c_b \rho_l \alpha_l \epsilon \tag{2.33}$$

Plugging equation (2.32) into (2.33) gives

$$f_0 = \frac{c_b}{4\pi}(\frac{\sigma}{\rho_l})^{-1}\alpha_l \frac{1}{\sum_{i=1}^{NG} a_i^2 f(a_i)\Delta a_i}\epsilon \tag{2.34}$$

The polydisperse bubble entrainment model is then given by

$$B(a_i) = \frac{c_b}{4\pi}(\frac{\sigma}{\rho_l})^{-1}\alpha_l \frac{f(a_i)\Delta a_i}{\sum_{i=1}^{NG} a_i^2 f(a_i)\Delta a_i}\epsilon \tag{2.35}$$

The air entrainment coefficient c_b determines how many bubbles are entrained into the water column. This coefficient has to be calibrated with measured data during the simulation. To complete the formulation, we still need to describe how to select the grid points where bubbles are entrained. It is straightforward to set a critical dissipation rate ϵ_c such that no bubbles are entrained if $\epsilon \leq \epsilon_c$ at the free surface. The criterion of choosing ϵ_c is to make sure bubbles are only entrained after the wave breaks.

2.5 Bubble Breakup Model

The intergroup mass transfer only accounts for bubble breakup

$$S_{g,i} = \beta_i^+ - \beta_i^- \tag{2.36}$$

where β_i^+ and β_i^- are source/sink terms due to bubble breakup.

The phenomenological model for bubble breakup proposed by Martínez-Bazán et al. (1999a,b) is employed. This model is based on the turbulence stress and surface tension force balance and was validated by experimental data. According to this model, the breakup frequency is given by

$$g(\epsilon, D_0) = K_g D_0^{-1}\sqrt{\beta(\epsilon D_0)^{2/3} - 12\sigma/(\rho_l D_0)} \tag{2.37}$$

where the constants $\beta = 8.2$, $K_g = 0.25$ have been found experimentally and D_0 is the bubble diameter.

The volume conserving probability density function of the daughter bubbles for binary breakup (Martínez-Bazán et al., 2010) is

$$D_0 f(D_i, D_0) = f^*(D^*) = \frac{D^{*2}[D^{*2/3} - \Lambda^{5/3}][(1 - D^{*3})^{2/9} - \Lambda^{5/3}]}{\int_{D^*_{min}}^{D^*_{max}} D^{*2}[D^{*2/3} - \Lambda^{5/3}][(1 - D^{*3})^{2/9} - \Lambda^{5/3}]d(D^*)} \tag{2.38}$$

where D^* is dimensionless diameter of the daughter bubble with respect to parent bubble, $D^* = D_i/D_0$, $\Lambda = D_c/D_0$, $D_c = (12\sigma/(\beta\rho_l))^{3/5}\epsilon^{-2/5}$ is a critical diameter for bubble break up, $D_{min} = (12\sigma/(\beta\rho_l D_0))^{3/2}\epsilon^{-1}$ and $D_{max} = D_0[1 - (D_{min}/D_0)^3]^{1/3}$.

Then, the breakup source is calculated as

$$\beta_i^+ = \int_{D_i}^{\infty} m(D_0) g(\epsilon, D_0) f(D_i, D_0) N_{g,0} dD_0 \tag{2.39}$$

where $m(D_0) = 2$ for binary breakup.

Similarly, the breakup sink term is estimated as

$$\beta_i^- = g(\epsilon, D_i) N_{g,i} \tag{2.40}$$

2.6 Free-surface Tracking

Free surface tracking is of great importance in simulating breaking waves. There are three widely used methods to track the movement of a free surface: the Marker-and-Cell (MAC) method (Harlow and Welch, 1965), the Volume-of-Fluid (VOF) method (Hirt and Nichols, 1981) and Level-Set method (Sussman et al., 1994). A detailed comparison of these three methods can be found in Lin and Liu (1999).

In this study, we employed the VOF method to track the air-water interface. A volume tracking algorithm developed by Rider and Kothe (1998) is utilized. This algorithm is proven to be robust and computationally efficient, having at least

second-order accuracy in space and maintaining local conservation and compact interface width (Wu, 2004). If the volume fraction of m^{th} fluid in a computational cell is f_m, then the VOF equation is given by

$$\frac{\partial f_m}{\partial t} + \nabla \cdot (\mathbf{u}_l f_m) = 0 \tag{2.41}$$

where the volume fractions f_m are bounded by $0 \leq f_m \leq 1$.

$$f_m = \begin{cases} 1 & \text{inside fluid m} \\ > 0, < 1 & \text{at the fluid m interface} \\ 0 & \text{outside fluid m} \end{cases} \tag{2.42}$$

During wave breaking, large-scale vortices are created on the air-side of the free surface. These vortices have high velocity, which tend to impact the Courant number and push the time step to be smaller, thus increasing the computational costs. In the present study, we only focus on the turbulent flow on the water-side. Vortices on the air-side of the free surface are not considered. Therefore, we ignore the computation on the air-side, which leads to the single-phase VOF method. It has been proven that the single-phase VOF method is sufficiently accurate in predicting complex flows such as wave breaking in the surf zone (Wu, 2004). At the surface cells, the air and dispersed bubbles could coexist. In reality, these cells involve intensive interactions between air and dispersed bubbles. These interactions are neglected in the present model. This ensures that the only bubbles introduced into the flow are through air entrainment model as in the study of Moraga et al. (2008).

2.7 Initial Conditions

In most cases, the initial conditions of the mean flow field are specified with the zero velocities and hydrostatic pressure. If LES is used for turbulence computation, the initial turbulence field is also set to be zero. The initial random perturbation is not imposed because the turbulence is generated by breaking waves.

However, if $k-\epsilon$ turbulence closure is employed to calculate eddy viscosity, we have to impose an initial value for k because the production term P in equation 2.22 is proportional to k. The turbulence will remain zero if k is zero initially. According to Lin and Liu (1998a,b) and Wu (2004), the initial values for k and ϵ are given by

$$k = \frac{1}{2}u_t^2 \tag{2.43}$$

where $u_t = \delta c$. δ is an arbitrary small number, which is chosen as 2.5e-3 in this thesis. c is the wave celerity on the inflow boundary. The value of ϵ is estimated by using equation $\epsilon = C_\mu \frac{k^2}{\nu_t}$ with $\nu_t = 0.1\nu$.

2.8 Boundary Conditions

To solve the governing equations, boundary conditions for all physical domains are needed. At the incident wave boundary, the analytical solutions of free surface and velocities for a solitary wave (Lee et al., 1982), linear waves and Cnoidal waves (Wiegel, 1960) are specified. The gradients of bubble velocities and bubble number density are zero. The distributions of k and ϵ have to be given on the inflow faces. In this thesis, the values of k and ϵ are given by the initial seeding values.

At the free surface, both kinematic and dynamic boundary conditions have to be prescribed. Because the computation on the air-side is ignored, the pressure on the free surface will be set to zero. The shear stresses for both liquid phase and bubble phase at the free surface are zero. The turbulence does not transport across the free surface, which means that the normal flux of k and ϵ should be zero on the free surface.

$$\frac{\partial k}{\partial n} = 0, \quad \frac{\partial \epsilon}{\partial n} = 0 \tag{2.44}$$

At the wall boundary, free-slip boundary conditions are prescribed for both liquid phase and bubble phase velocities. For the turbulence modeling, we normally cannot resolve the viscous sublayer near the wall. Therefore, the "law of the wall" boundary condition derived from the wall function is applied. For RANS simulation,

the wall boundary conditions for k and ϵ can be derived by assuming that the cell closest to the wall is located at the logarithmic boundary layer. In the logarithmic region of the boundary layer, the velocity profile is expressed as

$$u^+ = \frac{< u_T >}{u_*} = \frac{1}{\kappa} ln(Ey^+) \tag{2.45}$$

where $< u_T >$ is the mean velocity parallel to the wall, $\kappa = 0.41$ is the von Karman constant, E is an empirical constant related to the thickness of the viscous sublayer ($E \approx 9.0$ in a boundary layer over a smooth flat plate); y^+ is a dimensionless distance from the wall.

$$y^+ = \frac{\rho u_* y}{\mu} \tag{2.46}$$

where y is the distance from the wall. u_* is the friction velocity.

Assuming that the flow in the logarithmic layer is in local equilibrium, meaning that the turbulence production and dissipation are balanced.

$$\epsilon = P = - < u^{'} v^{'} > \frac{d < u >}{dy} \tag{2.47}$$

Based on the dimensional analysis, the mean velocity gradient in this region can be expressed as

$$\frac{d < u >}{dy} = \frac{u_*}{\kappa y} \tag{2.48}$$

Then we have

$$\epsilon = P = \frac{u_*^3}{\kappa y} \tag{2.49}$$

In the logarithmic boundary layer, the eddy viscosity ν_t is given by

$$\nu_t = \kappa u_* y \tag{2.50}$$

Substitution into equation 2.18, we have

$$k = \frac{u_*^2}{\sqrt{C_\mu}} \tag{2.51}$$

For the LES simulation, the eddy viscosity ν_t at the first cell adjacent to the wall is obtained from a RANS type mixing-length eddy viscosity model with near-wall damping. The damping function derived by Cabot and Moin (2000) is used.

$$\frac{\nu_t}{\nu} = \kappa y^+ (1 - e^{-y^+/A})^2 \tag{2.52}$$

where $A = 19$ is an empirical parameter (Cabot and Moin, 2000).

Chapter 3

NUMERICAL IMPLEMENTATION AND MODEL VALIDATIONS

In the previous chapter, we have introduced the governing equations and associated physics, initial and boundary conditions of a polydisperse two-fluid model. In this chapter, we will focus on the numerical method for solving the polydisperse two-fluid equations. Our model is developed based on the framework of 3D VOF code Truchas-2.4.1, which is originally developed in Los Alamos National Laboratory (LANL). The original code solves Navier-Stokes equations by the projection method with finite volume discretization, which is capable of addressing multi-fluids by using volume-of-fluid (VOF) method. However, the original code is not particularly designed for studying coastal problems. There are no incident wave boundaries and no suitable turbulence models available to simulate turbulent flow under breaking waves. Based on the original Truchas code, we added the incident wave boundaries, turbulence models and solved additional equations for bubble velocities and bubble number density, so as to study the turbulent bubbly flow field under breaking waves.

In this chapter, we will discuss the numerical implementation of the polydisperse two-fluid model first. Then we will present four benchmarks to validate our model, including solitary wave propagation in constant water depth, breaking solitary wave run-up on a sloping beach, turbulence in a spilling breaking wave and oscillatory bubble plume. From these benchmarks, we separately demonstrate the

model's capability of simulating wave propagation, wave breaking, turbulence and dispersed bubbles.

3.1 Numerical Implementation

3.1.1 Projection Method

The solution procedure of the two-fluid model follows the framework of 3D VOF code TRUCHAS (Francois et al., 2006). We first solve the bubble number density equation and update void fraction using bubble velocities at previous time step. Then the liquid velocities are obtained by solving liquid phase continuity and momentum equations with a projection-corrector two step method. The momentum equation of the liquid phase is obtained by substituting equation (2.6) into equation (2.4). Using equation (2.7), we have

$$\frac{\partial(\alpha_l\rho_l\mathbf{u}_l)}{\partial t}+\nabla\cdot(\alpha_l\rho_l\mathbf{u}_l\mathbf{u}_l)=-\nabla p+(\alpha_l\rho_l+\sum_{i=1}^{NG}\alpha_{g,i}\rho_{g,i})\mathbf{g}+\nabla\cdot\left[\alpha_l\mu_{eff,l}(\nabla\mathbf{u}_l+\nabla^T\mathbf{u}_l)\right] \tag{3.1}$$

The above equation can be divided into two equations by introducing an interim predicted velocity $\mathbf{u}_l^*$

$$\begin{aligned}\frac{\alpha_l^{n+1}\rho_l^{n+1}\mathbf{u}_l^*-\alpha_l^n\rho_l^n\mathbf{u}_l^n}{\Delta t}&=-\nabla\cdot(\alpha_l\rho_l\mathbf{u}_l\mathbf{u}_l)^n+(\alpha_l\rho_l+\sum_{i=1}^{NG}\alpha_{g,i}\rho_{g,i})^{n+1}\mathbf{g}\\&\quad-\nabla p^n+\nabla\cdot\left[\alpha_l^{n+1}\mu_{eff,l}^{n+1}(\nabla\mathbf{u}_l+\nabla^T\mathbf{u}_l)\right]\end{aligned} \tag{3.2}$$

$$\frac{\alpha_l^{n+1}\rho_l^{n+1}\mathbf{u}_l^{n+1}-\alpha_l^{n+1}\rho_l^{n+1}\mathbf{u}_l^*}{\Delta t}=-\nabla\delta p^{n+1} \tag{3.3}$$

By applying the solenoidal condition (equation (2.3)), we get

$$\nabla\cdot(\frac{\nabla\delta p^{n+1}}{\rho_l^{n+1}})=\frac{1}{\Delta t}\nabla\cdot(\alpha_l^{n+1}\mathbf{u}_l^*)+\frac{1}{\Delta t}\frac{\partial\alpha_l}{\partial t} \tag{3.4}$$

The above equation is so called the Poisson Pressure Equation (PPE). The pressure correction $\delta p^{n+1}=p^{n+1}-p^n$ is obtained by solving equation (3.4) using the preconditioned generalized minimal residual (GMRES) algorithm. The timestep is

completed by evaluating $\mathbf{u}_l^{n+1}$ via equation (3.3). With the newly updated pressure and liquid velocities, we finally solve the momentum equation for bubble phase, which is obtained by combining equation (2.6) with equations (2.7) - (2.11).

$$\begin{aligned} C_{VM}\frac{D\mathbf{u}_{g,i}}{Dt} = &-\frac{1}{\rho_l}\nabla p + \frac{\rho_{g,i}}{\rho_l}\mathbf{g} + C_{VM}(\frac{\partial \mathbf{u}_l}{\partial t} + \mathbf{u}_l \cdot \nabla \mathbf{u}_l) \\ &+ C_L(\mathbf{u}_l - \mathbf{u}_{g,i}) \times (\nabla \times \mathbf{u}_l) + \frac{3}{4}\frac{C_D}{d_{bi}}(\mathbf{u}_l - \mathbf{u}_{g,i}) \mid \mathbf{u}_l - \mathbf{u}_{g,i} \mid \end{aligned} \tag{3.5}$$

3.1.2 Finite Volume Discretization

In order to numerically solve the governing equations, the finite volume method (FVM) is used for spatial discretization. A high-order flux-limited advection scheme (Thuburn, 1996; Dendy et al., 2002) is employed to estimate fluxes across cell faces. This scheme is conservative, monotonic and highly shape preserving, which ensures no negative mixing. Without losing generality, we consider a pure-advection conservation system with density ρ and an additional conserved quantity ϕ. The equations are

$$\frac{\partial \rho}{\partial t} + \nabla \cdot (\rho \mathbf{u}) = 0 \tag{3.6}$$

and

$$\frac{\partial \rho\phi}{\partial t} + \nabla \cdot (\rho\phi \mathbf{u}) = 0 \tag{3.7}$$

The finite volume method starts from the volume integral form of equations (3.6) and (3.7). By applying the Gauss divergence theorem, we have

$$\int_V \frac{\partial \rho}{\partial t} dV + \oint d\mathbf{A} \cdot (\mathbf{u}\rho) = 0 \tag{3.8}$$

and

$$\int_V \frac{\partial \rho\phi}{\partial t} dV + \oint d\mathbf{A} \cdot (\mathbf{u}\rho\phi) = 0 \tag{3.9}$$

The volume integral can be considered as the integral over each computational cell, and the surface integral is over all the faces of the cell. Then equations (3.8) and (3.9) can be approximated by a discrete numerical scheme

$$\frac{\rho_k^{n+1} - \rho_k^n}{\Delta t} + \frac{1}{V_k} \sum_f [\mathbf{u} \cdot \mathbf{A}]_f \rho_f = 0 \tag{3.10}$$

and

$$\frac{\rho_k^{n+1} \phi_k^{n+1} - \rho_k^n \phi_k^n}{\Delta t} + \frac{1}{V_k} \sum_f [\mathbf{u} \cdot \mathbf{A}]_f \rho_f \phi_f = 0 \tag{3.11}$$

where V_k is the volume of cell k, the subscript f indicates the cell face.

In order to compute the updated value of ϕ, we follow Thuburn (1996) and Dendy et al. (2002) and have

$$\phi_k^{n+1} = \phi_k^n + \frac{\frac{1}{V_k} \sum_f \Delta t [\mathbf{u} \cdot \mathbf{A}]_f \rho_f (\phi_f - \phi_k^n)}{\rho_k^{n+1} + \epsilon} \tag{3.12}$$

where ϵ is a small number which is added to ensure smooth calculations in the limit as $\rho_k^{n+1} \to 0$.

The advection of the conserved quantity can be estimated as

$$ADV = \frac{\rho^{n+1} \phi_k^{n+1} - \rho^n \phi_k^n}{dt} \tag{3.13}$$

In the finite volume method, it is straightforward to use a collocated arrangement which defines all the computational variables at the cell centroids, including density, pressure, velocities, viscosity, k, ϵ and so on. Therefore, it is required to calculate the flux quantities at the cell faces from the cell-centered data. The algorithm is crucial because it determines the accuracy of the discretization method. In this thesis, the flux limiter presented by Thuburn (1996) and modified by Dendy et al. (2002) is employed to estimate flux quantities ρ_f and ϕ_f. It has been implemented in Truchas-2.4.1 by Dendy et al. (2002). The details of the flux limiter can be referred to these two papers.

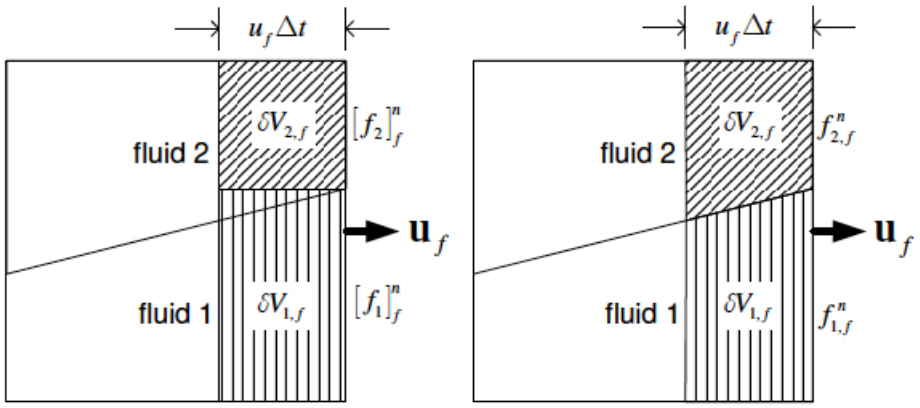

Figure 3.1: The advected mass through a cell face. The left one tends to have larger error than the right one (from Wu, 2004).

3.1.3 Volume Tracking Algorithm

As introduced in section 2.6, the free surface (air-water interface) is tracked by the VOF method. Using finite volume method, equation 2.40 can be discretized as

$$f_m^{n+1} = f_m^n - \frac{1}{V_k} \sum_f \Delta t [\mathbf{A} \cdot \mathbf{u}^n]_f [f_m]_f^n \tag{3.14}$$

where the second term on the right-hand side is the volume fluxes across the cell faces of fluid m. However, as pointed by Wu (2004), unless small Δt is used, the error could be large if the volume fluxes are estimated by the volume fraction on cell faces (figure 3.1). The volume fluxes can be estimated more precisely based on the geometric calculation.

$$f_m^{n+1} = f_m^n - \frac{1}{V_k} \sum_f \Delta t [\mathbf{A} \cdot \mathbf{u}^n]_f f_{m,f}^n \tag{3.15}$$

where $f_{m,f}^n$ is the volume fraction of δV_f^n associated with a particular material m across a cell face.

$$f_{m,f}^n = \frac{\delta V_{m,f}^n}{\delta V_f^n} \tag{3.16}$$

As shown in figure (3.1), in order to find $f^n_{m,f}$, we need the information of interface. In this thesis, a multidimensional PLIC (piecewise linear interface calculation) (Rider and Kothe, 1998) is utilized to construct the interface in every interface cell. The PLIC algorithm consists of two steps. At the first step, the fluid-fluid interface which is normally assume to be a plane is constructed. The orientations of the interface are estimated as the gradients of the volume fraction f^n_m of material m.

$$\mathbf{n} = \nabla f_m \tag{3.17}$$

and can be normalized as

$$\hat{\mathbf{n}} = \frac{\nabla f_m}{|\nabla f_m|} \tag{3.18}$$

By assuming the interface geometry is piecewise linear, the interface of each cell can be expressed as

$$\hat{\mathbf{n}} \cdot \mathbf{x} - C_p = 0 \tag{3.19}$$

where $\mathbf{x}$ is a point anywhere in the interface and C_p is the plane constant to be determined.

With the determined interfacial normal vector $\hat{\mathbf{n}}$ and volume fraction f_m, we can obtain the interface location iteratively. The plane constant C_p is found iteratively by solving the nonlinear function

$$F(C_p) = V_{tr}(C_p) - f_m * V_k \approx 0 \tag{3.20}$$

where $V_{tr}(C_p)$ is the fluid volume bounded by the interface plane with plane constant C_p, V_k is the volume of cell k.

As long as the interface plane is reconstructed, the volume flux of each material across every cell face is evaluated based on the geometry of the interface at the second step. The update of volume fraction f_m to new time step is completed using equation (3.15).

3.2 Model Validations

3.2.1 Breaking Solitary Wave Run-up on a Sloping Beach

This benchmark was widely used to validate breaking wave models (Liu and Lin, 1997; Lin et al.,1999). The corresponding laboratory experiment was conducted by Synolakis (1986). The beach slope is 1/20. The still water depth varies from 0.21 m to 0.29 m. A solitary wave which has a wave height to still water depth ratio of 0.28 was incident on the left. Wave gauges were used to record the free surface displacement during the run-up and run-down.

In the numerical simulation, the computational domain starts from the toe of the beach and extends to a location beyond the maximum run-up point. The entire domain is discretized by a $520 \times 65 \times 1$ uniform grid system with $\Delta x = 0.0125$ m, $\Delta y = 0.005$ m and $\Delta z = 0.01$ m. Turbulent eddy viscosity is calculated by Smagorinsky sub-grid model. Bubble effects are not considered in this case.

Since several different still water depths were used in the experiments, the results can only be compared after the normalization. The length scale is normalized by the still water depth d and the time scale is normalized by $\sqrt{g/d}$ (Lin et al., 1999). Figure 3.2 shows the comparisons of simulated and measured free surface profile during wave shoaling, breaking, run-up and run-down. The first two panels show the shoaling process of the solitary wave. The wave becomes more and more asymmetric and the wave height increases with decrease of water depth. Around $t\sqrt{g/d} = 20$, the wave starts to break, the surface profile is dramatically changed and the wave height is rapidly reduced. The wave continuously breaks as its turbulent front moves towards the shoreline. After the wave front passes the still-water shoreline, it collapses and the consequent run-up process commences. The run-up process is shown in the 4th-7th panels. After reaching the maximum run-up point, the front starts to run-down which is shown in the last panel. As we can see from the figure that comparisons between the simulation and experiment data are excellent. The

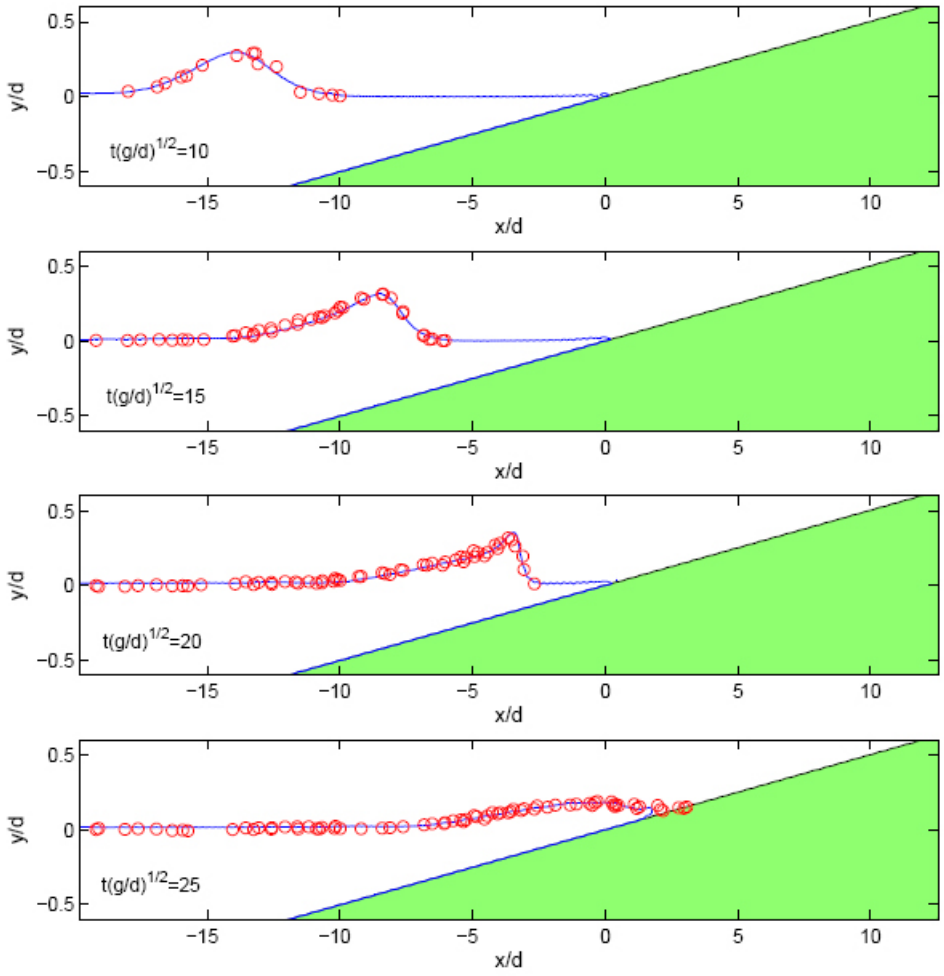

shoaling, breaking, run-up and run-down processes of the solitary wave are well reproduced.

3.2.2 Turbulence in a Spilling Breaking Wave

The nonlinear $k-\epsilon$ turbulence model was validated using the experimental data in a spilling breaking wave. The laboratory experiment was conducted by Ting and Kirby (1994, 1996). In their wave tank, a beach with a slope of 1/35 is connected to a region with a constant water depth $h = 0.4\ m$. The coordinate system is chosen so that $x = 0$ is located at the position where the still water depth

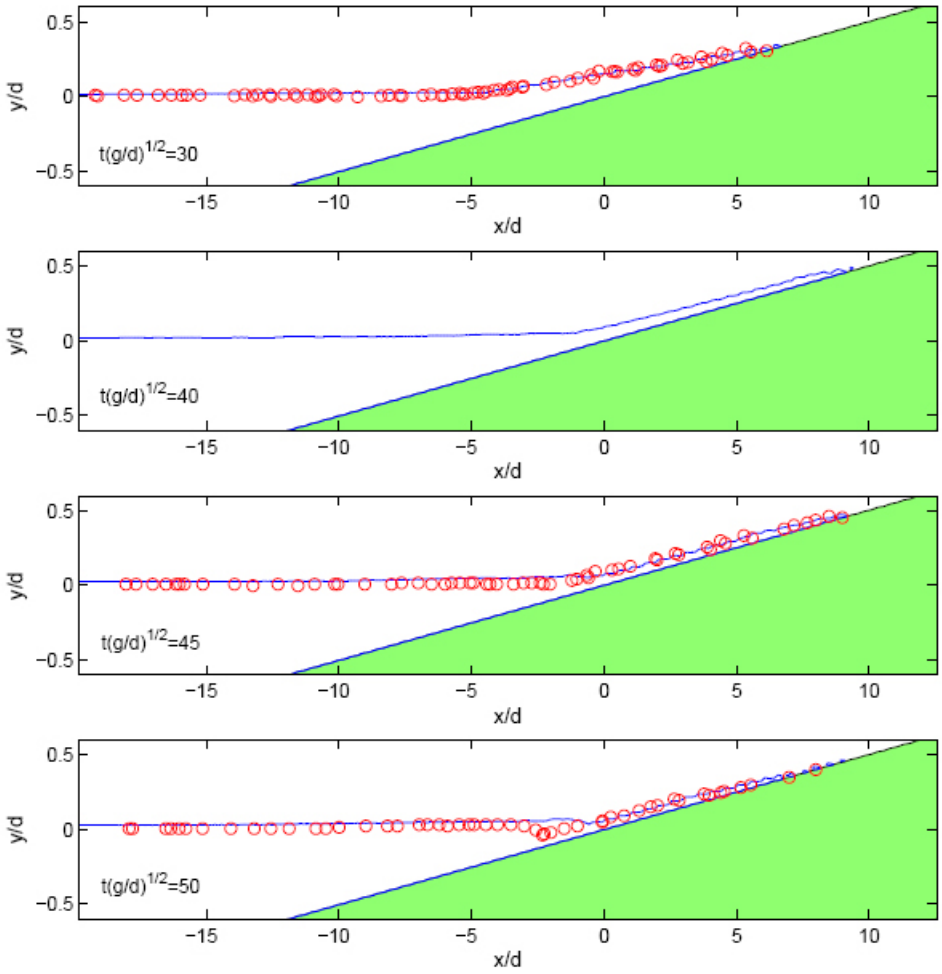

Figure 3.2: Breaking solitary wave run-up on a sloping beach

is $d_0 = 0.38\ m$. The incident waves are cnoidal waves with wave height $H = 0.125\ m$ in the constant water depth region and wave period $T = 2.0\ sec$. The velocities and free surface displacement are measured at four vertical cross sections shoreward of the breaking point, which is located at $x_b = 6.4\ m$ with time-averaged water depth $h_b = 0.199\ m$.

In the numerical simulation, the computational domain is 20.5 m long, 0.60 m high and 0.01 m wide (figure 3.3), and is discretized by $820 \times 60 \times 1$ uniform grid cells. The time step is automatically adjusted during the computation to satisfy the stability constraints. Cnoidal waves are imposed on the left boundary by specifying the free surface elevation and cell-face velocities. In this simulation, a non-linear $k - \epsilon$ turbulence model (Lin and Liu, 1998a,b; Wu, 2004) is selected to calculate turbulent eddy viscosity. At the flat bottom, a free-slip boundary condition is used. On the slope, the partial cell treatment and law-of-the-wall turbulence boundary conditions are implemented. On top of the computational domain, $p = 0$ is imposed as the boundary condition.

Figure 3.4 to 3.6 show the comparisons of free surface elevation, streamwise and vertical velocities, and turbulent kinetic energy. The free surface elevations are normalized by the deep water depth h, the velocities and turbulent kinetic energy are normalized by the local phase velocity $c = \sqrt{gh}$.

Figure 3.4 shows the comparisons at $x - x_b$=1.485 m, which is approximately $7.462h_b$. The agreement between the numerical results and the measurements are excellent except that the turbulent kinetic energy is a little overestimated. This discrepancy is consistent with the findings of Lin and Liu (1998a). The peak of the turbulent kinetic energy lags behind those of free surface elevation and velocities, which proves that the surface-generated turbulence is spread slowly downward by turbulent diffusion in a spilling breaker (Ting and Kirby, 1996). The temporal variation of turbulent kinetic energy in the upper level is more correlated to the free

surface profile than that in the lower level. As pointed out by Lin and Liu (1998a), this difference is mainly caused by the different turbulence transport mechanisms at different elevations.

Figure 3.5 and 3.6 show the comparisons at $x - x_b$=2.095 m and $x - x_b$=2.710 m respectively. As we can see, the overall agreements between numerical and experimental free surface elevation, velocities and turbulent kinetic energy are excellent. The evolutions of turbulent kinetic energy at these two sections are similar to that shown in figure 3.4. These comparisons demonstrate that the implemented nonlinear $k - \epsilon$ model is capable of simulating the turbulent flow field after wave breaking.

Figure 3.7 to 3.10 show the computed normalized turbulent kinetic energy $k/g(h+H)$, turbulent dissipation rate $\epsilon/g\sqrt{g(h+H)}$, mean vorticity $\omega/\sqrt{g/(h+H)}$ and turbulent eddy viscosity ν_t/ν at $t/T = 0.0, 0.3, 0.6, 0.9$. In this case, wave height H is 0.125 m. From these figures, we can clearly recognize the so-called 'roller' region for the entire wave period. At the very beginning and end of wave breaking process (i.e. figure 3.7 and 3.10), the highest turbulent kinetic energy k and turbulent energy dissipation ϵ happens in the roller region, while the highest mean vorticity ω is located at the wave front. The pattern of eddy viscosity ν_t is very similar to k and ϵ, the largest eddy viscosity is concentrated on the roller region. During the breaking, the wave front becomes more and more turbulent. The patterns of turbulent kinetic energy k, turbulent energy dissipation ϵ, mean vorticity ω and eddy viscosity ν_t become very similar. The numerical results are similar to those obtained by Wu (2004).

It is interesting to take a look at the bubble effects on liquid phase turbulence under breaking waves. The model setup is the same except that the bubble simulation is turned on. The critical turbulent dissipation rate ϵ_c which determines where and when bubbles are entrained is set to be 0.01 m^2/s^3. The bubble entrainment coefficient c_b is 0.18. In our model, the bubble effects on the liquid phase turbulence

are accounted for through two addition source terms S_{bk} and $S_{b\epsilon}$ in the equations (2.18) and (2.19). Generally, the bubble-induced turbulence production S_{bk} is comparable to shear production in the high void fraction region (Moraga et al., 2008). From our simulation, we noted that the characteristic frequency of bubble-induced turbulence destruction ω_b is much greater than the single-phase turbulence destruction frequency ϵ/k, indicating that the liquid-phase turbulence is more dissipative with bubbles. Figure 3.11 demonstrates the simulated turbulence dissipation rate at $(t - t_b)/T = 0.10$ with and without bubble effects. As we can see, the turbulence dissipation rate with bubbles is much larger than that without bubbles, indicating that the liquid phase turbulence is damped by the presence of bubbles.

Figure 3.12 shows the model/data comparisons of turbulent kinetic energy (TKE) at $x - x_b = 2.095\ m$ and $x - x_b = 2.710\ m$ with and without bubble effects. As noticed by Lin and Liu (1998a), the turbulent kinetic energy in the surf zone is normally overestimated by single-phase $k - \epsilon$ model. They argued that this overestimation of turbulence is because the RANS simulation cannot accurately predict the initiation of turbulence in a rapidly distorted shear flow such as breaking wave. From the figures, we can see that the TKE predicted by single-phase $k - \epsilon$ model without bubble effects has similar overestimation as Lin and Liu (1998a). However, if bubble effects are considered, the predicted TKE is significantly lower and compares much better with the measurements. From these comparisons, we can conclude that exclusion of bubble-induced turbulence suppression is also a main reason for the overestimation of turbulent intensity by single-phase $k - \epsilon$ model.

3.2.3 Oscillatory Bubble Plume

In this section, the two-fluid model was validated with laboratory experimental data for an oscillatory bubble plume. This test case has been widely used to validate two-phase bubbly flow models (Sokolichin and Eigenberger, 1999; Mudde and Simonin, 1999; Deen, 2001). The corresponding experiment was conducted by

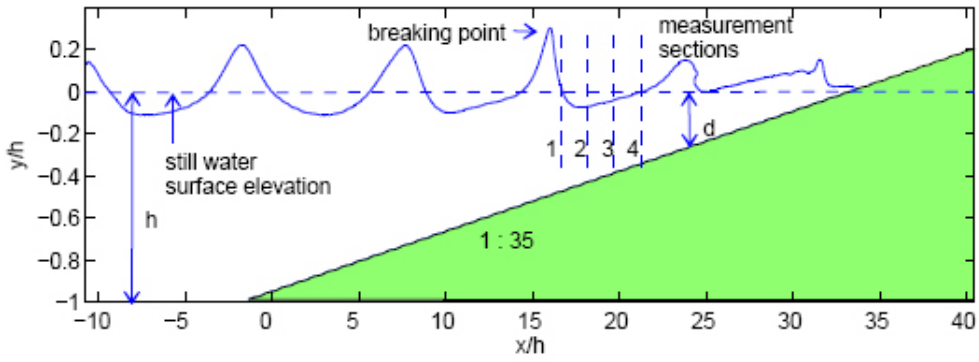

Figure 3.3: Sketch of experimental setup and computational domain. The still water depth is $h = 0.4\ m$. The beach slope is 1/35. The breaking location is at $x_b/h = 16.0$ and four measurement sections are located at $x/h = 16.6625, 18.1875, 19.7125, 21.2375$.

Becker et al. (1994). The experimental vessel is 200 cm in height, 50 cm in width and only 8 cm in depth, making it quasi two-dimensional. It is filled with water up to 150 cm. Bubbles are injected at the bottom using a circular sparger with 40 mm diameter, located 15 cm from the left wall of the vessel. One of the attractive features of the experiment is that the vertical liquid velocity at a monitor point (900 mm above the bottom plate and 35 mm from the left side wall) shows oscillations of relatively constant period on the order of 40 s, with a mean velocity close to zero and an amplitude of about 20 cm/s, at a gas flow rate of 1.6 l/min (figure 3.13).

In order to compare with experiment data, a large eddy simulation of 3-D bubbly flow was conducted. Bubbles are assumed to be in a single group with diameter of 40 mm. The grid size is 1 cm, thus the grid is $50 \times 200 \times 8$. The circular inlet is approximated with a square gas inlet of 4×4 grid cells. If we assume the gas void fraction is 1.0, then the gas velocity at the inlet becomes 0.0167 m/s. Along the wall, the standard wall functions were applied for the liquid phase. At the top of the computational domain, a pressure boundary ($p = 0$) was used. The free surface between water and atmosphere was captured by VOF method.

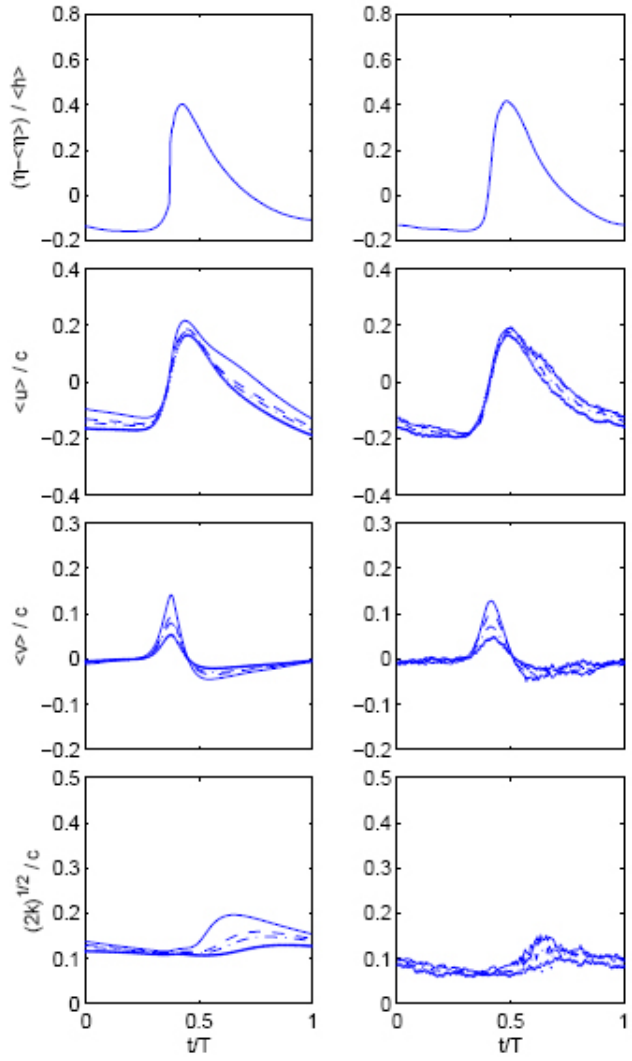

Figure 3.4: Comparisons of numerical (left) and experimental (right) results at $x - x_b = 1.485\ m$, $y = -0.06\ m$ (solid), -0.08 m (dashed), -0.10 m (dash-dot), -0.12 m (dotted).

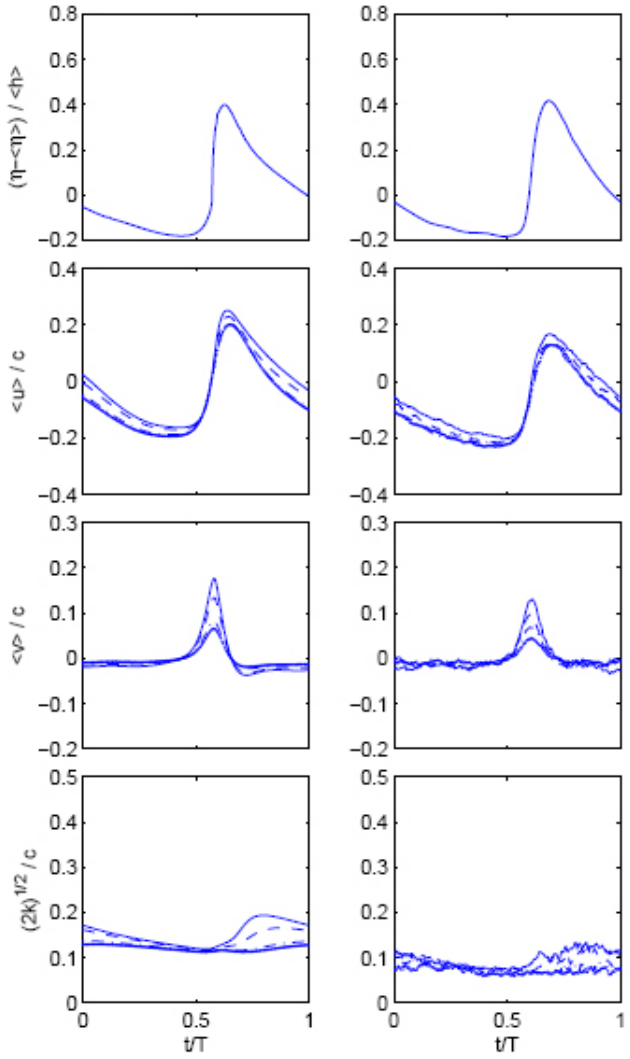

Figure 3.5: Comparisons of numerical (left) and experimental (right) results at $x - x_b = 2.095\ m$, $y = -0.04\ m$ (solid), -0.06 m (dashed), -0.08 m (dash-dot), -0.10 m (dotted).

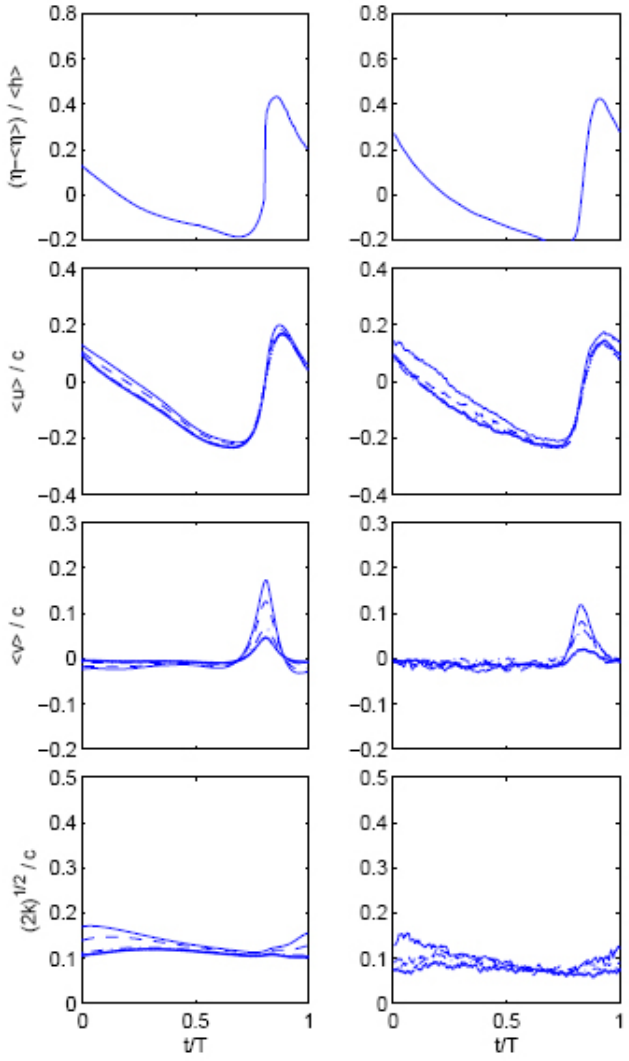

Figure 3.6: Comparisons of numerical (left) and experimental (right) results at $x - x_b = 2.710\ m$, $y = -0.04\ m$ (solid), -0.06 m (dashed), -0.08 m (dash-dot), -0.10 m (dotted).

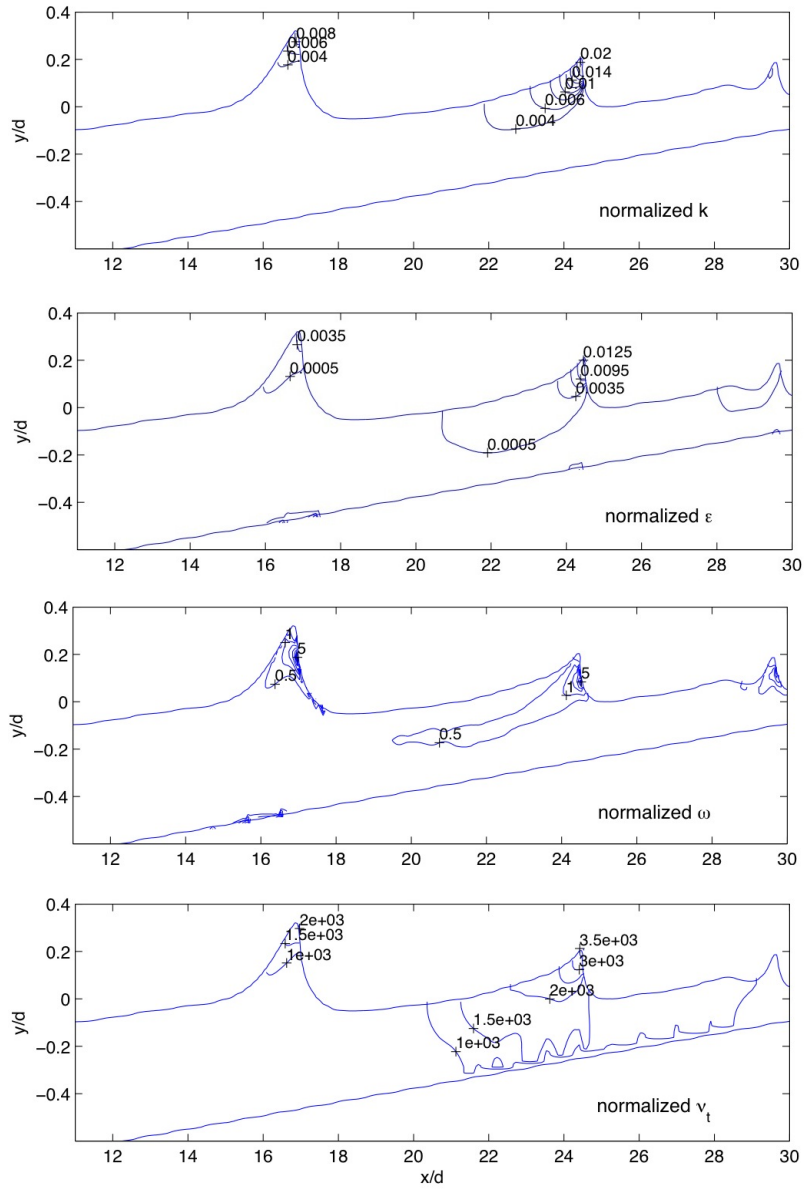

Figure 3.7: Computed normalized turbulent kinetic energy $k/g(h+H)$, turbulent energy dissipation rate $\epsilon/g\sqrt{g(h+H)}$, mean vorticity $\omega/\sqrt{g/(h+H)}$ and turbulent eddy viscosity ν_t/ν at $t/T = 0.0$.

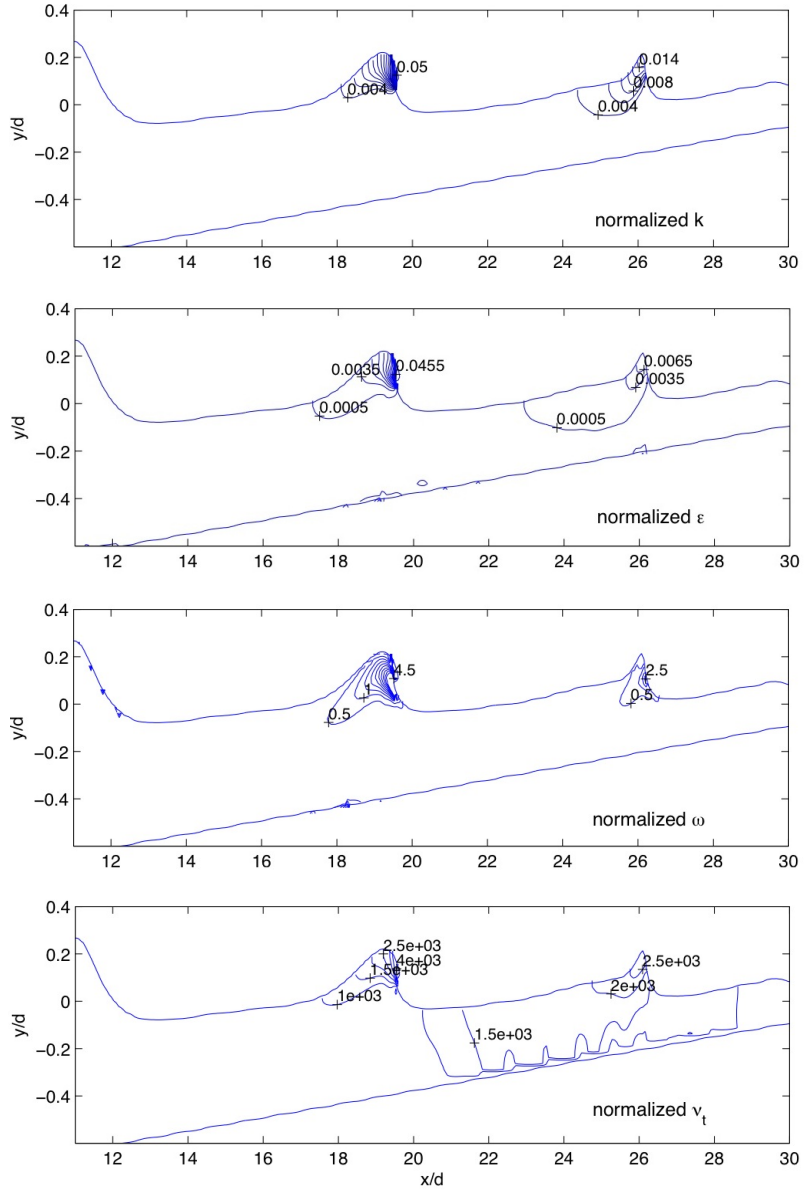

Figure 3.8: Computed normalized turbulent kinetic energy $k/g(h+H)$, turbulent energy dissipation rate $\epsilon/g\sqrt{g(h+H)}$, mean vorticity $\omega/\sqrt{g/(h+H)}$ and turbulent eddy viscosity ν_t/ν at $t/T = 0.3$

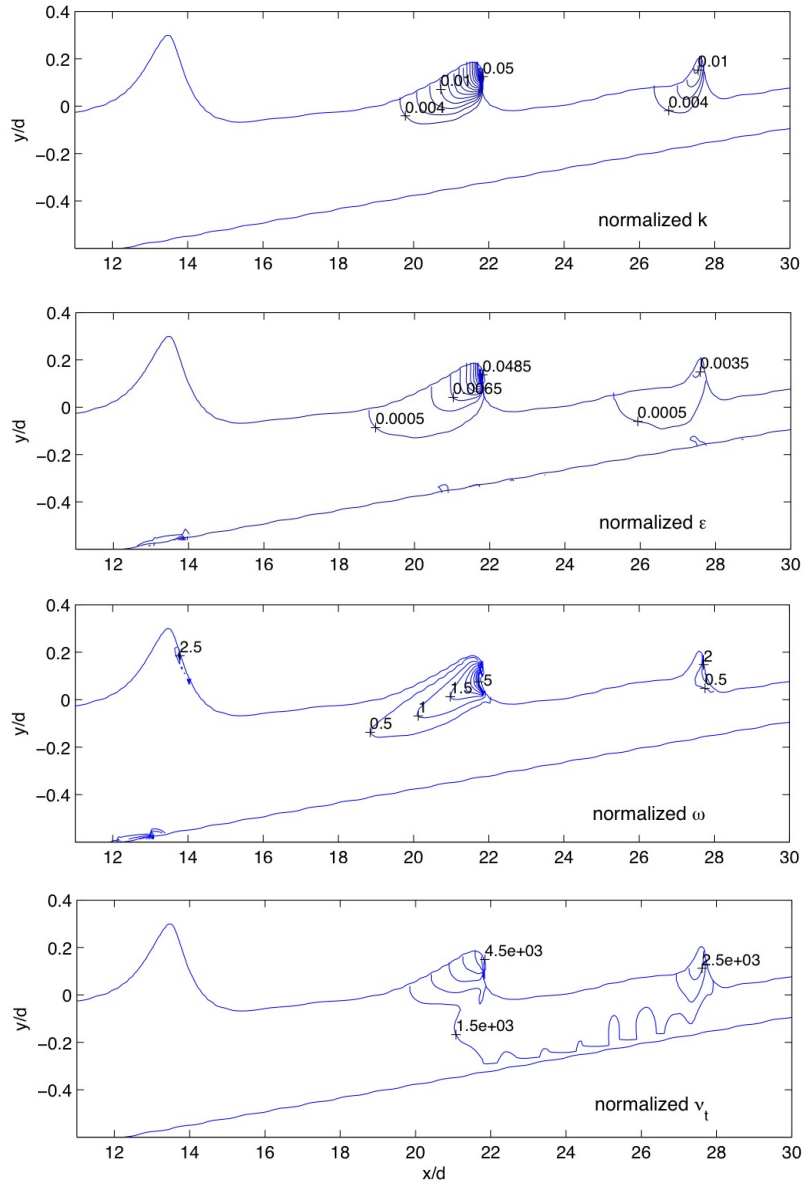

Figure 3.9: Computed normalized turbulent kinetic energy $k/g(h+H)$, turbulent energy dissipation rate $\epsilon/g\sqrt{g(h+H)}$, mean vorticity $\omega/\sqrt{g/(h+H)}$ and turbulent eddy viscosity ν_t/ν at $t/T = 0.6$

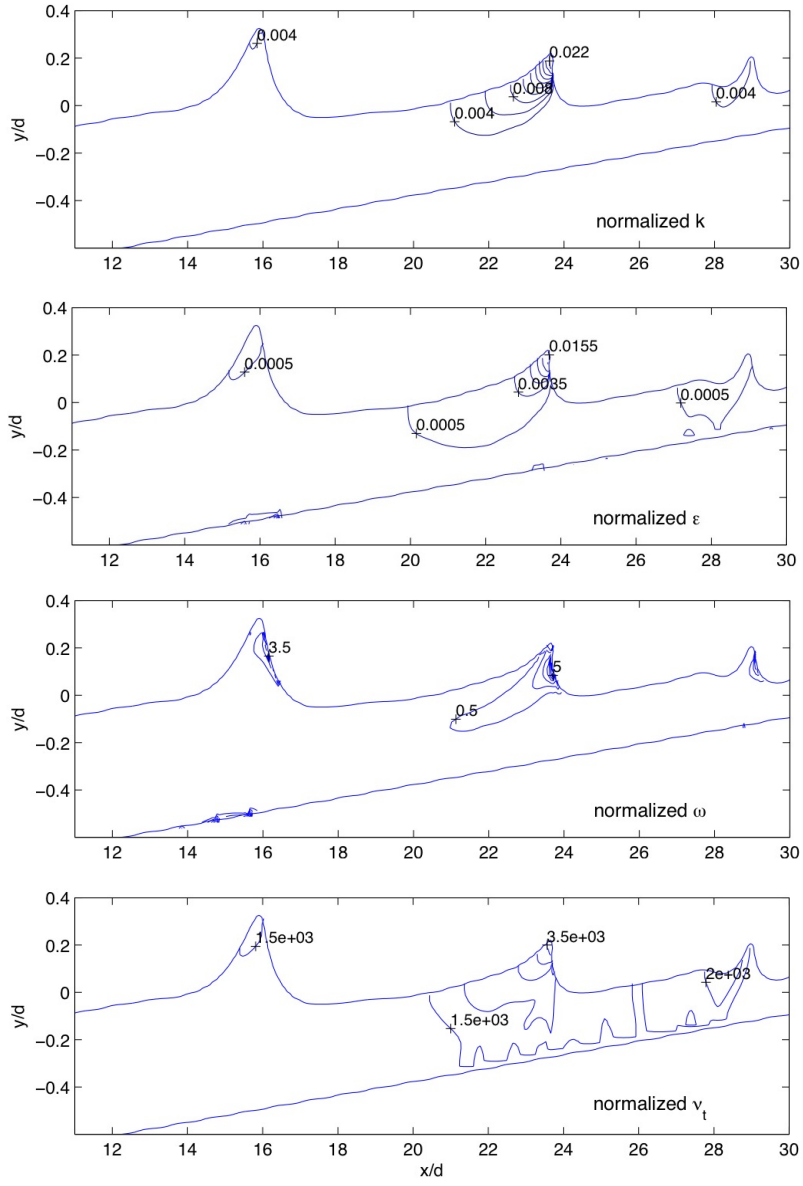

Figure 3.10: Computed normalized turbulent kinetic energy $k/g(h+H)$, turbulent energy dissipation rate $\epsilon/g\sqrt{g(h+H)}$, mean vorticity $\omega/\sqrt{g/(h+H)}$ and turbulent eddy viscosity ν_t/ν at $t/T = 0.9$

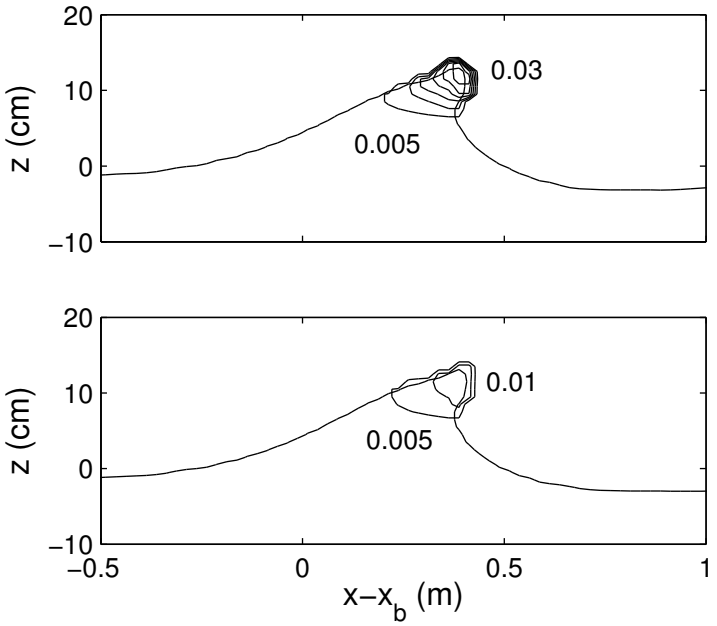

Figure 3.11: Turbulent dissipation rate normalized by $g\sqrt{g/(h+H)}$ at $(t - t_b)/T = 0.10$ with (upper panel) and without (lower panel) bubble effects, where h is the still water depth and H is incident wave height, t_b is time for initial breaking, x_b is breaking point. Contour increment is 0.005.

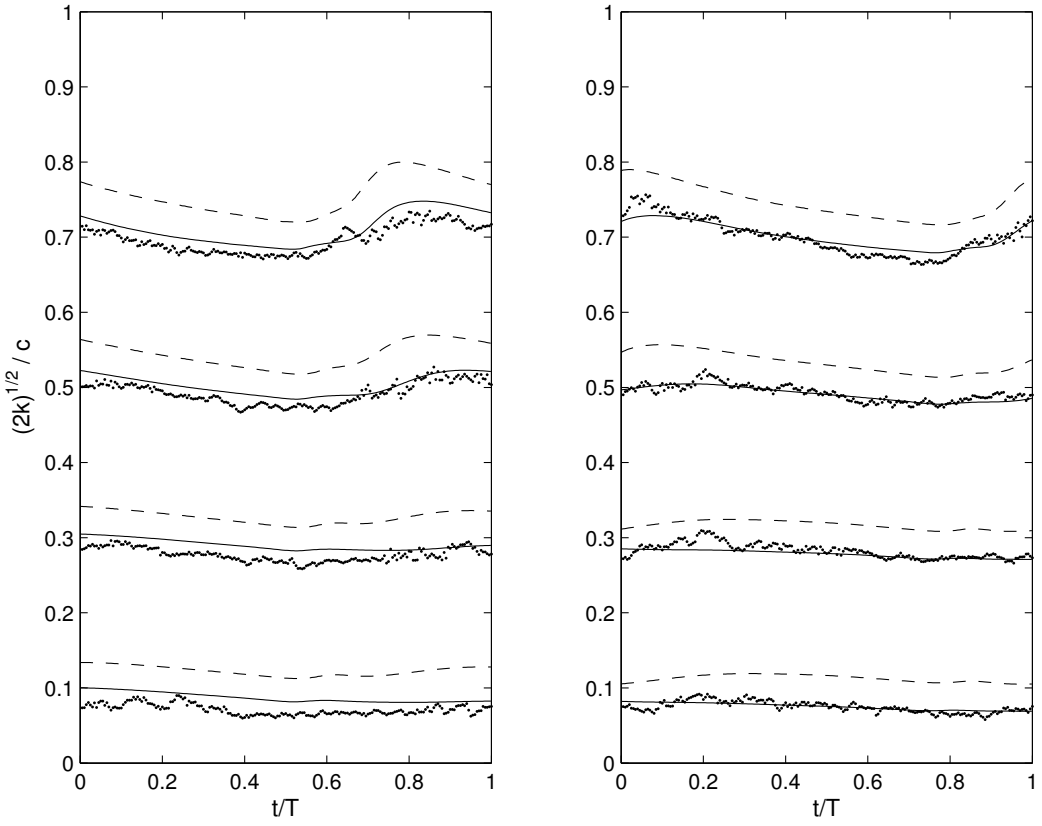

Figure 3.12: Comparisons of numerical and experimental (dotted lines) turbulent kinetic energy (normalized by phase speed c) at $x - x_b = 2.095\ m$ (left panel) and $x - x_b = 2.710\ m$ (right panel), $z =$ (a) -4.0 cm, (b) -6.0 cm, (c) -8.0 cm, (d) -10.0 cm with (solid lines) and without (dashed lines) bubble effects. The curves at different measurement locations are offset by 0.2. Experimental data by Ting and Kirby (1994, 1996).

Figure 3.14 shows the oscillation of bubble plume at 6 different times with interval of 10 s between each snapshot. The oscillating behavior of the plume is clearly observed with an oscillation period nearly 40 s. This qualitative behavior is in close agreement with the measurement and numerical results of Sokolichin and Eigenberger (1999). The calculated time averaged velocity is shown in figure 3.15, from which two large-scale vortices can be recognized. One is close to the upper left wall, and the other is in the middle of the bubble column. This flow pattern is consistent with the numerical result by Sokolichin and Eigenberger (1999).

Figure 3.16 demonstrates the simulated time series of vertical liquid velocities at two monitor points. Point A is located at 900 mm above the bottom plate and 35 mm from the left side wall which is in the bubbly flow region. Point B is located at (x = 450 mm, y = 1050 mm, z = 40 mm) which is in the bubble free zone. We can see the oscillations in both locations. The averaged oscillation period in these two locations is about 36 s, which is close to the measurement around 40 s as shown in figure 3.13. The model slightly under-predicts the peak velocity at point A which is around 0.4 m/s, while the measured peak velocity at point A is up to 0.5 m/s. The simulated liquid velocity at point B is not as periodic as that shown in the measurement (figure 3.13). At this moment, we have no sound reasons to interpret these discrepancies. They could be partially induced by the differences in the numerical (square)and experimental (circular) gas inlet design.

Figure 3.17 demonstrates comparisons of the time averaged vertical liquid velocity $U_{y,L}$, horizontal liquid velocity fluctuation $U^{'}_{x,L}$ and vertical liquid velocity fluctuation $U^{'}_{y,L}$ at ($y = 800mm$, $z = 40mm$), where $U^{'}_{x,L} =< (U_{x,L} - < U_{x,L} >)^2 >^{1/2}$ and $U^{'}_{y,L} =< (U_{y,L} - < U_{y,L} >)^2 >^{1/2}$. The simulated vertical liquid velocity matches well with the measurement. The comparisons of liquid velocity fluctuation are generally good, though the model under-predicts the horizontal liquid velocity fluctuation, especially in the bubbly flow region. The vertical liquid velocity fluctuation close

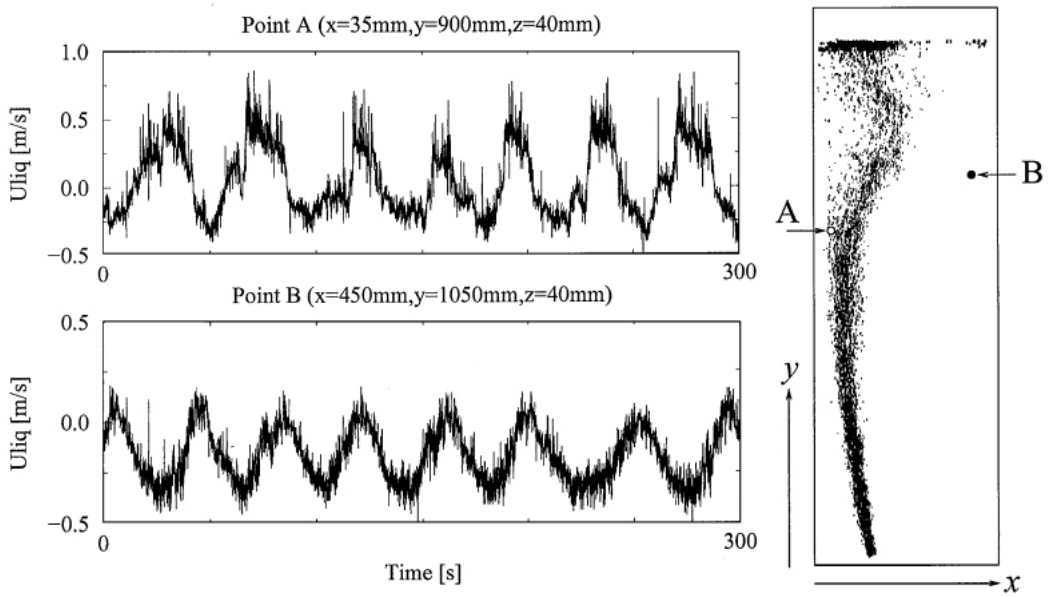

Figure 3.13: Local transient measurements of the vertical liquid velocity at positions A (bubbly flow) and B (bubble free zone) (from Sokolichin and Eigenberger, 1999).

to the left wall is also under-estimated. Although discrepancies between simulation and measurement exist, we can conclude from these comparisons that the model is able to reasonably simulate bubble-liquid interactions.

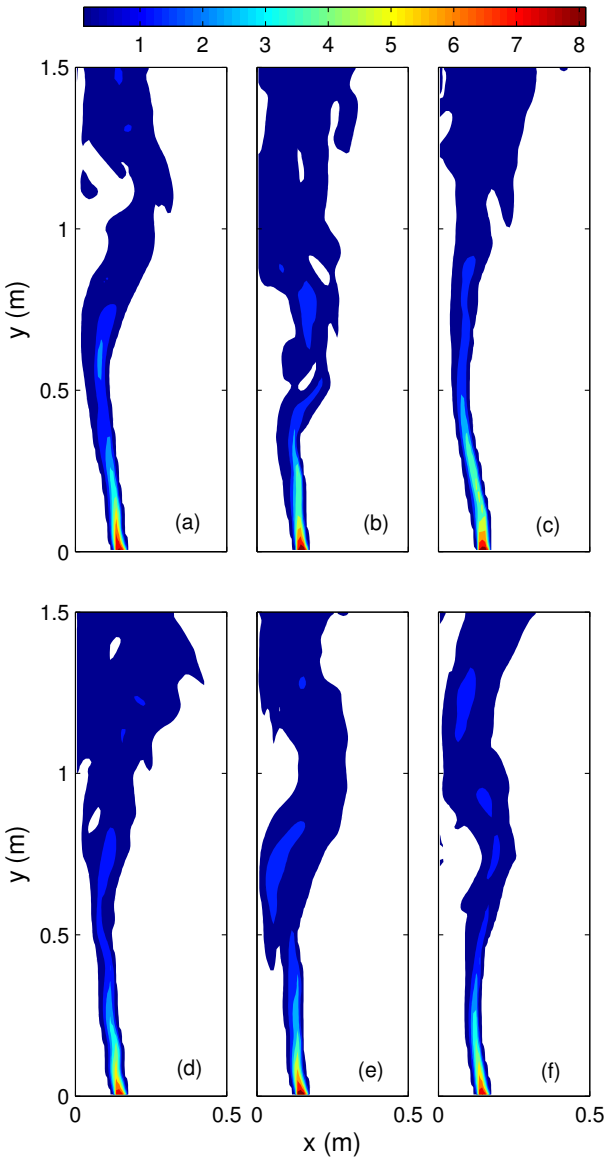

Figure 3.14: Simulated oscillatory bubble plume at (a) $t = t_0$; (b) $t = t_0 + 10s$; (c) $t = t_0 + 20s$; (d) $t = t_0 + 30s$; (e) $t = t_0 + 40s$; (f) $t = t_0 + 50s$. The contour is bounded by 0.1% void fraction.

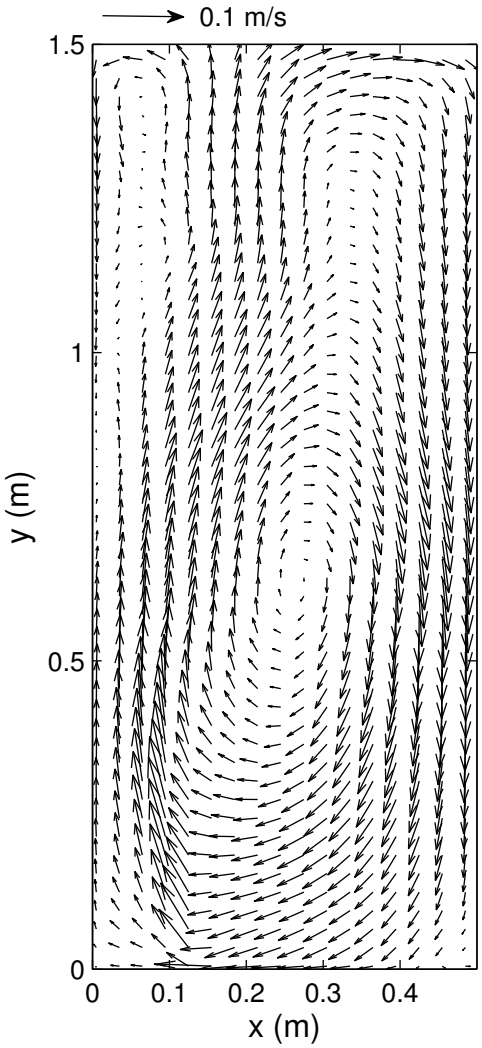

Figure 3.15: Time averaged liquid velocity field at $z = 40\ mm$.

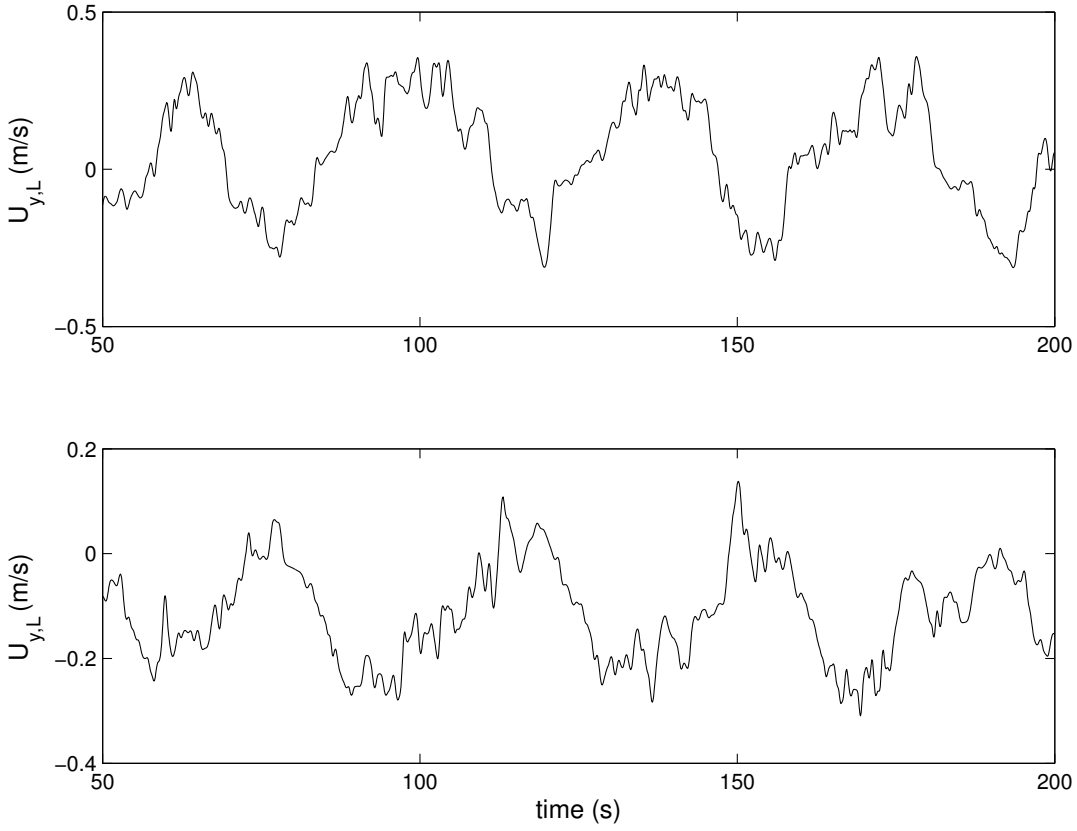

Figure 3.16: Simulated time series of vertical liquid velocity at monitor point A (upper panel) and B (lower panel).

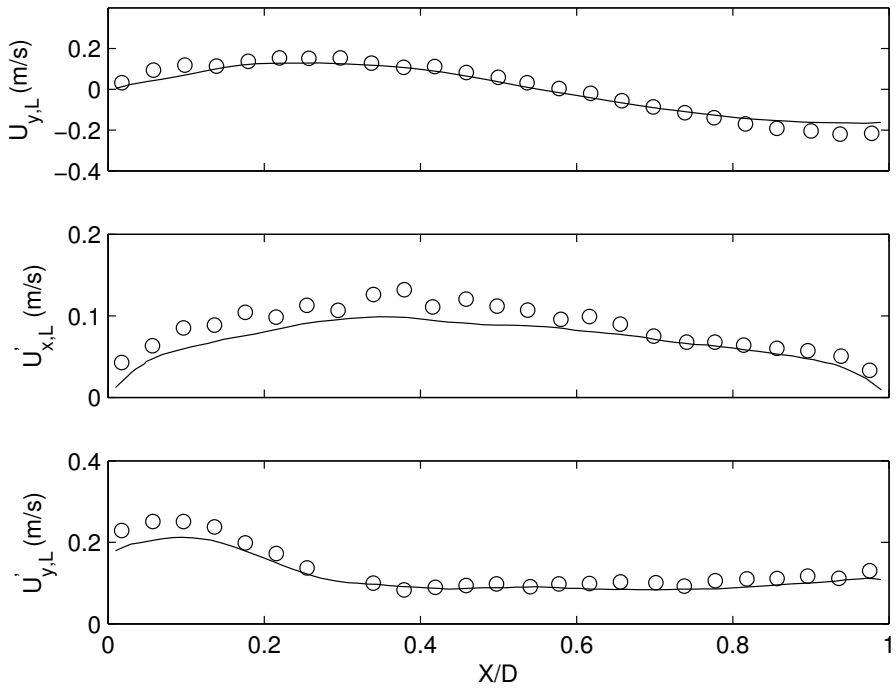

Figure 3.17: Comparisons of time averaged vertical liquid velocity $U_{y,L}$ (upper panel), horizontal liquid velocity fluctuation $U'_{x,L}$ (middle panel) and vertical liquid velocity fluctuation $U'_{y,L}$ (lower panel) at $y = 800\ mm$, $z = 40\ mm$, where $U'_{x,L} =< (U_{x,L} - < U_{x,L} >)^2 >^{1/2}$ and $U'_{y,L} =< (U_{y,L} - < U_{y,L} >)^2 >^{1/2}$. Line: simulation; circle: measurement. Experimental data by Becker et al. (1994).

Chapter 4

2D BUBBLE PLUME DYNAMICS AND VOID FRACTION EVOLUTION

In the previous chapter, we have shown that the model can reasonably simulate turbulence under surfzone breaking waves and bubble-flow interactions. In this chapter, we will focus on an application of the model to study the bubble plume dynamics under a spilling breaking wave. A 2D simulation with $k-\epsilon$ turbulence closure is conducted. The numerical results are compared with the laboratory measurements by Cox and Shin (2003).

4.1 Model Setup

The polydisperse two-fluid model is employed to study the bubbly flow under a laboratory surf zone breaking wave. Our attention will be focused on the void fraction distribution and bubble plume dynamics after wave breaking. Laboratory measurements by Cox and Shin (2003) are selected to test the model's capability. The experiment was conducted in a 36 m long by 0.95 m wide by 1.5 m high glass-walled flume. A beach with constant slope of 1/35 was installed with the toe 10 m from the wavemaker and intersecting the still water line at $x = 27.85\ m$. The flume was filled with tap water to a depth of $h = 0.51\ m$. Three cases of monochromatic waves were run. In a plunging breaker, large air cavities are formed during overturning and splash-up processes, which are subsequently fragmented under the action of shear and turbulence. Numerical simulation of these processes resorts to two-way

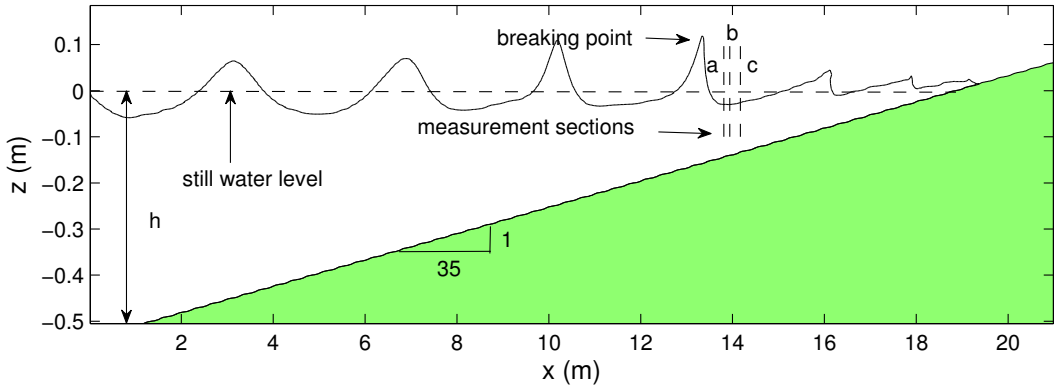

Figure 4.1: Computational domain and measurement sections. The computational domain is 21 m long by 0.7 m high, with the beach toe 1.0 m from the left boundary. The measured breaking point is located at $x_b = 13.07$ m. Three measurement sections are located at (a) $x = 13.81$ m; (b) $x = 13.94$ m and (c) $x = 14.17$ m, respectively.

coupling of VOF model which resolves large air cavities and dispersed bubble model. In the present study, we will not deal with such complex processes. Therefore, the test case we selected is characterized by a spilling breaker, in which the interactions between large air cavities and dispersed bubbles are negligible. The incident wave height is 0.11 m and wave period is 2.0 s.

A 2D simulation with a nonlinear $k-\epsilon$ turbulence model has been conducted. The computational domain is taken as 21 m long by 0.7 m high, with the beach toe 1.0 m from the left boundary (see figure 5.4). The measured breaking point is located at $x_b = 13.07$ m. Three measurement sections are located at (a) $x = 13.81$ m, (b) 13.94 m and (c) 14.17 m.

The computational domain is discretized by a uniform grid with $\Delta x = 0.03$ m, $\Delta z = 0.01$ m. The time step is automatically adjusted during the computation to satisfy stability constraints. Both mean velocities and free surface displacement are specified on the left boundary. On the top boundary, pressure is set to be zero.

Adjacent to a solid wall, the law-of-the-wall boundary conditions for k and ϵ are applied (Wu, 2004). Bubbles are divided into $NG = 20$ groups with a logarithmic distribution of bubble sizes. Moraga et al. (2008) pointed out that logarithmic distribution is preferable over an equally spaced distribution as it helps ensure that the ratio $\Delta d_{bi}/d_{bi}$ is small even for small d_{bi}, where Δd_{bi} is the width of the bin centered at d_{bi}. They also found no significant differences in the simulation results for $NG = 15, 30$ or 60, but $NG < 15$ should be avoided.

There are two free parameters in the bubble entrainment model that have to be determined during the simulation: the critical turbulent dissipation rate ϵ_c and bubble entrainment coefficient c_b. The critical turbulent dissipation rate determines when and where the bubbles are entrained. Its value is equal to the turbulent dissipation rate on the free surface cell at breaking point. In the current case, we take $\epsilon_c = 0.01 m^2/s^3$. The void fraction predictions are more sensitive to the bubble entrainment coefficient c_b, because it determines how many bubbles are entrained into the water column in a single wave breaking event. In order to calibrate the model, we have performed a series of test runs with different bubble entrainment coefficient c_b. It was found that c_b and mean void fraction have a nearly linear relation. An 50% increase of c_b could result in around 38% increase of mean void fraction. An 50% decrease of c_b could result in around 30% decrease of mean void fraction. In the current simulation, c_b was taken as 0.18, which leads to good comparisons with the experimental data as shown below.

4.2 Numerical Results

4.2.1 Comparisons with Experimental Data

In this section, we present the comparisons between experimental data and numerical results. Our comparisons are focused on wave height distribution, wave setup, skewness, free surface elevation, streamwise velocity, turbulence intensity and

void fraction. To quantitatively measure the model/data agreement, a model skill is assessed using the statistical method developed by Wilmott (1981).

$$\text{Skill} = 1 - \frac{\sum_{i=1}^{N} |X_{\text{mod}} - X_{\text{obs}}|^2}{\sum_{i=1}^{N} \left(|X_{\text{mod}} - \bar{X}_{\text{obs}}| + |X_{\text{obs}} - \bar{X}_{\text{obs}}| \right)^2} \tag{4.1}$$

where X is the variable being compared, $\bar{X}$ is its sample mean, and the subscripts $()_{\text{mod}}$ and $()_{\text{obs}}$ stand for model result and observation, respectively. As discussed by Li et al. (2005), this skill parameter measures the degree to which the observed deviations about the observed mean correspond to the predicted deviations about the observed mean. Perfect agreement between the model results and observations yields a skill of 1.0 whereas complete disagreement yields a skill of 0.

Figure 4.2 shows the comparison of simulated and measured wave height distribution, wave setup and skewness along the beach. The wave height is estimated from the free surface elevation, which is evaluated as $VOF = 0.5$. As we can see, the simulated wave height agrees reasonably well with the measurement. The predictive skill is up to 0.95, although the model predicts wave breaking a little earlier than measurement. The simulated breaking point is around $x = 12.5\ m$, which is 0.57 m on the left of the measured breaking point. This discrepancy is introduced by the traditional $k - \epsilon$ turbulence closure model, which cannot accurately predict the initiation of turbulence in a rapidly distorted shear flow such as breaking waves (Lin and Liu, 1998). The distance between the simulated and measured breaking point is short, which is extremely important for the bubble simulation because the location of breaking point determines the initiation of bubble entrainment. The wave setup is estimated from the surface elevation of three wave periods. The wave setdown and setup around breaking point are captured by the model. Comparisons with the measured wave setup at three sections show that the model slightly over-predicts the wave setup after wave breaking. In figure 4.2, we also plot the wave skewness and asymmetry, which are important indicators of nonlinear wave behavior. Skewness

is defined as

$$Skewness = \frac{<\eta^3>}{<\eta^2>^{3/2}} \tag{4.2}$$

where <> is the averaging operator; and the mean $\bar{\eta}$ has been removed from the time series of surface elevation. Asymmetry is defined as

$$Asymmetry = \frac{<H(\eta)^3>}{<\eta^2>^{3/2}} \tag{4.3}$$

where $H()$ is the Hilbert transform. Both skewness and asymmetry increase in magnitude as wave shoals toward the beach. Skewness reaches a maximum value around the breaking point, then decreases as the breaking bore propagates to the shoreline. Comparisons with the measurements at three sections demonstrate that the model slightly under-predicts skewness after wave breaking. The asymmetry increases slowly before wave breaking. After wave breaking, the wave becomes increasingly asymmetric. The model overestimates the wave asymmetry at the three measurement sections.

The free surface elevation, streamwise velocity and void fraction at all three sections have been compared with measurements. Since the Navier-Stokes equations are not solved in the air region, the velocity and void fraction are zero as long as the measured locations are completely exposed to air, which indicates that void fraction is only contributed by dispersed bubbles. This assumption is reasonable as no large air pockets are generated in a spilling breaker. Figure 4.3 shows the comparisons of surface elevation and streamwise velocities at section (a). The predicted surface elevation agrees well with the measurement, with predictive skill 0.97. However, the velocities, especially above the still water level (SWL), are poorly predicted. The comparisons are increasingly better inside the water column. The predictive skills at four locations of this section are 0.52, 0.45, 0.70 and 0.86, respectively. Figure 4.4 demonstrates the comparisons of surface elevation and streamwise velocities at section (b). The predictive skill of free surface elevation is high as 0.98, indicating that the free surface can be well tracked by the VOF approach. The comparisons of

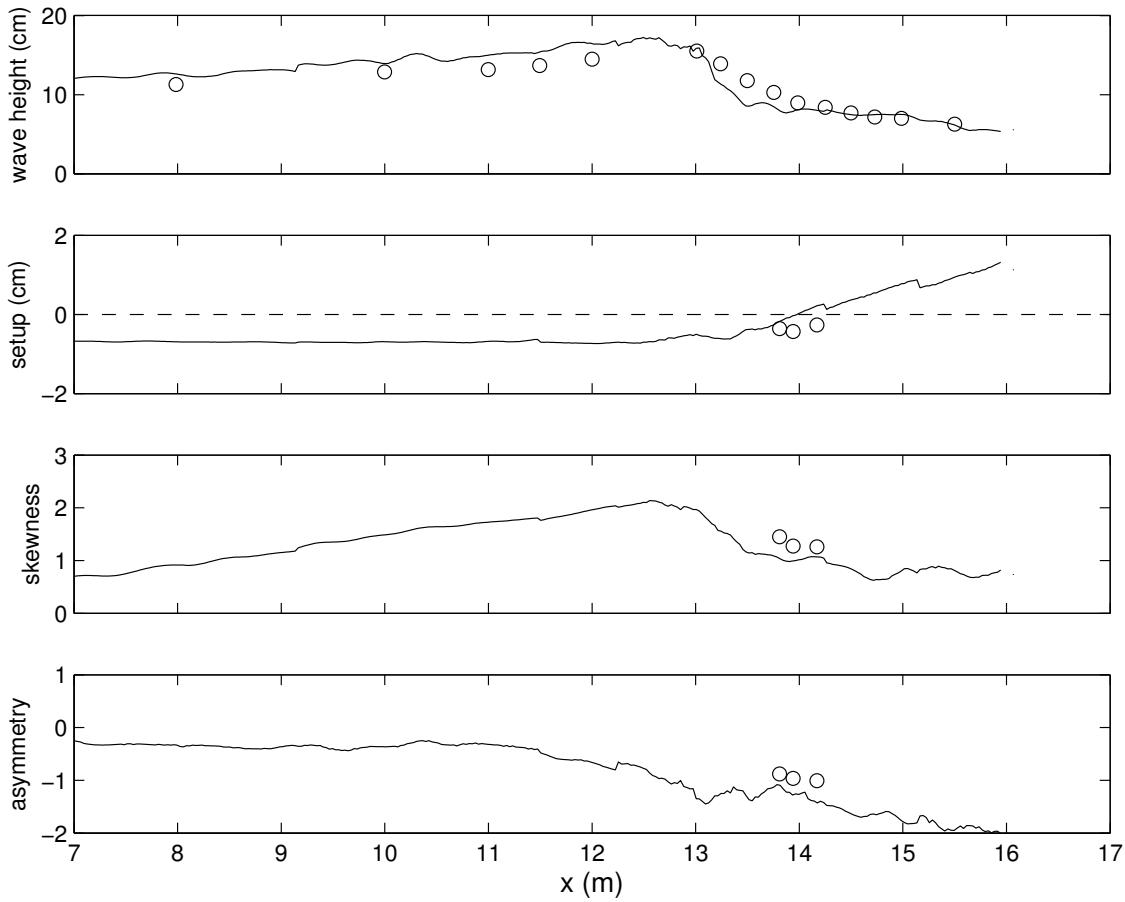

Figure 4.2: Comparisons of simulated and measured wave height distribution, wave setup/setdown, skewness and asymmetry. The predictive skill of wave height distribution is 0.95. Line: simulated; Circle: measured.

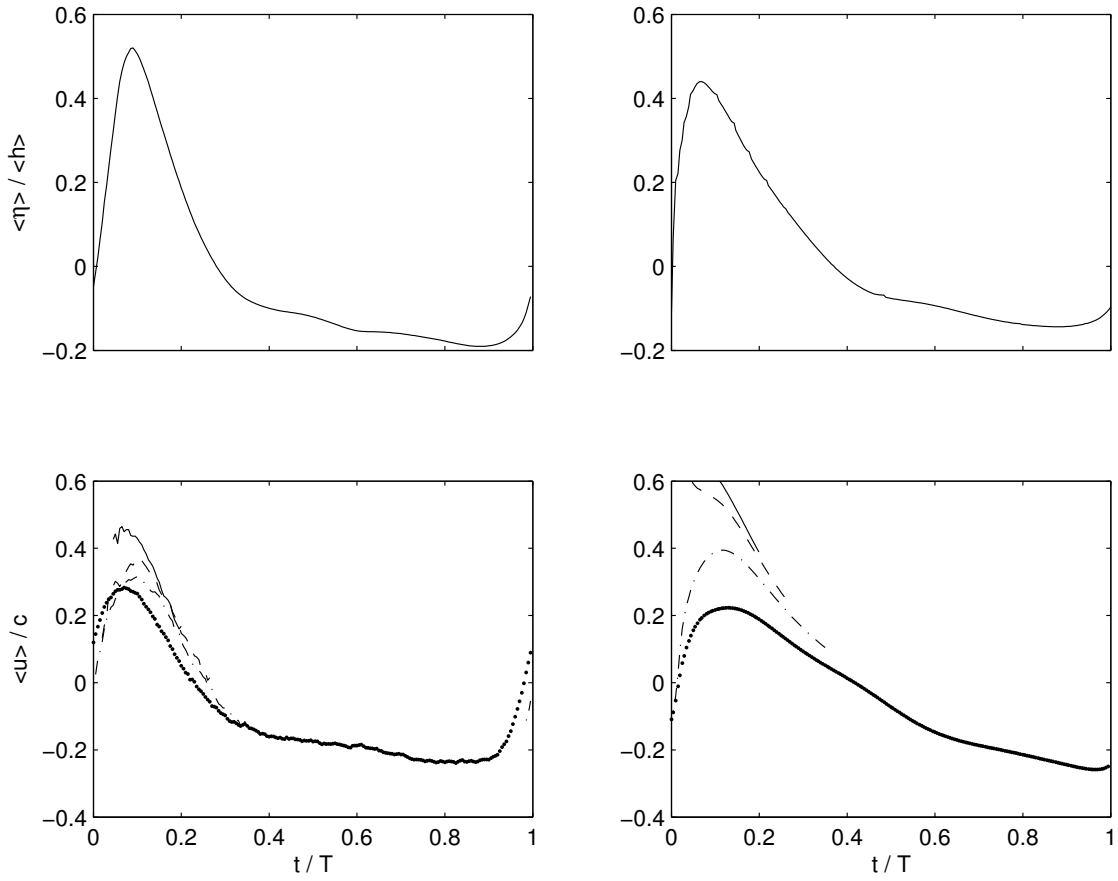

Figure 4.3: Comparisons of measured (left panels) and simulated (right panels) free surface and streamwise velocities at section (a). In the velocity panels, solid line: $z = 1.5\ cm$; dashed line: $z = 0.0\ cm$; dash-dotted line: $z = -1.5\ cm$; dotted line: $z = -4.5\ cm$.

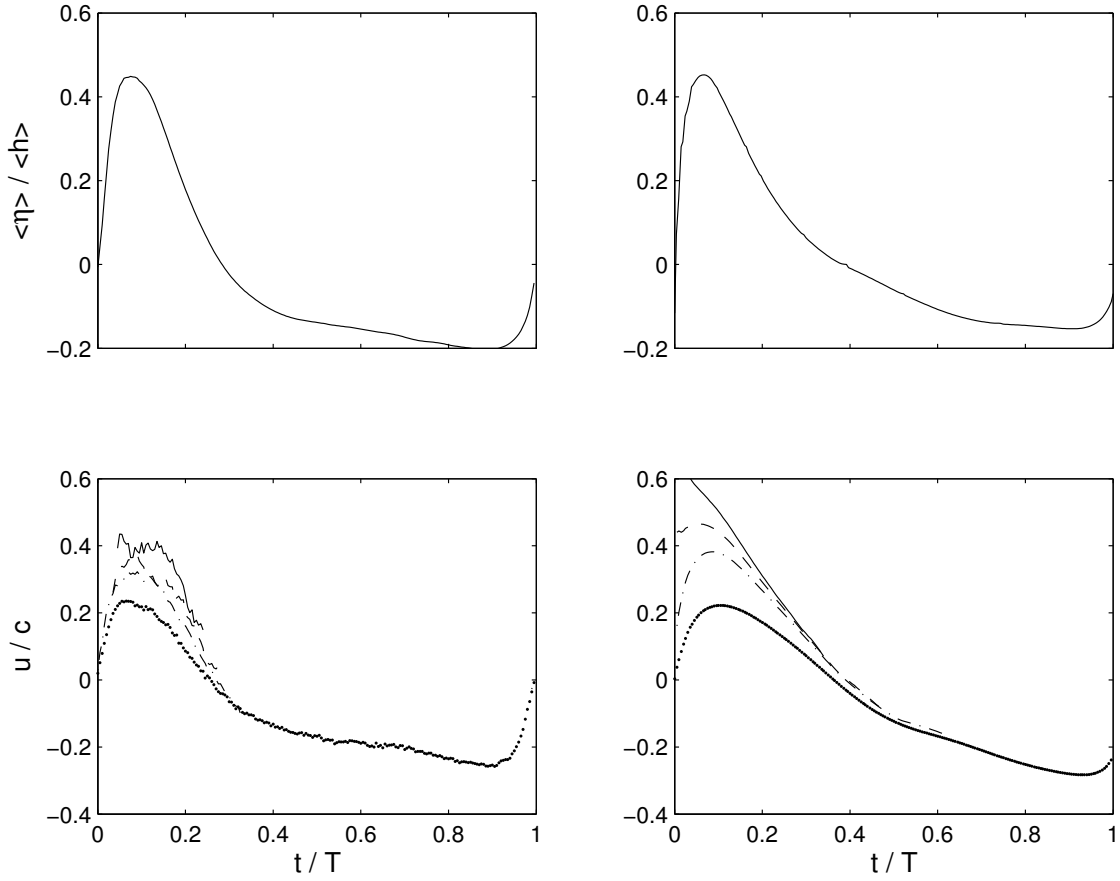

Figure 4.4: Comparisons of measured (left panels) and simulated (right panels) free surface and streamwise velocities at section (b). In the velocity panels, solid line: $z = 0.5\ cm$; dashed line: $z = -0.5\ cm$; dash-dotted line: $z = -1.5\ cm$; dotted line: $z = -4.5\ cm$.

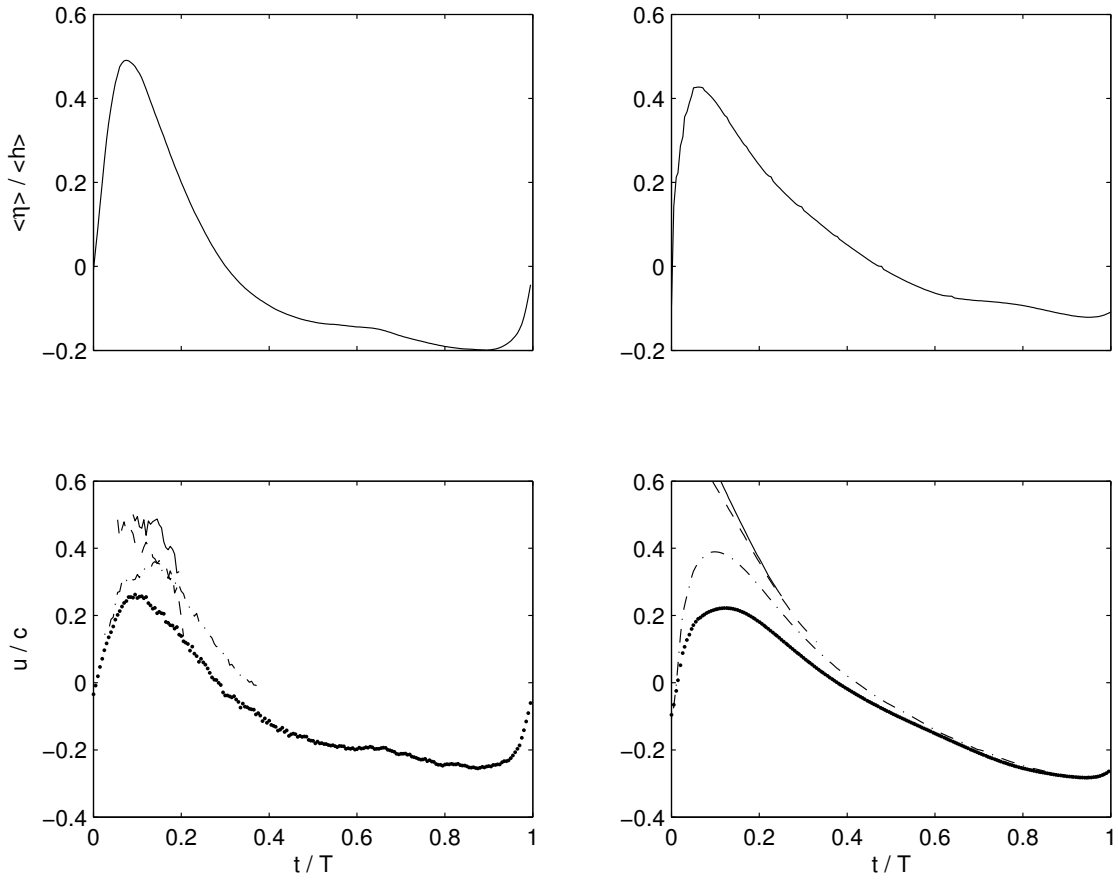

Figure 4.5: Comparisons of measured (left panels) and simulated (right panels) free surface and streamwise velocities at section (c). In the velocity panels, solid line: $z = 2.5\ cm$; dashed line: $z = 1.5\ cm$; dash-dotted line: $z = -1.5\ cm$; dotted line: $z = -4.5\ cm$.

streamwise velocities are reasonably good, with predictive skills of 0.83, 0.81, 0.84 and 0.97 at four elevations, respectively. The differences between simulation and measurement are mainly in the lee side of the wave. Meanwhile, the velocities above the SWL are overestimated. The same comparisons at section (c) are given in figure 4.5. Again, the surface elevation is well predicted, with skill of 0.94. The velocities above the SWL are again overpredicted. The predictive skills are 0.64, 0.58, 0.94 and 0.96 at four elevations, respectively. Because Cox and Shin (2003) only measured streamwise velocities, we cannot make direct comparisons of turbulent kinetic energy (TKE). Therefore, we compared measured $\sigma_u^2/\sigma_{umax}^2$ with simulated k/k_{max}, which is demonstrated in figure 4.6. As we can see, the general trends of turbulence intensity evolution at different vertical locations are captured by the model. There are some intense fluctuations in the measurement, which cannot be predicted by a RANS simulation. Figure 4.7 $\sim$ 4.9 give the comparisons of temporal variations of void fraction at different vertical locations of section (a), (b) and (c). At section (a), the numerical results agree fairly well with the measurements, with predictive skills 0.98, 0.90 and 0.92, respectively. At section (b), although the model underestimates the peak void fraction at some locations under the SWL, the general evolutions of void fraction are captured, with predictive skills 0.86, 0.88, 0.78, 0.81 and 0.80, respectively. The void fractions above the SWL are well predicted at section (c), with skills of 0.94 and 0.96. However, the void fraction below the SWL is largely underestimated.

4.2.2 Void Fraction Evolution

In this section, we examine the evolution of void fraction after wave breaking. Cox and Shin (2003) have shown that the temporal variation of void fraction above the SWL, normalized respectively by wave period and average void fraction, appears to be self-similar and can be modeled simply using the following equation with linear

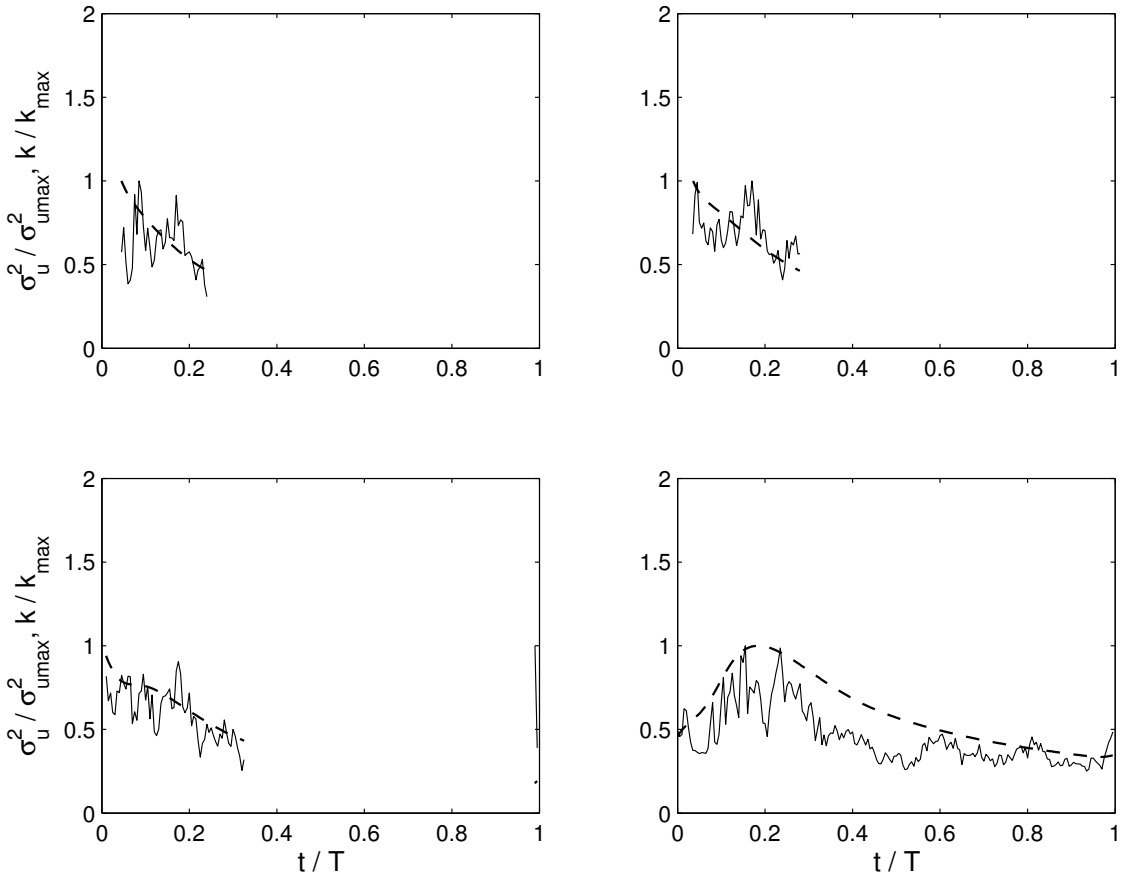

Figure 4.6: Comparisons of measured (solid line, $\sigma_u^2/\sigma_{umax}^2$) and simulated (dashed line, k/k_{max}) turbulence intensity of section (b) at different vertical locations (a) $z = 0.5\ cm$; (b) $z = -0.5\ cm$; (c) $z = -1.5\ cm$ and (d) $z = -4.5\ cm$.

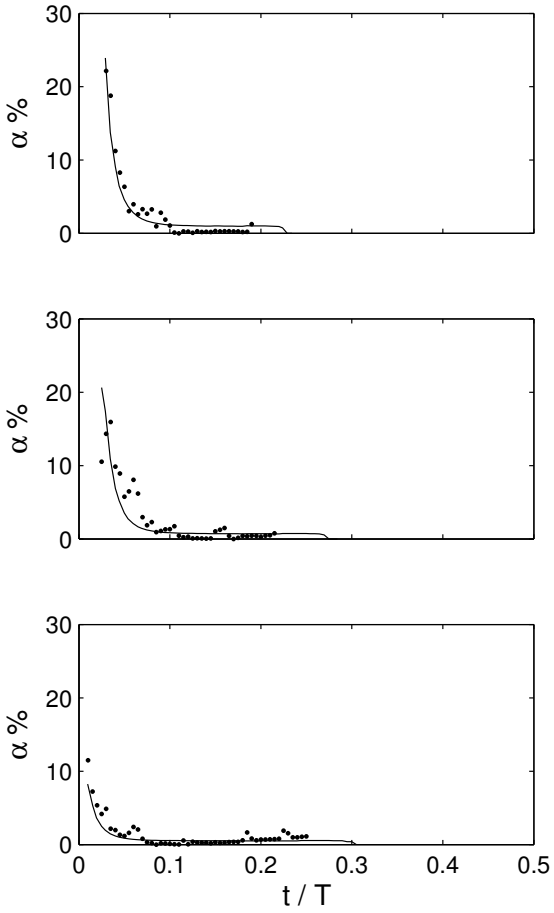

Figure 4.7: Comparisons of simulated and measured void fractions of section (a) at three vertical elevations (a) $z = 2.5\ cm$, (b) $z = 1.5\ cm$, (c) $z = 0.0\ cm$

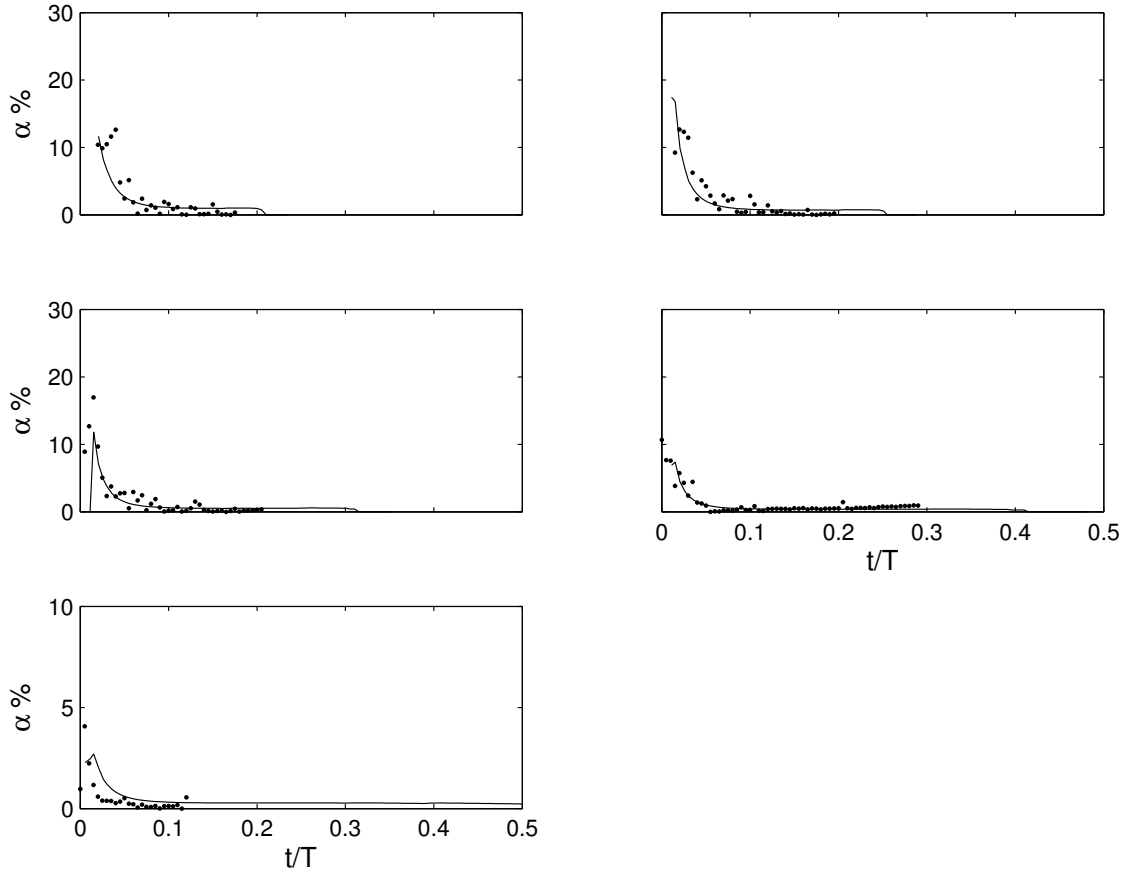

Figure 4.8: Comparisons of simulated and measured void fractions of section (b) at five vertical elevations (a) $z = 2.5\ cm$, (b) $z = 1.5\ cm$, (c) $z = 0.5\ cm$, (d) $z = -0.5\ cm$ and (e) $z = -1.5\ cm$.

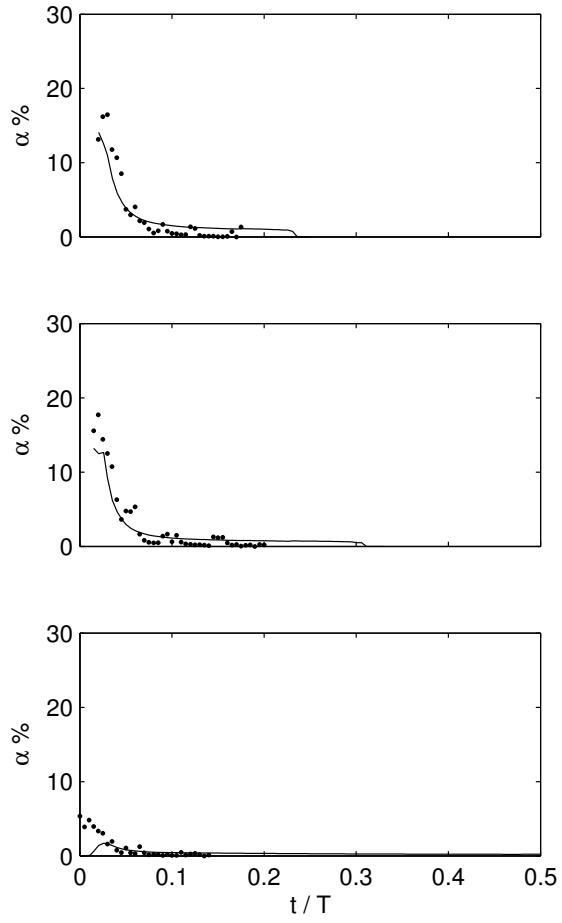

Figure 4.9: Comparisons of simulated and measured void fractions of section (c) at five vertical elevations (a) $z = 2.5\ cm$, (b) $z = 1.5\ cm$, (c) $z = -1.5\ cm$.

growth and exponential decay.

$$\frac{\alpha}{\alpha_{ave}} = a(\frac{t^{'}}{T})\exp[-b(\frac{t^{'}}{T})] \tag{4.4}$$

where $a = 800, b = 90$. They also showed that the temporal variation of void fraction below the SWL can be described by the same equation with a different parameter $b = 100$. These variations are also observed in our numerical results which are depicted in figure 4.10. Above the still water level, the exponential decay of simulated void fraction is well captured by the model, with excellent agreement between the measurements and equation 4.4. The linear growth of void fraction is associated with bubble entrainment in the acoustic phase. In the numerical simulations, bubbles are introduced by an entrainment formulation, which introduces a sudden increase of void fraction as shown in figure 4.10. The simulated maximum void fraction is approximately four times the average, which is greater than the measurement. The maximum void fraction can be adjusted by the entrainment coefficient c_b in the model. But with the considerations of overall comparisons, $c_b = 0.18$ was chosen to give the best results. Below the still water level, the general trend of void fraction decay is similar to that above the still water level. The predicted peak void fraction is close to the measured value, but the void fraction decays slightly more slowly than the measurement.

As the bubble entrainment in our model is directly related to turbulent dissipation rate, it is instructive to look at turbulent dissipation rate and void fraction distribution simultaneously. These snapshots are shown in figure 4.11, where the turbulent dissipation rate is normalized by $g\sqrt{g(h+H)}$, g is gravity acceleration, h is still water depth, H is incident wave height. The plotted void fractions are bounded by 0.3% following Lamarre and Melville (1991, 1994), who used 0.3% as a threshold to evaluate various moments of the void fraction field. In these two figures, x_b is the measured breaking point. We can see that the evolution patterns of turbulent dissipation rate and void fraction are generally similar. When waves

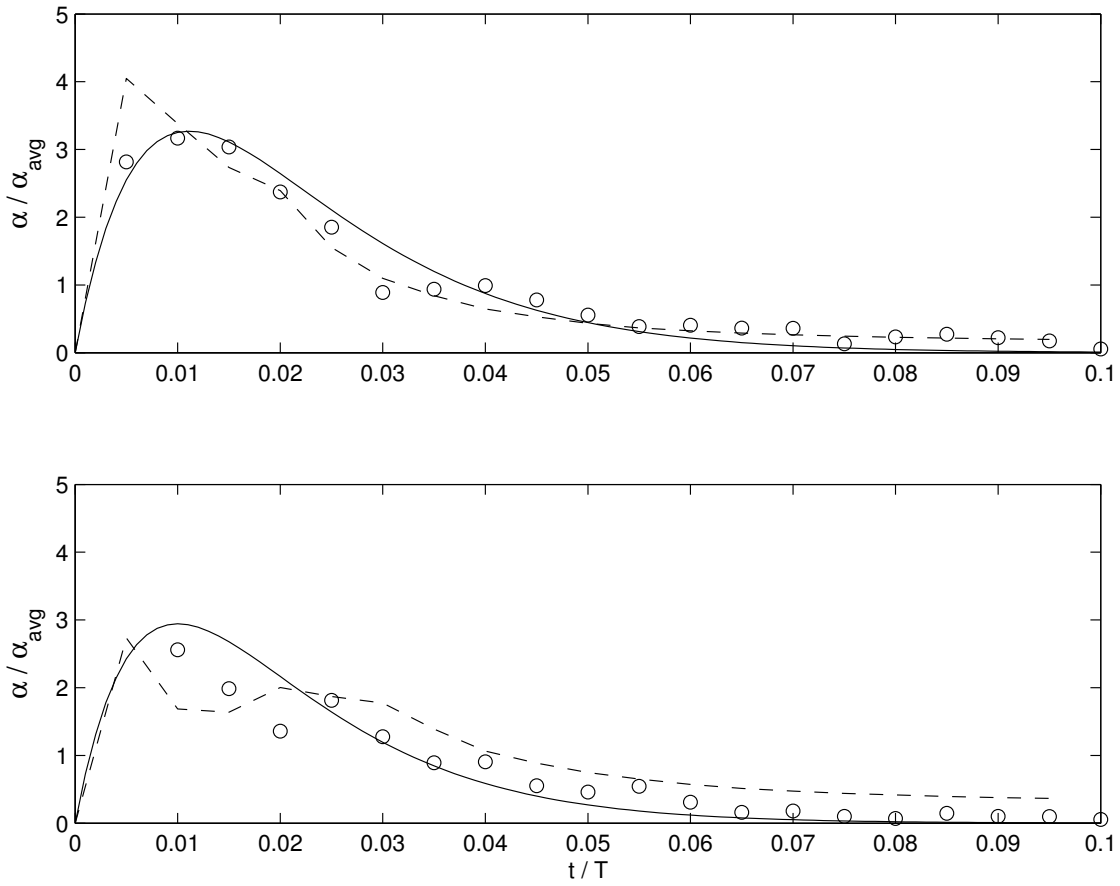

Figure 4.10: Temporal variations of mean void fraction above (upper panel) and below (lower panel) still water level. Line: Equation (4.4) with $a = 800$, $b = 90$ in the upper panel and $a = 800$, $b = 100$ in the lower panel; dashed line: simulations; circles: measurements.

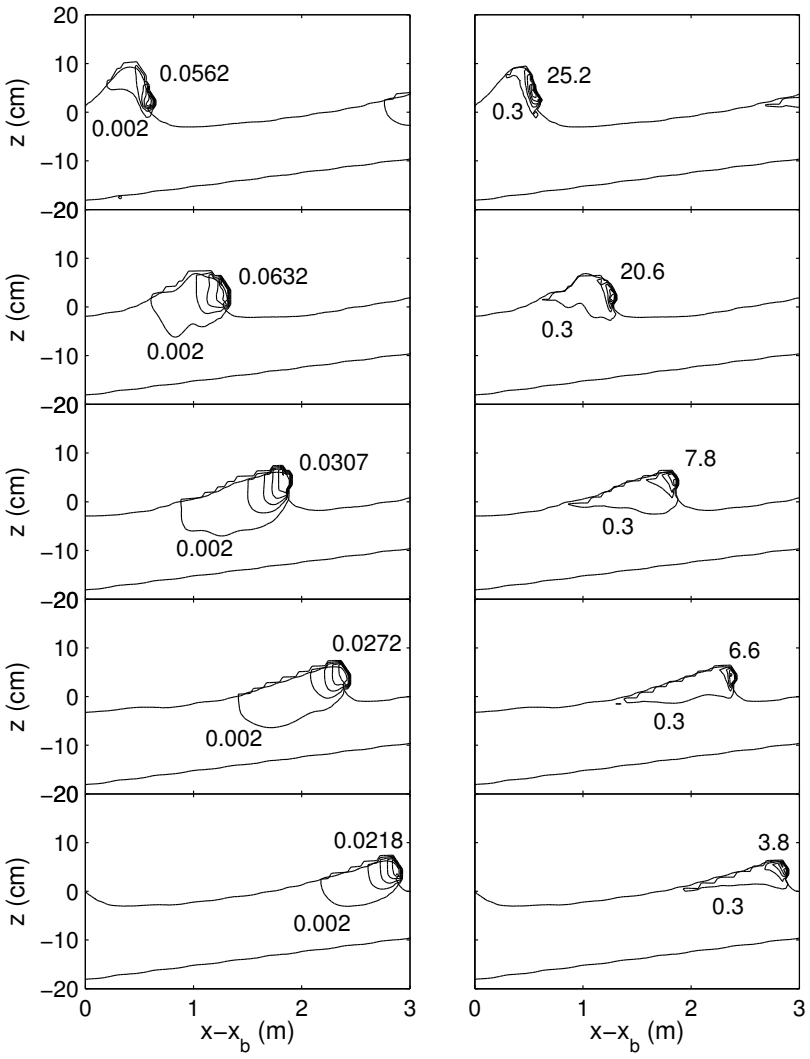

Figure 4.11: Snapshots of turbulence dissipation rate normalized by $g\sqrt{g(h+H)}$ (left panels) and void fraction (right panels) after wave breaking at (a) $(t-t_b)/T = 0.10$; (b) $(t-t_b)/T = 0.30$; (c) $(t-t_b)/T = 0.50$; (d) $(t-t_b)/T = 0.70$; (e) $(t-t_b)/T = 0.90$, where t_b is the time for initial breaking, $x_b = 12.5\ m$ is the simulated the breaking point, g is gravity acceleration, h is still water depth, H is incident wave height. The minimum and maximum values are shown in each snapshot. The contours are equally divided into 5 layers.

start to break, the turbulent dissipation rate is greater than ϵ_c, resulting in the commencement of bubble entrainment. As the breaking bore moves forward, both turbulent dissipation rate and void fraction increase rapidly and reach their maximum values shortly after wave breaking. Interestingly, the void fraction reaches its peak value earlier than the turbulent dissipation rate. The reason is possibly because the amount of bubbles entrained into the water column is not only determined by the dissipation rate, but also by void fraction at the surface layer as shown in the bubble entrainment model (equation 2.35). The peak void fraction appears around $0.15L$ onshore from the breaking point, where L is wavelength at breaking point. This result is consistent with the findings of Mori et al. (2007), who argued that the peak of void fraction happens at 0.1 to 0.2 wavelength onshore from the breaking point. After reaching the maximum, both the turbulent dissipation rate and void fraction start to decrease. The high turbulence region is persistently located at the breaking wave crest with a moderate time variation in its value, while the void fraction varies by an order of magnitude in a wave period. The higher void fractions are restricted to the roller region, but some bubbles are spread downstream and form a long tail of the bubble cloud under the water surface. The correlation between average turbulent dissipation rate and void fraction is displayed in figure 4.12, where the turbulent dissipation rate is normalized by $g\sqrt{g(h+H)}$. Similar to the findings of Cox and Shin (2003), the turbulent dissipation rate and void fraction are positively correlated. Above the still water level, where the turbulence intensity is relatively strong, the void fraction and turbulent dissipation rate are linearly correlated. In the low turbulence region which is normally located under the still water level, the void fraction and turbulent dissipation rate deviate from the linear relationship. The reason is possibly because bubble entrainment dominates void fraction simulation above the still water level, while turbulent diffusion plays the most important role under the still water level.

Figure 4.13 shows the void fraction contributions from the $1st$, $10th$ and $20th$ bubble group at $(t - t_b)/T = 0.3$. The characteristic radii of these bubble groups are 0.11 mm, 0.90 mm and 8.97 mm, with the bubble volume as 5.6 $\times 10^{-12}$ m^3, 3.0 $\times 10^{-9}$ m^3 and 3.0 $\times 10^{-6}$ m^3, respectively. The huge differences of bubble volumes among bubble groups are expected to result in different contributions to the void fraction. The $20th$ group bubbles contribute to the void fraction one order more than the $10th$ group, and $2 \sim 3$ orders more than the $1st$ group. Figure 4.14 demonstrates the number density distributions of the $1st$, $10th$ and $20th$ bubble group at $(t - t_b)/T = 0.3$. Since the rise velocities of small bubbles (for example, the $1st$ and $10th$ bubble groups) are much smaller than those of large bubbles (for example, the $20th$ bubble group), it is easier to transport small bubbles into the water column. Small bubbles can be transported downward to the bottom, while large bubbles are mainly restricted in the roller region near the surface. Owing to their longer retention time, small bubbles can interact with the next breaking wave event, whereas large bubbles generally have degassed from the water column after passage of the breaking wave crest.

4.2.3 Bubble Plume Kinematics

To study the kinematics of the bubble plume, we first calculate its horizontal centroid x_c and vertical centroid z_c

$$(x_c, z_c) = \frac{\int_A \alpha(x, z) dA}{\int_A \alpha dA} \tag{4.5}$$

where α is the void fraction, x is the distance from the breaking point, z is the distance from the free surface, A is the cross-sectional area of the bubble plume. Following Lamarre and Melville (1991, 1994), we use 0.3% as a threshold of void fraction to evaluate the centroid. The results are shown in figure 4.15 where the horizontal and vertical centroids are normalized by the breaking wave length and wave height, respectively. Within $t \leq 0.4T$, the horizontal centroid roughly moves at

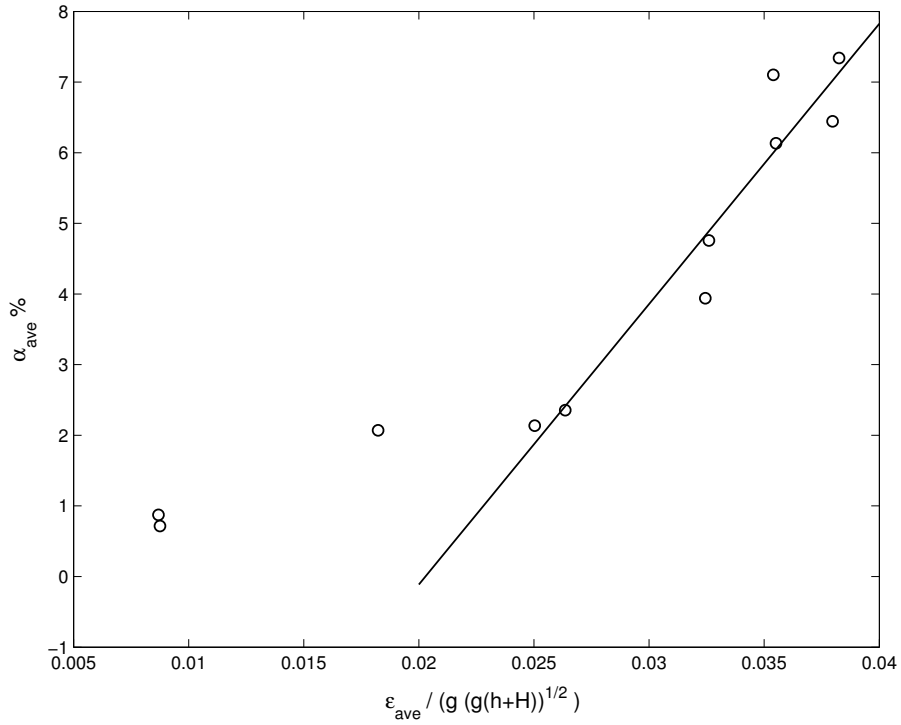

Figure 4.12: Relationship between average turbulent dissipation rate and void fraction estimated from the measurement locations. The turbulent dissipation rate is normalized by $g\sqrt{g(h+H)}$, where g is gravity acceleration, h is still water depth, H is incident wave height. The turbulent dissipation rate and void fraction are linearly correlated in the high turbulence region.

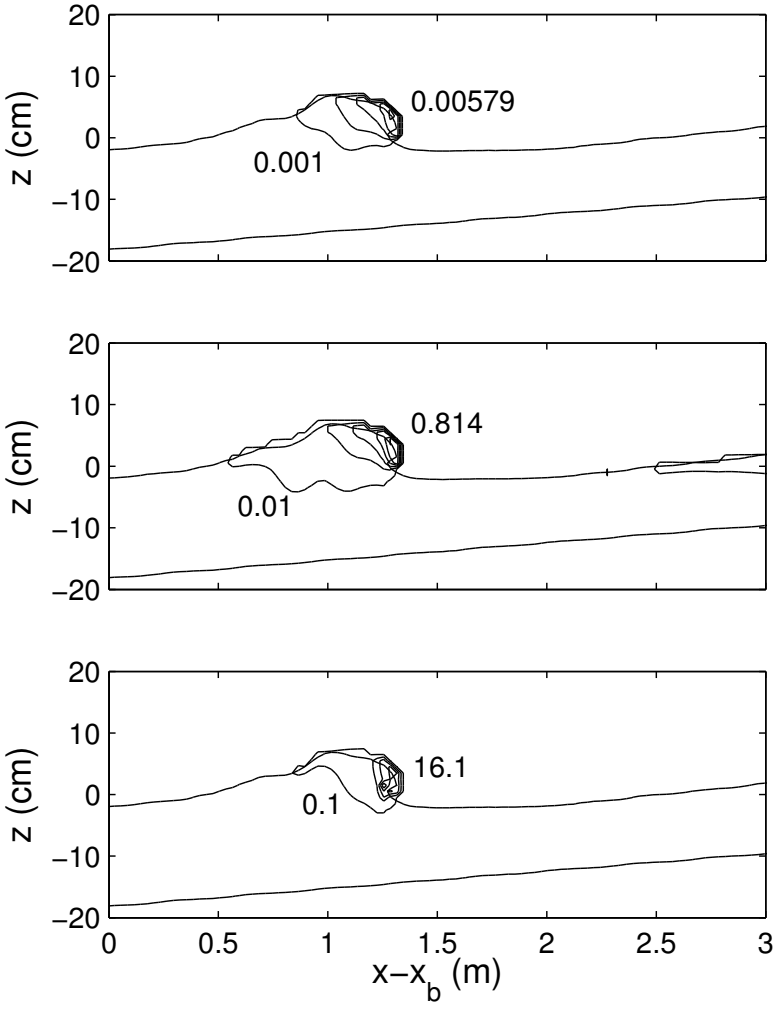

Figure 4.13: Void fraction contributions from the $1st$ (upper panel), $10th$ (middle panel), $20th$ (lower panel) bubble group at $(t - t_b)/T = 0.3$. The minimum and maximum void fractions are shown in each panel. The contours are equally divided into 5 layers.

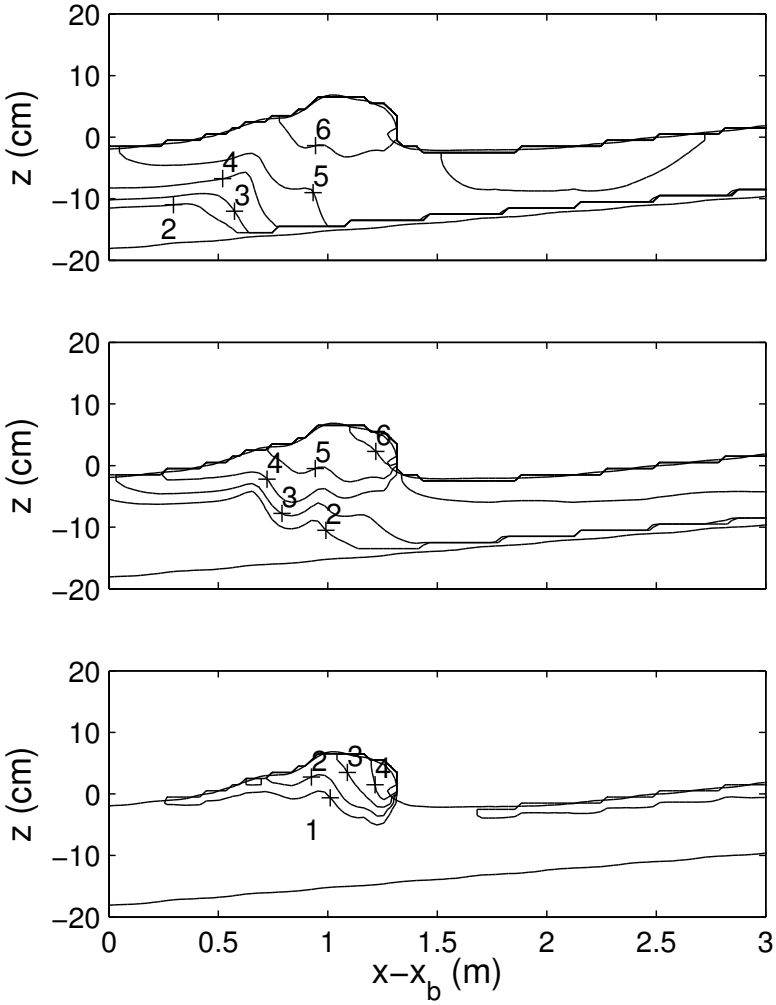

Figure 4.14: Bubble number density ($N_{g,i}$) distributions (in log_{10} values) of the $1st$ (upper panel), $10th$ (middle panel) and $20th$ (lower panel) bubble group at $(t - t_b)/T = 0.3$.

the phase speed of the breaking wave. This result is consistent with the finding in the 2-D deep-water breaking wave (Lamarre and Melville, 1991). After $0.4T$, bubbles are gradually spread downstream, and the horizontal centroid moves slightly slower than the breaking wave. In the vertical, the bubble plume moves quickly downwards to about $0.18H_b$ in about $0.4T$. In the following stage ($0.4T - 1.0T$), the vertical centroid starts to move upwards to about $0.1H_b$ after one wave period. From the temporal variations of horizontal and vertical centroids, we can conclude that the bubble plume first moves deeper in the water column, then spreads downstream behind the breaking wave crest.

Another important parameters describing the bubble plume are the total volume of entrained air V and the work required to keep the air entrained against the buoyancy force E (Lamarre and Melville, 1991). These two parameters are calculated as follows.

$$V = \int_A \alpha dA \tag{4.6}$$

$$E = \rho_l g \int_A \alpha z dA \tag{4.7}$$

where A is the total cross-sectional area of the bubble plume above a void-fraction threshold of 0.3%, ρ_l is the liquid density, g is the acceleration due to gravity. Figure 4.16 shows the temporal variation of V and E which are normalized by $V_0 = V(t = t_b)$ and $E_0 = E(t = t_b)$, respectively. In the early stage of wave breaking, bubbles are kept entraining into the water column, both V and E increase to their maximum values in about $0.35T$. After $t - t_b = 0.35T$, degassing becomes dominant rather than bubble entrainment, and the bubble plume starts to decay. From figure 4.16, we can see that the variation of both V and E after reaching the maximum can be described by an exponential decay. This decaying trend of the bubble plume has also been found by Lamarre and Melville (1991) in a 2-D deep-water breaking wave.

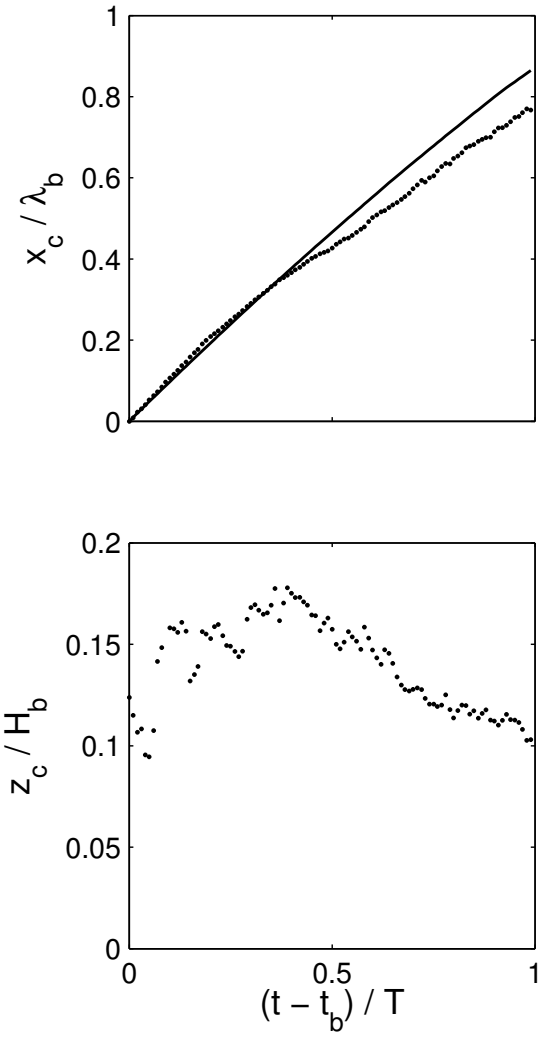

Figure 4.15: Horizontal centroid (upper panel) and vertical centroid (lower panel) of the bubble plume normalized by the breaking wave length and wave height. Solid line is the phase speed of the wave.

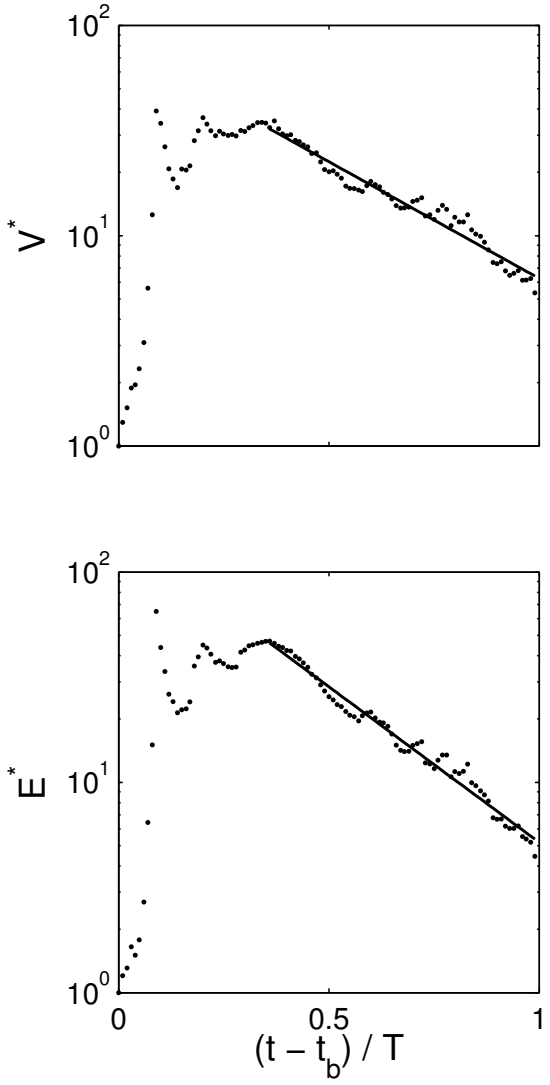

Figure 4.16: Normalized volume of air entrained per unit width (upper panel) and normalized potential energy of the bubble plume required to entrain the air against buoyancy. A linear best fit to the data after reaching the maximum are shown by solid lines.

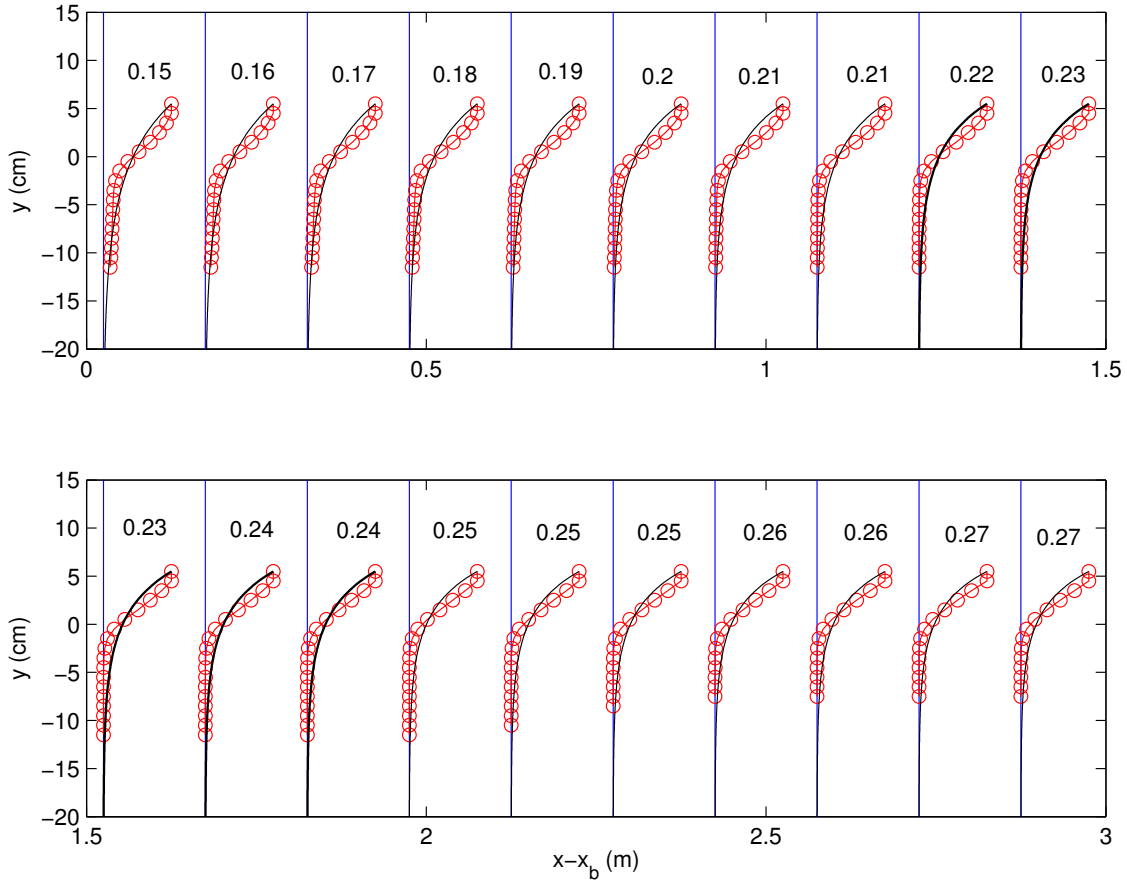

Figure 4.17: Vertical distributions of void fractions contributed by different bubble groups at $t = t_b + 0.5T$ (smallest to largest bubble group from left to right). The solid lines are the exponential fits of the distributions.

4.2.4 Parameterization of Bubble Plume

According to Wu (1988), the vertical distributions of void fractions can be parameterized as

$$C(z) = C_m exp(k_z(z - z_m)) \tag{4.8}$$

which satisfies the following conditions

$$C(z) = C_m \quad z = z_m \tag{4.9}$$

$$C(z) \to 0 \quad z \to -\infty \tag{4.10}$$

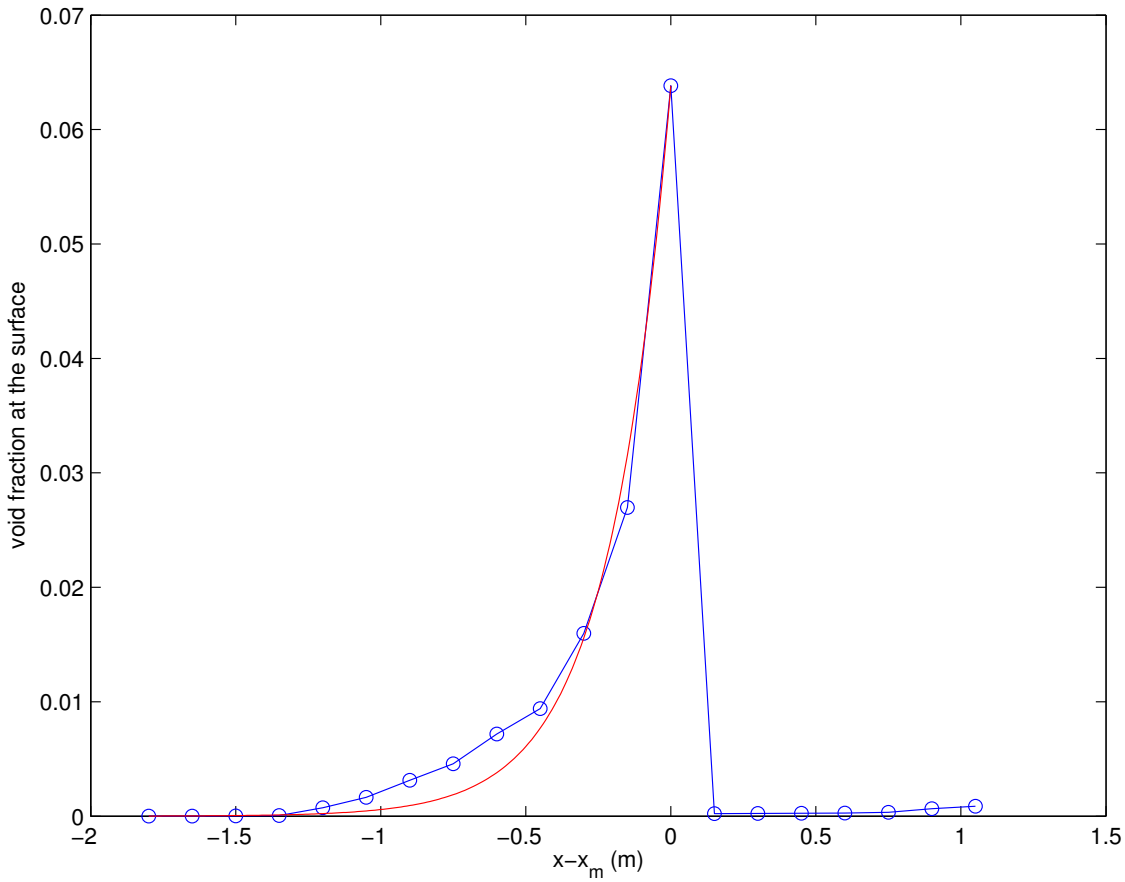

Figure 4.18: Distributions of void fractions at free surface in the cross-shore direction at $t = t_b + 0.5T$. Solid-circle line: simulated void fractions; Solid line: exponential fit with $k_x = 4.7$.

where C_m is the maximum void fraction, z_m is the vertical location of maximum void fraction, which is normally at the free surface. k_z is the decay rate, which depends on the vertical penetration of bubble clouds. Deeper penetration results in smaller values.

Figure 4.17 shows the simulated vertical distributions and parameterizations of void fractions contributed by different bubble groups at $t = t_b + 0.5T$. The decay rates for different groups are shown accordingly. As we can see that, the vertical distributions of void fractions contributed by different bubble groups can be well described by equation (4.8). Smaller bubbles can penetrate deeper into the water column with smaller decay rates. The decay rate of the largest bubbles can be approximately two times bigger than that of the smallest bubbles.

The cross-shore distributions of void fraction can also be described by an equation similar to equation 4.8, which is written as

$$C(x) = C_m exp(k_x(x - x_m)) \tag{4.11}$$

where k_x is the horizontal decay rate, x_m is the cross-shore location of maximum void fraction, which is usually located at the breaking wave front, C_m is the maximum void fraction at free surface in the cross-shore direction.

Figure 4.18 displays the cross-shore distribution of void fractions at free surface and the parameterization at $t = t_b + 0.5T$. We can see that the void fraction distribution can be well described by equation (4.11). The maximum void fraction is located at the wave front as expected. The void fraction drops to zero around $1.5m$ behind the wave crest.

4.3 Discussion

We have shown that the model compares reasonably well with experimental data. It is also capable of capturing physical mechanisms of the bubbly flow field in breaking waves such as void fraction evolution and bubble plume kinematics.

But some discrepancies still exist in terms of void fraction prediction. A primary source of these discrepancies comes from the 2D $k-\epsilon$ simulation, which cannot describe the detailed interactions between dispersed bubbles and large-scale turbulence. Bubble entrainment under breaking waves is a 3D phenomenon, involving intense interactions between bubbles, turbulence and coherent flow structures, such as obliquely descending eddies and downburst of turbulent fluid. Bubbles are preferentially trapped in vortex cores and then transported toward the bottom along with the descending eddies. This phenomenon cannot be simulated in 2D. Recently, Ting (2008) has observed in the laboratory that downburst of turbulent fluid is an efficient way to transport bubbles to the bottom. The simulation of these interactions requires use of a 3D numerical model, which is left for future work. Another possibility that introduces errors in the void fraction calculations could be because turbulence predictions at the surface cells are somehow contaminated by the air flow. The extensive DNS of counter-current two-phase flow studies of Fulgosi et al. (2003) have revealed the need for turbulence damping approaching deformable air-water interfaces in under-resolved simulations (Liovic and Lakehal, 2007). Currently, we haven't considered this effect in the turbulence simulation. We anticipate that a 3D large eddy simulation with interface dynamics (Lakehal and Liovic, 2010), which can resolve the large scale fluctuations of the velocity field and interface, will improve the simulations of bubbly flow under breaking waves.

In addition to void fraction, another important factor that affects acoustics and optical properties of the water column is bubble size distribution. Garrett et al. (2000) have studied theoretically the bubble size spectrum evolution as a function of time at any depth. Because of buoyancy forces, larger bubbles rise to the free surface faster than smaller ones, thus steepening the size spectrum. Another important process that affects the spectrum is dissolution, which makes bubbles smaller and hence changes the spectral shape (Garrett et al., 2000). Bubble breakup and coalescence

can influence the spectrum as well. During wave breaking, the turbulence intensity varies at different water depth, resulting in different breakup and coalescence rate. In the current simulation, gas dissolution and bubble coalescence haven't been taken into consideration. Therefore, the bubble size spectrum variation at different water depth is mainly caused by the buoyancy forces and bubble breakup.

Figure 4.19 shows the simulated bubble size spectrum at different measurement locations of section (b) at $(t - t_b)/T = 0.40$ without bubble breakup. At this section, bubbles are initially entrained at $(t - t_b)/T = 0.35$. As the water depth increases, the bubble size spectrum becomes steeper because of the buoyancy forces. Meanwhile, the spectrum slope of large bubbles (greater than 1 mm) steepens faster than that of small bubbles (less than 1 mm). At $z = 2.5$ cm, the spectrum slope of bubbles larger than 1 mm is clearly more different from its original value than that of bubbles less than 1 mm.

In order to study bubble breakup effects on the bubble size spectrum, we conducted a test simulation in which entrained bubbles are initially in the 20th group with identical bubble size 8.97 mm. Equation (2.30) with $c_b = 0.18$ was applied to determine how many bubbles are entrained into the water column. Figure 4.20 demonstrates the simulated bubble size distributions at different vertical locations of section (b) at $(t - t_b)/T = 0.40$, when bubbles are diffused all over the measurement locations. Notice that bubbles start entraining at this section at $(t - t_b)/T = 0.35$. The model reasonably predicts the -10/3 dependence for bubbles greater than 1 mm near the free surface. But the -3/2 law for bubbles smaller than 1 mm cannot be reproduced by the model. This result confirms the bubble creation mechanism suggested by Deane and Stokes (2002) that bubbles less than about 1 mm are generated by the jet/wave-face interaction, while bubbles larger than about 1 mm are created by the breakup of air cavities. Because the buoyancy forces dominate bubble size spectrum evolution with depth, the spectrum becomes steeper as the

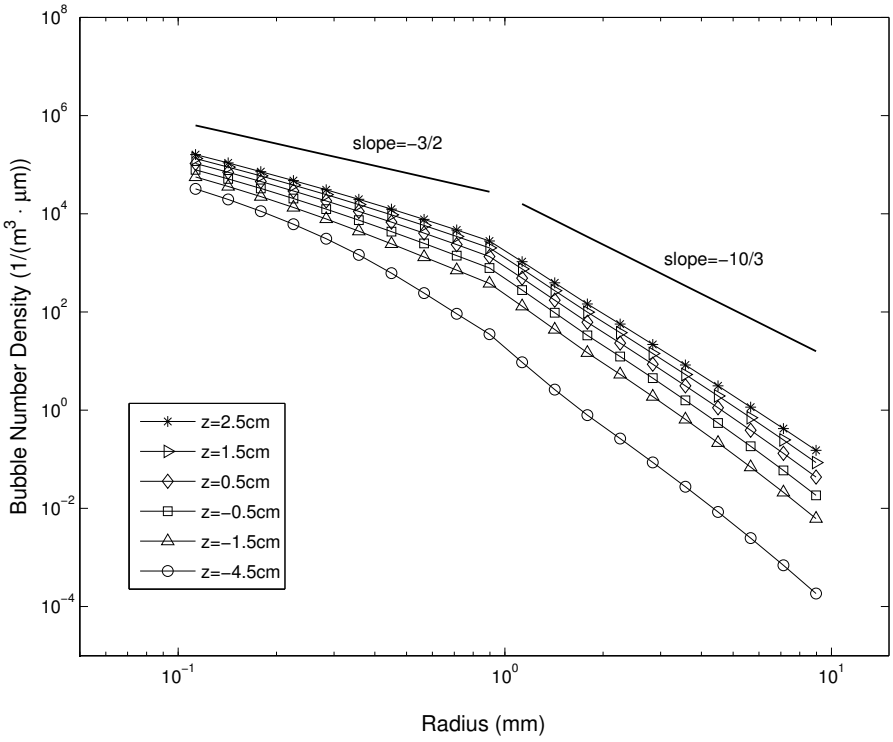

Figure 4.19: Simulated bubble size distribution without bubble breakup effects at different vertical locations of section (b) at $(t-t_b)/T = 0.40$. Bubbles start entraining at this section at $(t-t_b)/T = 0.35$. The solid lines are the measured spectrum slope (Deane and Stokes, 2002).

water depth increase, which is similar to the case without bubble breakup effects.

4.4 Conclusions

In this chapter, the polydisperse two-fluid was employed to study bubble plume dynamics under a spilling breaking wave. The numerical results was tested against the laboratory measurements by Cox and Shin (2003). After choosing the entrainment coefficient as $c_b = 0.18$, comparisons between experimental data and numerical results were reasonably good for wave height distribution, free surface, streamwise velocities and void fraction.

The model reproduces the exponential decay of void fraction as observed by Cox and Shin (2003). Because bubble entrainment is linearly related to turbulent

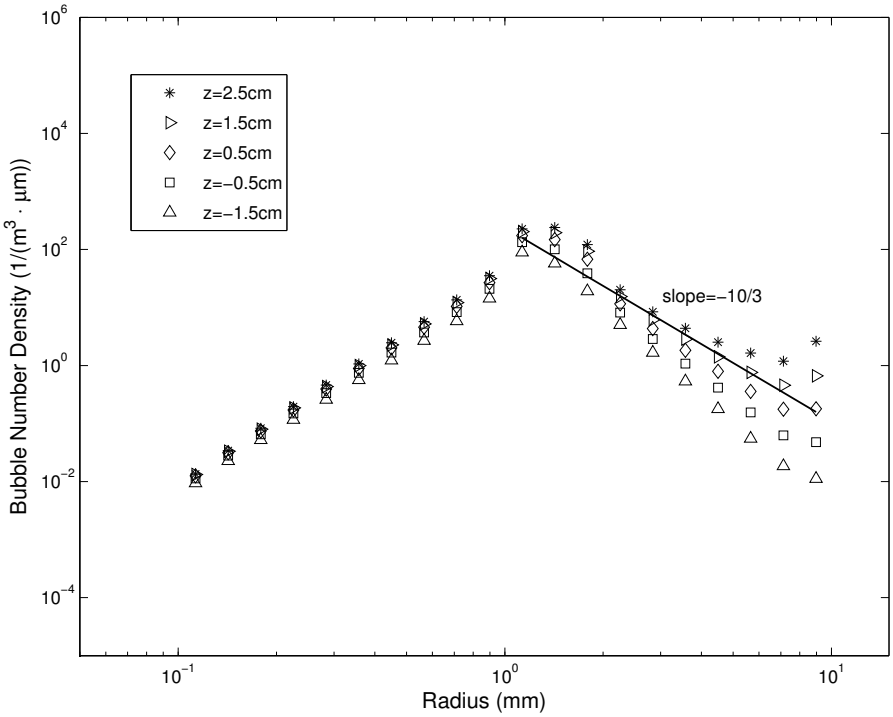

Figure 4.20: Bubble size distribution resulting from bubble breakup at section (b) at $(t - t_b)/T = 0.40$. Bubbles start entraining at this section at $(t - t_b)/T = 0.35$. The solid line is the measured spectrum slope $(= -10/3)$ for bubbles larger than 1 mm (Deane and Stokes, 2002).

dissipation rate in our model, the evolution of simulated void fraction follows that of turbulent dissipation rate. The peak void fraction appears around $0.15L$ (L is wave length) onshore from the breaking point. Through the analysis of different bubble groups, we found that the largest bubbles contribute several orders more to void fraction than the smallest bubbles in our simulation. Small bubbles can be transported to the bottom and spread downstream to interact with the next breaking event, whereas large bubbles have generally degassed after passage of the breaking wave crest.

To study the kinematics of the bubble plume, we also analyzed its centroids (x_c, z_c) and two moments associated with void fraction: the total volume of entrained air V and the work required to keep the air entrained against buoyancy forces E. Numerical results showed that, in the early stage of wave breaking, the horizontal centroid roughly moves at the phase speed of the wave and the vertical centroid moves quickly downstream to around $0.18H_b$. Both V and E increase to their maximum in about $0.35T$. After $0.35T$, the horizontal centroid moves slightly slower than the phase speed because some bubbles are spread downstream. The vertical centroid starts to decrease to about $0.1H_b$ after one wave period. Both V and E decays exponentially as functions of time.

The bubble size spectrum evolution at different water depth was captured by the model. The spectrum becomes steeper as the water depth increases because of the buoyancy. The bubble breakup model developed by Martínez-Bazán et al. (1999a,b; 2010) can reasonably predict the size spectrum for bubbles larger than 1 mm, but cannot capture the -3/2 law for bubbles smaller than 1 mm.

Chapter 5

INTERACTIONS BETWEEN TURBULENT COHERENT STRUCTURES AND DISPERSED BUBBLES

In the previous chapter, we have conducted a 2D RANS simulation to investigate bubble plume dynamics under a laboratory scale surfzone breaking wave. Several questions are still remaining to be answered. For instance, how are bubbles entrained into the water column? How do turbulent coherent structures under breaking waves interact with dispersed bubbles? How do bubbles affect liquid phase turbulence and vorticity field? In this chapter, we are attempting to address these issues. A 3D LES simulation will be conducted to study the detailed interactions between turbulence coherent structures (obliquely descending eddies and downbursts of turbulent fluid) and dispersed bubbles.

5.1 Grid Sensitivity

Numerical study of a breaking wave is initially performed in two-dimensions without bubble effects. The main purposes of the 2D simulations are to assess mesh dependence of the numerical results and to compare with the laboratory measurements. The numerical setup follows the laboratory experiment conducted by Ting and Nelson (2011). The computational domain is 15 m long and 0.60 m deep. The beach has a slope of 0.03, with the beach toe located at 0.563 m from the left boundary. The still water depth in the constant depth region is 0.36 m. A cnoidal wave with wave height of 0.122 m and wave period of 2.0 s is incident from the left boundary.

To assess mesh dependence of the numerical results, we conducted three simulations with different grid size from $(\Delta x, \Delta z) = (0.06, 0.0075)$ down to $(\Delta x, \Delta z) = (0.02, 0.0075)$. Figure 5.1 displays the phase-averaged surface elevations at breaking point (5.127 m from the beach toe) with increased mesh refinement. The evolution of predicted surface elevation with different grid sizes is quite similar. However, the peak surface elevation calculated from a coarse grid $(\Delta x, \Delta z) = (0.06, 0.0075)$ is smaller than those from finer grids. The phase-averaged surface elevations with increased mesh refinement from $(\Delta x, \Delta z) = (0.04, 0.0075)$ to $(\Delta x, \Delta z) = (0.02, 0.0075)$ converge, indicating that the second-finest grid resolution $(\Delta x, \Delta z) = (0.04, 0.0075)$ is adequate for large eddy simulation of the breaking wave.

Figure 5.2 shows the comparison of simulated and measured wave height distribution along the beach using the grid with $(\Delta x, \Delta z) = (0.04, 0.0075)$. The simulated wave heights are determined from a segment of time series five wave periods long. We can see that the simulated wave height compares fairly well with the measurement. Figure 5.3 demonstrates the comparisons of simulated and measured phase-averaged surface elevations at different locations before and after wave breaking. Again, five wave periods are used to obtain phase-averaged surface elevations. Before wave breaking, the surface elevations are accurately predicted by the model (figure 5.3a,b,c). Right after wave breaking, the peak surface elevation is slightly underestimated by the model (figure 5.3d,e). However, as the wave propagates further onshore, the model can predict the surface elevation well again (figure 5.3f).

5.2 Model Setup

A 3D simulation has been conducted to investigate turbulent flow structures and bubble entrainment under a laboratory-scale surfzone breaking wave. The computational domain is tilted off-vertical to match bottom boundary with the $tan\beta = 0.03$ bed slope as shown in figure 5.4. The domain size is taken as 15 m long, 0.3 m wide and 0.6 m high, with the beach toe located at the left boundary.

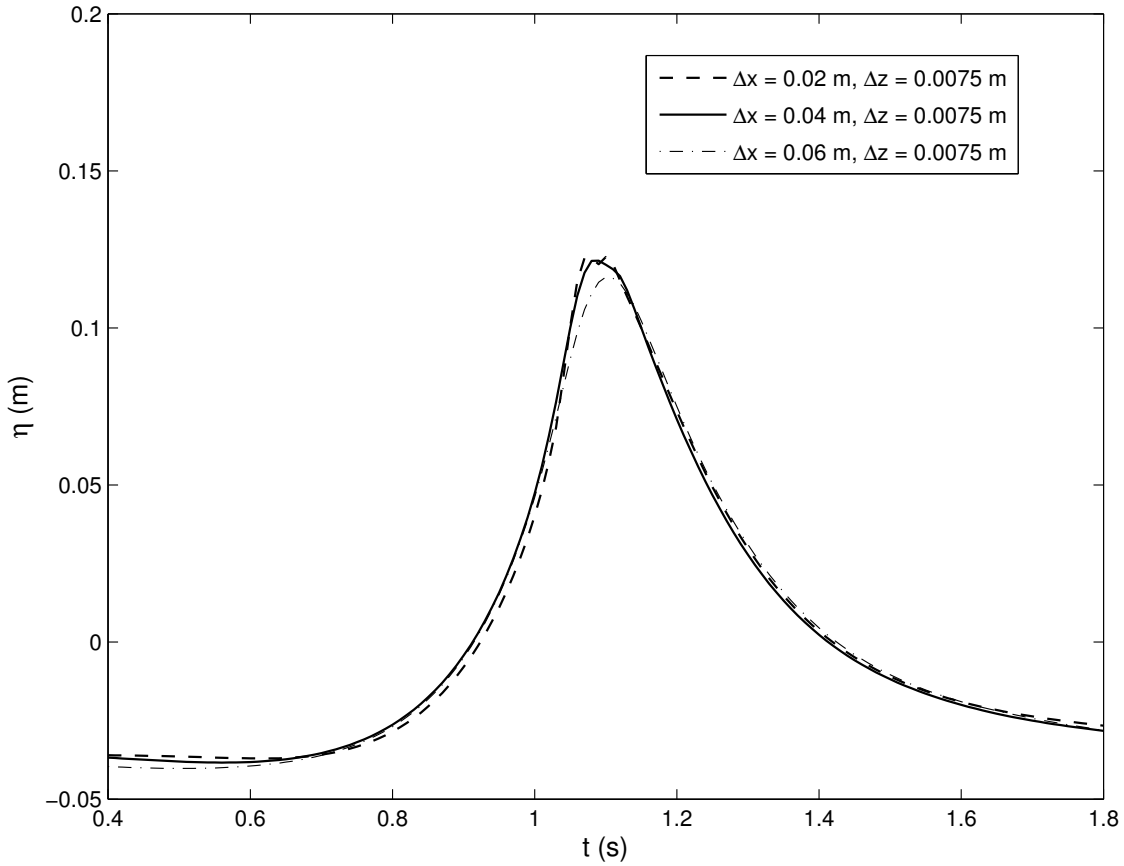

Figure 5.1: Mesh dependence of phase-averaged surface elevation at $x = x_b$. x_b (5.127 m from the beach toe) is the location of breaking point.

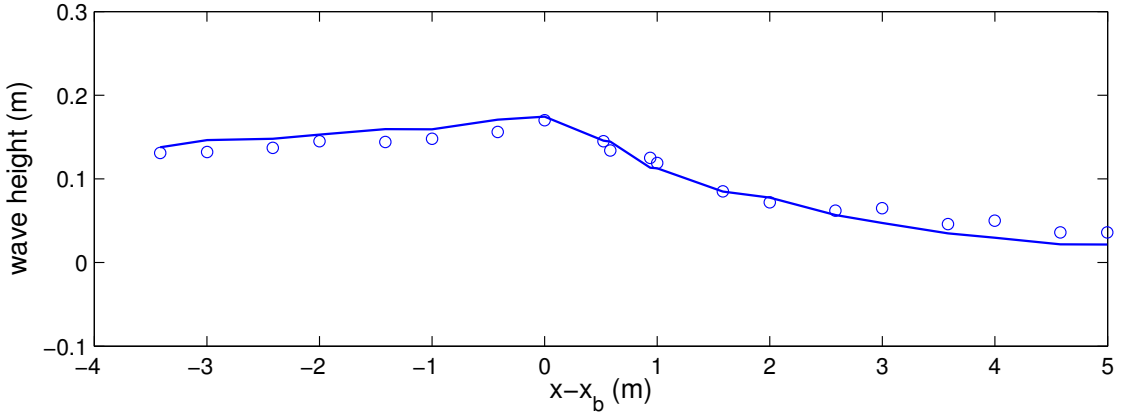

Figure 5.2: Comparisons between numerical (solid line) and experimental (circles) wave height.

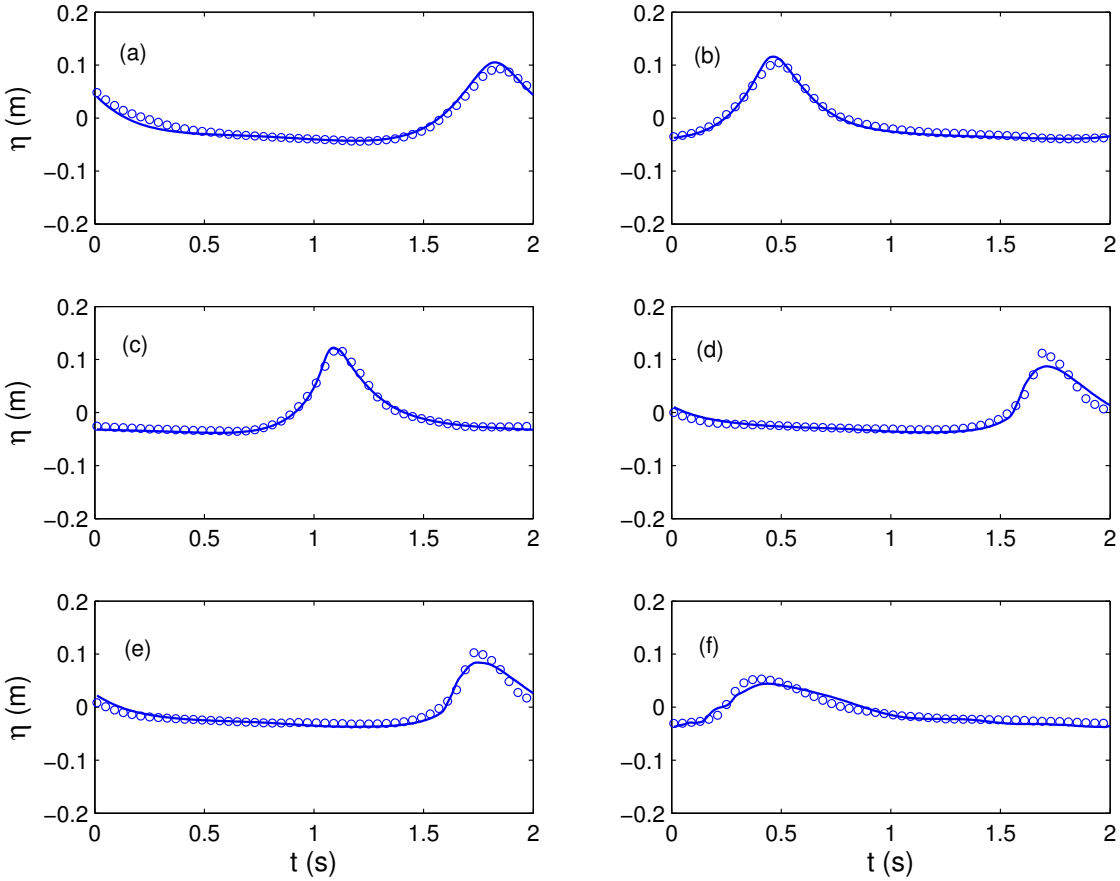

Figure 5.3: Comparisons between numerical (solid line) and experimental (circles) phase-averaged surface elevations at six wave gauges: (a) $x - x_b = -2.414\ m$; (b) $x - x_b = -1.415\ m$; (c) $x - x_b = 0.0\ m$; (d) $x - x_b = 0.938\ m$; (e) $x - x_b = 1.999\ m$; (f) $x - x_b = 3.582\ m$.

The still water depth at the beach toe is 0.36 m. Similar to the 2D simulation, a cnoidal wave with wave height of 0.122 m and wave period of 2.0 s is incident from the left boundary.

Before performing numerical simulations, the computational grid has to be carefully chosen. For a successful LES, we must have a filter width (Δ) in the inertial sub-range, and all scales of motion larger than Δ must be accurately resolved on the numerical grid. However, for the polydisperse two-fluid model, a basic requirement of grid resolution is that the control volume size is large enough to encompass all the interface details associated with dispersed bubbles (Dhotre et al., 2008). Milelli (2002) conducted an analysis of the minimum ratio of bubble and grid size for LES two-fluid model and came up with the criterion $\Delta/d_B > 1.5$. Based on these considerations and the mesh dependence study in 2D simulation, a uniform grid with $(\Delta x, \Delta y, \Delta z) = (0.04, 0.0075, 0.0075)$ is chosen for the 3D simulation. The maximum bubble diameter is taken as 8 mm as used by Moraga et al. (2008), which ensures that the minimum ratio of the bubble and grid size ($\Delta/d_B \approx 1.6$) falls within the Milelli criteria. Bubbles are divided into $NG = 20$ groups with a logarithmic distribution of bubble sizes. The minimum bubble diameter is taken as 0.2 mm, which is consistent with the observations by Dean and Stokes (2002).

Figure 5.5 presents a wave breaking event after 10 wave periods. The free surface at each time frame is marked by the $f = 0.5$ isosurface. According to Battjes (1974), the breaking wave characteristics can be correlated to the surf similarity parameter $\zeta = tan\beta/\sqrt{2\pi H/gT^2}$, where $\zeta = 0.21$ for the current case, indicating that the breaking wave is characterized by a spilling/weakly plunging breaker. As shown in figure 5.5, the crest of the wave slightly curls over when wave breaking starts. However, the jet thrown forward from the top of the front face collapses near the crest to form a breaking wave roller, resembling a spilling/weakly plunging breaker. As wave breaks, the free surface becomes unstable. Some small-scale

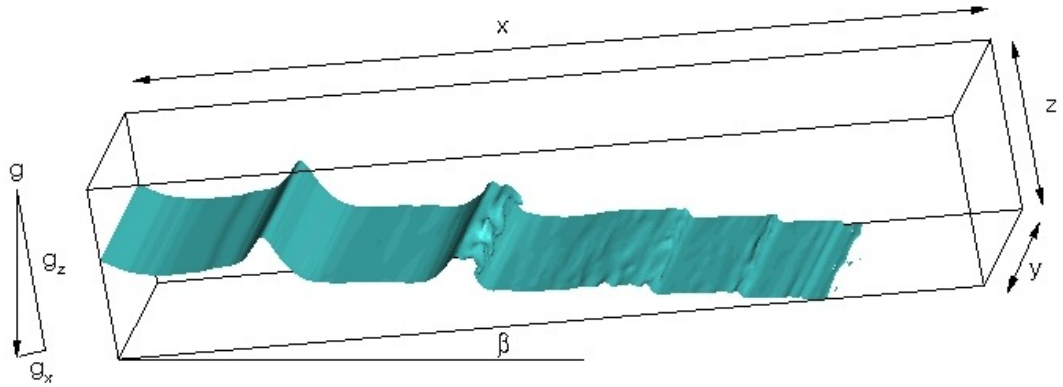

Figure 5.4: Computational domain and model setup for the spilling breaking wave. The domain size is 15 m long, 0.3 m wide and 0.6 m high. The domain boundary matches the $tan\beta = 0.03$ bed slope.

surface deformations with wrinkles in the longshore direction are formed. This process is known as 'small-scale breaking' (Lakehal and Liovic, 2011). Ting (2008) argued that these three-dimensional water surface deformations play a key role in the formation and evolution of turbulent coherent structures.

5.3 Analysis of Flow Field

5.3.1 Coherent Vortical Structures

In the past few decades, a number of vortex identification schemes have been developed, among which the λ_2 method proposed by Jeong and Hussain (1995) has been widely used in various turbulence studies. In this method, λ_2 is the second largest eigenvalue of the tensor $\mathbf{S}^2 + \mathbf{\Omega}^2$, where $\mathbf{S}$ and $\mathbf{\Omega}$ are the symmetric and antisymmetric parts of the velocity gradient tensor $\nabla\mathbf{u}$, respectively. The interiors of vortex cores are recognized as the regions with λ_2 smaller than a negative threshold.

Figure 5.6 shows the evolution of instantaneous vortical structures after wave breaking, which are identified by the isosurface of $\lambda_2 = -2.0$. At the beginning of

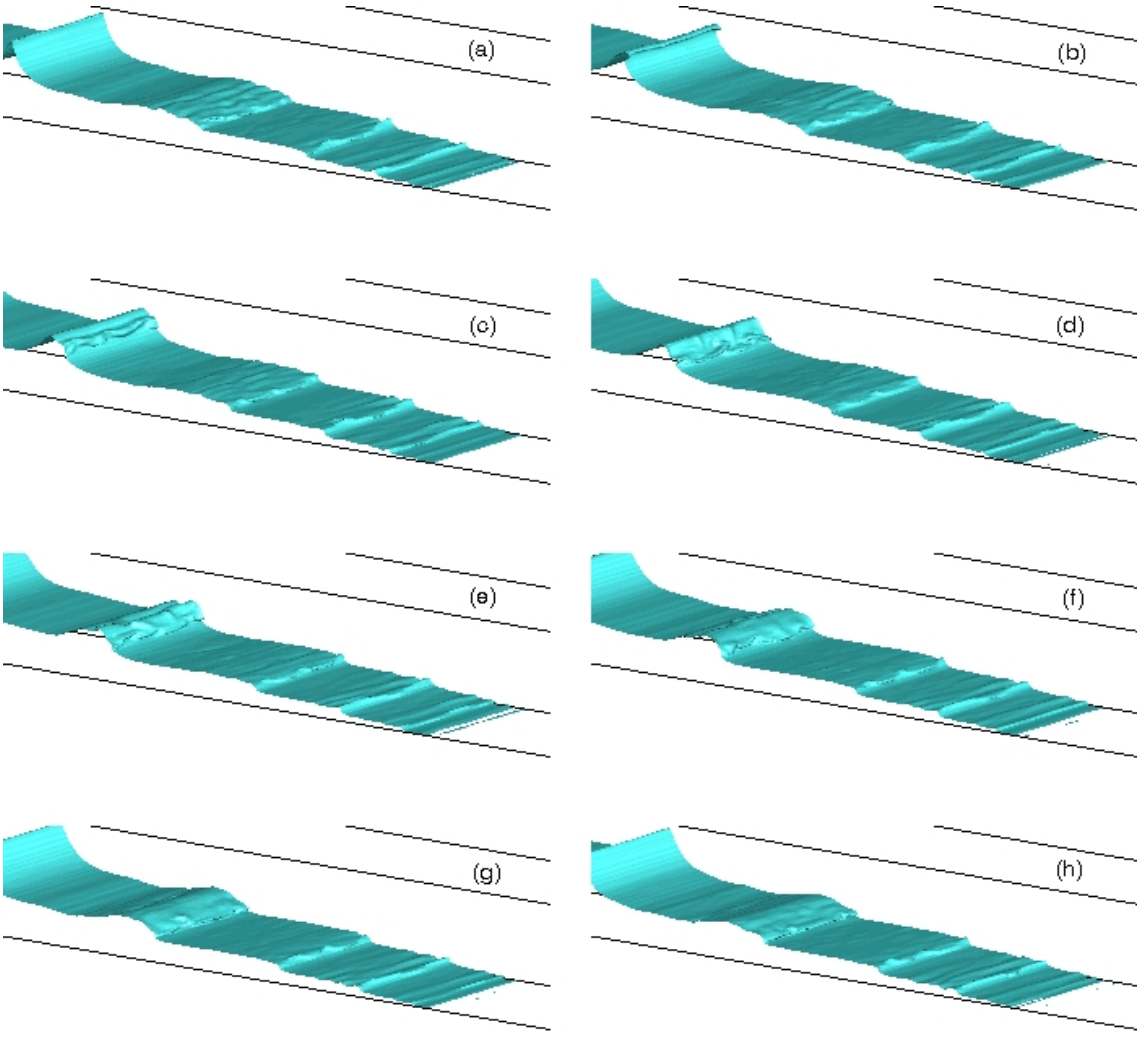

Figure 5.5: Free surface profile of a spilling breaking wave at (a) $t = t_b$; (b) $t = t_b + 1/8T$; (c) $t = t_b + 2/8T$; (d) $t = t_b + 3/8T$; (e) $t = t_b + 4/8T$; (f) $t = t_b + 5/8T$; (g) $t = t_b + 6/8T$; (h) $t = t_b + 7/8T$. t_b is time for initial wave breaking, T is wave period.

wave breaking, a small jet from the wave crest consecutively spills down the front wave face (figure 5.5a-d), leading to the development of large-scale spanwise vortices (figure 5.6a,b). These spanwise vortices are primarily located at the wave front, specifically in the roller region. After a short period of time, some vortical structures under the wave roller start developing (figure 5.6b,c). These vortical structures are mainly in vertical direction, with inclinations to streamwise direction. The mechanisms that induce the development of these vortical structures is postulated to be correlated with downbursts of turbulent fluid (Ting, 2008), which will be discussed later. As the breaking wave propagates further onshore to shallower region, some vortical structures oriented primarily in streamwise direction show up behind the wave crest. These streamwise vortices which are characterized as counter-rotating vortices are well-known as obliquely descending eddies (Nadaoka et al., 1989). Due to the constraint imposed by the presence of the bed, these descending eddies tend to diverge when approaching the bottom and form elongated shapes.

To investigate the characteristics of turbulent vortical structures, we conducted a statistical study of vortex inclination angles (Moin and Kim, 1985; Yang and Shen, 2009). The two-dimensional inclination angles of the streamwise direction to the projections of the vorticity vector in (x, y) and (x, z) planes are defined as $\theta_{xy} = tan^{-1}(\omega_y/\omega_x)$ and $\theta_{xz} = tan^{-1}(\omega_z/\omega_x)$, respectively. The sign convention for the angles is given in figure 5.7. The statistics of the inclination angles are weighted by the magnitudes of the respective projected vorticity vectors (Yang and Shen, 2009). Figure 5.8 shows the probabilities of θ_{xy} and θ_{xz} at $t = t_b + 5/8T$ and $t = t_b + 7/8T$, where t_b is the time for initial breaking. The breaking wave is separated into two parts: upstream of the wave crest AB and downstream of the wave crest BC, so that we can see the differences of vortex structures between the upstream part and downstream part. At $t = t_b + 5/8T$, θ_{xy} in the downstream BC is concentrated around 270^o, indicative of spanwise vortices. In the upstream AB,

θ_{xy} is broadly distributed, indicating the coexistence of spanwise and streamwise vorticities. In the (x, z) plane, θ_{xz} in the downstream BC is concentrated around 245^o and 65^o. The dominant vortices are relatively vertical, with an inclination to the streamwise direction. In the upstream AB, θ_{xz} has a similar distribution as the downstream, except that the probabilities of vortex angles within $0^o \sim 45^o$ and $180^o \sim 225^o$ are higher, indicative of more streamwise vortices behind the wave crest. At $t = t_b + 7/8T$, the distributions of θ_{xy} is similar to that at $t = t_b + 5/8T$. The spanwise vortices are concentrated on the wave front. However, the distributions of θ_{xz} are different. In the downstream BC, θ_{xz} is concentrated around 260^o and 80^o, indicating that the dominant vortices are more vertical than those at $t = t_b + 5/8T$. In the upstream AB, θ_{xz} is concentrated within $0^o \sim 90^o$ and $180^o \sim 270^o$ with larger probabilities in the range of $0^o \sim 45^o$ and $180^o \sim 225^o$, indicating that the streamwise vortices are dominant behind the wave crest. These results show that the vertical vortices in the downstream and streamwise vortices in the upstream of the wave crest are all strengthened as the wave propagates onshore into shallower region.

5.3.2 Downburst of Turbulent Fluid

During wave breaking, a turbulent and aerated water mass is produced when the water spills down the front of the breaking wave. A downburst is formed when this aerated water mass descends toward the bottom without a great deal of rotation (Ting, 2008). Kubo and Sunamura (2001) observed that downbursts produced more sediment movement than obliquely descending eddies. Ting (2006, 2008) conducted systematic research on downbursts. He found that downbursts and attached counter-rotating vortices were the primary source of turbulent energy in the breaking wave field.

Following Lakehal and Liovic (2011), we interpret the spanwise averaged flow field and free surface as the organized motion. The deviation from this average is

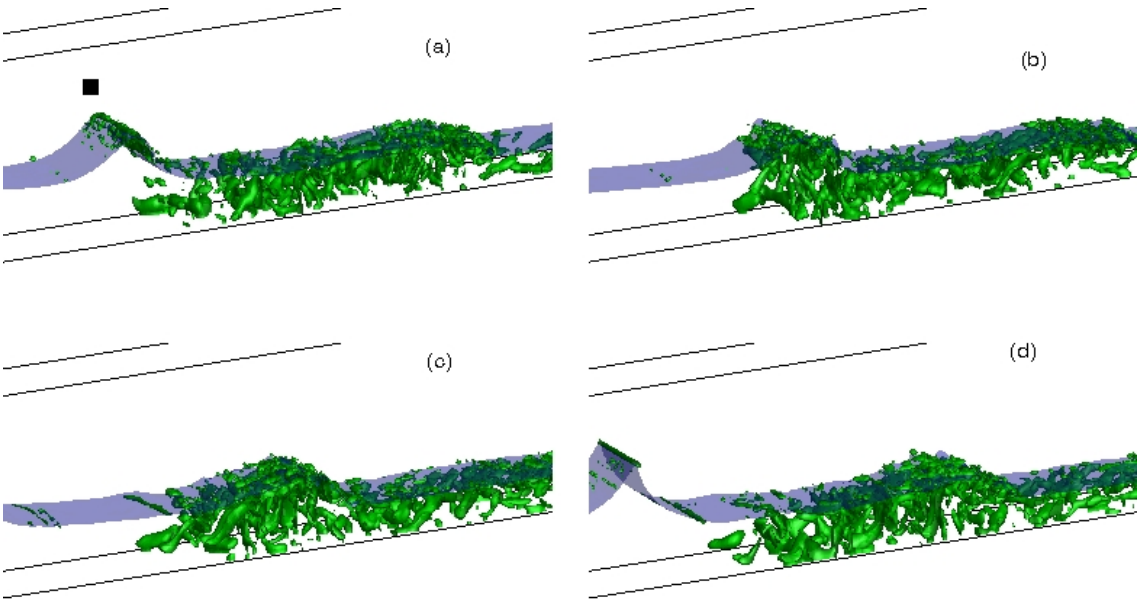

Figure 5.6: Evolution of coherent vortical structures in a spilling breaking wave at (a) $t = t_b + 1/8T$; (b) $t = t_b + 3/8T$; (c) $t = t_b + 5/8T$; (d) $t = t_b + 7/8T$. t_b is time for initial wave breaking, T is wave period. The vortical structures are identified by the isosurface of $\lambda_2 = -2.0$

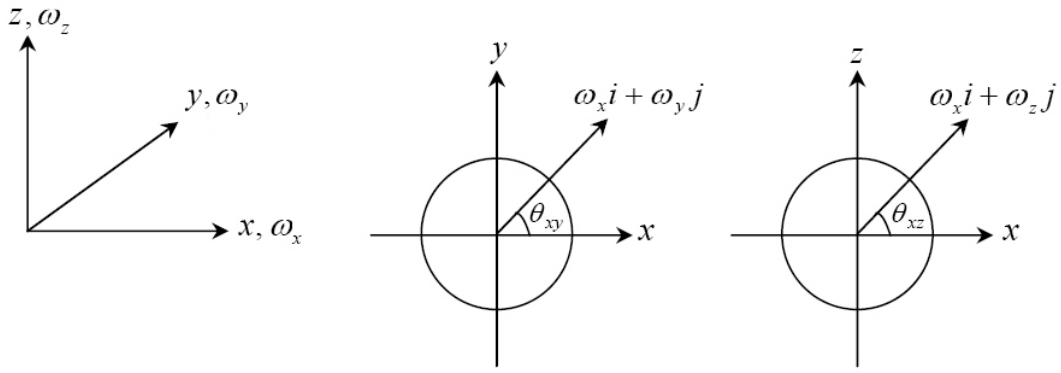

Figure 5.7: Sign convention for vorticity inclination angles θ_{xy} and θ_{xz}, where θ_{xy} is the angle from the $+x$-axis to $\omega_x\mathbf{i} + \omega_y\mathbf{j}$ in the (x, y) plane and θ_{xz} is the angle from the $+x$-axis to $\omega_x\mathbf{i} + \omega_z\mathbf{k}$ in the (x, z) plane (adapted from Yang and Shen, 2009).

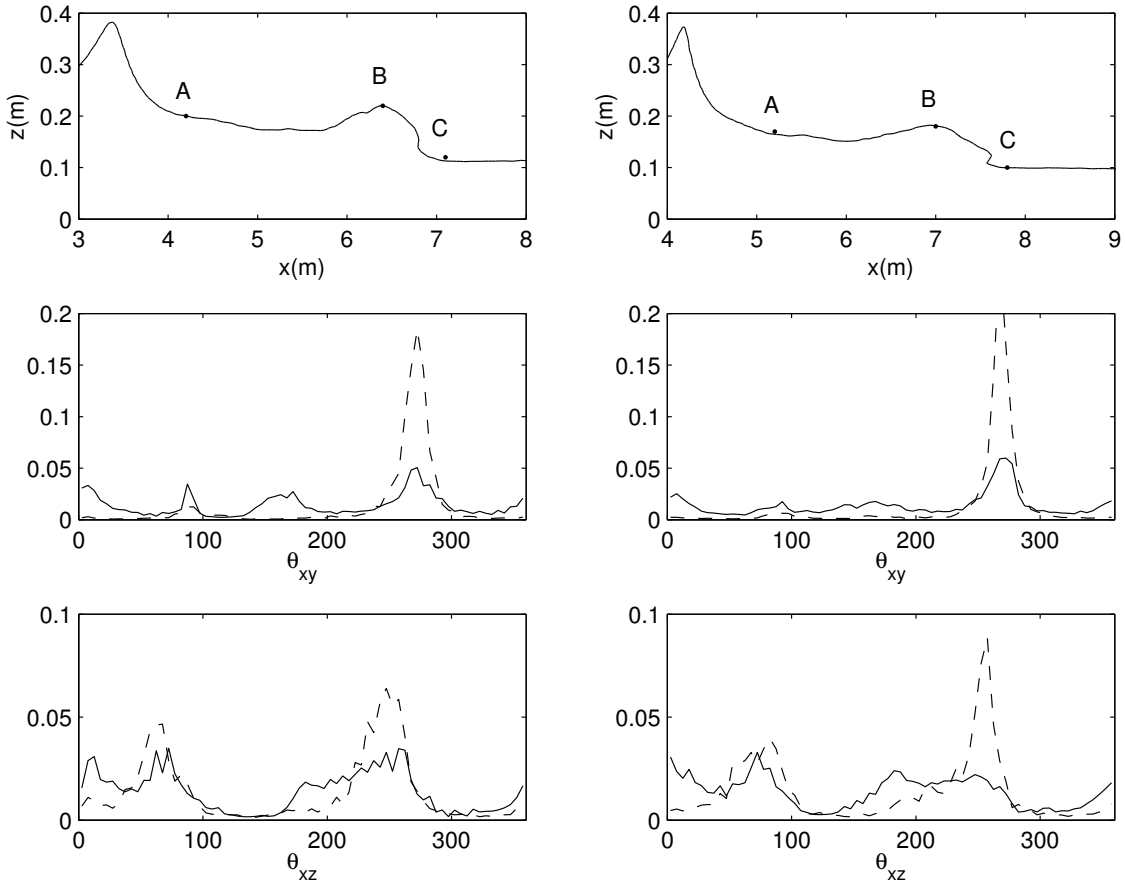

Figure 5.8: Probabilities of two-dimensional vorticity angles at the upstream AB and downstream BC of the wave crest at $t = t_b + 5/8T$ (left) and $t = t_b + 7/8T$ (right). Solid line: upstream part; dashed line: downstream part.

considered as the turbulent fluctuating field. This approach has been shown to be useful for wave breaking studies (Lakehal and Liovic, 2011). Therefore, the instantaneous velocity field is decomposed into two parts: $u =< u > +u^{'}$, where $< \cdot >$ represents the spanwise averaged velocity and $u^{'}$ is the fluctuating turbulent velocity. The turbulent kinetic energy is defined as $k = 1/2(u^{'2} + v^{'2} + w^{'2})$.

Figure 5.9 shows the distributions of vertical velocity fluctuation $w^{'}$ and turbulent kinetic energy k in an $x - y$ plane located approximately 17 cm above the bed. Several downburst events identified as negative $w^{'}$ can be recognized, all of which are associated with high turbulent kinetic energy. A typical downburst of turbulent fluid is shown in figure 5.10. The core of this downburst is located at $x = 6.25\ m$ and $y = 0.17\ m$. As observed, the downburst is associated with high turbulent kinetic energy k and Reynolds stress $-u^{'}w^{'}$, and accompanied by two counter-rotating vortices with nearly equal vorticity. The core of the downburst is located at the region between these two vortices, indicating that the downburst itself does not have a lot of rotation. The highest turbulent kinetic energy and Reynolds stress are also found in the region between the vortices, whereas the vortex centers have relatively low turbulence and Reynolds stress. These features of downburst are consistent with the laboratory observations by Ting (2006, 2008), although the simulated downburst is more organized.

The 3D structure of the downburst can be found in figure 5.11, which demonstrates the vertical velocity fluctuation $w^{'}$ and vertical vorticity ω_z at a set of $x - y$ planes with different vertical locations. The cores of the regions with negative $w^{'}$ are nearly in the same position of the planes, indicating that the structure of downburst is relatively vertical. As the water depth increases, the downburst becomes weaker and smaller. This downburst hasn't reached the bottom yet, however, it can bring a lot of turbulent kinetic energy and Reynolds stress to the middle part of the water column. From figure 5.11, we can also see the evolution of the counter-rotating

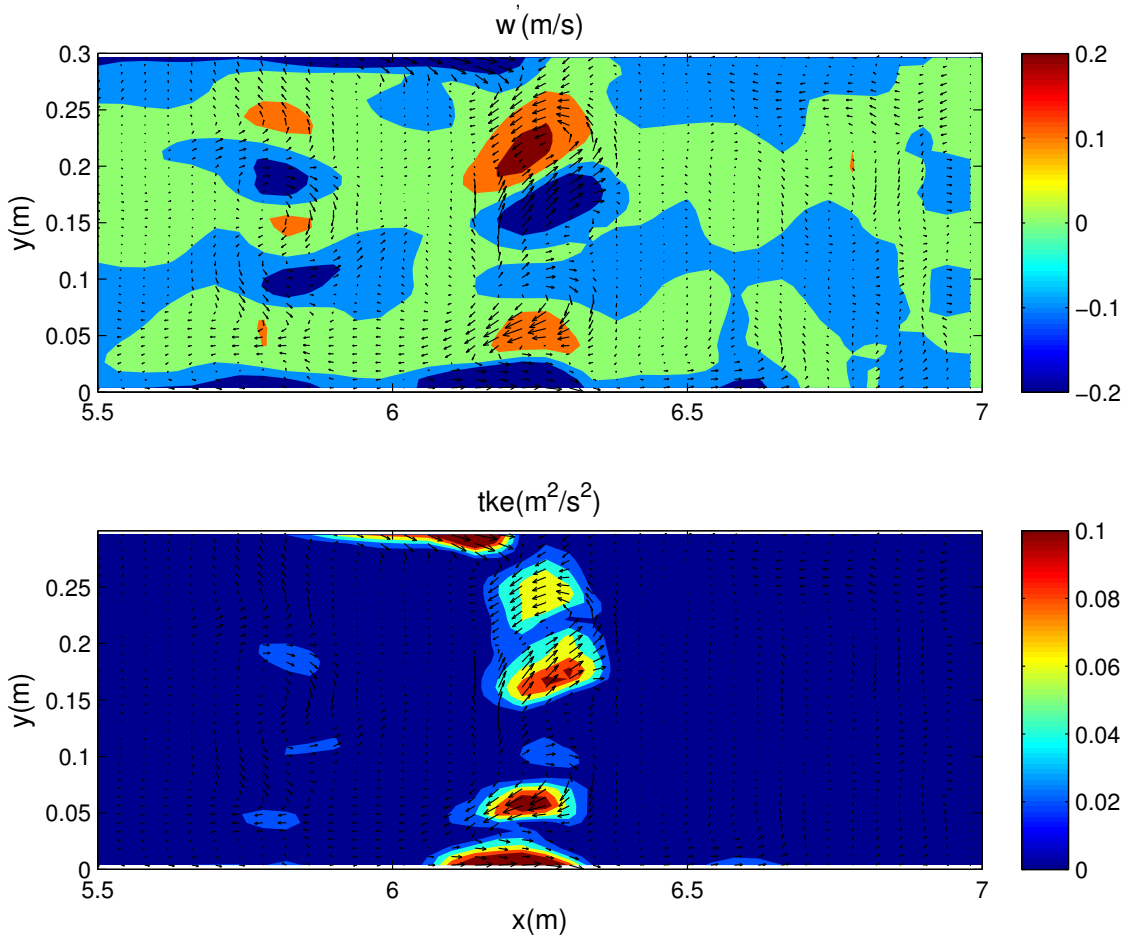

Figure 5.9: Instantaneous turbulence velocity $u^{'}$, $v^{'}$ and $w^{'}$ (in m/s) and turbulent kinetic energy $k = 1/2(u^{'2} + v^{'2} + w^{'2})$ (in m^2/s^2) at a x-y slice 17 cm above the bed at $t = t_b + 5/8T$.

vortices attached to the downburst. With the water depth increasing, the vortices becomes weaker and smaller as well. Meanwhile, the distance between vortex cores becomes smaller. Because the vortices cannot end in the interior of the fluid (Ting, 2008), they must merge somewhere between $z = 10cm$ and $z = 13cm$. As argued by Ting (2008), these counter-rotating vortices are parts of a vortex loop extending to the free surface.

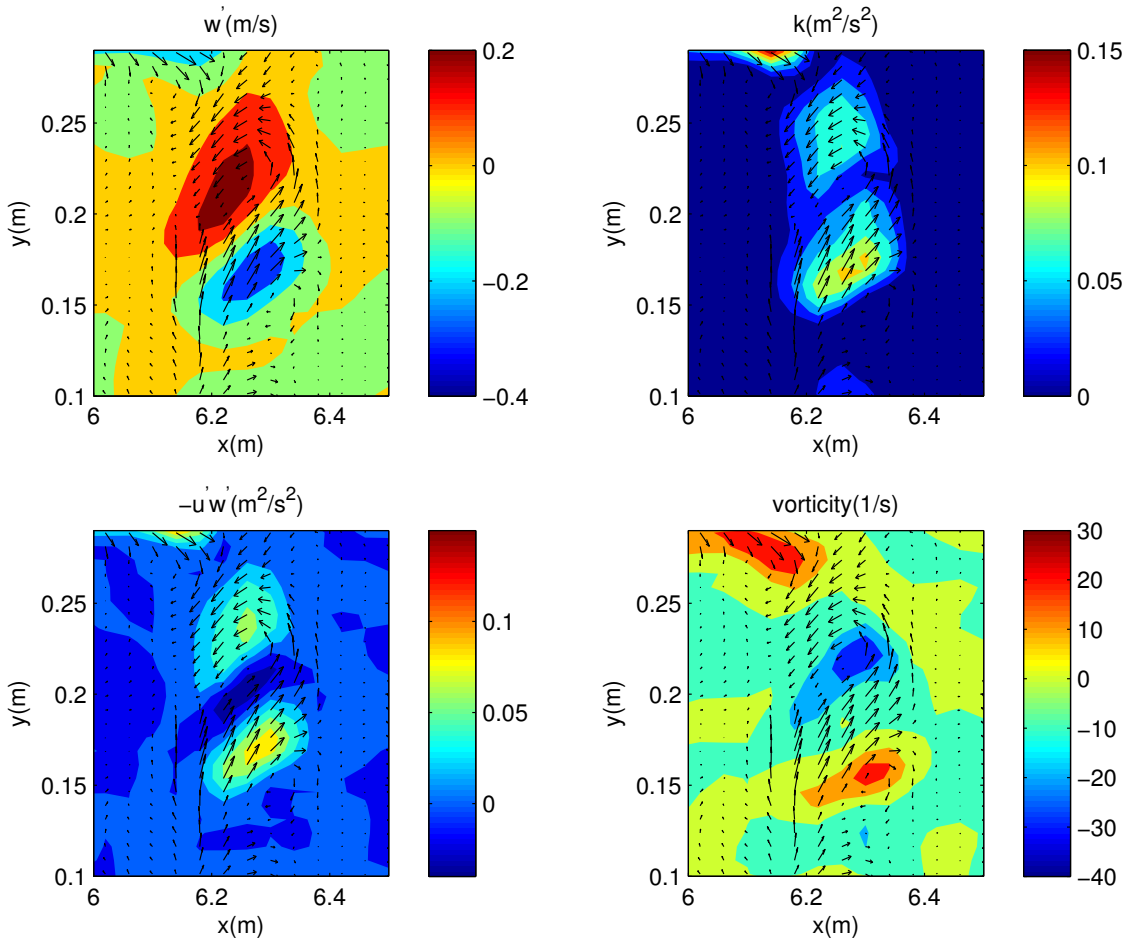

Figure 5.10: Instantaneous turbulence velocity $u^{'}$, $v^{'}$ and $w^{'}$ (in m/s), turbulent kinetic energy $k = 1/2(u^{'2} + v^{'2} + w^{'2})$ (in m^2/s^2), Reynolds stress $-u^{'}w^{'}$ (in m^2/s^2) and vorticity $du^{'}/dy - dv^{'}/dx$ (in $1/s$) from a downburst at $t = t_b + 5/8T$. The focus area is located at 17 cm above the bed.

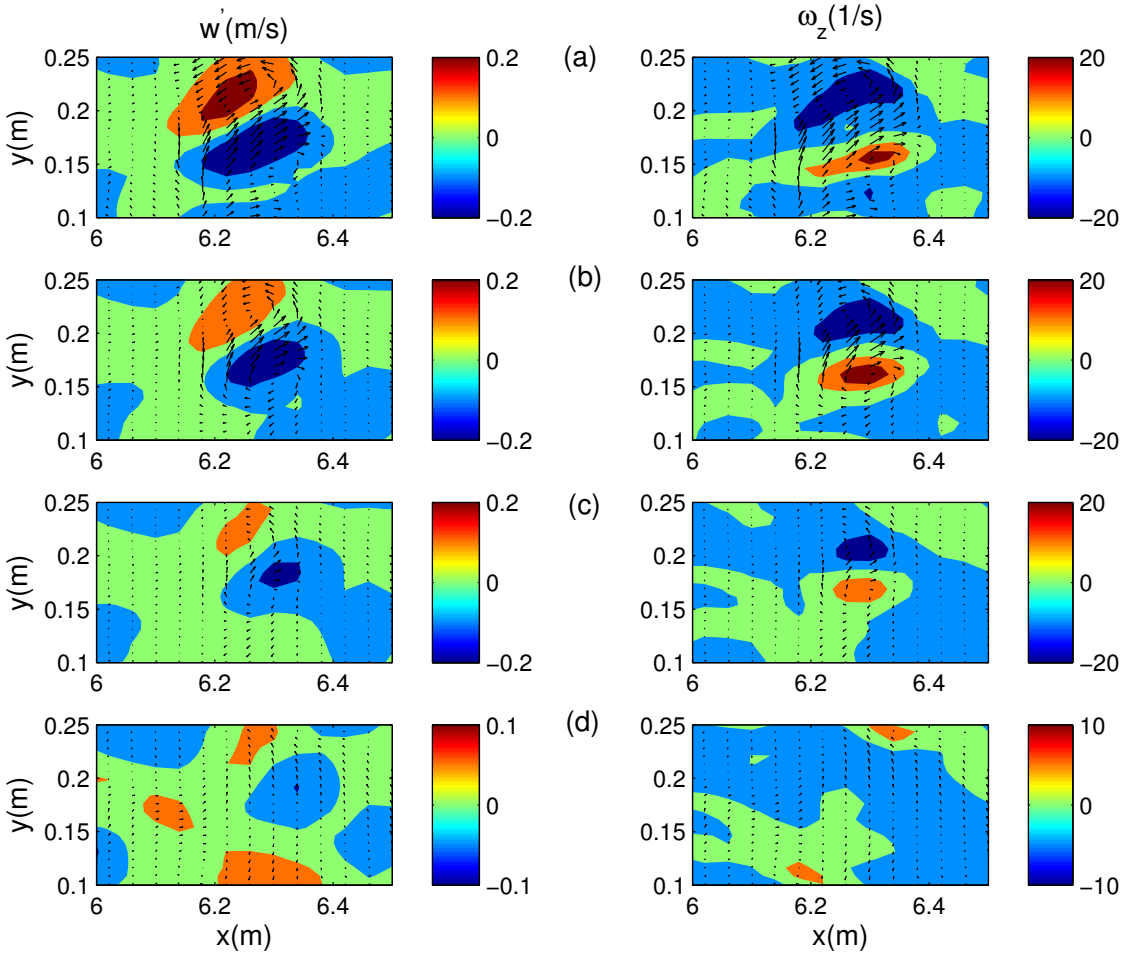

Figure 5.11: Evolution of the downburst in the vertical direction at (a) $z = 17cm$; (b) $z = 15cm$; (c) $z = 13cm$ and (d) $z = 10cm$.

5.3.3 Turbulent Kinetic Energy and Momentum Transport

In this section, we will study the effects of coherent structures on turbulent kinetic energy (TKE) and momentum transport. Figure 5.12 shows the spanwise averaged TKE distributions at different phases over a single wave period. As expected, high TKE levels are persistently located at the front part of the breaking wave crest. The highest turbulence appears when the jet from the crest collapses at the front wave face (figure 5.12b). At $t = t_b + 5/8T$, there is a strong downward transport of TKE behind the wave crest, which is mainly attributed to the downbursts of turbulent fluid as illustrated in figure 5.10. As the wave propagates onshore, this high-TKE region almost remains at the entrainment location and is detached from the wave front (figure 5.12d). From figure 5.12, we also notice that the high-TKE is transported obliquely into the water column, which is correlated to the obliquely descending eddies. This feature is more clearly seen from the downward spread of high-TKE generated by the previous breaking wave event. Figure 5.13 demonstrates the streamwise vorticity ω_x and TKE distributions at a $y - z$ slice ($x = 8.0m$) at $t = t_b + 5/8T$, from which we can find the correlations between obliquely descending eddies and TKE transport. As shown, the high-TKE is always located at the region between the counter-rotating vortices or the outer core of the vortices, where strong downward velocities occur. Inside the vortex core, the turbulence is relatively low. The transport of high-TKE is determined by the movements of these streamwise vortices.

The turbulent coherent structure effects on momentum transport are examined by looking at the Reynolds stress distributions. Figure 5.14 demonstrates spatial distributions of Reynolds stress $-u^{'}w^{'}$ at four different phases after wave breaking. Notice the dark red regions represent $-u^{'}w^{'} < 0$. These regions are primarily located near the bottom, where the turbulence is seldom affected by the wave breaking. In other words, the breaking-induced Reynolds shear stress is mainly

characterized by $-u'w' > 0$. Here we only focus on the wave breaking generated Reynolds stress. The spatial distribution of Reynolds stress is quite similar to that of TKE. The high stress is localized at the front part of wave crest. The highest level of Reynolds stress appears at the wave roller when the jet from the crest hits the front wave face as shown in figure 5.14b. Right behind the wave crest, there is a strong downward transport of Reynolds stress at $t = t_b + 5/8T$, which is attributed to the downburst events. The Reynolds stress can be transported down to the bottom by the downbursts. Again, the strong Reynolds stress behind wave crest remains and decays at the entrainment location as the wave propagates onshore (figure 5.14d). From the distributions of Reynolds stress generated by the previous breaking event, the stress is transported obliquely into the water column behind the wave crest, supporting the conclusion that the obliquely descending eddies are effective not only on the TKE transport but also on the momentum transport. This is more clearly seen in figure 5.13. The pattern of Reynolds stress distributed by streamwise vortices is similar to that of TKE. As with TKE, the high Reynolds stress is always located at the regions between the counter-rotating vortices or the outer core of the vortices, where strong downward velocities occur. However, the Reynolds stress seems to be transported slightly deeper into the water column by the obliquely descending eddies.

5.3.4 Bubble Entrainment

In this section, we examine the effects of turbulent coherent structures on bubble entrainment and downward spread. Figure 5.15 shows the spanwise averaged void fraction distributions at four phases in a wave breaking event. In our model, bubble entrainment at the surface is correlated to the turbulent dissipation rate ϵ, which must be greater than a critical value to trigger bubble entrainment. This primarily happens in the surface roller associated with wave breaking. As shown in figure 5.15, the high void fractions are consistently located at the roller region of

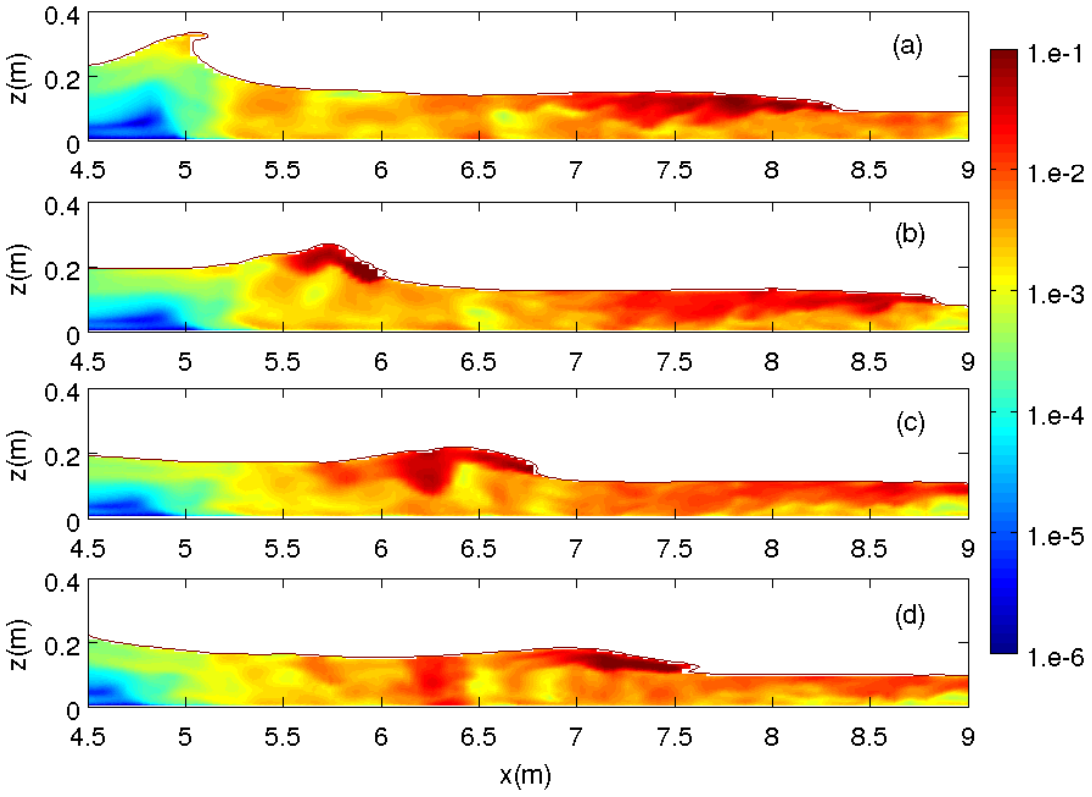

Figure 5.12: Spanwise averaged turbulent kinetic energy at (a) $t = t_b + 1/8T$; (b) $t = t_b + 3/8T$; (c) $t = t_b + 5/8T$ and (d) $t = t_b + 7/8T$.

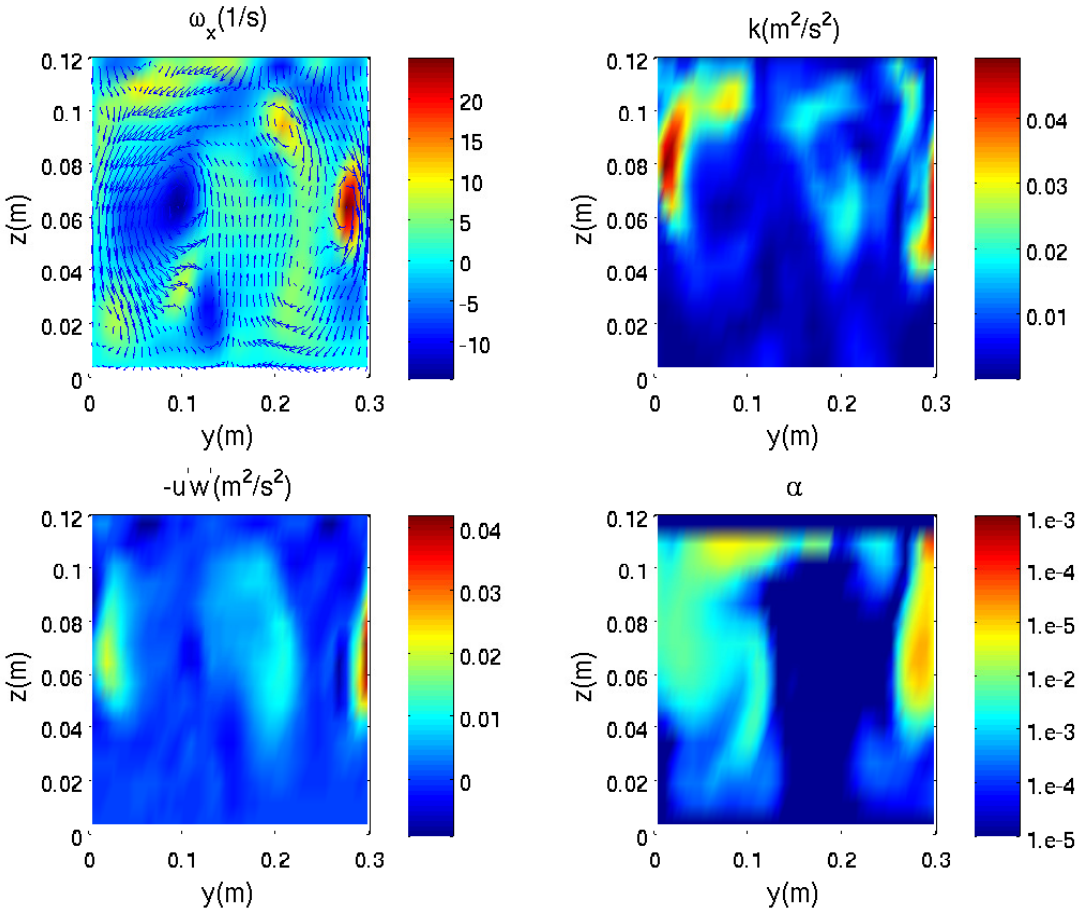

Figure 5.13: Instantaneous velocity field v and w, streamwise vorticity ω_x, turbulent kinetic energy k, Reynolds stress $-u^{'}w^{'}$ and void fraction distribution α at a $y-z$ slice ($x = 8.0m$) at $t = t_b + 5/8T$.

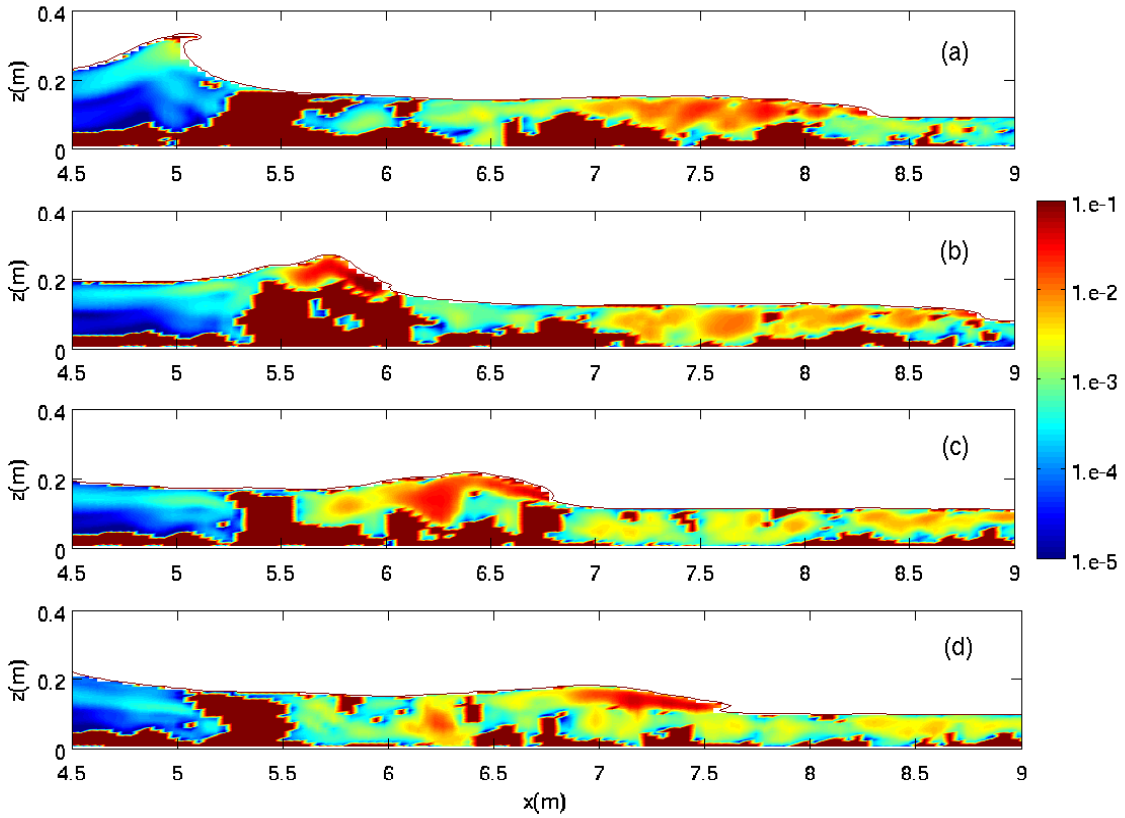

Figure 5.14: Spanwise averaged Reynolds stress $-u^{'}w^{'}$ distributions at (a) $t = t_b + 1/8T$; (b) $t = t_b + 3/8T$; (c) $t = t_b + 5/8T$ and (d) $t = t_b + 7/8T$. Dark red denotes $-u^{'}w^{'} < 0$.

the breaking wave front. Quantitatively, the void fractions in this region fall in the range of $0.2 \sim 0.4$, which is consistent with laboratory experiments, for example, Lamarre and Melville (1991) or Cox and Shin (2003). As bubbles are entrained into the water column, a bubble plume is formed under the free surface of the wave front. This bubble plume tends to be spread backward as shown in figure 5.15b, indicating that the plume moves slower than the breaking wave, consistent with the 2D simulations (Ma et al., 2011). Figure 5.15c demonstrates that the bubble plume is further spread seaward, and subsequently downward. The oblique downward spread of the bubble plume is correlated with the obliquely descending eddies and downbursts of turbulent fluid behind the wave crest. It is also noticed that the bubble plume pattern is quite similar to that of turbulent kinetic energy (TKE) presented in figure 5.12, indicating that the mixing mechanism of dispersed bubbles is closely related to the subsurface production, transport and diffusion of turbulence, as found by Lakehal and Liovic (2011). The primary bubble plume tends to be detached from the wave front as the breaking wave propagates onshore (figure 5.15d). These bubbles are trapped by the vortex structures, which will be discussed later. At this phase, the bubble plume will slowly disperse as bubbles rise to the surface. In the figure, we also notice the bubbles generated by the previous wave breaking event, which are transported obliquely into the water column. This result indicates that obliquely descending eddies have a significant effect on bubble entrainment and dispersion. This conclusion is further supported by figure 5.13, which shows the connection between obliquely descending eddies (streamwise vortices) and void fraction distribution at a $y - z$ slice at $x = 8.0m$. Similar to TKE and Reynolds stress, the bubbles are mainly transported downward in the region between the counter-rotating vortices or the outer core of the vortices, where there are strong downward velocities. However, the bubbles can be trapped into the core of the streamwise vortices, which is different from the TKE and Reynolds stress. This is

due to the preferential accumulation or clustering of bubbles by the vorticity field (Aliseda and Lasheras, 2011).

The effects of turbulent vortex structures on bubble transport and dispersion is also shown in the 3D plots of figure 5.16. The vortex structures are the same as those in figure 5.6, but represented by a stricter criterion $\lambda_2 = -5.0$. The void fraction distributions are illustrated by the isosurfaces of $\alpha = 0.01\%$, which is mostly contributed by small bubbles. A strong downward transport of bubbles right behind the wave crest is found at $t = t_b + 5/8T$. This relatively vertical downward transport of bubbles is attributed to the downbursts of turbulent fluid, further described in figure 5.19. Another efficient mechanism for transporting bubbles into the water column is through the obliquely descending eddies. As shown in figure 5.16, the bubble concentration is always high along the vortex structures. This is more clearly observed in figure 5.17, which displays the instantaneous flow field v and w, streamwise vorticity ω_x and void fraction α distributions at $y - z$ slices demonstrated in figure 5.15 at $t = t_b + 5/8T$ and $t = t_b + 7/8T$. Similar to that shown in figure 5.13, the high concentration of bubbles is located at the regions between the counter-rotating vortices and the outer core of the vortices, where strong downward velocities occur. These strong downward flows can counteract buoyancy force, transporting bubbles downward into the water column. The bubbles are able to be trapped into the vortex core due to the preferential accumulation. At $t = t_b + 5/8T$, four pairs of counter-rotating vortices attached to the free surface can be recognized, all of which are involved in entrainment of bubbles with high void fractions. At $t = t_b + 7/8T$, vortices are transported downward to the middle of the water column, which is accompanied by the downward transport of bubbles. The strong vortex located at the left bottom corner traps large volumes of bubbles near the bottom, which corresponds to the bubble plume shown in figure 5.15d and 5.16d.

The turbulent transport of dispersed bubbles represented by $-w^{'}\alpha^{'}$ (α is the

void fraction) is displayed in figure 5.18. As expected, the distributions of $-w^{'}\alpha^{'}$ is quite similar to that of void fraction. The strongest downward transport of bubbles occurs in the roller region at $t = t_b + 3/8T$, when the small jet thrown forward from the wave crest hits the front face. Behind the wave crest, bubbles are initially transported seaward parallel to the free surface (figure 5.18b) due to the obliquely descending eddies, and then have a strong downward transport (figure 5.18c), which is partly attributed to the downbursts of turbulent fluid. This is supported by figure 5.19, which shows bubble transport in a downburst event at $t = t_b + 5/8T$. The bubble transport associated with downburst is much stronger than the neighboring regions, indicating that the downburst is efficient in downward transport of dispersed bubbles. At $t = t_b + 7/8T$, the downward transport of bubbles is becoming weaker. The bubbles start rising back to the free surface, and bubble plume disperses with void fraction decaying.

5.4 Discussions

5.4.1 Vortex Stretching and Bending

In the previous section, we have shown that the model is able to simulate the generation of streamwise vortices behind the wave crest of breaking waves. However, it is still debatable how these streamwise vortices are generated during wave breaking processes. Nadaoka et al. (1989) suggested that the formation and evolution of the obliquely descending eddies are related to the stretched velocity field around the saddle point of streamlines between adjacent spanwise vortices. Watanabe et al. (2005) conducted a LES study of plunging and spilling breaking waves and suggested that the mechanism for the development of streamwise vortices in breaking waves is similar to that in a mixing layer as proposed by Lasheras and Choi (1988). They argued that the obliquely descending eddies are essentially counter-rotating streamwise vortices, which are vortex loops produced by stretching and bending of perturbed vorticity in the saddle region between the rebounding jet and

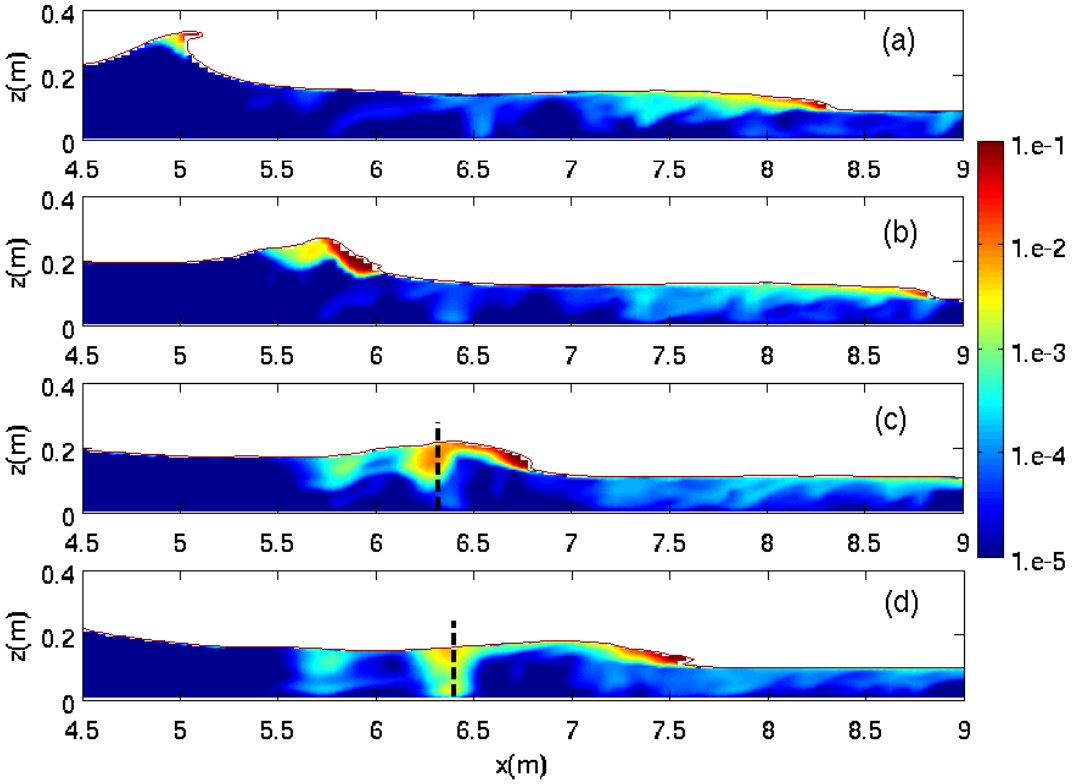

Figure 5.15: Spanwise averaged void fraction distributions at (a) $t = t_b + 1/8T$; (b) $t = t_b + 3/8T$; (c) $t = t_b + 5/8T$ and (d) $t = t_b + 7/8T$. Two dashed lines shown in (c) and (d) indicate the locations of $y-z$ slices for figure 5.17.

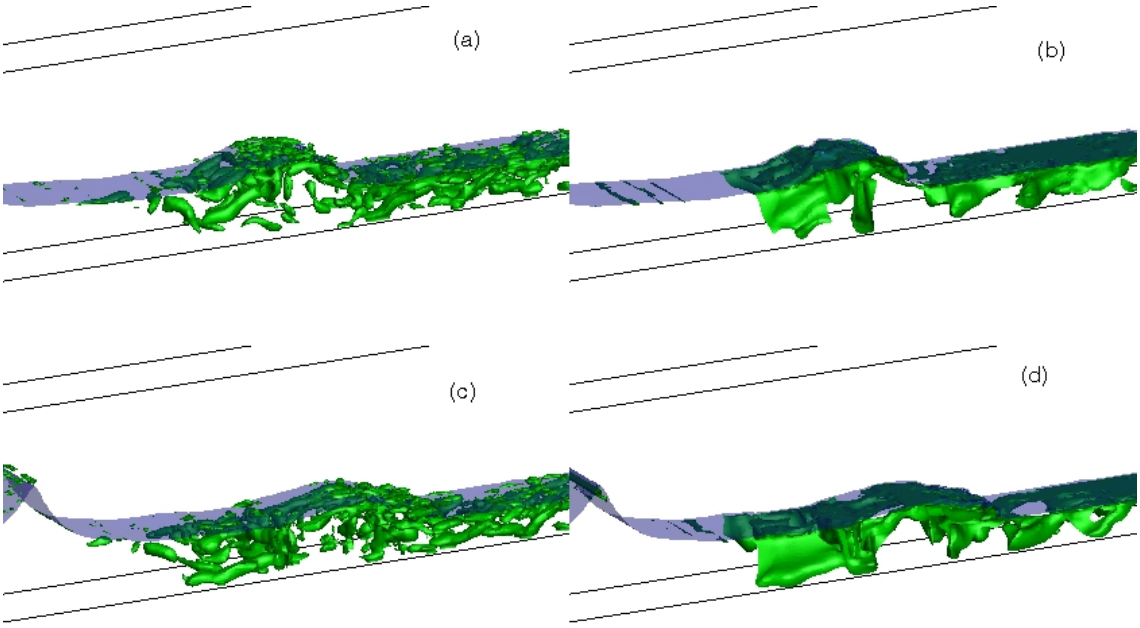

Figure 5.16: The effects of vortex structures (recognized by isosurfaces of $\lambda_2 = -5.0$) on void fraction distributions (isosurfaces of $\alpha = 0.01\%$). (a) vortex structures at $t = t_b + 5/8T$; (b) void fraction distribution at $t = t_b + 5/8T$; (c) vortex structures at $t = t_b + 7/8T$; (d) void fraction distribution at $t = t_b + 7/8T$.

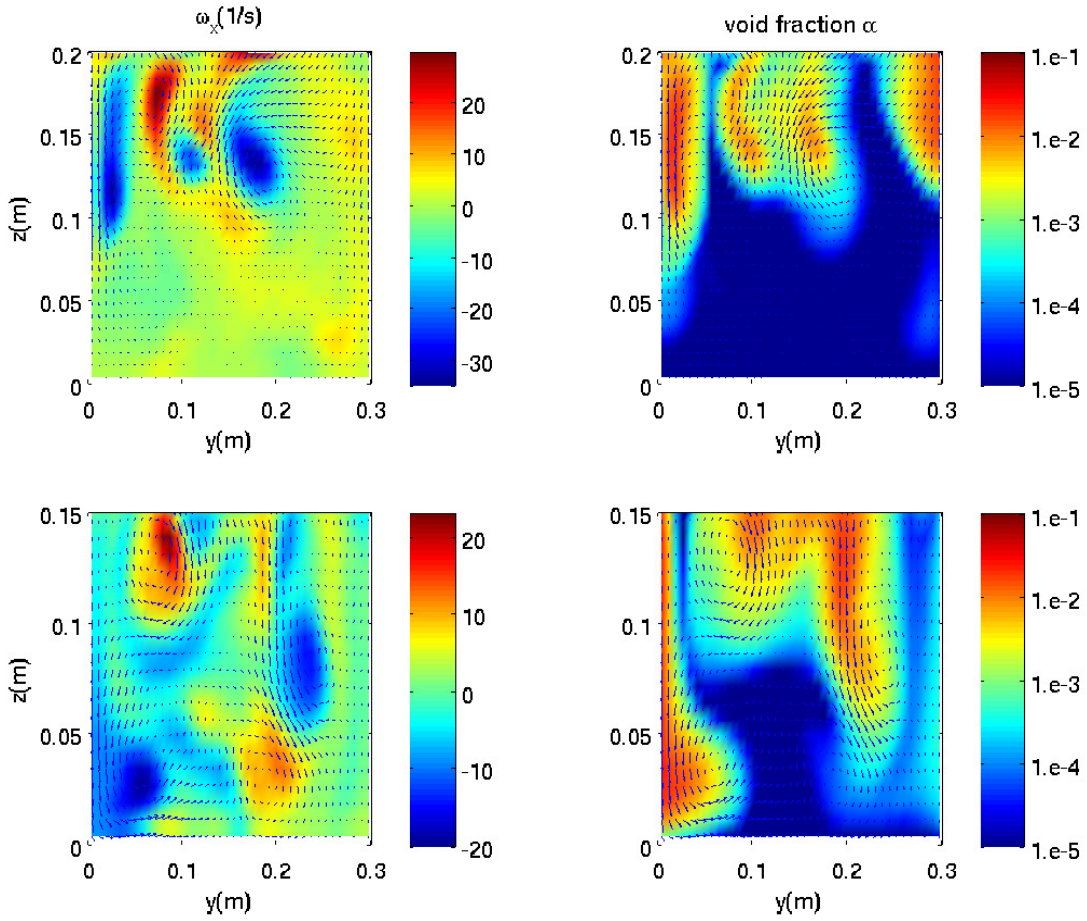

Figure 5.17: Streamwise vorticity ω_x and void fraction distribution α at $y-z$ slices as shown in figure 5.15 at $t = t_b + 5/8T$ (upper pannels) and $t = t_b + 7/8T$ (lower pannels).

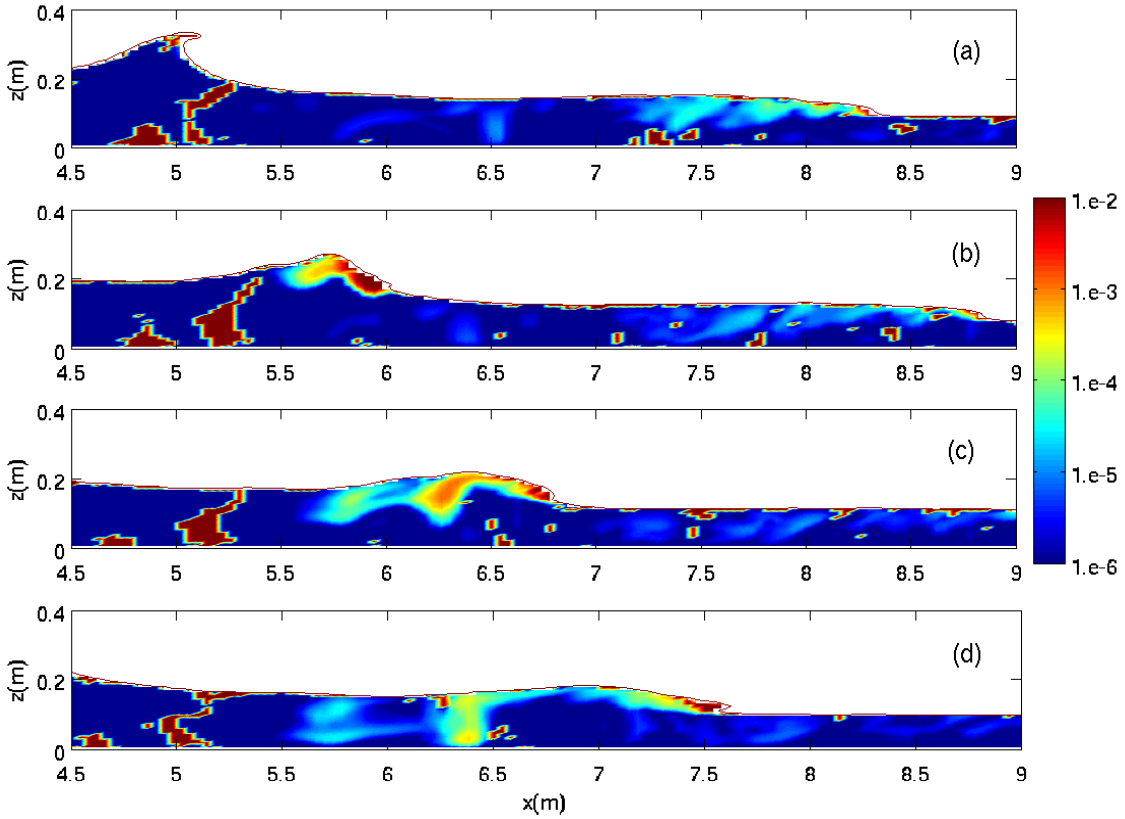

Figure 5.18: Spanwise averaged turbulent transport of bubbles $-w^{'}\alpha^{'}$ at (a) $t = t_b + 1/8T$; (b) $t = t_b + 3/8T$; (c) $t = t_b + 5/8T$ and (d) $t = t_b + 7/8T$. Dark red denotes $-w^{'}\alpha^{'} < 0$.

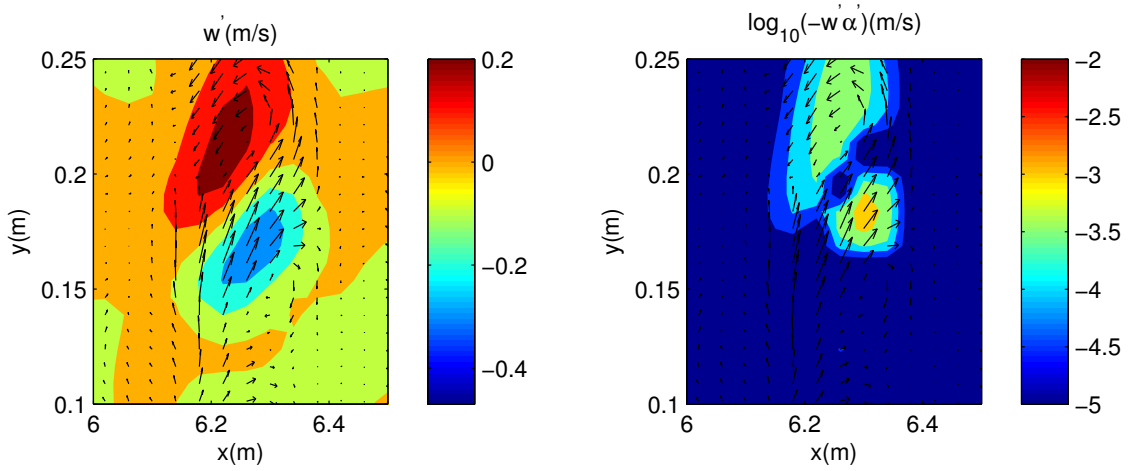

Figure 5.19: Bubble transport by a downburst event at $t = t_b + 5/8T$. The downburst is identified by negative $w^{'}$, and the bubble transport associated with the downburst are much stronger than neighboring regions.

the primary spanwise vortex. As these streamwise vortices continue developing, a so-called rib structure is formed, involving the vortex loops wrapping around the adjacent spanwise vortices. These vortices could intertwine and entangle together to form a complex vorticity field. However, Ting (2006, 2008) questioned the similarity of the mechanism for the generation and evolution of vortex structures in a breaking wave and a mixing layer, as the breaking wave is strongly influenced by gravity which is of minor importance for a mixing layer. Moreover, the primary spanwise vortices maintained their two-dimensionality during the formation of secondary streamwise vortices (Lasheras and Choi, 1988), which is not the case in breaking waves (Ting, 2008). Ting (2006, 2008) observed in the laboratory experiments that three-dimensional water surface deformations during wave breaking play a key role in the formation and evolution of counter-rotating vortices. Ting (2008) speculated that the counter-rotating vortices are produced by stretching and bending of primary spanwise vortex structures generated in the wave breaking process, as a result of non-uniform breaking in the transverse direction. The counter-rotating

vortices are then carried downward by downburst, which is associated with falling water from the broken wave. These counter-rotating vortices are further subject to stretching and bending to form obliquely descending eddies.

To understand how vortex structures evolve under breaking waves, we now study the enstrophy transport equation to quantitively investigate the effects of vortex stretching and bending on the vortex evolution processes. The equation for enstrophy transport is given by

$$\frac{D(\frac{1}{2}\omega_i\omega_i)}{Dt} = \omega_i\omega_j\frac{\partial u_i}{\partial x_j} + \nu\frac{\partial^2(\frac{1}{2}\omega_i\omega_i)}{\partial x_j\partial x_j} - \nu\frac{\partial\omega_i}{\partial x_j}\frac{\partial\omega_i}{\partial x_j} \tag{5.1}$$

where D/Dt is the material derivative, and the terms on the right hand side represent, from left to right, the stretching and bending terms, viscous diffusion and viscous dissipation for enstrophy, respectively.

The stretching and bending term determines whether there is an increase due to stretching or a decrease due to compression of enstrophy by the combination of the signs of ω_i, ω_j and $\frac{\partial u_i}{\partial x_j}$. It includes nine-components, which are given by

$$\begin{aligned}\omega_i\omega_j\frac{\partial u_i}{\partial x_j} =& \underbrace{\omega_x\omega_x\frac{\partial u}{\partial x}}_{\Gamma_{11}} + \underbrace{\omega_x\omega_y\frac{\partial u}{\partial y}}_{\Gamma_{21}} + \underbrace{\omega_x\omega_z\frac{\partial u}{\partial z}}_{\Gamma_{31}} + \\ & \underbrace{\omega_y\omega_x\frac{\partial v}{\partial x}}_{\Gamma_{12}} + \underbrace{\omega_y\omega_y\frac{\partial v}{\partial y}}_{\Gamma_{22}} + \underbrace{\omega_y\omega_z\frac{\partial v}{\partial z}}_{\Gamma_{32}} + \\ & \underbrace{\omega_z\omega_x\frac{\partial w}{\partial x}}_{\Gamma_{31}} + \underbrace{\omega_z\omega_y\frac{\partial w}{\partial y}}_{\Gamma_{32}} + \underbrace{\omega_z\omega_z\frac{\partial w}{\partial z}}_{\Gamma_{33}}\end{aligned} \tag{5.2}$$

where each row on the right hand side accounts respectively for the rate of change in the $(\frac{1}{2}\omega_x\omega_x)$, $(\frac{1}{2}\omega_y\omega_y)$ and $(\frac{1}{2}\omega_z\omega_z)$ components of the total enstrophy due to stretching and compression of vortices.

We analyze each term in equation 5.2 by a zonal averaging approach (Lakehal and Liovic, 2011) to identify the vortex evolution processes. The breaking wave is separated into two zones: upstream zone AB and downstream zone BC, which are

shown in figure 5.8. Figure 5.20 shows the zonal averaged stretching and bending terms at $t = t_b + 5/8T$. At the downstream zone BC, the vortex stretching and bending mainly happens in the upper part of the water column, primarily above the still water level. For the streamwise component ($\frac{1}{2}\omega_x\omega_x$), Γ_{11} and Γ_{31} are positive, while Γ_{21} is negative, indicating that the streamwise component of enstrophy is increased by the vortex stretching in streamwise direction and vortex bending from the vertical vortices, but decreased by the spanwise vortices. For the vertical component ($\frac{1}{2}\omega_z\omega_z$), Γ_{23} is positive while both Γ_{13} and Γ_{33} are negative, indicating that the vortex bending from the spanwise vortices will increase the vertical component of enstrophy, and the vortex bending from streamwise vortices and vortex stretching in vertical direction will decrease it. These results indicate that, at the wave front, the vertical vortices mainly gain energy from the primary spanwise vortices, and the streamwise vortices mainly gain energy from vertical vortices and vortex stretching. At the upstream zone AB, the vortex evolution processes are more complicated. The strongest evolution of vortices occurs in the middle of water column, where the streamwise vorticity is strengthened by the vortex stretching and bending from vertical vortices, and the vertical vortices are mainly strengthened by the bending from spanwise vortices. However, the vortex evolution processes are different in the upper part of the water column. The streamwise component of enstrophy is increased by Γ_{11} and Γ_{21}, indicating that the streamwise vortices are strengthened by the vortex stretching and bending from spanwise vortices. The vertical component of enstrophy is increased by Γ_{13} and Γ_{33}, indicating that the vertical vortices mainly gain energy from vortex stretching in the vertical direction and vortex bending from streamwise vortices.

Figure 5.21 shows the zonal averaged vortex stretching and bending terms at $t = t_b + 7/8T$. At the downstream zone BC, the vortex evolution processes are the same as those at $t = t_b + 5/8T$. The streamwise vortices mainly gain energy from

vortex stretching in streamwise direction and vortex bending from vertical vortices. The vertical vortices gain energy from the vortex bending from the primary spanwise vortices. At the upstream zone AB, the vortex evolution mechanisms are similar all over the water column, which is different from that at $t = t_b + 5/8T$. It's perhaps because the wave breaking ceases at this phase. The vortex evolution processes are similar to that at the upwind zone. The streamwise vorticity is strengthened by the vortex stretching and vortex bending from the vertical vortices, and the vertical vorticity is strengthened by the vortex bending from the spanwise vortices.

From the above analysis, the following conclusion can be drawn. The vortex stretching and bending plays an important role in the generation of streamwise vortices or obliquely descending eddies. The dominant mechanism of vortex evolution processes is that vertical vortices are produced by the bending of primary spanwise vortices. These vertical vortices are further subject to vortex stretching and bending to generate streamwise vortices. This conclusion is consistent with Ting's (2008) hypothesis. Of course, there also exists the possibility that the streamwise vortices are directly evolved from spanwise vortices behind the wave crest during wave breaking. This mainly happens in the upper part of water column behind the wave crest, where the free surface may affects vortex evolution processes.

5.4.2 3D Effects on Bubble Entrainment

In the above sections, we have shown that the turbulent coherent structures play an important role in bubble entrainment and downward dispersion. Then a question may rise. Are bubbles transported deeper with the effects of turbulent coherent structures? To answer this question, we conducted a 2D simulation with bubbles. The model setup is the same as that in 3D simulation except that only one computational cell is chosen in the spanwise direction. Figure 5.22 shows the void fraction distributions from the 2D simulation at different phases after wave breaking. As we can see, it is significantly different from the spanwise-averaged void fraction

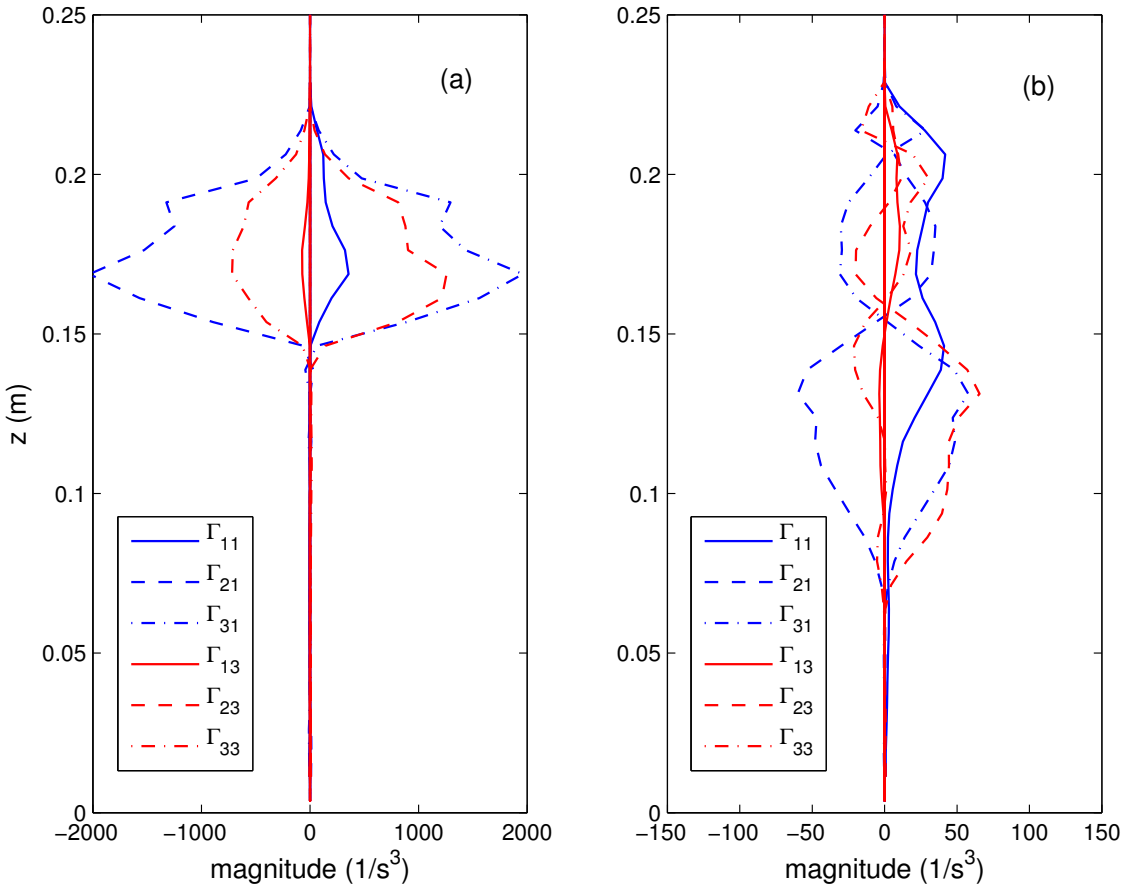

Figure 5.20: Zonal averaged stretching and bending terms in the enstrophy equation at (a) downstream zone BC and (b) upstream zone AB at $t = t_b + 5/8T$, in which $\Gamma_{11} = \omega_x\omega_x\frac{\partial u}{\partial x}$, $\Gamma_{21} = \omega_x\omega_y\frac{\partial u}{\partial y}$, $\Gamma_{31} = \omega_x\omega_z\frac{\partial u}{\partial z}$, $\Gamma_{13} = \omega_z\omega_x\frac{\partial w}{\partial x}$, $\Gamma_{23} = \omega_z\omega_y\frac{\partial w}{\partial y}$ and $\Gamma_{33} = \omega_z\omega_z\frac{\partial w}{\partial z}$.

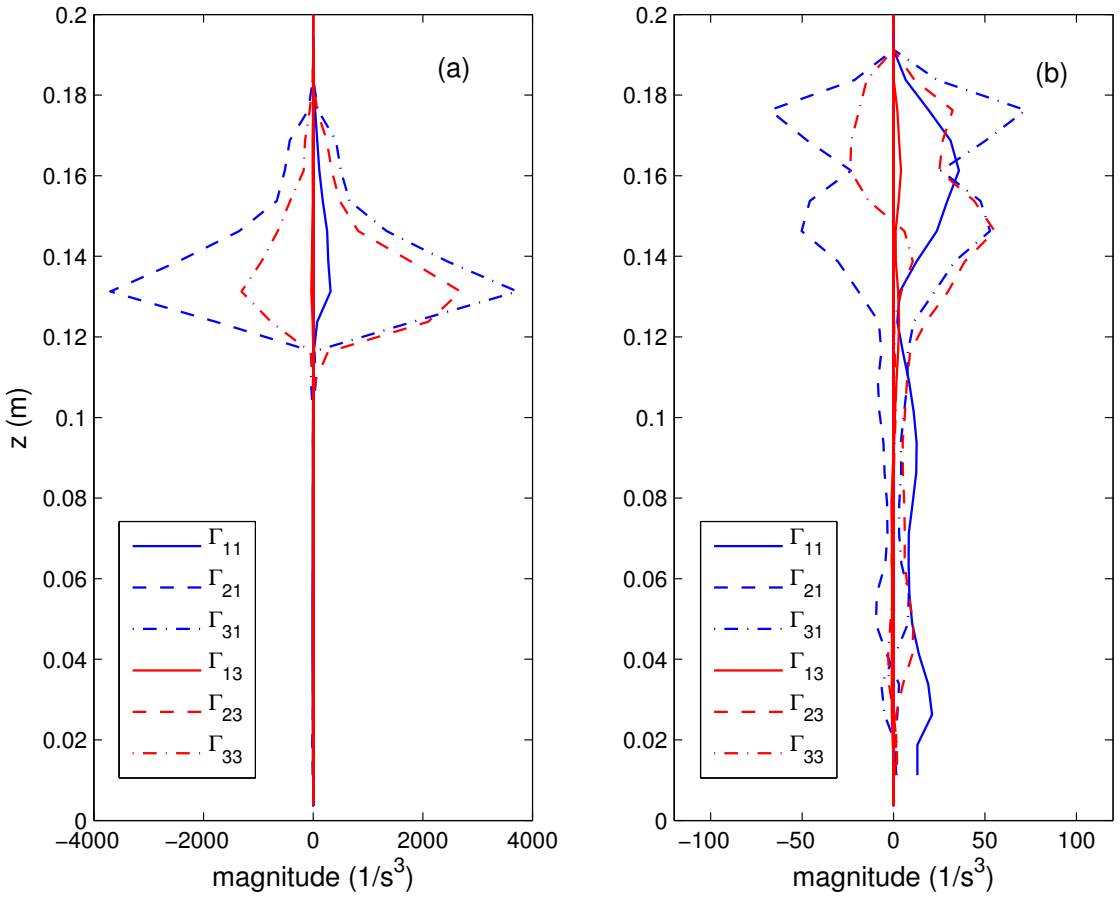

Figure 5.21: Zonal averaged stretching and bending terms in the enstrophy equation at (a) downstream zone BC and (b) upstream zone AB at $t = t_b + 7/8T$, in which $\Gamma_{11} = \omega_x\omega_x\frac{\partial u}{\partial x}$, $\Gamma_{21} = \omega_x\omega_y\frac{\partial u}{\partial y}$, $\Gamma_{31} = \omega_x\omega_z\frac{\partial u}{\partial z}$, $\Gamma_{13} = \omega_z\omega_x\frac{\partial w}{\partial x}$, $\Gamma_{23} = \omega_z\omega_y\frac{\partial w}{\partial y}$ and $\Gamma_{33} = \omega_z\omega_z\frac{\partial w}{\partial z}$.

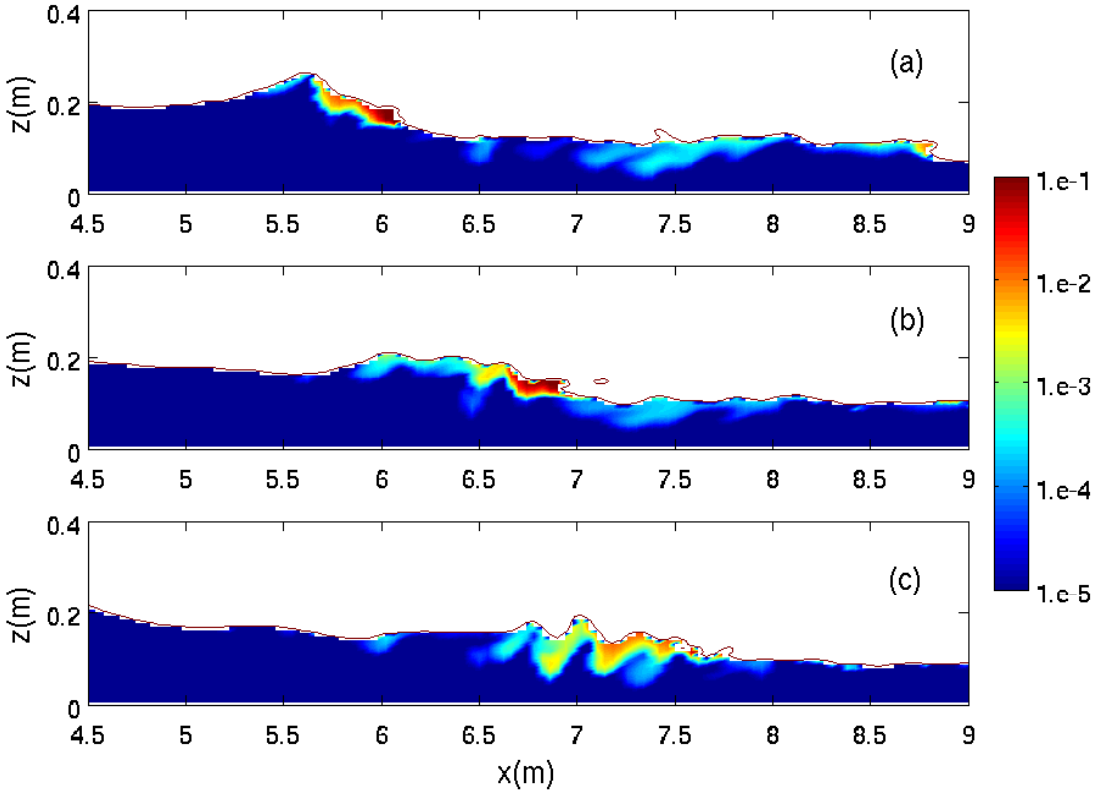

Figure 5.22: Void fraction distributions from a 2D simulation at (a) $t = t_b + 3/8T$; (b) $t = t_b + 5/8T$ and (c) $t = t_b + 7/8T$.

distributions of the 3D simulation (figure 5.15). The free surface fluctuates more in the 2D simulation due to the lack of surface wrinkles in the spanwise direction and the lack of conversion of horizontal spanwise eddies to 3D vortex structures. The void fractions are restricted in the regions close to the fluctuating surfaces. Apparently, both offshore and downward dispersion of bubbles are weakened. These differences are primarily attributed to the effects of 3D turbulent coherent structures, which may transport bubbles offshore and more deeply into the water column.

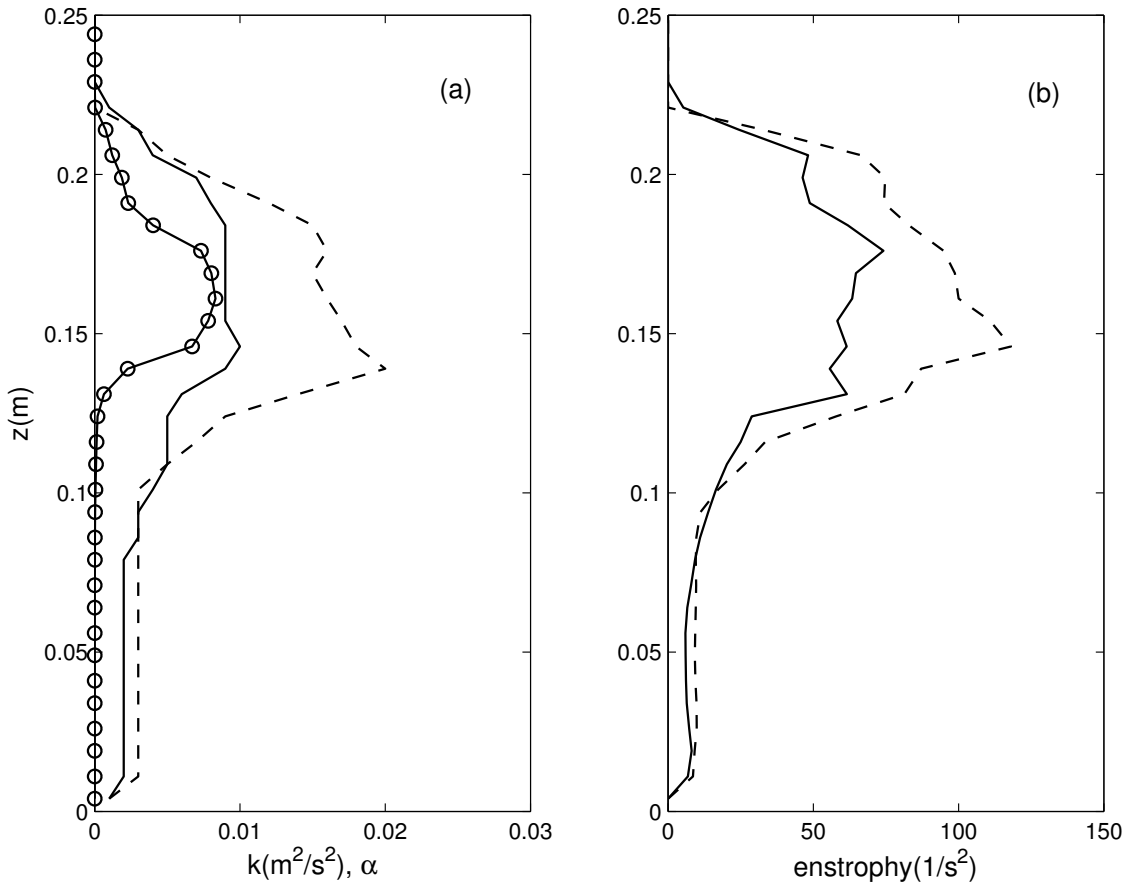

Figure 5.23: Zonal averaged turbulent kinetic energy and enstrophy with (solid lines) and without (dashed lines) bubble effects at $t = t_b + 5/8T$. The solid-circle line shows the zonal averaged void fraction distribution. The zone used to do averaging covers the whole wave length.

5.4.3 Bubble Effects on Turbulence and Vorticity Field

Another question we may pose is how bubbles affect turbulence and the vorticity field. As found in our previous study (Ma et al., 2011), the presence of bubbles can suppress liquid phase turbulence and alter its vertical distribution. In order to further confirm this conclusion, we performed a 3D simulation without bubbles. Figure 5.23a presents the comparisons of zonal averaged turbulent kinetic energy with and without bubble effects at $t = t_b + 5/8T$. The zone used to do averaging covers the whole wave length (zone AC shown in figure 5.8). The turbulent kinetic energy and void fraction are set to zero in the air side of the free surface. The zonal averaged void fraction is shown in solid-circle line in figure 5.23a. We can see that the bubble effects on the vertical distributions of turbulent kinetic energy are significant. In the upper part of the water column ($z \geq 0.13m$), the void fraction is high. The turbulent kinetic energy with bubble effects is much smaller than that without bubble effects, indicating that the turbulence is greatly suppressed by the presence of bubbles. In the lower part of the water column, the void fraction is low. The high turbulence at the upper water column has not been transported down to the lower part of the water column (figure 5.12c). Therefore, the bubble effect on turbulent kinetic energy at this part is not significant. This scenario is illustrated in detail by comparing the spanwise averaged turbulent velocity $\sqrt{w'^2}$ with and without bubble effects, which is shown in figure 5.24. In the wave roller, the turbulence is significantly suppressed by bubbles since the void fraction in this region is high (see figure 5.15c). Behind the wave crest, we notice a high turbulent region with bubbles (figure 5.24a), which corresponds to the bubble plume shown in figure 5.15c and strong downburst events shown in figure 5.10. Without bubble effects, the high turbulent region behind the wave crest appears more offshore. Generally, the turbulence behind wave crests is also decreased by bubbles. In addition to the turbulent kinetic energy, the bubbles can also affect vortex structures and

vorticity field. Due to the complexity of the vortex structures under breaking waves, we cannot observe the bubble effects on a single vortex. Therefore, we only take a look at the vorticity field represented by the zonal averaged enstrophy $< \frac{1}{2}\omega_i\omega_i >$, which is shown in figure 5.23b. The bubble effect on the enstrophy is similar to that on turbulent kinetic energy. In the upper part of the water column, because the turbulence is suppressed by bubbles, the vorticity is also decreased by the presence of bubbles. In the lower part of the water column, the vorticity field is not significantly affected by bubbles since the void fraction is low. The bubble effects on the statistics of turbulent vortex structures are displayed in figure 5.25. Bubbles seldom influence the shape of the free surface. The probability distributions of θ_{xy} with and without bubbles both show the co-existence of spanwise and streamwise vortices. Three peaks can be recognized in the distribution of θ_{xy} at the upstream part. Two peaks around 90^o and 270^o are corresponding to the spanwise vortices, while another peak around 180^o is corresponding to the streamwise vortices. We notice that bubbles rarely affect the spanwise vortices. However, they can affect the generation of streamwise vortices. This is also found in the downstream part, where the distribution of θ_{xy} peaks smaller than 270^o without bubbles, indicating that more streamwise vortices are generated without bubble effects. Because the streamwise vortices are evolved from the spanwise and vertical vortices as discussed above, these results demonstrate that bubbles may attenuate the evolution processes of turbulent vortex structures. This conclusion is further and more clearly illustrated by the probability distribution of θ_{xz}, particularly in the upstream part. With bubbles, the distribution of θ_{xz} peaks around 260^o, whereas it peaks around 180^o without bubbles, indicating that more vertical vortices are evolved into streamwise vortices without bubble effects. This occurs because the presence of bubbles suppresses turbulence, and subsequently attenuates vortex evolution processes.

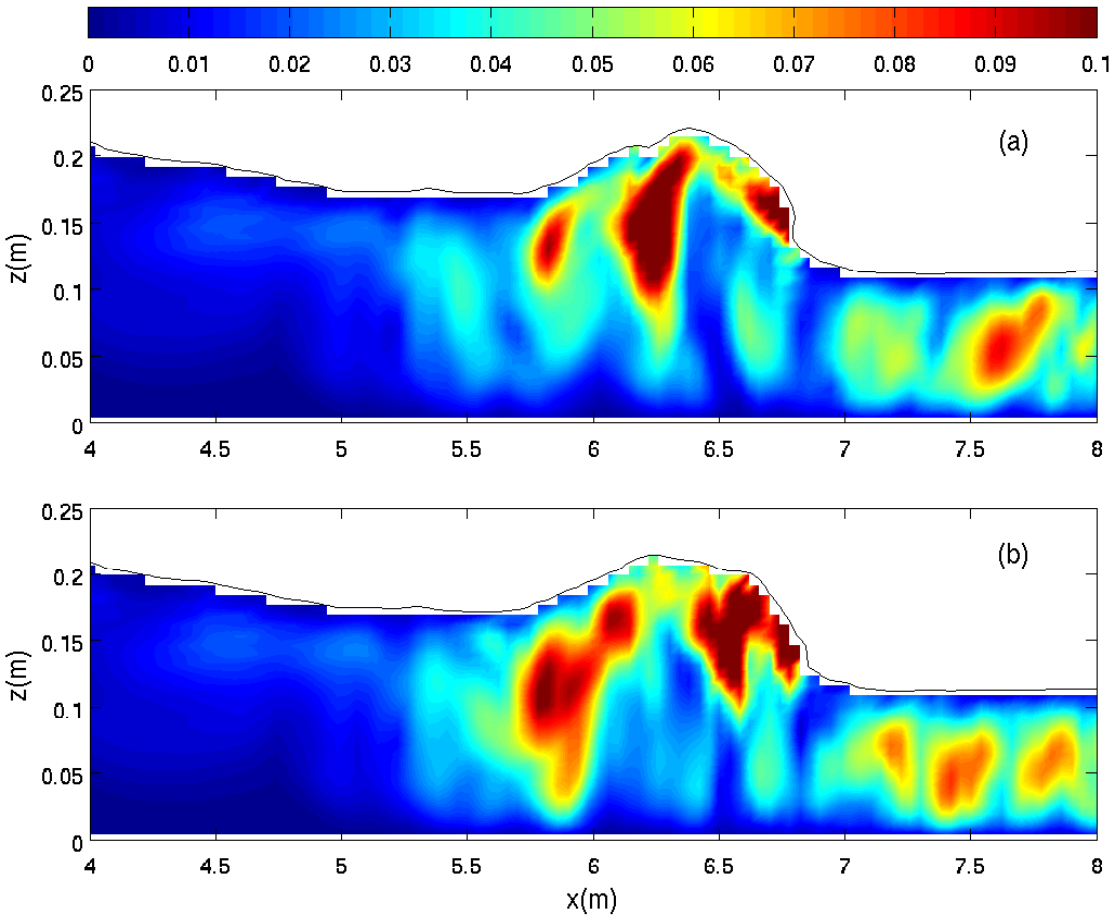

Figure 5.24: The spanwise averaged vertical turbulent velocity $\sqrt{w'^2}$ at $t = t_b + 5/8T$ with (a) and without (b) bubble effects.

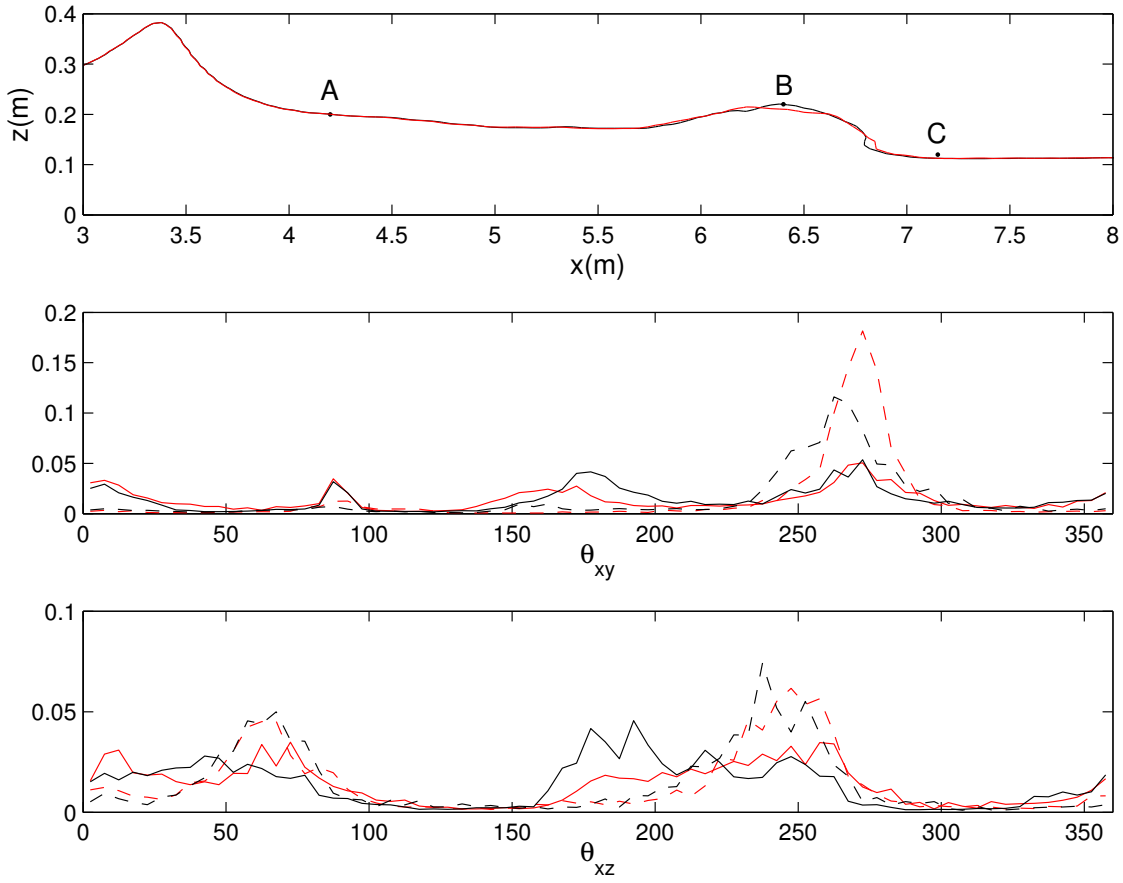

Figure 5.25: Bubble effects on the statistics of vortex structures at $t = t_b + 5/8T$. Dark solid line: upstream without bubbles; Dark dashed line: downstream without bubbles; Red solid line: upstream with bubbles; Red dashed line: downstream with bubbles.

5.5 Conclusions

A large-eddy simulation of polydisperse bubbly flow under a surfzone spilling breaking wave was performed to investigate the interactions between turbulent coherent structures and bubble entrainment. The numerical model, solving the two-phase (gas-liquid) flow equations with volume-of-fluid (VOF) surface tracking scheme and Smagorinsky subgrid turbulence closure, explicitly accounts for dispersed bubble effects on momentum and turbulence in the liquid phase as well as turbulent transport on dispersed bubbles. The model was shown to predict free surface evolution and wave height distribution fairly well in a laboratory-scale surfzone, and was capable of capturing large-scale turbulent coherent structures such as obliquely descending eddies (streamwise vortices) and downbursts of turbulent fluid under breaking waves.

The numerical model was then utilized to study turbulent coherent structure effects on turbulent kinetic energy and momentum transport as well as bubble entrainment. The results showed that the downburst of turbulent fluid is efficient on the downward transport of TKE and Reynolds stress. The obliquely descending eddies also play an important role on TKE and momentum transport. The high levels of TKE and Reynolds stress are always located at the regions between the counter-rotating vortices or the outer core of the vortices, where has strong downward velocities. The effects of turbulent coherent structures on bubble entrainment are also significant. Similar to the TKE and Reynolds stress, bubbles are also transported downward at the regions between the counter-rotating vortices. Moreover, bubbles can be trapped into the vortex core due to the preferential accumulation by the vorticity field. The coherent structures tend to transport bubbles offshore and more deeply into the water column.

The mechanisms for the generation of streamwise vortices or obliquely descending eddies were discussed by analyzing the vortex stretching and bending terms

in the enstrophy transport equation. It was found that the vortex stretching and bending plays an important role in the generation of streamwise vortices. The dominant mechanism of vortex evolution processes is that vertical vortices are produced by the bending of primary spanwise vortices, which are further subject to vortex stretching and bending to generate streamwise vortices. This finding is consistent with that speculated by Ting (2008). We also discussed the bubble effects on turbulence and vorticity field. It was found that both turbulent kinetic energy and enstrophy are decreased by the presence of bubbles. The evolution processes of turbulent vortex structures are attenuated as well.

Chapter 6

NON-HYDROSTATIC WAVE MODEL NHWAVE

In the previous two chapters, we have studied bubble plume dynamics and bubble-turbulence interactions under surfzone breaking waves. These studies have greatly enhanced our understandings of bubble dynamics and interactions among bubbles, mean flow and turbulence in the surf zone. The remaining questions are, "Can we model bubble generation and transport in a large-scale domain ($\sim 1km$) with the wave energy input and bathymetry?" and "What kind of model do we need to simulate these processes?". Essentially, we need a phase-resolving, fully dispersive wave model, which is able to simulate wave breaking, surfzone turbulence, wave-driven circulations as well as vertical structures of longshore and rip currents. In this chapter, we develop a non-hydrostatic wave model that accounts for all of these processes. The model is parallelized by MPI with non-blocking communication, which makes the model applicable to large-scale domain simulations.

6.1 Introduction

Wave propagation from deep water to coastal region is subject to wave refraction, diffraction, shoaling and breaking. Accurate prediction of these phenomena is crucial to studying nearshore hydrodynamics and solute transport in the coastal area. Boussinesq-type wave models with improved nonlinearity and dispersion characteristics provide an efficient and well-tested tool for the simulation of wave propagation, especially in shallow water regions (Madsen and Sørensen, 1992; Nwogu,

1993; Wei et al., 1995). Means for extending these models to higher order in dispersion have been developed (see Gobbi et al (2000), Lynett and Liu (2002) and Agnon et al (1999), for example), and more recently, extensions to the model formulation to account for turbulent structure of the flow field and the resulting effects on depth-averaged solute or contaminant transport have been developed (Kim et al, 2009; Kim and Lynett, 2011). All of these extensions lead to a great deal of complexity in the resulting model equations.

An alternative approach is to solve the Navier-Stokes equations directly with proper free surface tracking techniques, such as the marker-and-cell (MAC) method (Harlow and Welch, 1965), the volume-of-fluid (VOF) method (Hirt and Nichols, 1981) and the level-set method (Osher and Sethian, 1988). These approaches have wide applications on the simulations of wave shoaling and breaking in the surf zone; see, for example, Lin and Liu (1998a,b), Watanabe et al. (2005), Christensen (2006), Shi et al. (2010) and Ma et al. (2011). The main drawbacks of these types of models are: (1) They are computationally expensive, making applications to large-scale domains infeasible; (2) The free surface normally crosses the computational cell arbitrarily, which brings the difficulty of applying the pressure boundary condition precisely on the free surface and may eventually affect the accuracy of velocity computation (Lin and Li, 2002); and (3) The grid resolution in the surf zone and swash zone, where the water depth is relatively shallow, is usually poor due to the use of Cartesian grid system on most of applications.

A direct simplification of the above-mentioned approach is to assume that the free surface elevation is a single value function of the horizontal coordinates. By doing so, the free surface is always located at the upper computational boundary and can be determined by applying the free surface boundary conditions. It is computationally more efficient with the lack of free surface tracking. The pressure boundary

condition at the free surface can be accurately prescribed with some proper treatments. This simplification leads to a new set of non-hydrostatic models, which are not only suitable for modeling short wave propagation but also for the simulation of turbulence and solute transport in the surf zone. To solve the non-hydrostatic equations, the pressure is decomposed into hydrostatic and non-hydrostatic components. The governing equations can be discretized by finite difference method (Casulli and Stelling, 1998; Casulli, 1999; Namin et al., 2001; Casulli and Zanolli, 2002; Lin and Li, 2002; Chen, 2003; Stelling and Zijlema, 2003; Zijlema and Stelling, 2005; Yuan and Wu, 2004; Lee et al., 2006; Young et al., 2007, 2009, 2010; Wu et al., 2010), finite element method (Walters, 2005) and finite volume method (Bradford, 2005; Fringer et al., 2006; Ai and Jin, 2010; Lai et al., 2010; Ma et al., 2012). A major concern addressed in recent developments of non-hydrostatic models is the accurate prediction of wave dispersion characteristics with relatively few vertical grid points. It has been recognized that $10 \sim 20$ vertical layers are normally required to describe wave dispersion up to an acceptable level with some simple treatments of pressure boundary conditions at the top layer, for example, Casulli and Stelling (1998), Casulli (1999), Casulli and Zanolli (2002), Li and Fleming (2001), Namin et al. (2001), Lin and Li (2002), Chen (2003). To address this issue, Stelling and Zijlema (2003) proposed the Keller-box method to replace the staggered grid in the vertical direction, which enables the pressure to be located at the cell faces rather than the cell centers. The pressure boundary condition at the free surface can be exactly assigned to zero without any approximation. Yuan and Wu (2004a,b) proposed an integral method to remove the top-layer hydrostatic assumption using a staggered grid framework. Young and Wu (2010) used the Boussinesq-type-like equations with the reference velocity to provide an analytical-based non-hydrostatic pressure distribution at the top layer. All of these methods significantly reduce the errors in dynamic pressure estimation and allow for use of a very small number of vertical

layers for accurate simulation of dispersive waves.

It is non-trivial to apply non-hydrostatic models to the simulation of breaking waves in the surf zone and wave run-up in the swash region, because the numerical scheme involved must treat shock propagation adequately in order to model broken waves (Zijlema and Stelling, 2008). Shock-capturing schemes based on Godunov-type approach, which can deal with discontinuous flow, are well-suited for breaking wave simulations. These schemes are able to track actual location of wave breaking without requiring any criterion that tells the model when and where the wave breaking happens. An application of this approach to simulation of breaking waves in the surf zone was given by Bradford (2011). It was showed that the non-hydrostatic model with Godunov-type scheme can predict wave height distribution, turbulence and undertow under breaking waves at least as accurate as the VOF model. However, eight or more vertical layers are needed in his model to accurately predict the surface elevation around the outer surf zone as well as velocity profiles within the surf zone.

In this chapter, we describe a new nonhydrostatic model (called NHWAVE, for Non Hydrostatic WAVE model) based on a Godunov-type scheme. NHWAVE solves the incompressible Navier-Stokes equations in terrain and surface-following σ coordinates. Bottom movement is included in order to simulate tsunami generation by three-dimensional underwater landslides. To apply Godunov-type scheme, the velocities are defined at cell centers. The dynamic pressure is defined at vertically-facing cell faces as in the Keller-box method, allowing the pressure boundary condition at the free surface to be precisely imposed. The hydrostatic equations are solved by a well-balanced finite volume method. The fluxes at cell faces are estimated by HLL Riemann approximation. To obtain second-order temporal accuracy, the nonlinear Strong Stability-Preserving (SSP) Runge-Kutta scheme (Gottlieb et al., 2001) is adopted for adaptive time stepping. The model is fully parallelized using

Message Passing Interface (MPI) with non-blocking communication. The poisson equation is solved by the high performance preconditioner HYPRE software library (http://acts.nersc.gov/hypre/).

This chapter is organized as follows. In section 2, the governing equations in conservative form are presented. The numerical method, boundary conditions and wetting-drying scheme are introduced in section 3. Finally, seven test cases are given in section 4 to show the model's capability of simulating wave refraction, diffraction, shoaling, breaking, landslide tsunami generation and longshore current.

6.2 Governing Equations

The incompressible Navier-Stokes equations in Cartesian coordinates (x_1^*, x_2^*, x_3^*), where $x_1^* = x^*$, $x_2^* = y^*$ and $x_3^* = z^*$ and time t^* are given by

$$\frac{\partial u_i}{\partial x_i^*} = 0 \tag{6.1}$$

$$\frac{\partial u_i}{\partial t^*} + u_j \frac{\partial u_i}{\partial x_j^*} = -\frac{1}{\rho}\frac{\partial p}{\partial x_i^*} + g_i + \frac{\partial \tau_{ij}}{\partial x_j^*} \tag{6.2}$$

where $(i, j) = 1, 2, 3$, u_i is velocity component in the x_i^* direction, p is total pressure, ρ is water density, $g_i = -g\delta_{i3}$ is the gravitational body force and $\tau_{ij} = \nu_t(\partial u_i/\partial x_j^* + \partial u_j/\partial x_i^*)$ is turbulent stress with ν_t the turbulent kinematic viscosity.

In order to accurately represent bottom and surface geometry, a σ-coordinate developed by Phillips (1957) is adopted in this study.

$$t = t^* \quad x = x^* \quad y = y^* \quad \sigma = \frac{z^* + h}{D} \tag{6.3}$$

where $D(x, y, t) = h(x, y, t) + \eta(x, y, t)$, h is water depth, η is surface elevation. This coordinate transformation basically maps the varying vertical coordinate in the physical domain to a uniform transformed space where σ spans from 0 to 1 (Lin

and Li, 2002). Using the principle of chain differentiation, the partial differentiation of a variable $f = f(x^*, y^*, z^*, t^*)$ in the physical domain is transformed as follows.

$$\begin{aligned}
\frac{\partial f}{\partial t^*} &= \frac{\partial f}{\partial t} + \frac{\partial f}{\partial \sigma}\frac{\partial \sigma}{\partial t^*} \\
\frac{\partial f}{\partial x^*} &= \frac{\partial f}{\partial x} + \frac{\partial f}{\partial \sigma}\frac{\partial \sigma}{\partial x^*} \\
\frac{\partial f}{\partial y^*} &= \frac{\partial f}{\partial y} + \frac{\partial f}{\partial \sigma}\frac{\partial \sigma}{\partial y^*} \\
\frac{\partial f}{\partial z^*} &= \frac{\partial f}{\partial \sigma}\frac{\partial \sigma}{\partial z^*}
\end{aligned} \tag{6.4}$$

Plugging equation (6.4) into (6.1) and (6.2), we obtain the governing equations in the new coordinate (x, y, σ) and time t.

$$\frac{\partial D}{\partial t} + \frac{\partial Du}{\partial x} + \frac{\partial Dv}{\partial y} + \frac{\partial \omega}{\partial \sigma} = 0 \tag{6.5}$$

$$\frac{\partial \mathbf{U}}{\partial t} + \frac{\partial \mathbf{F}}{\partial x} + \frac{\partial \mathbf{G}}{\partial y} + \frac{\partial \mathbf{H}}{\partial \sigma} = \mathbf{S}_h + \mathbf{S}_p + \mathbf{S}_\tau \tag{6.6}$$

where $\mathbf{U} = (Du, Dv, Dw)^T$. The fluxes are

$$\mathbf{F} = \begin{pmatrix} Duu + \frac{1}{2}gD^2 \\ Duv \\ Duw \end{pmatrix} \quad \mathbf{G} = \begin{pmatrix} Duv \\ Dvv + \frac{1}{2}gD^2 \\ Dvw \end{pmatrix} \quad \mathbf{H} = \begin{pmatrix} u\omega \\ v\omega \\ w\omega \end{pmatrix}$$

The source terms are given by

$$\mathbf{S}_h = \begin{pmatrix} gD\frac{\partial h}{\partial x} \\ gD\frac{\partial h}{\partial y} \\ 0 \end{pmatrix} \quad \mathbf{S}_p = \begin{pmatrix} -\frac{D}{\rho}(\frac{\partial p}{\partial x} + \frac{\partial p}{\partial \sigma}\frac{\partial \sigma}{\partial x^*}) \\ -\frac{D}{\rho}(\frac{\partial p}{\partial y} + \frac{\partial p}{\partial \sigma}\frac{\partial \sigma}{\partial y^*}) \\ -\frac{1}{\rho}\frac{\partial p}{\partial \sigma} \end{pmatrix} \quad \mathbf{S}_\tau = \begin{pmatrix} DS_{\tau_x} \\ DS_{\tau_y} \\ DS_{\tau_z} \end{pmatrix}$$

where the total pressure has been divided into two parts: dynamic pressure p (use p as dynamic pressure hereinafter for simplicity) and hydrostatic pressure $\rho g(\eta - z)$. ω is the vertical velocity in the σ coordinate image domain, given by

$$\omega = D\left(\frac{\partial \sigma}{\partial t^*} + u\frac{\partial \sigma}{\partial x^*} + v\frac{\partial \sigma}{\partial y^*} + w\frac{\partial \sigma}{\partial z^*}\right) \tag{6.7}$$

with

$$\begin{aligned}
\frac{\partial \sigma}{\partial t^*} &= \frac{1}{D}\frac{\partial h}{\partial t} - \frac{\sigma}{D}\frac{\partial D}{\partial t} \\
\frac{\partial \sigma}{\partial x^*} &= \frac{1}{D}\frac{\partial h}{\partial x} - \frac{\sigma}{D}\frac{\partial D}{\partial x} \\
\frac{\partial \sigma}{\partial y^*} &= \frac{1}{D}\frac{\partial h}{\partial y} - \frac{\sigma}{D}\frac{\partial D}{\partial y} \\
\frac{\partial \sigma}{\partial z^*} &= \frac{1}{D}
\end{aligned} \tag{6.8}$$

In the current study, turbulent diffusion terms $S_{\tau_x}, S_{\tau_y}, S_{\tau_z}$ are included for the cases involving wave breaking, which are given by

$$\begin{aligned}
S_{\tau_x} &= \frac{\partial \tau_{xx}}{\partial x} + \frac{\partial \tau_{xx}}{\partial \sigma}\frac{\partial \sigma}{\partial x^*} + \frac{\partial \tau_{xy}}{\partial y} + \frac{\partial \tau_{xy}}{\partial \sigma}\frac{\partial \sigma}{\partial y^*} + \frac{\partial \tau_{xz}}{\partial \sigma}\frac{\partial \sigma}{\partial z^*} \\
S_{\tau_y} &= \frac{\partial \tau_{yx}}{\partial x} + \frac{\partial \tau_{yx}}{\partial \sigma}\frac{\partial \sigma}{\partial x^*} + \frac{\partial \tau_{yy}}{\partial y} + \frac{\partial \tau_{yy}}{\partial \sigma}\frac{\partial \sigma}{\partial y^*} + \frac{\partial \tau_{yz}}{\partial \sigma}\frac{\partial \sigma}{\partial z^*} \\
S_{\tau_z} &= \frac{\partial \tau_{zx}}{\partial x} + \frac{\partial \tau_{zx}}{\partial \sigma}\frac{\partial \sigma}{\partial x^*} + \frac{\partial \tau_{zy}}{\partial y} + \frac{\partial \tau_{zy}}{\partial \sigma}\frac{\partial \sigma}{\partial y^*} + \frac{\partial \tau_{zz}}{\partial \sigma}\frac{\partial \sigma}{\partial z^*}
\end{aligned} \tag{6.9}$$

and the stresses in the transformed space are calculated as

$$\begin{aligned}
&\tau_{xx} = 2\nu_t\left(\frac{\partial u}{\partial x} + \frac{\partial u}{\partial \sigma}\frac{\partial \sigma}{\partial x^*}\right) \quad \tau_{xy} = \tau_{yx} = \nu_t\left(\frac{\partial u}{\partial y} + \frac{\partial u}{\partial \sigma}\frac{\partial \sigma}{\partial y^*} + \frac{\partial v}{\partial x} + \frac{\partial v}{\partial \sigma}\frac{\partial \sigma}{\partial x^*}\right) \\
&\tau_{yy} = 2\nu_t\left(\frac{\partial v}{\partial y} + \frac{\partial v}{\partial \sigma}\frac{\partial \sigma}{\partial y^*}\right) \quad \tau_{xz} = \tau_{zx} = \nu_t\left(\frac{\partial u}{\partial \sigma}\frac{\partial \sigma}{\partial z^*} + \frac{\partial w}{\partial x} + \frac{\partial w}{\partial \sigma}\frac{\partial \sigma}{\partial x^*}\right) \\
&\tau_{zz} = 2\nu_t\left(\frac{\partial w}{\partial \sigma}\frac{\partial \sigma}{\partial z^*}\right) \qquad \tau_{yz} = \tau_{zy} = \nu_t\left(\frac{\partial v}{\partial \sigma}\frac{\partial \sigma}{\partial z^*} + \frac{\partial w}{\partial y} + \frac{\partial w}{\partial \sigma}\frac{\partial \sigma}{\partial y^*}\right)
\end{aligned} \tag{6.10}$$

The turbulent kinematic viscosity ν_t is estimated by the Smagorinsky subgrid model.

$$\nu_t = (C_s\Delta)^2\sqrt{2S_{ij}S_{ij}} \tag{6.11}$$

where C_s is the Smagorinsky coefficient, which is taken as 0.1$\sim$0.2, Δ is the filter width, which is calculated as $\Delta = (\Delta x \Delta y \Delta \sigma D)^{1/3}$, and $S_{ij} = \frac{1}{2}\left(\frac{\partial u_i}{\partial x_j^*} + \frac{\partial u_j}{\partial x_i^*}\right)$ is the stress tensor.

Integrating equation (6.5) from $\sigma = 0$ to 1 and using the boundary conditions at the bottom and surface for ω, we get the governing equation for free surface movement.

$$\frac{\partial D}{\partial t} + \frac{\partial}{\partial x}\left(D\int_0^1 u d\sigma\right) + \frac{\partial}{\partial y}\left(D\int_0^1 v d\sigma\right) = 0 \tag{6.12}$$

6.3 Numerical Method

A combined finite-volume and finite-difference scheme with a Godunov-type method was applied to discretize equations (6.6) and (6.12). It is straightforward to define all dependent variables at cell centers to solve Riemann problem. However, this treatment results in checkerboard solutions in which the pressure and velocity become decoupled when they are defined at the same location (Patankar, 1980). Therefore, most existing models use a staggered grid in which the pressure is defined at the centers of computational cells and the velocities are defined at cell faces (Bradford, 2005). However, staggered grids do not lend themselves as easily as co-located grids to the use of Godunov-type schemes. Meanwhile, difficulty in treating the cell-centered pressure at the top layer may arise when applying the pressure boundary condition at the free surface (Yuan and Wu, 2004).

With these considerations, a different kind of staggered grid framework is introduced, in which the velocities are placed at the cell centers and the pressure is defined at the vertically-facing cell faces as shown in figure 6.1. The momentum equations are solved by a second-order Godunov-type finite volume method. The HLL approximate Riemann solver (Harten et al., 1983) is used to estimate fluxes at the cell faces. As in Stelling and Zijlema (2003), the pressure boundary condition at the free surface can be precisely assigned to zero.

6.3.1 Time Stepping

To obtain second-order temporal accuracy, the two-stage second-order non-linear Strong Stability-Preserving (SSP) Runge-Kutta scheme (Gottlieb et al., 2001) was adopted for time stepping. At the first stage, an intermediate quantity $\mathbf{U}^{(1)}$ is evaluated using a typical first-order, two-step projection method given by

$$\frac{\mathbf{U}^* - \mathbf{U}^n}{\Delta t} = -\left(\frac{\partial \mathbf{F}}{\partial x} + \frac{\partial \mathbf{G}}{\partial y} + \frac{\partial \mathbf{H}}{\partial \sigma}\right)^n + \mathbf{S}_h^n + \mathbf{S}_\tau^n \tag{6.13}$$

$$\frac{\mathbf{U}^{(1)} - \mathbf{U}^*}{\Delta t} = \mathbf{S}_p^{(1)} \tag{6.14}$$

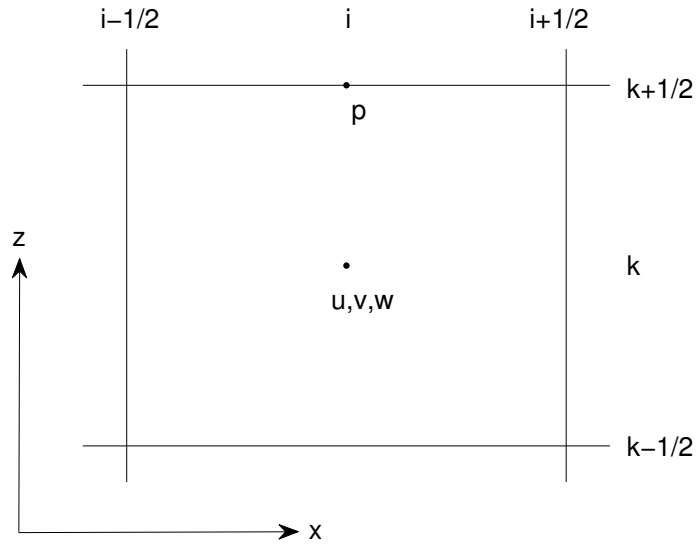

Figure 6.1: Layout of computational variables. Velocities (u, v, w) are placed at cell center and dynamic pressure (p) is defined at vertical cell face.

where $\mathbf{U}^n$ represents $\mathbf{U}$ value at time level n, $\mathbf{U}^*$ is the intermediate value in the two-step projection method, and $\mathbf{U}^{(1)}$ is the final first stage estimate. In the second stage, the velocity field is again updated to a second intermediate level using the same projection method, after which the Runge-Kutta algorithm is used to obtain a final value of the solution at the $n+1$ time level.

$$\frac{\mathbf{U}^* - \mathbf{U}^{(1)}}{\Delta t} = -\left(\frac{\partial \mathbf{F}}{\partial x} + \frac{\partial \mathbf{G}}{\partial y} + \frac{\partial \mathbf{H}}{\partial \sigma}\right)^{(1)} + \mathbf{S}_h^{(1)} + \mathbf{S}_\tau^{(1)} \tag{6.15}$$

$$\frac{\mathbf{U}^{(2)} - \mathbf{U}^*}{\Delta t} = \mathbf{S}_p^{(2)} \tag{6.16}$$

$$\mathbf{U}^{n+1} = \frac{1}{2}\mathbf{U}^n + \frac{1}{2}\mathbf{U}^{(2)} \tag{6.17}$$

Each stage of the calculation requires the specification of the nonhydrostatic component of the pressure force as expressed through the quantities $\mathbf{S}_p$. The pressure field needed to specify these is based on the solution of the Poisson equation described below. Also at each stage, the surface elevation is obtained by solving equation (6.12) explicitly. The time step Δt is adaptive during the simulation, following the Courant-Friedrichs-Lewy (CFL) criterion

$$\Delta t = C\min\left[\min\frac{\Delta x}{|u_{i,j,k}| + \sqrt{gD_{i,j}}}, \min\frac{\Delta y}{|v_{i,j,k}| + \sqrt{gD_{i,j}}}, \min\frac{\Delta \sigma D_{i,j}}{|w_{i,j,k}|}\right] \tag{6.18}$$

where C is the Courant number, which is taken to be 0.5 to ensure accuracy and stability in the current model.

6.3.2 Spatial Finite Volume Scheme

We discretize equation (6.13) and (6.15) using a second-order Godunov-type finite volume method. It is noticed that applying a standard finite volume Godunov-type scheme directly to the equation does not lead to an automatic preservation of steady state (Zhou et al., 2001; Kim et al, 2008; Liang and Marche, 2009). Therefore, It is desirable to reformulate the equation so that the flux and source terms can be automatically balanced at the discrete level in the steady state. In this study, the

method by Liang and Marche (2009) is employed. Taking the x component source term as an example, notice that the total water depth is $D = h + \eta$. The source term can be rewritten as

$$g(h+\eta)\frac{\partial h}{\partial x} = \frac{\partial}{\partial x}\left(\frac{1}{2}gh^2\right) + g\eta\frac{\partial h}{\partial x} \tag{6.19}$$

in which the first term in the right hand side can be combined together with the flux terms.

Based on this, the flux and source terms may be expressed as

$$\mathbf{F} = \begin{pmatrix} Duu + \frac{1}{2}g\eta^2 + gh\eta \\ Duv \\ Duw \end{pmatrix} \quad \mathbf{G} = \begin{pmatrix} Duv \\ Dvv + \frac{1}{2}g\eta^2 + gh\eta \\ Dvw \end{pmatrix} \quad \mathbf{S}_h = \begin{pmatrix} g\eta\frac{\partial h}{\partial x} \\ g\eta\frac{\partial h}{\partial y} \\ 0 \end{pmatrix}$$

The main advantage of the above formulation is that the flux and source terms are well-balanced so that no artificial flow due to bottom slope will be generated.

To solve equation (6.13) and (6.15), fluxes based on the conservative variables are required at the cell faces. In high-order Godunov-type methods, the values of the conservative variables within a cell are calculated using a reconstruction method based on the cell center data (Zhou et al., 2001). Usually a piecewise linear reconstruction is used, leading to a second order scheme. For $\mathbf{U}$ in the cell i, we have

$$\mathbf{U} = \mathbf{U}_i + (x - x_i)\Delta\mathbf{U}_i \tag{6.20}$$

where $\Delta\mathbf{U}_i$ is the gradient of $\mathbf{U}$, which is calculated by

$$\Delta\mathbf{U}_i = \text{avg}\left(\frac{\mathbf{U}_{i+1} - \mathbf{U}_i}{x_{i+1} - x_i}, \frac{\mathbf{U}_i - \mathbf{U}_{i-1}}{x_i - x_{i-1}}\right) \tag{6.21}$$

in which avg is a slope limiter which is used to avoid spurious oscillations in the reconstruction data at the cell faces. In this study, the van Leer limiter is adopted, which is given by

$$\text{avg}(a, b) = \frac{a|b| + |a|b}{|a| + |b|} \tag{6.22}$$

The left and right values of $\mathbf{U}$ at cell face $(i+\frac{1}{2})$ are given by

$$\mathbf{U}^L_{i+\frac{1}{2}} = \mathbf{U}_i + \frac{1}{2}\Delta x_i \Delta \mathbf{U}_i \quad \mathbf{U}^R_{i+\frac{1}{2}} = \mathbf{U}_{i+1} - \frac{1}{2}\Delta x_{i+1} \Delta \mathbf{U}_{i+1} \tag{6.23}$$

The flux $\mathbf{F}(\mathbf{U}^L, \mathbf{U}^R)$ is calculated by solving a local Riemann problem at each horizontally-facing cell face. In the present study, HLL Riemann solver is employed. The flux at the cell interface $(i+\frac{1}{2})$ is determined by

$$\mathbf{F}(\mathbf{U}^L, \mathbf{U}^R) = \begin{cases} \mathbf{F}(\mathbf{U}^L) & \text{if} \quad s_L \geq 0 \\ \mathbf{F}^*(\mathbf{U}^L, \mathbf{U}^R) & \text{if} \quad s_L < 0 < s_R \\ \mathbf{F}(\mathbf{U}^R) & \text{if} \quad s_R \leq 0 \end{cases} \tag{6.24}$$

where

$$\mathbf{F}^*(\mathbf{U}^L, \mathbf{U}^R) = \frac{s_R \mathbf{F}(\mathbf{U}^L) - s_L \mathbf{F}(\mathbf{U}^R) + s_L s_R (\mathbf{U}^R - \mathbf{U}^L)}{s_R - s_L} \tag{6.25}$$

with wave speed s_L and s_R defined by

$$s_L = \min(u^L - \sqrt{gD_L}, u_s - \sqrt{gD_s}) \tag{6.26}$$

$$s_R = \max(u^R + \sqrt{gD_R}, u_s + \sqrt{gD_s}) \tag{6.27}$$

where u_s and $\sqrt{gD_s}$ are estimated by

$$u_s = \frac{1}{2}(u^L + u^R) + \sqrt{gD_L} - \sqrt{gD_R} \tag{6.28}$$

$$\sqrt{gD_s} = \frac{\sqrt{gD_L} + \sqrt{gD_R}}{2} + \frac{u^L - u^R}{4} \tag{6.29}$$

To obtain the non-hydrostatic velocity field, the dynamic pressure p has to be calculated first. From equation (6.14) and (6.16), we get

$$u^{(k)} = u^* - \frac{\Delta t}{\rho}\left(\frac{\partial p}{\partial x} + \frac{\partial p}{\partial \sigma}\frac{\partial \sigma}{\partial x^*}\right)^{(k)} \tag{6.30}$$

$$v^{(k)} = v^* - \frac{\Delta t}{\rho}\left(\frac{\partial p}{\partial y} + \frac{\partial p}{\partial \sigma}\frac{\partial \sigma}{\partial y^*}\right)^{(k)} \tag{6.31}$$

$$w^{(k)} = w^* - \frac{\Delta t}{\rho}\frac{1}{D^{(k)}}\frac{\partial p^{(k)}}{\partial \sigma} \tag{6.32}$$

where $k = 1, 2$ represents the kth stage in the Runge-Kutta integration.

Applying equation (6.3) and (6.4), the continuity equation (6.1) is transformed as

$$\frac{\partial u}{\partial x} + \frac{\partial u}{\partial \sigma}\frac{\partial \sigma}{\partial x^*} + \frac{\partial v}{\partial y} + \frac{\partial v}{\partial \sigma}\frac{\partial \sigma}{\partial y^*} + \frac{1}{D}\frac{\partial w}{\partial \sigma} = 0 \tag{6.33}$$

Substituting equation (6.30) $\sim$ (6.32) into (6.33), we obtain the Poisson equation in (x, y, σ) coordinate system

$$\begin{aligned}
&\frac{\partial}{\partial x}\left[\frac{\partial p}{\partial x} + \frac{\partial p}{\partial \sigma}\frac{\partial \sigma}{\partial x^*}\right] + \frac{\partial}{\partial y}\left[\frac{\partial p}{\partial y} + \frac{\partial p}{\partial \sigma}\frac{\partial \sigma}{\partial y^*}\right] + \frac{\partial}{\partial \sigma}\left(\frac{\partial p}{\partial x}\right)\frac{\partial \sigma}{\partial x^*} + \\
&\frac{\partial}{\partial \sigma}\left(\frac{\partial p}{\partial y}\right)\frac{\partial \sigma}{\partial y^*} + \left[\left(\frac{\partial \sigma}{\partial x^*}\right)^2 + \left(\frac{\partial \sigma}{\partial y^*}\right)^2 + \frac{1}{D^2}\right]\frac{\partial}{\partial \sigma}\left(\frac{\partial p}{\partial \sigma}\right) = \\
&\frac{\rho}{\Delta t}\left(\frac{\partial u^*}{\partial x} + \frac{\partial u^*}{\partial \sigma}\frac{\partial \sigma}{\partial x^*} + \frac{\partial v^*}{\partial y} + \frac{\partial v^*}{\partial \sigma}\frac{\partial \sigma}{\partial y^*} + \frac{1}{D}\frac{\partial w^*}{\partial \sigma}\right)
\end{aligned} \tag{6.34}$$

The above equation is discretized with the second-order space-centered finite difference method. The velocities of (u^*, v^*, w^*) at vertical cell faces are interpolated from adjacent cell-centered values. The resulting linear equation is given by

$$\begin{aligned}
&a_1 p_{i,j-1,k-1} + a_2 p_{i-1,j,k-1} + a_3 p_{i,j,k-1} + a_4 p_{i+1,j,k-1} + a_5 p_{i,j+1,k-1} + \\
&a_6 p_{i,j-1,k} + a_7 p_{i-1,j,k} + a_8 p_{i,j,k} + a_9 p_{i+1,j,k} + a_{10} p_{i,j+1,k} + a_{11} p_{i,j-1,k+1} + \\
&a_{12} p_{i-1,j,k+1} + a_{13} p_{i,j,k+1} + a_{14} p_{i+1,j,k+1} + a_{15} p_{i,j+1,k+1} = R_p
\end{aligned} \tag{6.35}$$

where

$$a_1 = -\left(\frac{(\sigma_y)_{i,j-1,k}}{2\Delta y(\Delta\sigma_k + \Delta\sigma_{k-1})} + \frac{(\sigma_y)_{i,j,k}}{2\Delta y(\Delta\sigma_k + \Delta\sigma_{k-1})}\right)$$

$$a_2 = -\left(\frac{(\sigma_x)_{i-1,j,k}}{2\Delta x(\Delta\sigma_k + \Delta\sigma_{k-1})} + \frac{(\sigma_x)_{i,j,k}}{2\Delta x(\Delta\sigma_k + \Delta\sigma_{k-1})}\right)$$

$$a_3 = -\frac{(\sigma_x^2 + \sigma_y^2 + \frac{1}{D^2})_{i,j,k}}{0.5(\Delta\sigma_k + \Delta\sigma_{k-1})\Delta\sigma_{k-1}}$$

$$a_4 = \frac{(\sigma_x)_{i+1,j,k}}{2\Delta x(\Delta\sigma_k + \Delta\sigma_{k-1})} + \frac{(\sigma_x)_{i,j,k}}{2\Delta x(\Delta\sigma_k + \Delta\sigma_{k-1})}$$

$$a_5 = \frac{(\sigma_y)_{i,j+1,k}}{2\Delta y(\Delta\sigma_k + \Delta\sigma_{k-1})} + \frac{(\sigma_y)_{i,j,k}}{2\Delta y(\Delta\sigma_k + \Delta\sigma_{k-1})}$$

$$a_6 = a_{10} = -\frac{1}{\Delta y^2} \quad a_7 = a_9 = -\frac{1}{\Delta x^2}$$

$$a_8 = \frac{2}{\Delta x^2} + \frac{2}{\Delta y^2} + \frac{(\sigma_x^2 + \sigma_y^2 + \frac{1}{D^2})_{i,j,k}}{0.5(\Delta\sigma_k + \Delta\sigma_{k-1})\Delta\sigma_k} + \frac{(\sigma_x^2 + \sigma_y^2 + \frac{1}{D^2})_{i,j,k}}{0.5(\Delta\sigma_k + \Delta\sigma_{k-1})\Delta\sigma_{k-1}}$$

$$a_{11} = \frac{(\sigma_y)_{i,j-1,k}}{2\Delta y(\Delta\sigma_k + \Delta\sigma_{k-1})} + \frac{(\sigma_y)_{i,j,k}}{2\Delta y(\Delta\sigma_k + \Delta\sigma_{k-1})}$$

$$a_{12} = \frac{(\sigma_x)_{i-1,j,k}}{2\Delta x(\Delta\sigma_k + \Delta\sigma_{k-1})} + \frac{(\sigma_x)_{i,j,k}}{2\Delta x(\Delta\sigma_k + \Delta\sigma_{k-1})}$$

$$a_{13} = -\frac{(\sigma_x^2 + \sigma_y^2 + \frac{1}{D^2})_{i,j,k}}{0.5(\Delta\sigma_k + \Delta\sigma_{k-1})\Delta\sigma_k}$$

$$a_{14} = -\left(\frac{(\sigma_x)_{i+1,j,k}}{2\Delta x(\Delta\sigma_k + \Delta\sigma_{k-1})} + \frac{(\sigma_x)_{i,j,k}}{2\Delta x(\Delta\sigma_k + \Delta\sigma_{k-1})}\right)$$

$$a_{15} = -\left(\frac{(\sigma_y)_{i,j+1,k}}{2\Delta y(\Delta\sigma_k + \Delta\sigma_{k-1})} + \frac{(\sigma_y)_{i,j,k}}{2\Delta y(\Delta\sigma_k + \Delta\sigma_{k-1})}\right)$$

$$R_p = -\frac{\rho}{\Delta t}\left(\frac{\partial u^*}{\partial x} + \frac{\partial u^*}{\partial \sigma}\frac{\partial \sigma}{\partial x^*} + \frac{\partial v^*}{\partial y} + \frac{\partial v^*}{\partial \sigma}\frac{\partial \sigma}{\partial y^*} + \frac{1}{D}\frac{\partial w^*}{\partial \sigma}\right)$$

where $\sigma_x = \frac{\partial \sigma}{\partial x^*}$ and $\sigma_y = \frac{\partial \sigma}{\partial y^*}$.

Uniform gridding is used in the horizontal direction while gridding in the vertical direction is generalized to be non-uniform in order to capture the bottom and surface boundary layers when desired. The coefficient matrix is asymmetric and has a total of 15 diagonal lines. The linear system is solved using the high performace preconditioner HYPRE software library. With p solved, the non-hydrostatic velocities at each stage can be updated from equation (6.30) to (6.32).

6.3.3 Boundary Conditions

To solve the governing equations, boundary conditions are required for all the physical boundaries. At the free surface, the continuity of normal and tangential stresses is enforced. With wind effects absent, the tangential stress equals zero, resulting in

$$\frac{\partial u}{\partial \sigma}|_{z=\eta} = \frac{\partial v}{\partial \sigma}|_{z=\eta} = 0 \tag{6.36}$$

The vertical velocity w at the ghost cells is obtained to ensure that w at free surface satisfies the kinematic boundary condition.

$$w|_{z=\eta} = \frac{\partial \eta}{\partial t} + u\frac{\partial \eta}{\partial x} + v\frac{\partial \eta}{\partial y} \tag{6.37}$$

The zero pressure condition on the free surface is applied when the Poisson equation is solved.

$$p|_{z=\eta} = 0 \tag{6.38}$$

At the bottom, the normal velocity and the tangential stress are prescribed. The normal velocity w is imposed through the kinematic boundary condition.

$$w|_{z=-h} = -\frac{\partial h}{\partial t} - u\frac{\partial h}{\partial x} - v\frac{\partial h}{\partial y} \tag{6.39}$$

For the horizontal velocities, either free-slip boundary conditions

$$\frac{\partial u}{\partial \sigma}|_{z=-h} = \frac{\partial v}{\partial \sigma}|_{z=-h} = 0 \tag{6.40}$$

or bottom shear stresses are considered.

$$\nu_t \frac{\partial \mathbf{u}}{\partial \sigma}|_{z=-h} = D c_d |\mathbf{u}_b| \mathbf{u}_b \tag{6.41}$$

where c_d is the bed drag coefficient, which can be computed from the law of the wall for fully rough, turbulent flow as $c_d = 0.16[ln^2(15\Delta z_1/k_s)]^{-2}$, $\Delta z_1 = D\Delta\sigma_1$ is the thickness of the cell above the bed, k_s is the bottom roughness height. $\mathbf{u}_b$ is velocity at the cell above the bed.

The Neumann boundary condition is used for dynamic pressure, which is directly obtained from the governing equation for w.

$$\frac{\partial p}{\partial \sigma}|_{z=-h} = -\rho D \frac{dw}{dt}|_{z=-h} \tag{6.42}$$

where w at $z = -h$ is given by (6.39). In the application to an underwater landslide in section 4.6 below, we linearize the resulting boundary condition which gives

$$\frac{\partial p}{\partial \sigma}|_{z=-h} = \rho D \frac{\partial^2 h}{\partial t^2} \tag{6.43}$$

At the closed boundaries or vertical walls, free-slip boundary conditions are imposed, so that the normal velocity and the tangential stress are set to zero. The normal pressure gradient is zero. At inflow, both free surface and velocities calculated from the analytical solutions are specified. In the lateral direction, periodic boundary conditions can be applied. To facilitate the parallel implementation, we used two ghost cells at each boundaries. The boundary conditions are specified at the ghost cells.

6.3.4 Wetting-Drying Treatment

It is straightforward to use a wetting-drying scheme for modeling moving boundaries. In the present study, a simple wetting-drying scheme is implemented. The wet and dry cells are judged by total water depth D. If a cell has the total water depth D greater than D_{min}, it's a wet cell with $\text{Mask}_{i,j} = 1$. Otherwise it's a dry cell with $\text{Mask}_{i,j} = 0$. D_{min} is the minimum water depth allowed for computation. The surface elevation in the dry cells are defined as $\eta_{i,j} = D_{min} - h_{i,j}$. For a dry cell surrounded by wet cells, $\text{Mask}_{i,j}$ has to reevaluated as

$$\begin{aligned} \text{Mask}_{i,j} &= 1 \quad \text{if} \quad \eta_{i,j} \leq \eta_{neighbor} \\ \text{Mask}_{i,j} &= 0 \quad \text{if} \quad \eta_{i,j} > \eta_{neighbor} \end{aligned} \tag{6.44}$$

In the dry cells, the normal flux at cell faces are set to zero. The wave speed of equation (6.26) and (6.27) for a dry bed are modified as (Zhou et al., 2001)

$$s_L = u^L - \sqrt{gD_L} \quad s_R = u^L + 2\sqrt{gD_L} \quad \text{(right dry bed)} \tag{6.45}$$

$$s_L = u^R - 2\sqrt{gD_R} \quad s_R = u^R + \sqrt{gD_R} \quad \text{(left dry bed)} \tag{6.46}$$

6.4 Numerical Benchmarks

The numerical method presented in the above section has been tested with several analytical solutions and laboratory experiments. Seven test cases are given in this section: (1) standing wave in closed basin; (2) solitary wave propagation

in constant depth; (3) periodic wave over submerged bar; (4) wave transformation over an elliptical shoal on a sloped bottom; (5) breaking solitary wave runup; (6) tsunami generation by three-dimensional rigid underwater landslides; and (7) longshore current on a plane beach. These test cases have been widely used to validate non-hydrostatic models.

6.4.1 Standing Wave in Closed Basin

The numerical model was first tested by the analytical solution of a standing wave in closed basin with length of $L = 20\ m$ and depth of $D = 10\ m$. This test case has been studied by various researchers, for example, Casulli and Stelling (1998), Casulli (1999) and Chen (2003). They used more than 20 vertical layers in order to correctly simulate wave dispersion. With Keller-box scheme, Stelling and Zijlema (2003) obtained good agreement with analytical solution by using two layers. These models are all solved in Cartesian coordinate system. In this section, we will show that the present model in σ coordinates can reproduce accurate waves with relatively few vertical layers.

The initial surface elevation is given by

$$\eta = a\cos(\frac{\pi x}{10}) \tag{6.47}$$

where η is the surface elevation in meters, $a = 0.1\ m$ is the amplitude of the standing wave. The wave length equals the length of the basin. Since $kD = \pi > 1$, the wave is highly dispersive. From the dispersion relationship $\sigma^2 = gk\tanh(kD)$, where $\sigma = 2\pi/T$, $k = 2\pi/L$, we can calculate wave period $T = 3.59\ s$. The linearized analytical solution for this standing wave is

$$\eta = a\cos(kx)\cos(\sigma t) \tag{6.48}$$

For the numerical setup, a uniform grid spacing of $0.2\ m$ was used in the horizontal direction. This is a finely resolved horizontal mesh corresponding to 100 grid

cells per wavelength. Hence one does not expect large discretization errors due to the horizontal grid effects. In the vertical direction, five layers are employed. Figure 6.2 shows the comparisons of numerical and analytical surface elevations at $x = 0.1$ m and $x = 17.5$ m. The computed surface elevations agree very well with the analytical solution. The amplitude of the wave has no significant change. Figure 6.3 gives the normalized root-mean square errors at $x = 17.5$ m as a function of the number of vertical layers and wave dispersion parameter kD, which is obtained by varying water depth D. The numerical error is defined as $error = \frac{1}{H}\sqrt{\frac{1}{N}\sum_{j=1}^{N}(\eta_a - \eta_j)^2}$, where N is the number of data that are compared, η_a is the analytical solution, H is the wave height at $x = 17.5$ m. The simulation time is 30 s. As expected, the numerical errors are decreased by increasing the number of vertical layers. The numerical results are less accurate for higher dispersive wave with the same vertical layers. Therefore, more vertical layers are required to obtain sufficiently accurate predictions for highly dispersive waves.

6.4.2 Solitary Wave Propagation in Constant Depth

The second test case is the solitary wave propagation in constant water depth. The computational domain is two-dimensional with length of 200 m and water depth of 1.0 m. The solitary wave is initially at $x = 8.0$ m. An exact solution of the fully nonlinear equations, obtained using Tanaka's (1986) method, was used to specify the initial surface elevation and velocity field ($t = 0$ s at figure 6.4 and 6.5). The solitary wave has the wave height to the still water depth ratio $H/h = 0.5$, indicating that the solitary wave is highly nonlinear. The domain is discretized by a uniform grid in the horizontal direction with $\Delta x = 0.1$ m and three layers in the vertical direction. The time step Δt is adjusted during the simulation based on the Courant number, which is taken as 0.5.

Figure 6.4 shows the comparisons of simulated surface elevations and Tanaka solutions at $t = 10, 20, 40$ s. We can see that the agreements are almost perfect. As

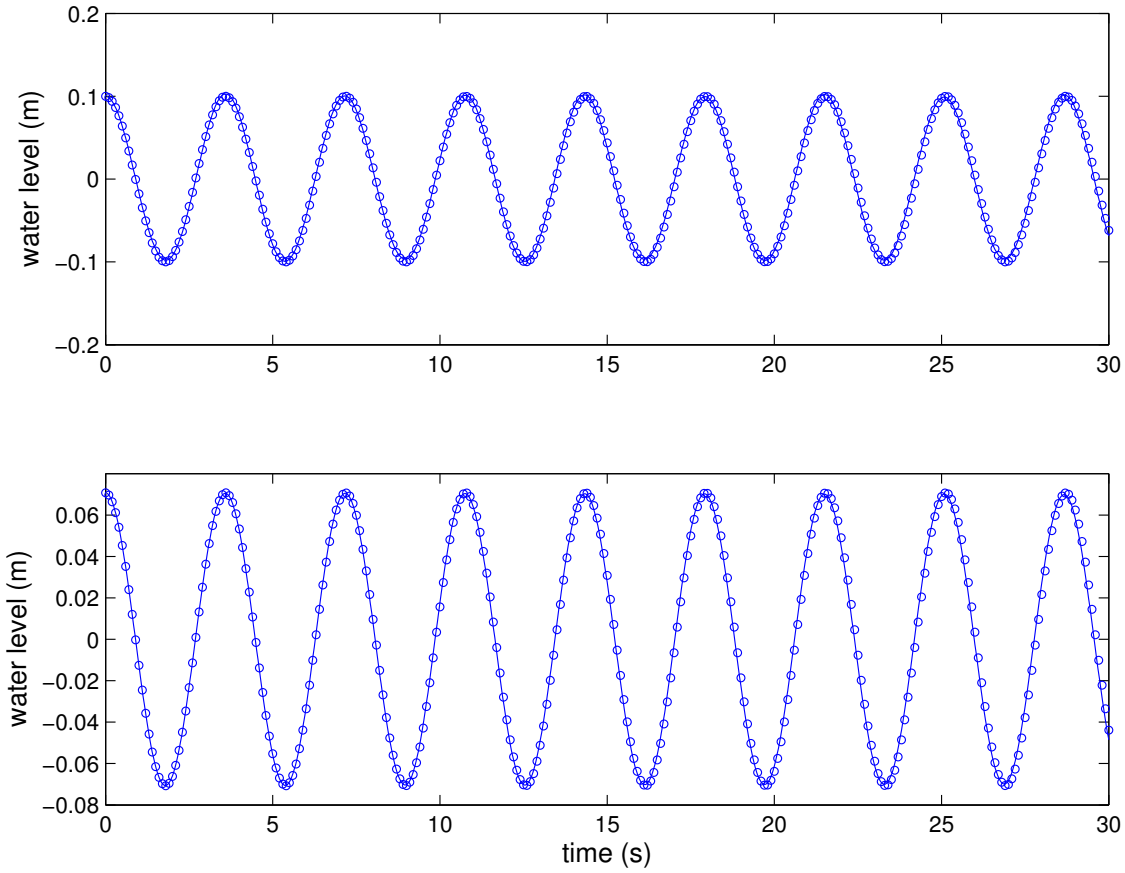

Figure 6.2: Comparisons between numerical (solid line) and analytical (circles) surface elevations at $x = 0.1\ m$ (upper panel) and $x = 17.5\ m$ (lower panel) for the standing wave in closed basin.

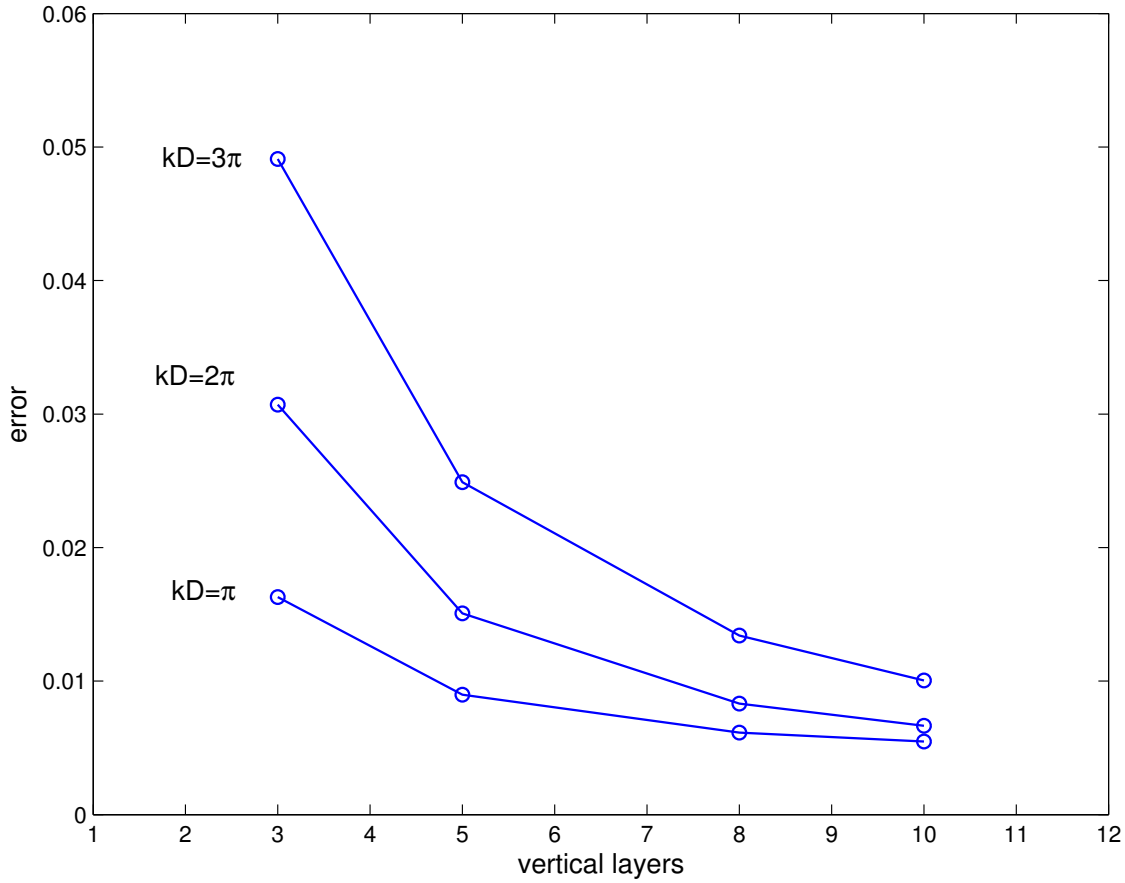

Figure 6.3: Numerical errors at $x = 17.5\ m$ as a function of the number of vertical layers and wave dispersion parameter kD.

the wave propagates to the right, the wave shape hardly change. Figure 6.5 shows the comparisons of horizontal and vertical velocities at the middle elevation between numerical results and Tanaka solutions (Tanaka, 1986). The good agreement of vertical velocity indicates that the dynamic pressure has been well simulated by the model with three vertical layers. To quantitively assess the comparisons, we calculate the relatively error $|(\phi_{comp} - \phi_{ana})/\phi_{ana}|$, where ϕ is the peak value of surface elevation and velocities. At $t = 40s$, the relatively errors for surface elevation η, horizontal velocity u and vertical velocity w are 2.7%, 2.6% and 0.8%, respectively. These relatively small errors indicate that the solitary wave is rarely decayed by the numerical diffusion.

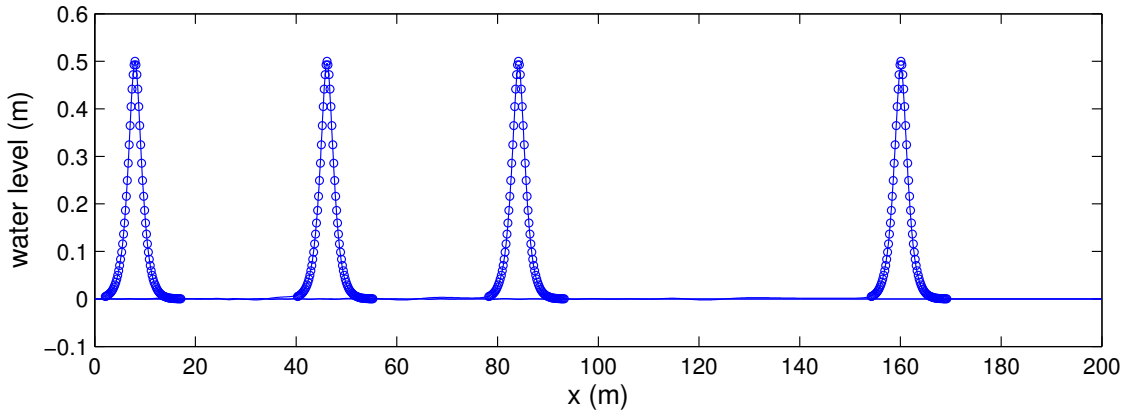

Figure 6.4: Comparisons between simulated surface elevations (solid line) and Tanaka solutions (circles) at $t = 0, 10, 20, 40$ s for solitary wave propagation in constant depth.

6.4.3 Periodic Wave Over Submerged Bar

In this section, the model is applied to simulate wave shoaling over a submerged bar. The experimental data by Beji and Battjes (1993) is used to validate our non-hydrostatic model. This case has been used to verify a number of non-hydrostatic free surface models including Casulli (1999), Lin and Li (2002), Chen (2003), Stelling and Zijlema (2003), Yuan and Wu (2004) and Bradford (2005). The

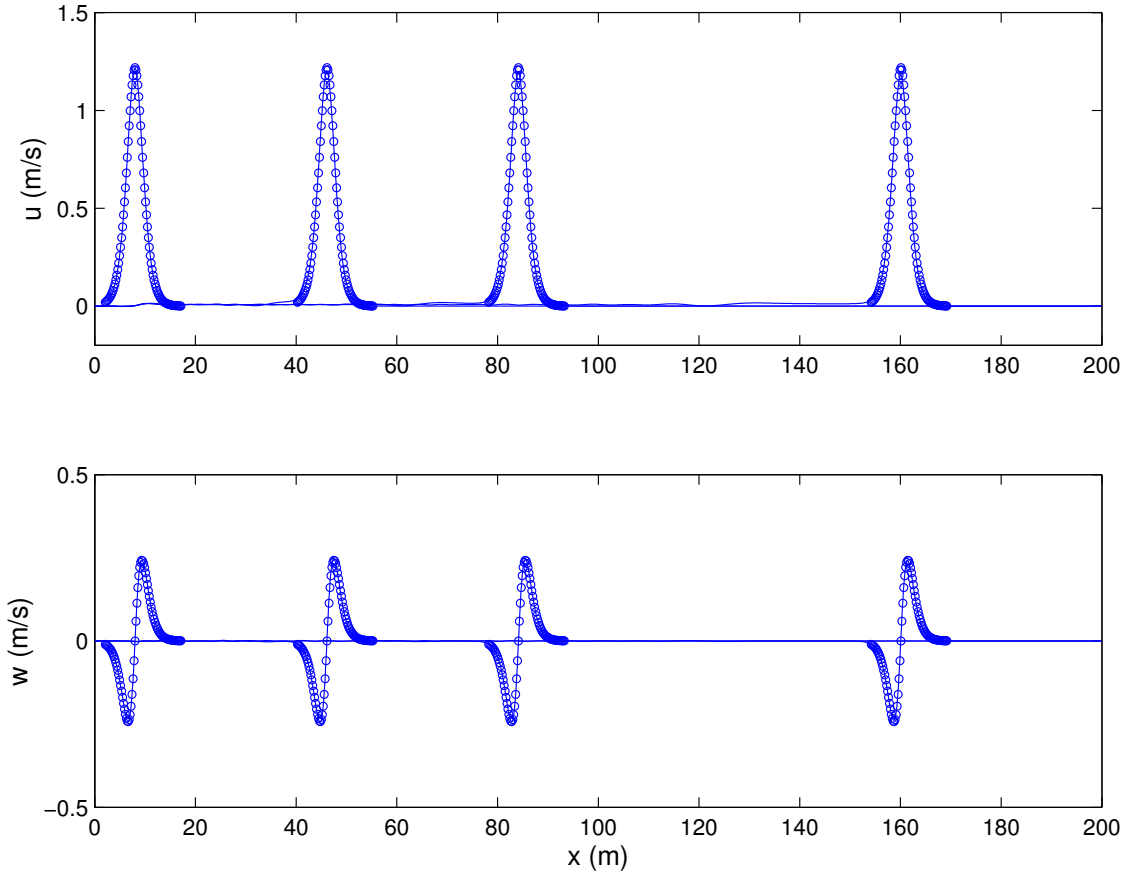

Figure 6.5: Comparisons between simulated velocities (solid line) and Tanaka solutions (circles) at $t = 0, 10, 20, 40$ s for solitary wave propagation in constant depth.

data has also frequently been used as a test of Boussinesq models, as the case falls outside the range of typical $O(\mu^2)$ models such as Wei et al (1995), but is handled by various higher order approaches such as Gobbi and Kirby (1999) or Lynett and Liu (2002).

The model setup and bottom geometry is shown in figure 6.6. The wave flume has a length of 30 m. The still water depth is 0.4 m, which is reduced to 0.1 m at the bar. The offshore slope of the bar is 1/20 and the onshore slope is 1/10. Periodic waves with period 2.02 s and amplitude 1.0 cm are incident at the left boundary. The computational domain is 35 m long with 10 m of sponge layer at the right end. The sponge layer technique introduced by Larsen and Dancy (1983) is employed. This technique has been widely used to absorbing shortwaves (Chen et al., 1999). To discretize the computational domain, 1750 constant horizontal grids and three vertical layers are used to ensure that the free higher harmonics can be properly calculated.

Figure 6.7 shows the comparisons of free surface elevation at six measurement locations between numerical results and experimental data. Wave shoaling at station a and propagation over the bar at station b are well simulated by the model. The bound higher harmonics generated by the nonlinear shoaling wave on the upward slope of the bar become free on the downward slope, resulting in irregular wave pattern at station c to f. The model generally predicts free surface evolution at these stations well, indicating that the dispersion for higher frequency components is well simulated with three vertical layers.

6.4.4 Wave Transformation Over An Elliptical Shoal on A Sloped Bottom

This example is to test the model's capability of simulating wave refraction and diffraction over a 3D uneven bottom. The corresponding experiment was conducted by Berkhoff et al. (1982). The model setup and bottom geometry is shown

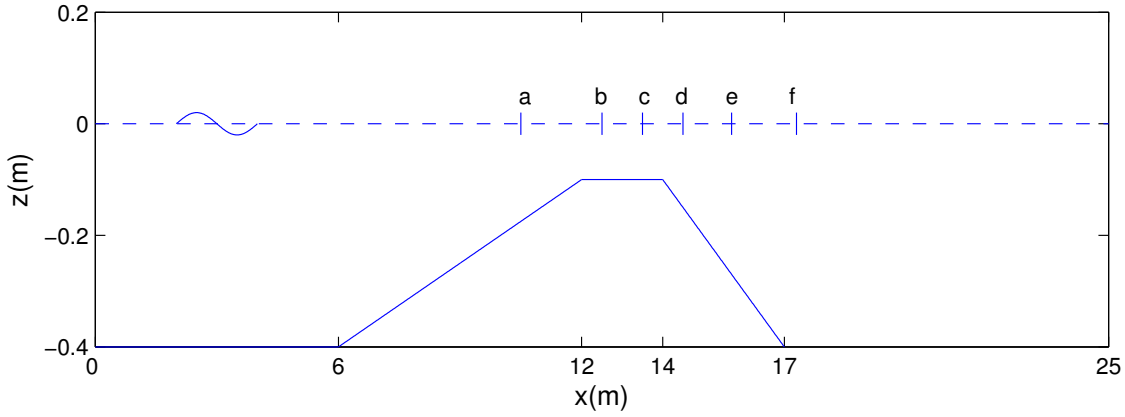

Figure 6.6: Bottom geometry and location of wave gauges used in the computation (a) $x = 10.5\ m$; (b) $x = 12.5\ m$; (c) $x = 13.5\ m$; (d) $x = 14.5\ m$; (e) $x = 15.7\ m$; (f) $x = 17.3\ m$.

in figure 6.8. An elliptical shoal is located on a plane beach with a slope of 1/50. Let (x', y') be the slope-oriented coordinates, which are related to (x, y) coordinate system by means of rotation over -20^o. The still water depth without shoal is given by

$$\begin{aligned} h &= 0.45 \quad x' < -5.84 \\ h &= max(0.07, 0.45 - 0.02(5.84 + x')) \quad x' \geq -5.84 \end{aligned} \tag{6.49}$$

Since the minimum water depth is $0.07\ m$, the wave is non-breaking. The boundary of the shoal is given by

$$\left(\frac{x'}{3}\right)^2 + \left(\frac{y'}{4}\right)^2 = 1 \tag{6.50}$$

where the thickness of the shoal is

$$d = -0.3 + 0.5\sqrt{1 - \left(\frac{x'}{3.75}\right)^2 - \left(\frac{y'}{5}\right)^2} \tag{6.51}$$

Regular wave with wave period of $1.0\ s$ and wave height of $4.64\ cm$ are incident at the left boundary $x = -12\ m$. At the right end, waves are completely absorbed by a sponge layer with $L = 5\ m$. Two walls are located at $y = -10\ m$ and $10\ m$, where free-slip boundary conditions are imposed.

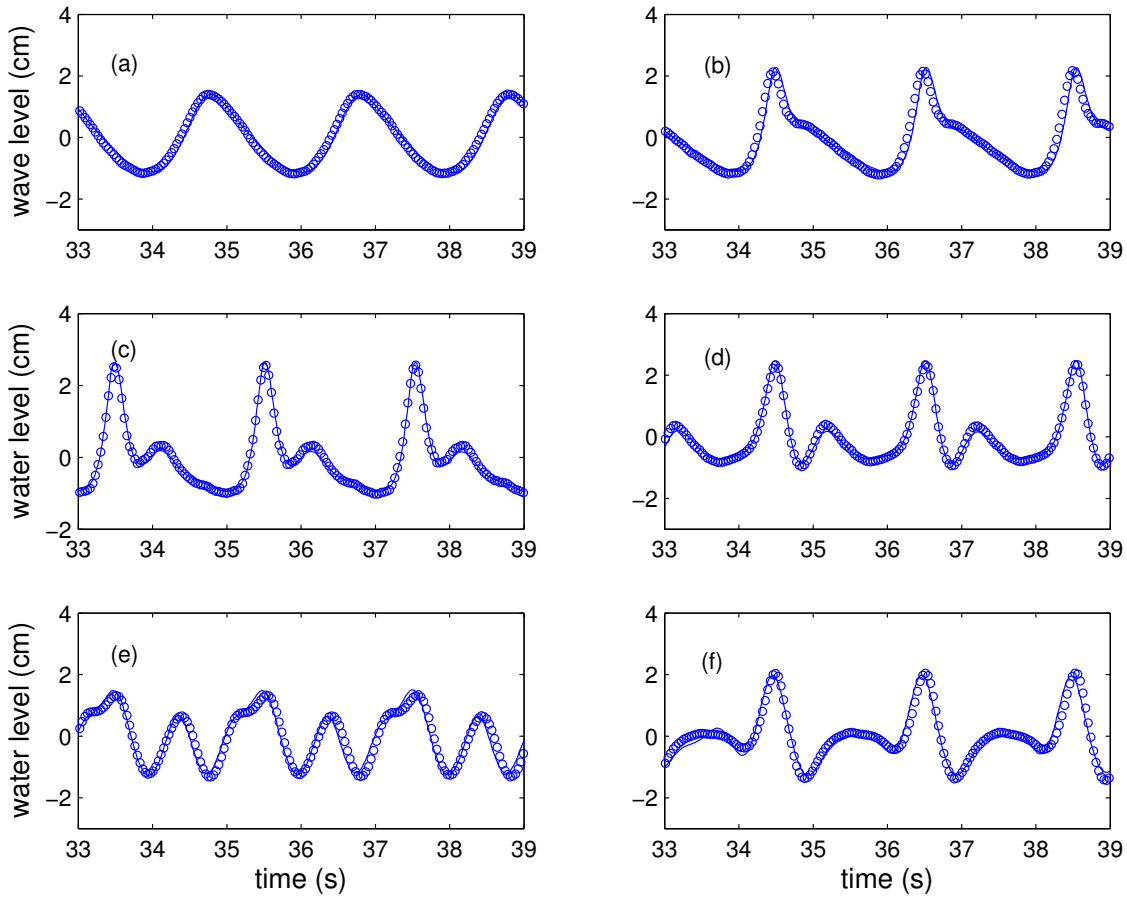

Figure 6.7: Comparisons between numerical (solid line) and experimental (circles) surface elevations at (a) $x = 10.5\ m$; (b) $x = 12.5\ m$; (c) $x = 13.5\ m$; (d) $x = 14.5\ m$; (e) $x = 15.7\ m$; (f) $x = 17.3\ m$.

To well simulate wave refraction and diffraction, a fine grid with $\Delta x = 0.025$ m and $\Delta y = 0.05$ m is used. Five vertical layers are used in the vertical direction. The time step is adjusted during the simulation, with courant number 0.5. The simulation period is 30 s. The final five waves are employed to estimate wave height. To quantitively assess the model results, we calculate normalized root mean square error $rms = \frac{1}{\overline{X}_{obs}} \sqrt{\frac{1}{N} \sum_{i=1}^{N} (X_{mod} - X_{obs})^2}$, where X is the variable being compared, *mod* and *obs* stand for model results and observations, $\overline{X}$ is mean value. Figure 6.9 shows the comparisons of wave height between numerical results and experiment data at eight measurement sections. Due to refraction, wave focussing occurs behind the shoal with a maximum wave height of approximately 2.2 times the incident wave height (around $x = 5$ m, $y = 0$ m). The model slightly under-predicts the peak wave height at section 3 and 5. However, the wave height variations along these two section are well captured. The normalized rms errors for both sections are 0.11. In other sections, the predictions agree quite well with the measurements. For example, the normalized rms error at section 1 is 0.07. These results demonstrate that wave refraction and diffraction can be well simulated by the model.

6.4.5 Breaking Solitary Wave Run-up

To show the model's capability of simulating breaking waves and wetting-drying, we applied the model to study breaking solitary wave run-up and run-down in a slope beach. The corresponding laboratory experiment was conducted by Synolakis (1987). The beach slope is 1/20. The still water depth varies from 0.21 m to 0.29 m. A solitary wave which has a wave height to still water depth ratio of 0.28 was incident on the left. Wave gauges were used to record the free surface displacement during the run-up and run-down.

In the numerical simulation, the solitary wave is initially at 1.5 m on the left from the toe of the beach. An exact solution of the fully nonlinear equations,

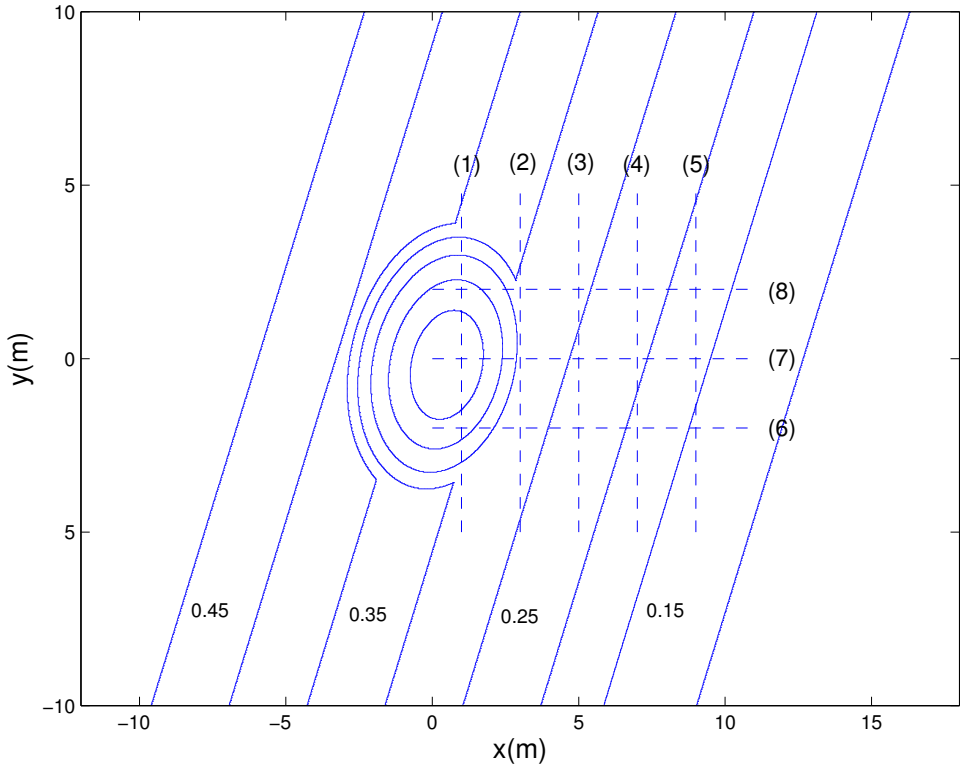

Figure 6.8: Bottom geometry for periodic wave propagation over an elliptical shoal, experimental setup by Berkhoff et al. (1982)

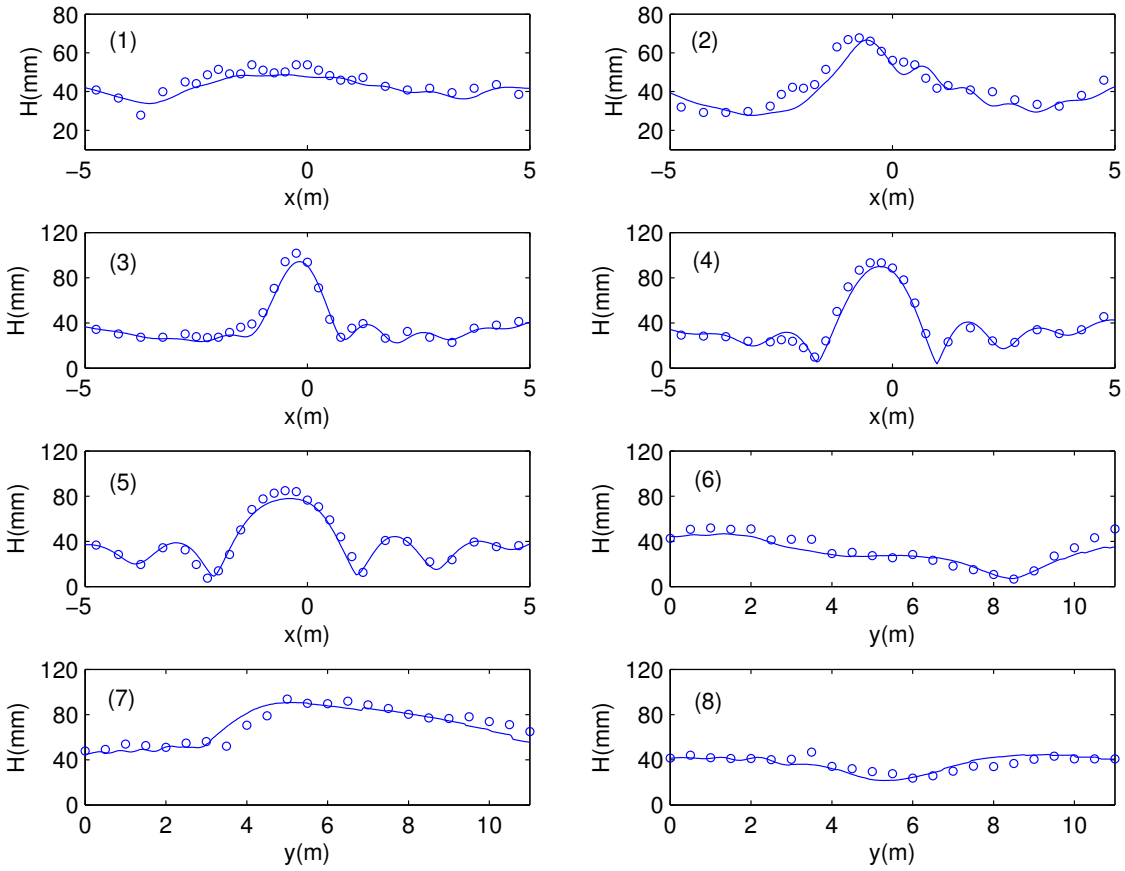

Figure 6.9: Comparisons between numerical (solid line) and experimental (circles) wave height at eight stations.

obtained using Tanaka's (1986) method, was used to specify the initial surface elevation and velocity field, see figure 6.10. The computational domain extends to a location beyond the maximum run-up point. The entire domain is discretized by 550 uniform grid in the horizontal with $\Delta x = 0.02\ m$. Three layers are used in the vertical direction. The minimum water depth is 5 mm, which determines wetting-and-drying of the computational cells.

The numerical results were compared with the experimental data after normalization. The length scale is normalized by the still water depth d and the time scale is normalized by $\sqrt{g/d}$. Figure 6.11 shows comparisons of simulated and measured free surface profile during wave shoaling, breaking, run-up and run-down. Panels (a) and (b) show the shoaling process of the solitary wave. The wave becomes more asymmetric and the wave height increases as water depth decreases. Around $t\sqrt{g/d} = 20$, the wave starts to break as shown in panel (c), the surface profile is dramatically changed and the wave height is rapidly reduced. The wave continuously breaks as its turbulent front moves towards the shoreline. After the wave front passes the still-water shoreline, it collapses and the consequent run-up process commences. The run-up process is shown in the panel (d) and (e). After reaching the maximum run-up point, the front starts to run-down which is shown in the panel (f). The comparisons between the simulation and experiment data are fairly good. The shoaling, breaking, run-up and run-down processes of the solitary wave are well reproduced. In figure 6.11, we also shown the numerical results without including turbulent diffusion terms. During wave shoaling and breaking, the predicted surface elevation is seldom impacted by neglecting turbulence. This result is consistent with the findings by Bradford (2011) and Zijlema and Stelling (2008). However, the model without turbulence model slightly overpredicts wave runup as shown in panel (e) and (f).

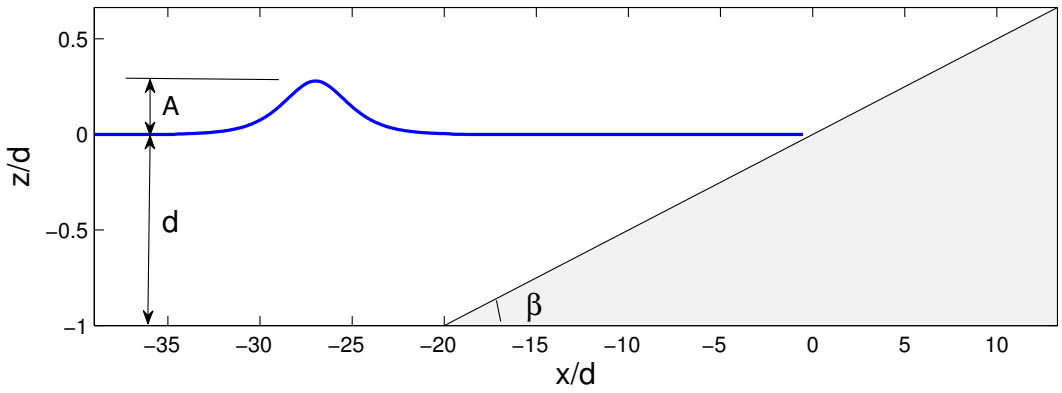

Figure 6.10: Computational domain and model setup. The beach slope is 1/20. The still water depth is 0.21 m. The amplitude of solitary wave is 0.0588 m.

6.4.6 Tsunami Generation by Three-dimensional Underwater Landslides

Submarine landslides are one of the most dangerous mechanisms for tsunami generation in the coastal areas. In this section, we applied the model to simulate tsunami generation by an idealized three-dimensional underwater landslides. Experiments have recently been performed by Enet and Grilli (2007) in a 3.7 m wide, 1.8 m deep and 30 m long wave tank with a plane underwater slope with $\theta = 15^o$ angle. This data set has also been used recently by Fuhrman and Madsen (2009) to test the accuracy of a higher-order Boussinesq model.

The vertical cross section of the landslide is shown in figure 6.12. The geometry is defined using truncated hyperbolic secant functions.

$$\zeta = \frac{T}{1-\epsilon}[\text{sech}(k_b x)\text{sech}(k_w y) - \epsilon] \tag{6.52}$$

where $k_b = 2C/b$, $k_w = 2C/w$ and $C = acosh(1/\epsilon)$. The landslide has length $b = 0.395\ m$, width $w = 0.680\ m$ and thickness $T = 0.082\ m$. The truncation parameter $\epsilon = 0.717$. The landslide is initially located at the submergence depth d.

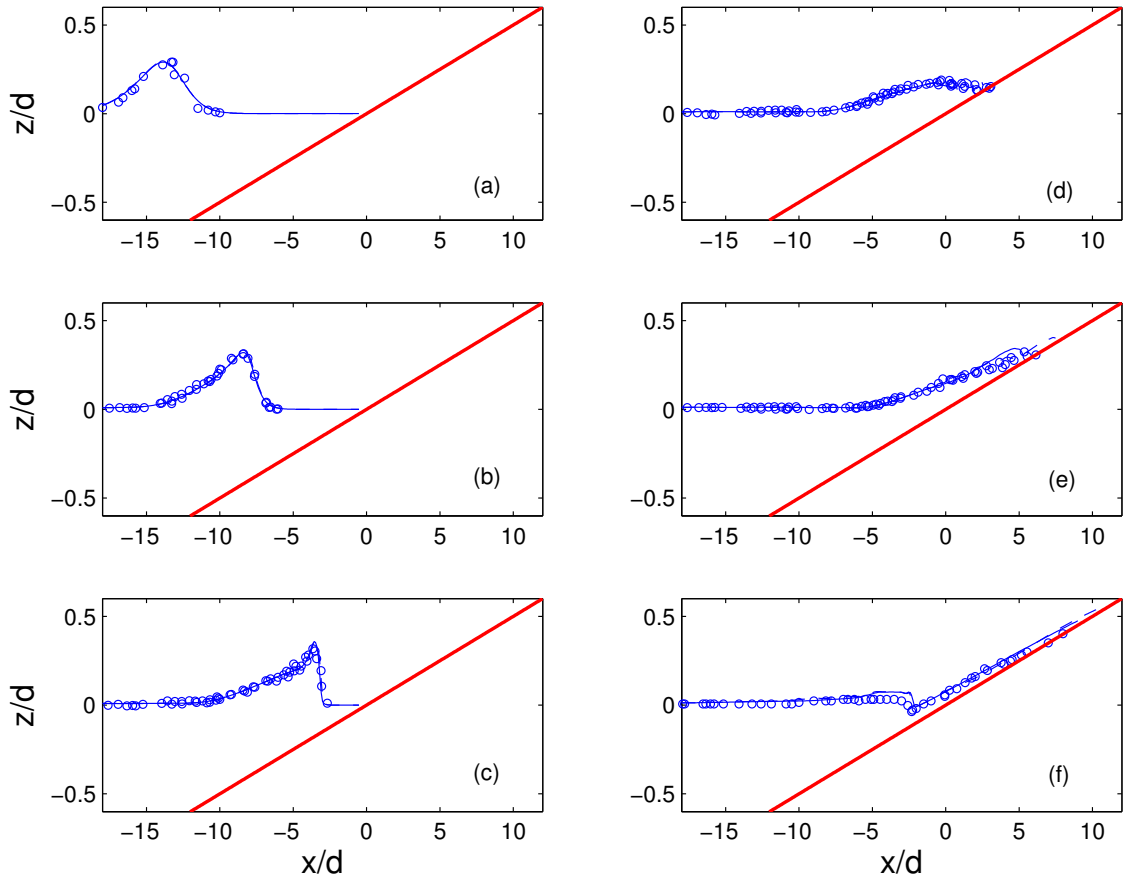

Figure 6.11: Comparisons between numerical (with subgrid model: solid line; without subgrid model: dashed line) and experimental (circles) free surface elevation for breaking solitary wave run-up and run-down at (a) $t\sqrt{g/d} = 10$; (b) $t\sqrt{g/d} = 15$; (c) $t\sqrt{g/d} = 20$; (d) $t\sqrt{g/d} = 25$; (e) $t\sqrt{g/d} = 30$; (f) $t\sqrt{g/d} = 50$.

The movement of the landslide is prescribed as

$$s(t) = s_0 \ln(\cosh \frac{t}{t_0}) \tag{6.53}$$

which closely approximates the landslide displacement measured in experiments. s_0 and t_0 are given by

$$s_0 = \frac{u_t^2}{a_0}, \quad t_0 = \frac{u_t}{a_0} \tag{6.54}$$

where u_t and a_0 are the landslide terminal velocity and initial acceleration, respectively. To represent the landslide, the horizontal domain is discretized by a uniform grid with $\Delta x = 0.02\ m$ and $\Delta y = 0.02\ m$. Three vertical layers are employed in the simulation. The landslide parameters are $u_t = 1.70\ m/s$ and $a_0 = 1.12\ m/s^2$.

Three wave gauges are located at (x, y) locations $(1469, 350), (1929, 0)$ and $(1929, 500)$, where all distances are in mm and where x denotes distance from the still water shoreline and y denotes distances off the centerline axis of the sliding mass. Model results are presented as time series in comparison to measured data at each of the three gages, with two representative tests chosen. Figure 6.13 shows model/data comparisons for the case of an initial submergence of the landslide center of $d = 61$ mm. The model is seen to represent the amplitude and the phase structure of the generated wave train well. As would be expected, wave heights are highest at the gage lying along the axis of the landslide motion and drop off with distance away from the centerline axis. Figure 6.13 also displays the results of a hydrostatic model simulation, which are obtained by neglecting the pressure correction steps indicated in the equation (6.14) and (6.16). These results are markedly different from the non-hydrostatic model results, indicating the great importance of dispersion in this test. The hydrostatic result basically consists of a strong drawdown of the water column immediately behind the sliding mass. This drawdown first grows in magnitude and then decreases as the relative depth of submergence becomes larger. In contrast, the nonhydrostatic model result consists of a packet of dispersive waves which lag behind the relatively faster moving slide as the slide accelerates. This behavior is

further illustrated in snapshots of the generated wave trains at times $t = 1$, 2 and 3 s shown in figure 6.14 and 6.15, with nonhydrostatic behavior shown in the sequence of panels in figure 6.14 and hydrostatic behavior shown in the sequence in figure 6.15. The absence of dispersion in the generated waves in figure 6.15 is clear, emphasizing the importance of frequency dispersion in the present example. We note that the results of Fuhrman and Madsen (2009), obtained using a higher-order Boussinesq model, showed comparable capabilities in predicting wave phase structure as the nonhydrostatic model here, but tended to overpredict crest and trough heights to some degree in comparison to the results here; see their figure 14.

Figure 16 illustrates similar results for the case of an initial depth of submergence of $d = 120$ mm. Generated wave heights are lower here than in the previous case due to the greater depth of submergence, but the pattern of sea surface response is qualitatively similar to the previous case. Hydrostatic results for this case have not been computed as the problem is in relatively deeper water than the previous case.

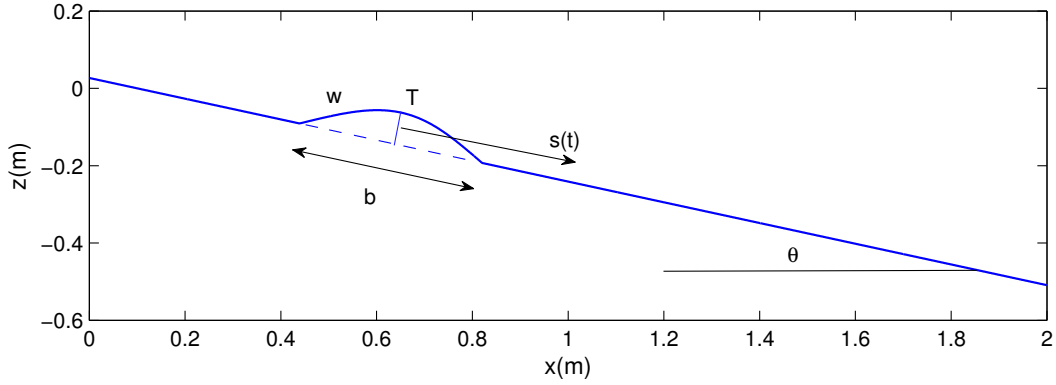

Figure 6.12: Vertical cross section for numerical setup of tsunami landslide. The gaussian shape landslide model has length $b = 0.395\ m$, width $w = 0.680\ m$ and thickness $T = 0.082\ m$ and is initially located at submergence depth d. The beach slope has an angle of $\theta = 15^o$.

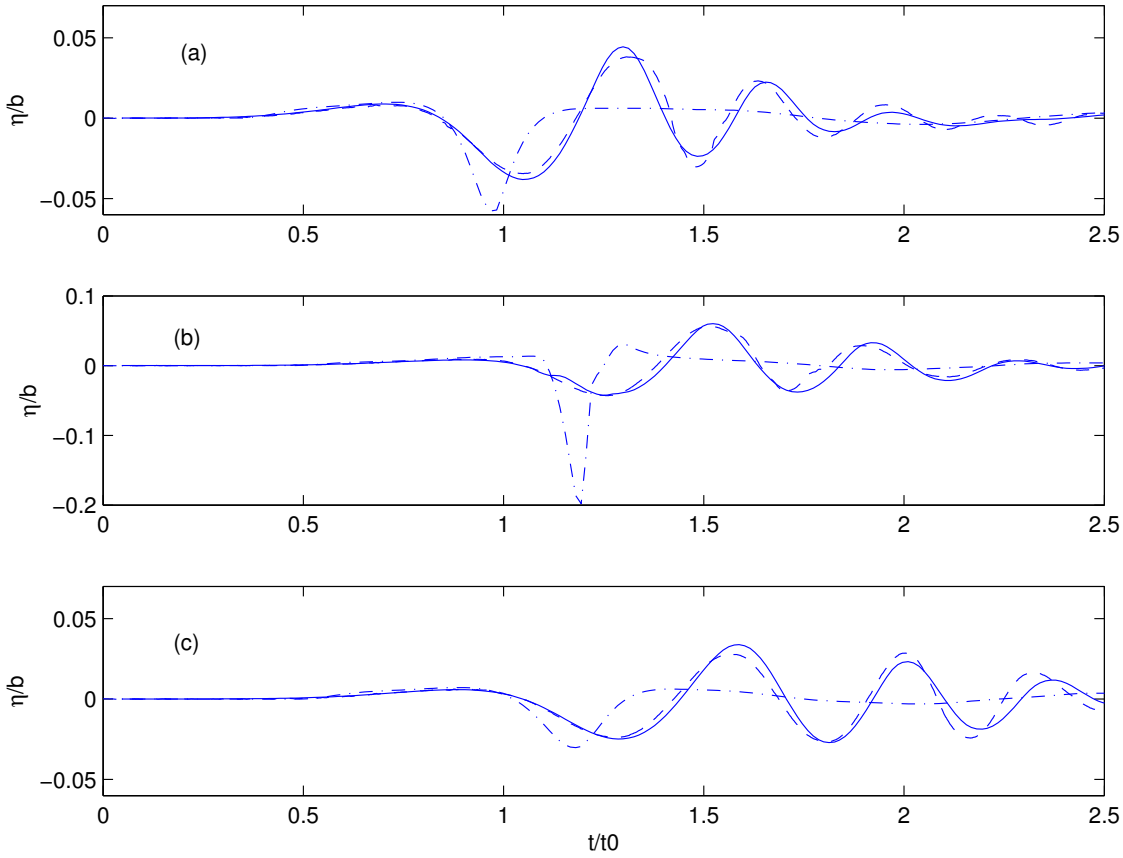

Figure 6.13: Comparisons between nonhydrostatic numerical results (solid lines), hydrostatic numerical results (dash-dot lines) and experimental data (dashed lines) for free surface elevation for landslide-generated waves at three wave gauges with initial depth of submergence $d = 61$ mm. Gauge coordinates (x, y): (a) (1469, 350)mm; (b) (1,929, 0) mm; (c) (1929, 500) mm, where x is distance from shoreline and y is perpendicular distance from the axis of the shore-normal slide trajectory.

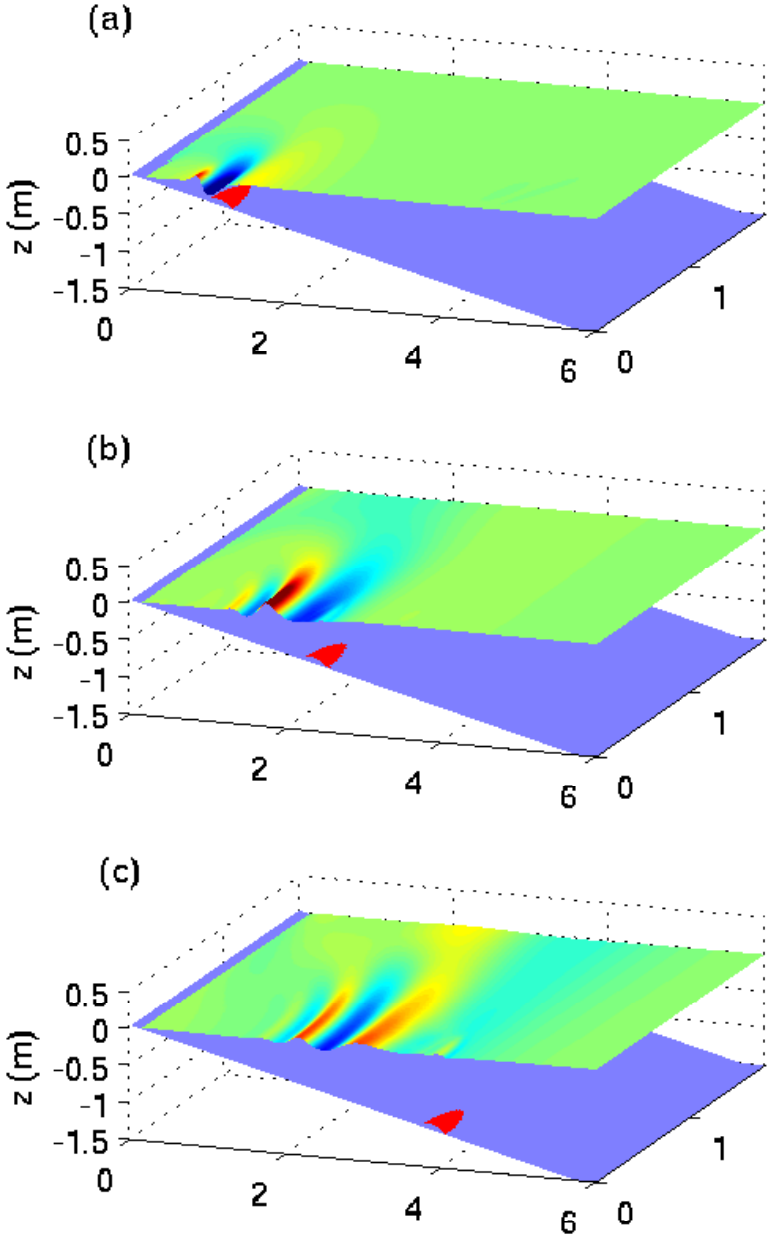

Figure 6.14: Snapshots of landslide-generated waves simulated using nonhydrostatic model at times (a) $t = 1.0\ s$; (b) $t = 2.0\ s$ and(c) $t = 3.0\ s$ after release of the sliding mass. The surface elevation is exaggerated 5 times.

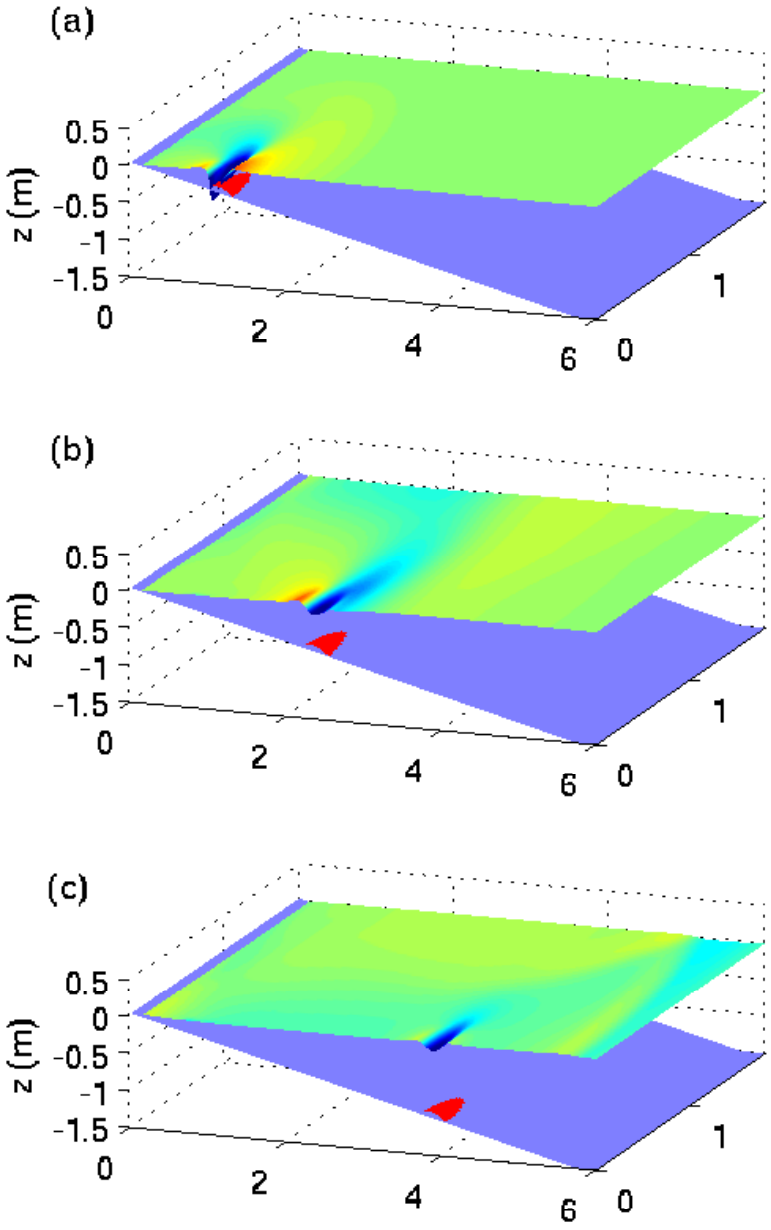

Figure 6.15: Snapshots of landslide-generated waves simulated using hydrostatic model at times (a) $t = 1.0\ s$; (b) $t = 2.0\ s$ and(c) $t = 3.0\ s$ after release of the sliding mass. The surface elevation is exaggerated 5 times.

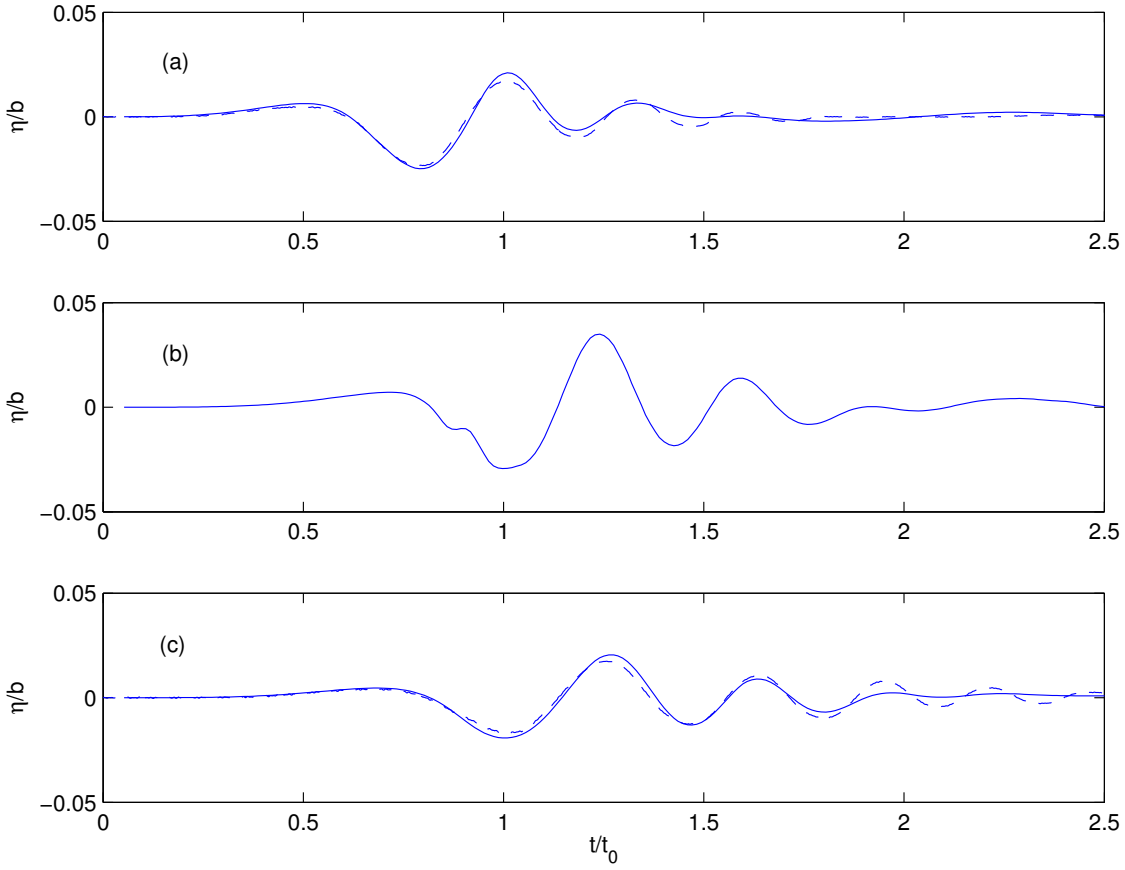

Figure 6.16: Comparisons between numerical nonhydrostatic results (solid lines) and experimental data(dashed lines) for free surface elevation for landslide-generated waves at three wave gauges with initial depth of submergence $d = 120$ mm. Gauge coordinates (x, y): (a) (1469, 350) mm; (b) (1929, 0) mm; (c) (1929, 500) mm. Experimental data are not available for (b).

6.4.7 Longshore Current on A Plane Beach

The implementations of turbulence closure and periodic boundary condition enable us to simulate longshore current in the surf zone. The laboratory measurements of breaking-generated longshore currents on plane beaches reported by Visser (1991) are employed to demonstrate the capability of the model. We particularly choose case 4 in Visser's (1994) experiments. This data set has been employed by Chen et al. (2003) to test wave-resolving Boussinesq model. In the physical model, the slope of the smooth concrete beach is 1:20, which starts from an offshore water depth of 35 cm. The obliquely incident, regular wave train has an amplitude of 3.9 cm, with a period of 1.02 s and an angle of incidence of 15.4 degrees in the offshore boundary.

The computational domain is chosen to be 8.4 m long with a 0.6 m flat bottom placed in front of the slope. The width of the domain is determined on the basis of periodic lateral boundary condition. The domain is discretized by 280×128 grid cells with $\Delta x = 0.03m$ and $\Delta y = 0.04325m$. Five vertical layers are used. Turbulence model is turned on to account for wave breaking-induced energy dissipation. The bottom roughness height is chosen as $k_s = 0.08cm$ by tuning the model to match the measurement.

Figure 6.17 shows a snapshot of computed surface elevation. Due to the nonlinear shoaling effects, the wave crest becomes narrow and asymmetric near the shoreline. The wave height is greatly reduced by the depth-limited wave breaking. The breaking-generated longshore current is obtained by time-averaging the depth-averaged current over five wave periods, which is demonstrated in figure 6.18. The computed time-averaged flow field is longshore uniform and no shear instabilities occur, which is consistent with the Boussinesq model simulation (Chen et al., 2003). The cross-shore velocity is nearly zero, indicating that the mass is balanced. Figure 6.19 gives the comparisons of computed wave setup and longshore current with the

laboratory measurements. Generally, the comparisons are quite good. The model slightly underestimates wave setdown near the breaking region. It might be because the breaking wave is a plunging breaker in the laboratory experiment, which cannot be well simulated by the model. The computed longshore current is estimated at $t = 110s$. We notice that the difference of computed longshore currents at $t = 100s$ and $t = 110s$ is minor, indicating that a steady solution of longshore current has been achieved at the end of simulation. The magnitude and the location of maximum longshore current are well predicted by the model. The correct prediction of cross-shore variation of longshore current indicates that the model can reasonably simulate wave breaking and associated energy dissipation.

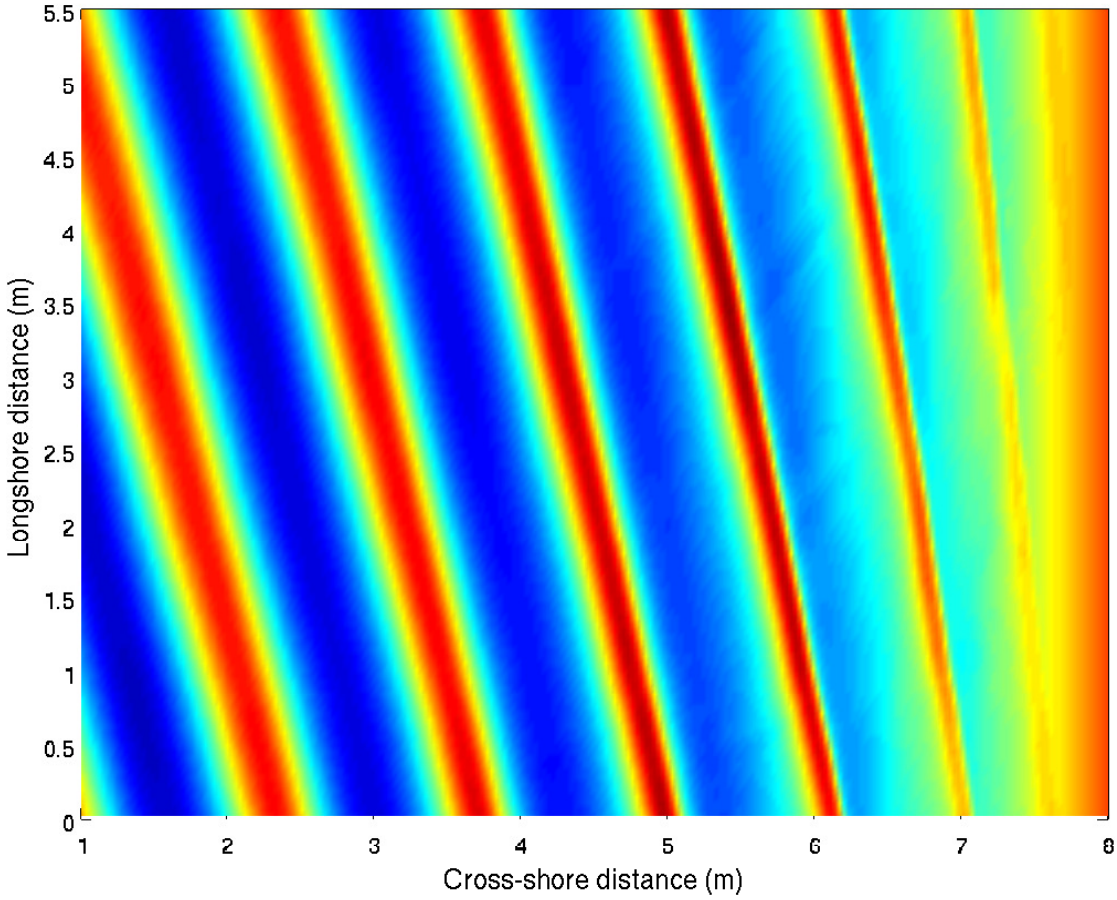

Figure 6.17: A snapshot of computed surface elevation of case 4 in Visser's experiment (1991).

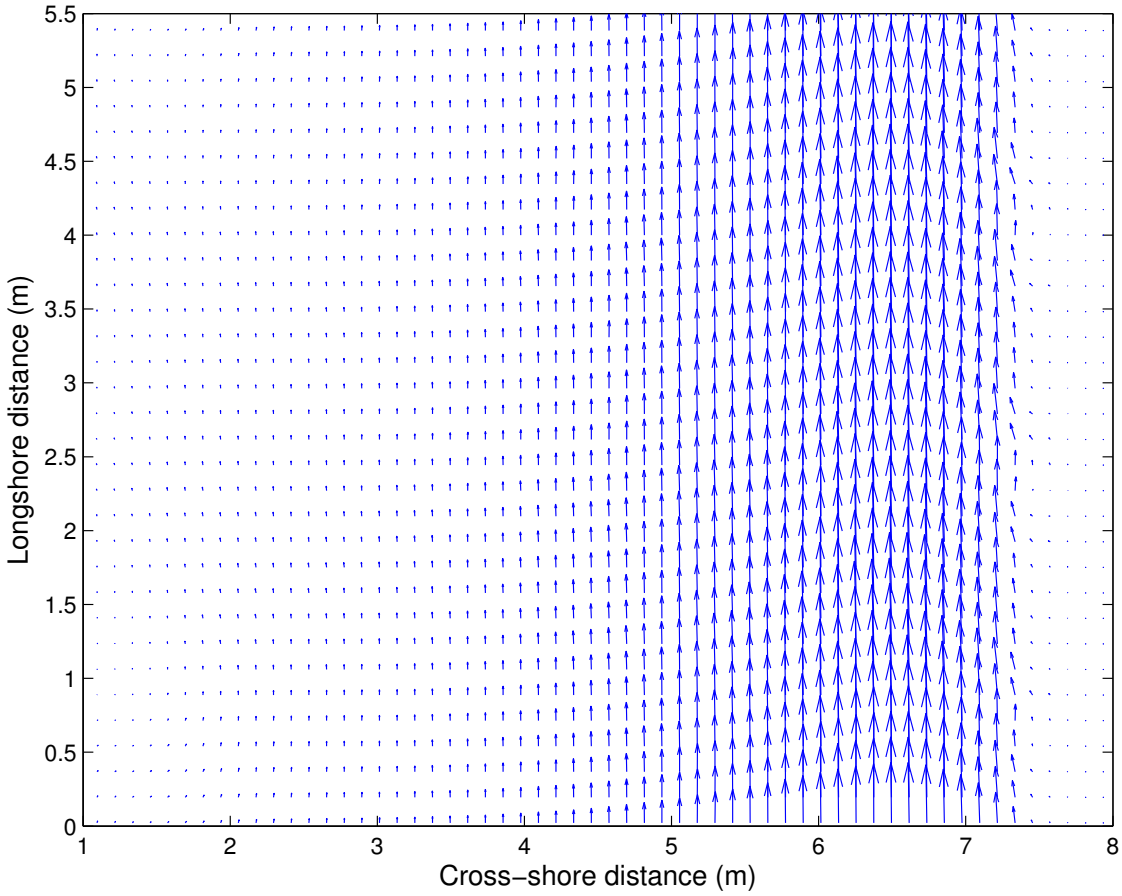

Figure 6.18: Phase-averaged current field (averaged by 5 waves) of case 4 in Visser's experiment (1991).

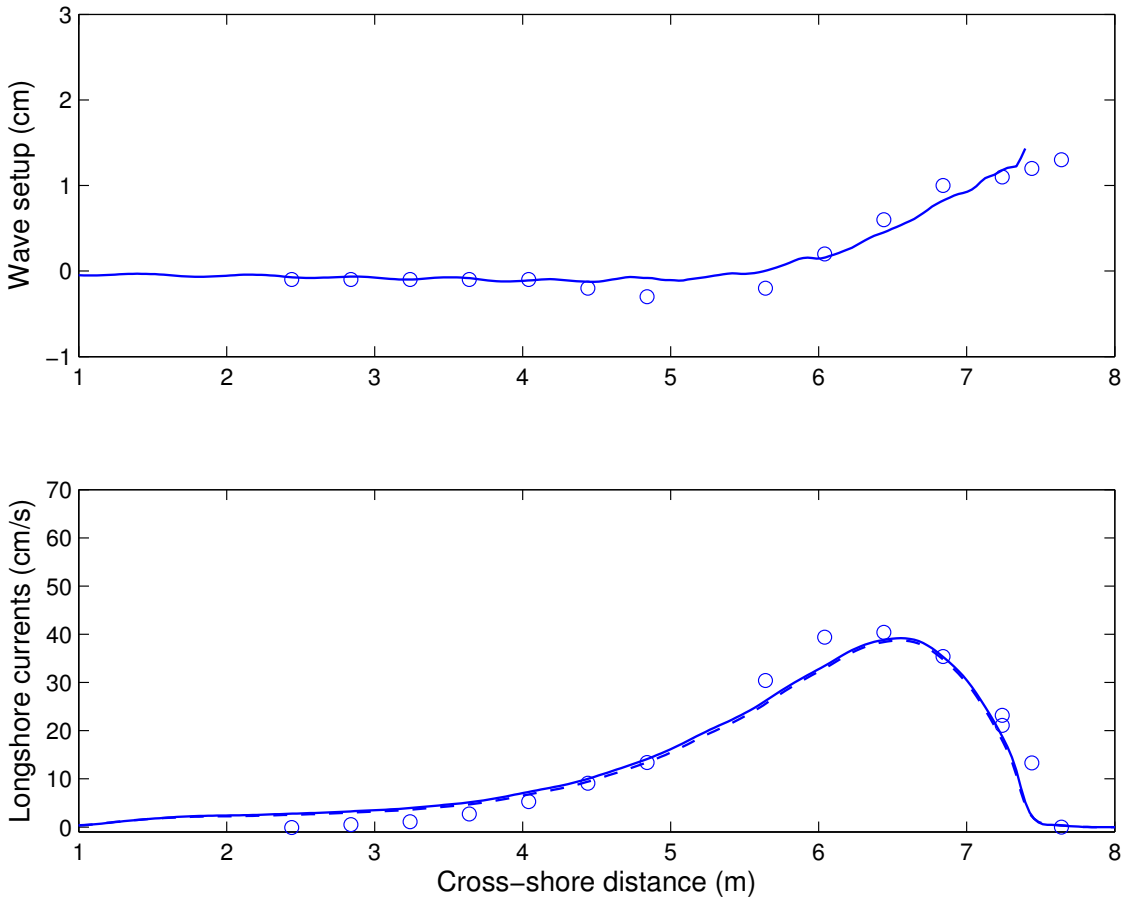

Figure 6.19: Comparisons of computed wave setup (upper panel) and longshore currents (lower panel) at $t = 110s$ with experimental data (Visser, 1991). The dashed line shows the computed phase-averaged longshore current at 100 s.

Chapter 7

LARGE-SCALE BUBBLE PROCESSES IN THE SURF ZONE

Wave breaking in the surf zone entrains large volumes of air bubbles into the water column. These bubbles are subsequently subject to turbulent transport by wave-driven currents, degassing at the free surface as well as gas dissolution into the water column. To account for all these processes, we develop a bubble entrainment and transport model based on the non-hydrostatic wave model NHWAVE. The model is based on the mixture theory as used by Shi et al. (2010). In this chapter, we first introduce the model formulations. Then the numerical model is validated by the laboratory measurements by Cox and Shin (2003). Finally, the model is applied to study bubble generation and transport in sandy city beach, CA, which consists of several rip channels. The effects of rip currents and large-scale vortices on bubble transport are investigated.

7.1 Governing Equations

7.1.1 Mixture Phase

The governing equations of a two-fluid model based on the mixture theory were derived by Buscaglia et al. (2002). Their model basically considers the air-water mixture as a mixture fluid phase with density ρ_m, velocity field $\mathbf{u}_m$ and pressure p_m. The density of the mixture is estimated by

$$\rho_m = (1-\alpha)\rho_l + \alpha\rho_b \tag{7.1}$$

where α is the void fraction, ρ_l is the liquid density and ρ_b is the gas density. The mixture phase velocity $\mathbf{u}_m$ is defined as

$$\rho_m \mathbf{u}_m = (1-\alpha)\rho_l \mathbf{u}_l + \alpha \rho_b \mathbf{u}_b \tag{7.2}$$

where $\mathbf{u}_l$ is the liquid phase velocity and $\mathbf{u}_b$ is the bubble phase velocity.

Assuming the liquid phase to be incompressible with reference density ρ_0, we can adopt the Boussinesq approximation replacing ρ_m by ρ_0 in all terms but the gravity one. Then the resulting balance equations are given by

$$\nabla \cdot \mathbf{u}_m = 0 \tag{7.3}$$

$$\frac{\partial \mathbf{u}_m}{\partial t} + \nabla \cdot (\mathbf{u}_m \mathbf{u}_m) = -\frac{1}{\rho_0}\nabla p_m - \frac{\rho_m}{\rho_0}\mathbf{g} + \nabla \cdot \mathbf{T}_m \tag{7.4}$$

Notice that the Boussinesq approximation only holds for values of α leading to the same magnitude of density change, i.e. $\alpha < 10^{-2}$. In the surf zone, especially at the roller of breaking wave, this is not the case. The void fraction at the wave roller can be up to $20 \sim 30\%$ according to the laboratory measurements by Cox and Shin (2003). However, the approximation is still applied in the current study considering that the regions with high void fraction ($\alpha > 1\%$) under breaking waves are relatively small.

We further assume that the surface elevation is a single value function of the horizontal coordinates. Similar to the approach introduced in the last chapter, a σ coordinate is adopted. The above two equations can be transformed as

$$\frac{\partial D}{\partial t} + \frac{\partial D u_m}{\partial x} + \frac{\partial D v_m}{\partial y} + \frac{\partial \omega_m}{\partial \sigma} = 0 \tag{7.5}$$

$$\frac{\partial \mathbf{U}}{\partial t} + \frac{\partial \mathbf{F}}{\partial x} + \frac{\partial \mathbf{G}}{\partial y} + \frac{\partial \mathbf{H}}{\partial \sigma} = \mathbf{S}_h + \mathbf{S}_p + \mathbf{S}_\tau \tag{7.6}$$

where $\mathbf{U} = (Du_m, Dv_m, Dw_m)^T$. The fluxes are

$$\mathbf{F} = \begin{pmatrix} Du_m u_m \\ Du_m v_m \\ Du_m w_m \end{pmatrix} \quad \mathbf{G} = \begin{pmatrix} Du_m v_m \\ Dv_m v_m \\ Dv_m w_m \end{pmatrix} \quad \mathbf{H} = \begin{pmatrix} u_m \omega_m \\ v_m \omega_m \\ w_m \omega_m \end{pmatrix}$$

The source terms are given by

$$\mathbf{S}_h = \begin{pmatrix} -\frac{\rho_m}{\rho_0} gD\frac{\partial \eta}{\partial x} \\ -\frac{\rho_m}{\rho_0} gD\frac{\partial \eta}{\partial y} \\ 0 \end{pmatrix} \quad \mathbf{S}_p = \begin{pmatrix} -\frac{D}{\rho}(\frac{\partial p_m}{\partial x} + \frac{\partial p_m}{\partial \sigma}\frac{\partial \sigma}{\partial x^*}) \\ -\frac{D}{\rho}(\frac{\partial p_m}{\partial y} + \frac{\partial p_m}{\partial \sigma}\frac{\partial \sigma}{\partial y^*}) \\ -\frac{1}{\rho}\frac{\partial p_m}{\partial \sigma} \end{pmatrix} \quad \mathbf{S}_\tau = \begin{pmatrix} DS_{\tau_x} \\ DS_{\tau_y} \\ DS_{\tau_z} \end{pmatrix}$$

where the total pressure has been divided into two parts: dynamic pressure p_m (use p_m as dynamic pressure hereinafter for simplicity) and hydrostatic pressure $\rho_m g(\eta - z)$. ω_m is the vertical velocity in the σ coordinate image domain, given by

$$\omega_m = D\left(\frac{\partial \sigma}{\partial t^*} + u_m\frac{\partial \sigma}{\partial x^*} + v_m\frac{\partial \sigma}{\partial y^*} + w_m\frac{\partial \sigma}{\partial z^*}\right) \tag{7.7}$$

From the above derivations, we can see that the governing equations for the mixture phase are similar to those of NHWAVE. Therefore, we implemented the model following the framework of NHWAVE.

7.1.2 Bubble Phase

In the surf zone, bubbles have a spectrum of bubble sizes, ranging from $O(0.1mm)$ to $O(10mm)$. In this study, we develop a polydisperse bubble phase model. The bubbles are split into $NG = 20$ groups. Each group has a constant bubble size $r_{b,i}, i = 1, 2, \cdots, NG$. To simplify the problem, the bubble size change due to pressure, gas dissolution as well as bubble breakup and coalescence are all not considered. The bubble population is calculated by solving the bubble number density equation, which is given by

$$\frac{\partial N_{b,i}}{\partial t} + \nabla \cdot (N_{b,i}\mathbf{u}_{b,i}) = \mathbf{S}_{b,i} + \nabla \cdot (D_{b,i}\nabla N_{b,i}) \tag{7.8}$$

where $N_{b,i}$ is the bubble number density for the ith bubble group, $\mathbf{u}_{b,i}$ is the bubble velocity, $\mathbf{S}_{b,i}$ accounts for the bubble source at the free surface due the bubble entrainment, $D_{b,i}$ is the bubble turbulent diffusivity. The bubble velocity $\mathbf{u}_{b,i}$ is calculated by

$$\mathbf{u}_{b,i} = \mathbf{u}_m + w_s(r_{b,i})\mathbf{k} \tag{7.9}$$

in which $w_s(r_{b,i})$ is the slip velocity for bubbles, which is assumed to depend on the bubble radius following Clift et al. (1978).

$$w_s(r_{b,i}) = \begin{cases} 4474m/s \times r_{b,i}^{1.357} & \text{if} \quad 0 \leq r_{b,i} \leq 7 \times 10^{-4}m \\ 0.23m/s & \text{if} \quad 7 \times 10^{-4} < r_{b,i} \leq 5.1 \times 10^{-3}m \\ 4.202m/s \times r_{b,i}^{0.547} & \text{if} \quad r_{b,i} > 5.1 \times 10^{-3}m \end{cases} \tag{7.10}$$

The bubble diffusivity is given by

$$D_{b,i} = \frac{\mu_t}{\rho_0 \sigma_t} \tag{7.11}$$

where σ_t is the Schmidt number of gas (Buscaglia et al., 2002). The void fraction can be calculated by

$$\alpha = \sum_{i=1}^{NG} \frac{4}{3} \pi r_{b,i}^3 N_{b,i} \tag{7.12}$$

7.1.3 Turbulence Model

In this study, the nonlinear $k - \epsilon$ model (Lin and Liu, 1998a) is employed to simulate turbulence generation and transport under breaking waves in the surf zone. The equations are given by

$$\frac{\partial Dk}{\partial t} + \nabla \cdot (D\mathbf{u}_m k) = \nabla \cdot \left[D \left(\nu + \frac{\nu_t}{\sigma_k} \right) \nabla k \right] + D \left(P_s + P_b - \epsilon \right) \tag{7.13}$$

$$\frac{\partial D\epsilon}{\partial t} + \nabla \cdot (D\mathbf{u}_m \epsilon) = \nabla \cdot \left[D \left(\nu + \frac{\nu_t}{\sigma_\epsilon} \right) \nabla \epsilon \right] + \frac{\epsilon}{k} D \left(C_{1\epsilon} P_s + C_{3\epsilon} P_b - C_{2\epsilon} \epsilon \right) \tag{7.14}$$

where $\sigma_k, \sigma_\epsilon, C_{1\epsilon}, C_{2\epsilon}$ and $C_{3\epsilon}$ are empirical coefficients (Rodi, 1980).

$$\sigma_k = 1.0, \quad \sigma_\epsilon = 1.3, \quad C_{1\epsilon} = 1.44, \quad C_{2\epsilon} = 1.92, \quad C_{3\epsilon} = -1.4 \tag{7.15}$$

P_s is the shear production given by eq. 2.20. P_b is the buoyancy production, which is formulated as

$$P_b = -\frac{1}{\rho_0} g \nu_t \frac{\partial \rho_m}{\partial z} \tag{7.16}$$

7.2 Model Validation

We first validate the model with the laboratory measurements by Cox and Shin (2003). As introduced in Chapter 4, the experiment was conducted in a 36 m long by 0.95 m wide by 1.5 m high glass-walled flume. A beach with constant slope of 1/35 was installed with the toe 10 m from the wavemaker and intersecting the still water line at x = 27.85 m. The flume was filled with tap water to a depth of h = 0.51 m. Here, we only conducted a 2D simulation, with the computational domain 25 m long. The left boundary is located at 5 m from the beach toe. Twenty layers are used in the vertical direction. Waves are generated by an internal wavemaker, which is located at 1.3 m from the beach toe. A sponge layer with 3.4 m long is placed at the left boundary in order to avoid wave reflection.

Figure 7.1 to 7.3 show the model-data comparisons of void fraction at different vertical locations at three sections. In this simulation, the bubble entrainment coefficient is calibrated as $C_b = 0.08$. The minimum and maximum bubble radius are chosen as $0.1mm$ and 10 mm respectively according to the laboratory measurements by Deane and Stokes (2002). Generally, the comparisons are quite good. The temporal variations of void fraction are captured by the model. At section 1, the bubble plume is still developing. The model slightly underestimates the highest void fraction. At section 2 and section 3, the simulations agree fairly well with the measurements.

Figure 7.4 displays the temporal variations of the bubble plume after wave breaking. Similar to that predicted by the VOF model (Chapter 4), the highest void fraction is always located at the wave roller. The wave breaks around $x = 17.07$ m. At $t - t_b = 1/4T$, the bubble plume has been well developed. The void fraction reaches its maximum value shortly after the wave breaking. After $t - t_b = 1/4T$, the bubble plume decays and disperses with bubbles spread behind the wave crest.

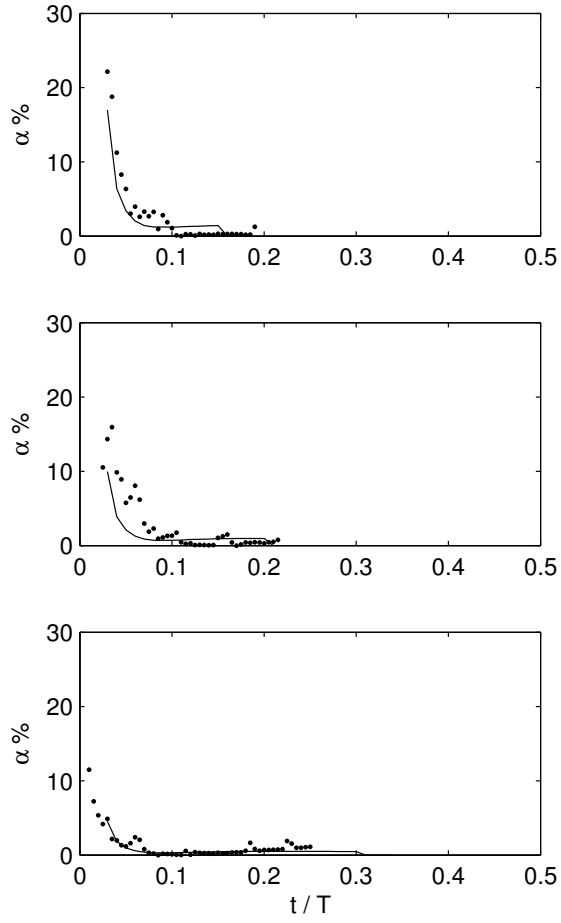

Figure 7.1: Comparisons between simulated (solid line) and measured (dots) void fraction evolution at $z = 2.5, 1.5, 0.0\ cm$ at section 1.

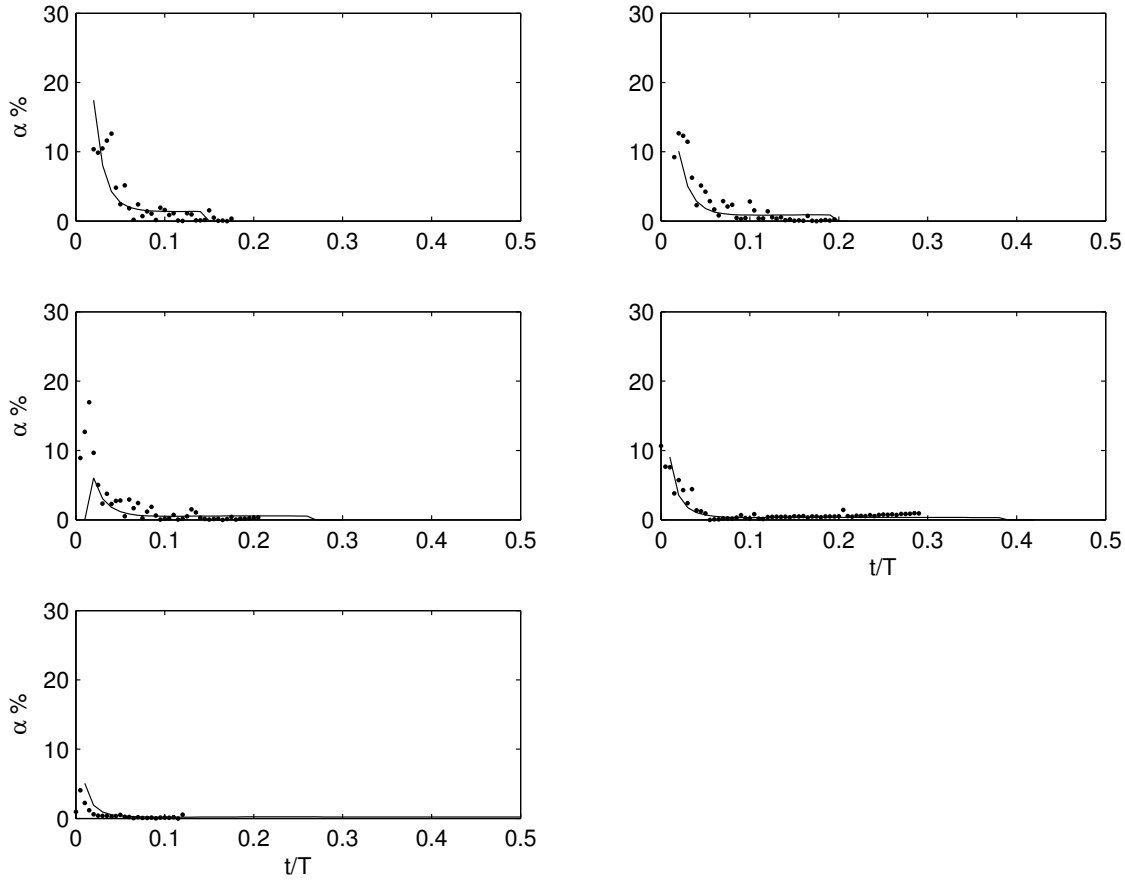

Figure 7.2: Comparisons between simulated (solid line) and measured (dots) void fraction evolutions at $z = 2.5, 1.5, 0.5, -0.5, -1.5\ cm$ at section 2.

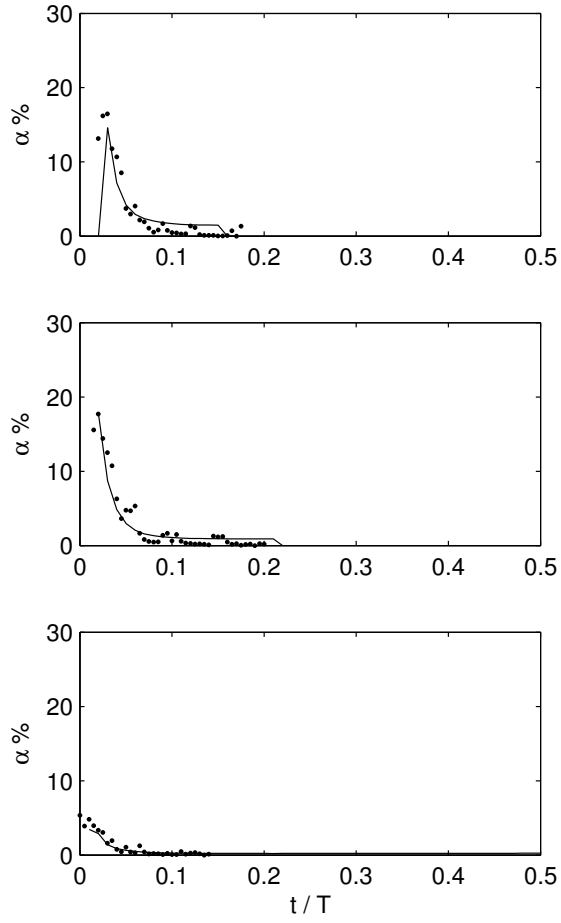

Figure 7.3: Comparisons between simulated (solid line) and measured (dots) void fraction evolutions at $z = 2.5, 1.5, -1.5\ cm$ at section 3.

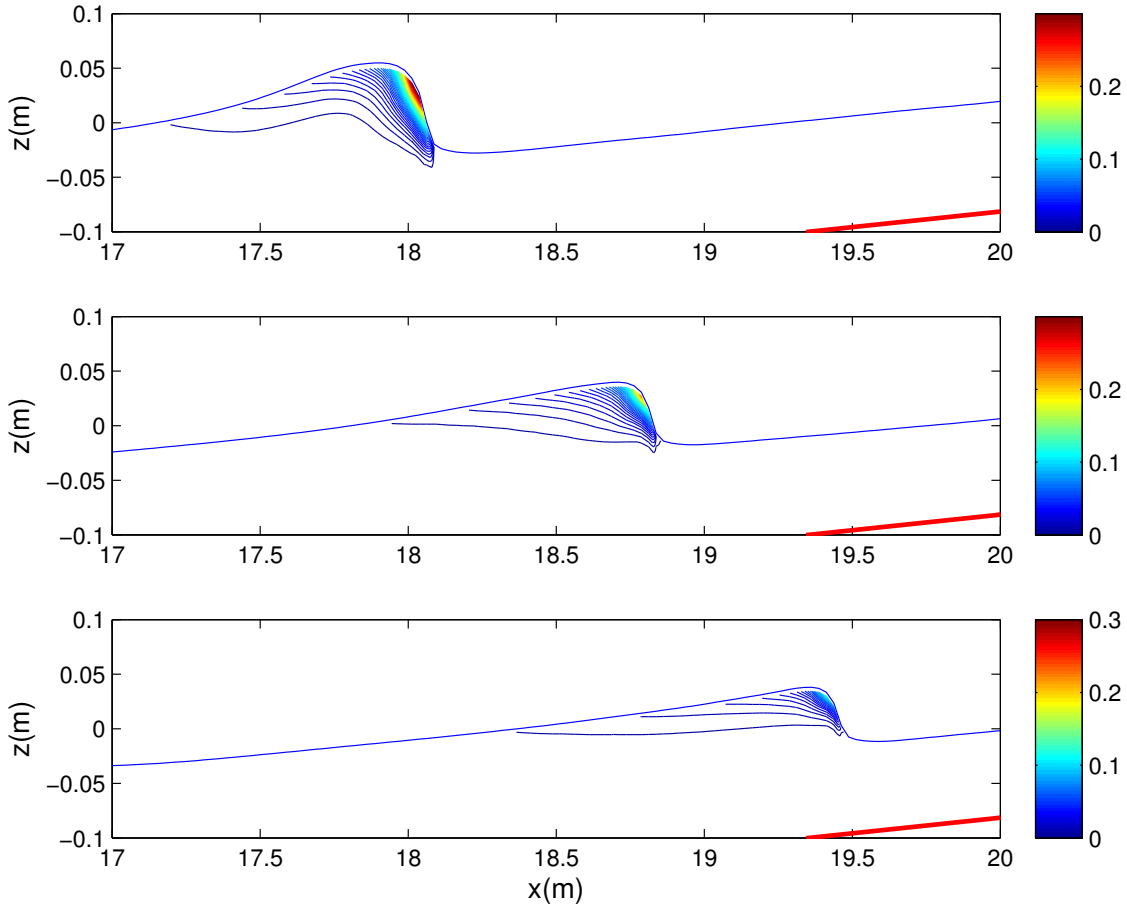

Figure 7.4: Simulated bubble plume under a wave-breaking event at $t - t_b = 1/4T, 2/4T, 3/4T$.

7.3 Rip Current Experiment RCEX

In this section, we apply the model to study a rip current field experiment (RCEX), which was conducted on seven different days in May, 2007 in Sand City, Monterey, California (Brown et al., 2009; MacMahan et al., 2010). Drifter deployments on one of those seven days, yearday 124, saw nearly shore normal incident waves, leading to the developments of rip currents and large-scale eddies inside the surf zone. We concentrate here on this particular day to investigate how bubbles are transported by rip currents and nearshore eddies, which have been numerically studied by Renier et al. (2009) using a wave averaged model Delft3D. Geiman et al. (2011) conducted a numerical study of wave-averaging effects on estimates of surf-zone mixing, using the phase-resolving Boussinesq model FUNWAVE and the wave averaged model Delft3D. They found that both models could reproduce the time averaged Eulerian velocity field. However, the spatial distribution of wave height inside the surf zone was different due to different representations for wave breaking. Shi et al. (2012) employed the newest implementation of FUNWAVE which uses a TVD shock-capturing algorithm that more accurately simulate wave breaking and runup to study wave-induced currents in RCEX. The rip current system and large-scale vortices inside surf zone are simulated well by the model.

In the present study, the rip currents and nearshore eddies are investigated by a non-hydrostatic fully dispersive wave model NHWAVE. Comparing to other phase-resolving models such as FUNWAVE, NHWAVE simulates wave breaking by using the shock-capturing scheme and a two-equation $k-\epsilon$ turbulence model. The model is capable of capturing vertical structures of nearshore circulation. In addition, a bubble transport model was implemented into the model so that the bubble effects on wave-induced currents can also be studied. The model setup is similar to that of Geiman et al. (2011). Figure 7.5 shows the computational domain and bathymetry as well as the locations of ten wave gauges. The water depth is periodic in the

longshore direction so that we can use periodic lateral boundary conditions in the simulations. The domain is discretized by 280×256 grid cells with $\Delta x = 2.02778$ m and $\Delta y = 2.66406$ m. Eight vertical layers are used in order to capture the vertical structure of rip currents. The internal wavemaker is located at $x = 420$ m. The directional spectra observed at 13 m water depth is given in figure 7.6. The calculated RMS wave height $H_{rms} = 0.65$ m and wave period $T_{mo} = 10.5$ s. The waves are dominantly incident in normal direction. In order to decrease the simulation time, the waves are assumed to be normally incident with wave height 0.65 m and wave period 10.5 sec in the simulation. A 100 m wide sponge layer is placed on the right boundary to absorb wave energy. The total simulation time is 3000 s.

Figure 7.7 shows the model-data comparisons of RMS wave height at wave gauges. The comparisons are fairly good with averaged relative RMS error 13.9%. This result is comparable to that obtained by FUNWAVE model (Geiman et al., 2011; Shi et al., 2012), indicating that the wave breaking is correctly simulated by the turbulence closure. Figure 7.8 demonstrates the wave averaged velocity field, from which we can see that the rip currents and large-scale eddies inside the surf zone are captured by the model. Similar wave-averaged velocity patterns were also found from the FUNWAVE simulations. The red vectors represent the wave averaged velocities observed at ten wave gauges. The simulations agree well with the measurements inside the surf zone. However, the simulated rip current slightly deviates from the measured direction.

Figure 7.9 shows the distributions of instantaneous vertical vorticity, turbulent kinetic energy and void fraction. Large-scale counter-rotating vortices are generated inside surf zone. These vortices are mostly confined to the surf zone. However, some vortices can be transported to the outer surf zone by the rip currents. The high turbulent kinetic energy is mainly located at the shoals where wave

breaking occurs. From the void fraction distribution, we can see that the bubble transport is dominated by the vorticity field. Bubbles can be transported to the outer surf zone by the rip currents.

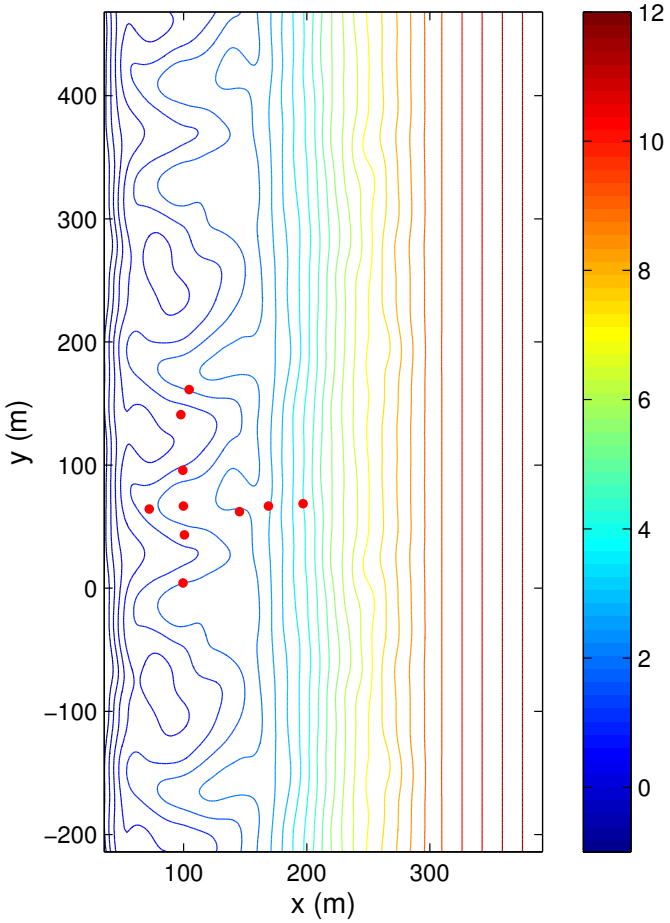

Figure 7.5: The computational domain and bathymetry. The red dots represent wave gauges.

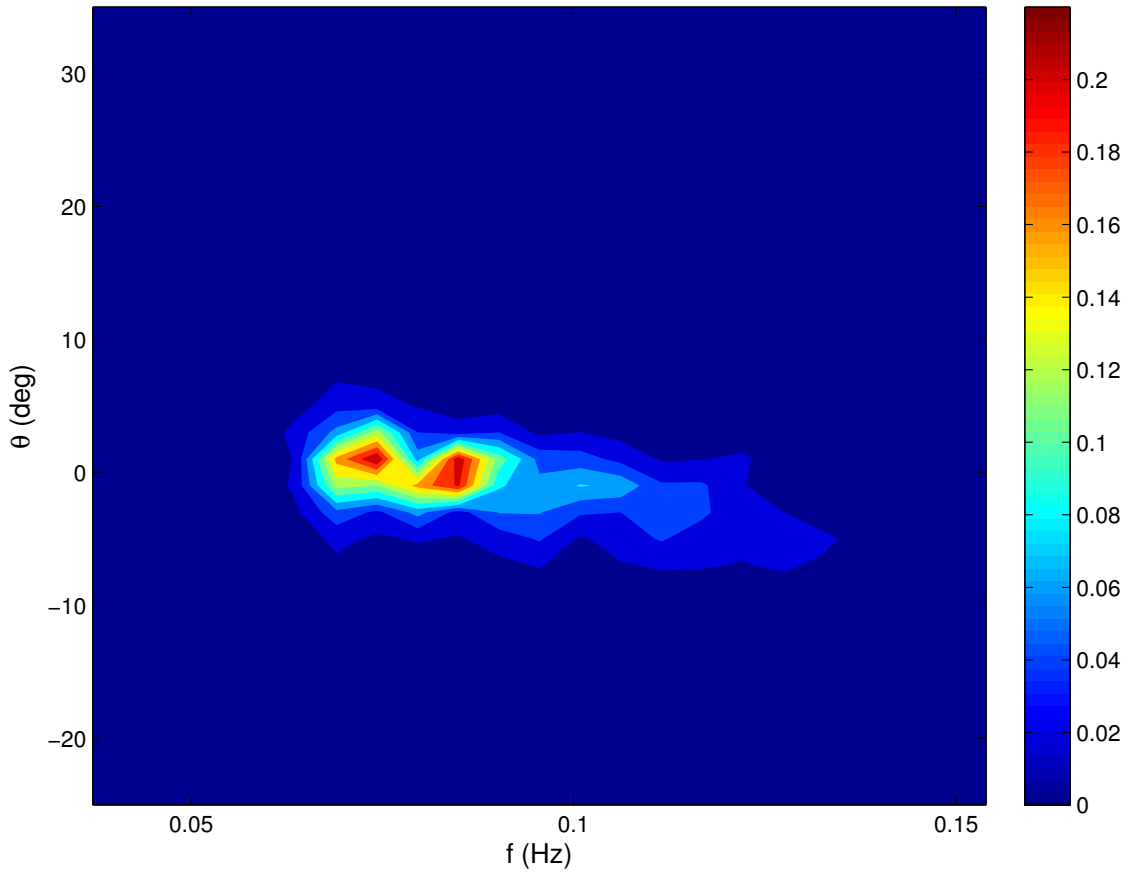

Figure 7.6: Wave spectrum $S(f, \theta)$ in $m^2/(Hz \times deg)$ from the offshore ADCP at 13 m water depth, averaged over the entire yearday 124. θ has been rotated so that the shore normal direction is $\theta = 0^o$ and positive values represent northward.

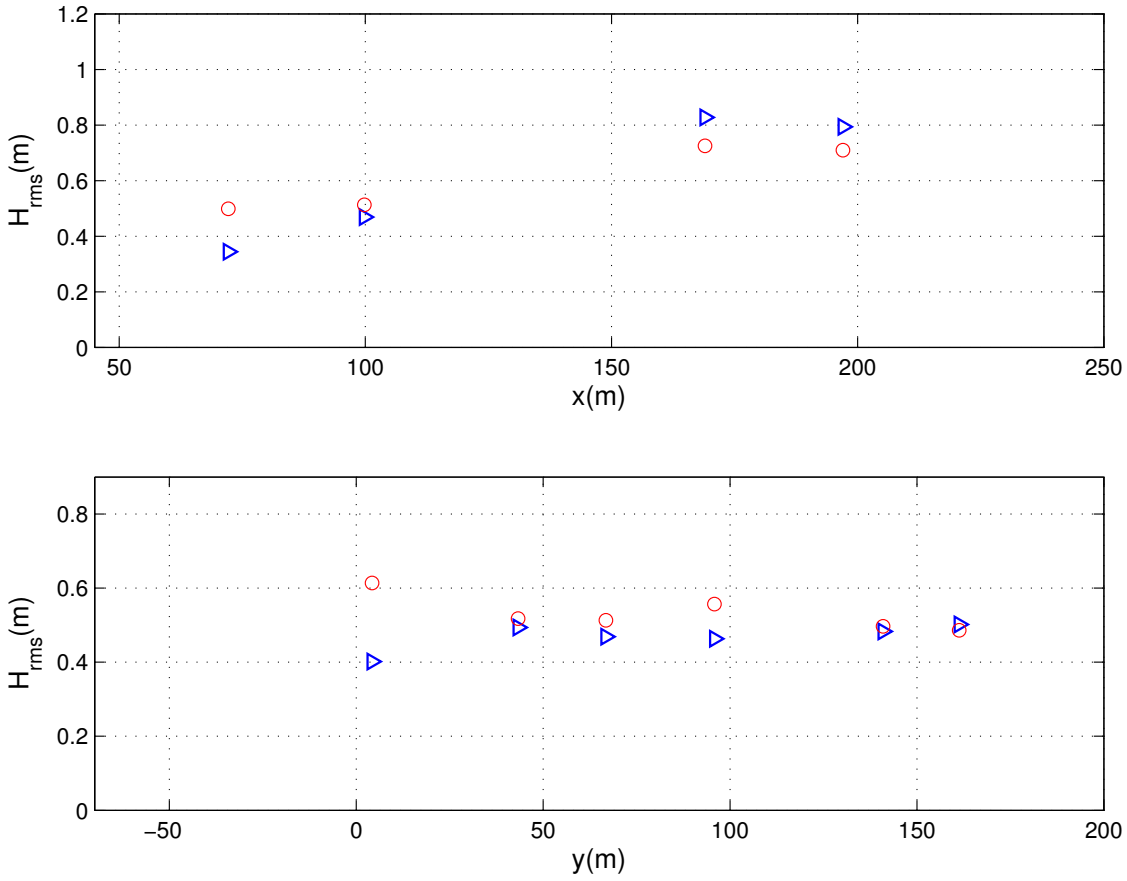

Figure 7.7: Comparisons of H_{rms} between simulations and measurements at wave gauges. Circles: measurements; Triangles: simulations.

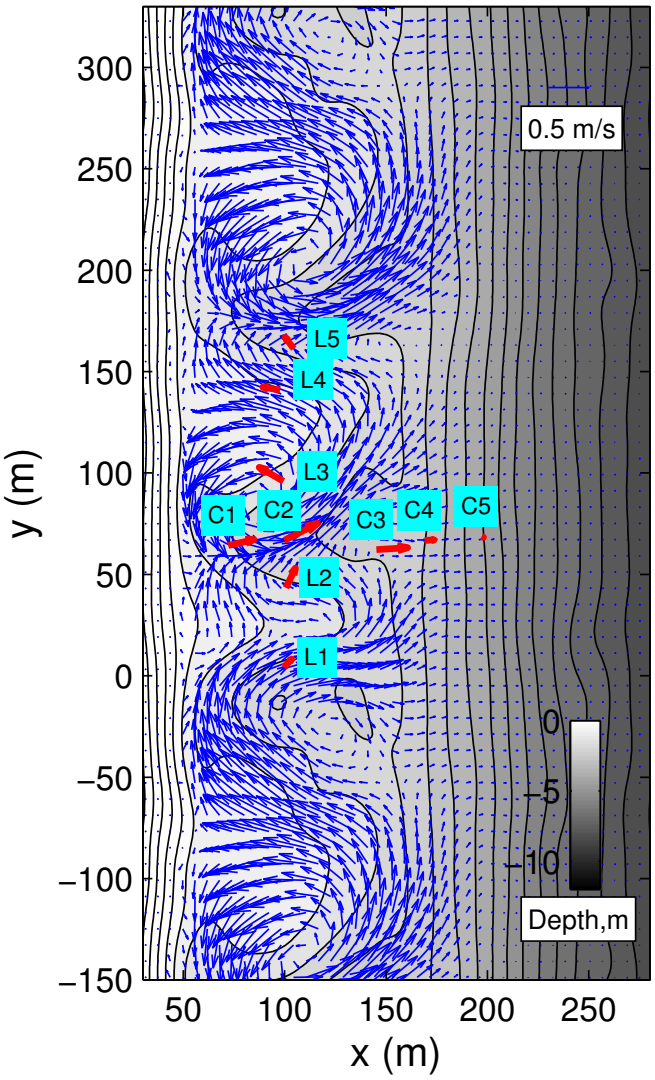

Figure 7.8: Wave averaged velocity field. The red vectors represent measurements at ten wave gauges.

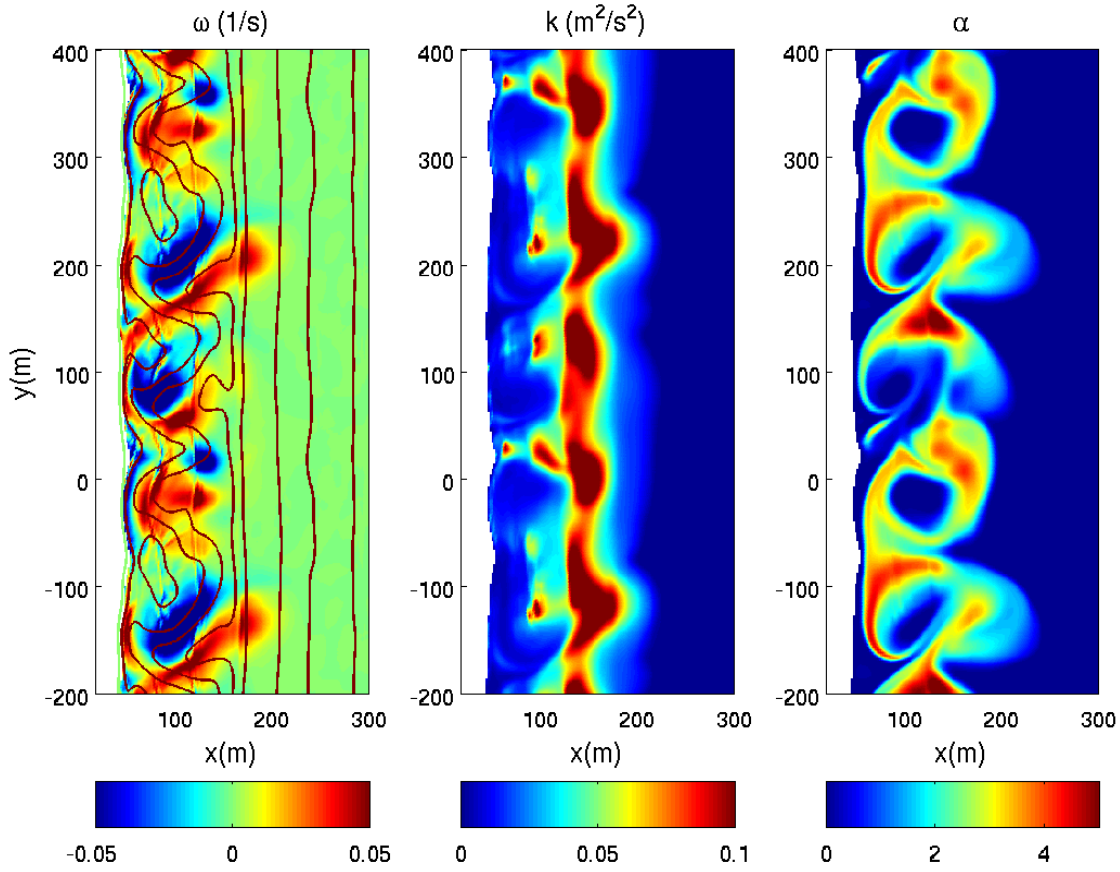

Figure 7.9: The simulated instantaneous distributions of vorticity ω_z (left), turbulent kinetic energy k (middle) and void fraction α (right).

Chapter 8

CONCLUSIONS

Wave breaking in the surf zone entrains large volumes of air bubbles into the water column. These bubbles are subsequently involved in intense interactions with mean flow and turbulence, producing a complex two-phase bubbly flow field. Meanwhile, bubbles are also subject to the transport by wave-driven currents and large-scale nearshore vortices, degassing at the air-water interface as well as gas dissolution into the water column. The bubble entrainment and transport in the surf zone are highly complicated with the involvement of a variety of physical processes that operate over a wide range of temporal and spatial scales.

In this thesis, we have conducted multiscale numerical studies of bubble entrainment and transport in the surf zone with two distinct models. One is a polydisperse two-fluid model which is developed to study the bubble plume dynamics and void fraction evolution as well as turbulent coherent structures and their interactions with dispersed bubbles under laboratory scale surf-zone breaking waves. The other is a Non-Hydrostatic WAVE model NHWAVE which is capable of simulating surface wave processes, wave-driven circulations, surf zone turbulence as well as bubble transport. The model is used to study the bubble generation and transport by wave-driven circulations and large-scale nearshore vortices in a real beach. In this chapter, we summarize our findings.

8.1 Laboratory Scale Studies

A ploydisperse two-fluid model was developed to study the bubbly flow field under a laboratory surf-zone spilling breaking wave. A bubble entrainment model which linearly correlates bubble entrainment rate to turbulent dissipation rate was proposed to account for bubble source due to entrainment at the free surface, which was captured by the Volume-of-Fluid (VOF) approach. The model was tested against laboratory measurements by Cox and Shin (2003). In order to understand the turbulent bubbly flow field under breaking waves, both 2D and 3D simulations were performed. Conclusions are summarized as below:

(1) The polydisperse two-fluid model reasonably predicted the cross-shore distributions of wave height, wave setup, skewness and asymmetry. The evolutions of free surface, velocities as well as void fraction were captured by the model;

(2) The predicted temporal variations of void fraction compared well with the measurements. Both simulations and measurements show that the void fraction has a linear growth and exponential decay in time;

(3) Both turbulent dissipation rate and void fraction reach the maximum values shortly after wave breaking. The peak void fraction appears around $0.15L$, where L is wave length at breaking point. The turbulent dissipation rate and void fraction are positively correlated. At the strong turbulence regions, the turbulent dissipation rate and void fraction have a linear correlation;

(4) At the early stage of wave breaking ($\leq 0.4T$), the 2D bubble plume follows the wave propagation and moves quickly downward to about $0.18H_b$, where H_b is breaking wave height. At the later stage of wave breaking, the bubble plume travels slower than the breaking wave as bubbles are spread behind the wave crest. The bubble plume disperses and degases as bubbles rise back to the free surface. Both the total volume of entrained air V and the work required to keep the air entrained against buoyancy E show growth at the early stage of wave breaking and

exponential decay at the late stage of wave breaking;

(5) The vertical distributions of void fraction can be well described as an exponential function of distance to the free surface. Smaller bubbles have deeper penetration to the water column. The bubble size spectrum becomes steeper as the water depth increases;

(6) The polydisperse two-fluid model was capable of capturing large-scale turbulent coherent structures, such as obliquely descending eddies (streamwise vortices) and downbursts of turbulent fluid;

(7) From the analysis of vortex stretching and bending terms in the enstrophy transport equation, it was found that there is a close connection between the turbulent vortex structures and downbursts. At the beginning of wave breaking, primary spanwise vortices are generated at the wave roller. Because of the downbursts of turbulent fluid, these spanwise vortices are tilted to form counter-rotating vertical vortices, which are eventually evolved into streamwise vortices under the action of shear and turbulence. This is the dominant vortex evolution processes under surf-zone breaking waves;

(8) The turbulent coherent structures play a significant role on the turbulent and bubble transport under breaking waves. The high turbulent kinetic energy and Reynolds stress are located at the regions with strong downward velocities, which are found at the outer core of streamwise vortices. However, due to the preferential accumulation by the vorticity field, bubbles are not only located at outer core of vortices, but also inside the vortices. As the streamwise vortices move downward, bubbles are carried to the lower part of the water column. This is the dominant mechanism for bubble transport under breaking waves. The turbulent coherent structures tend to transport bubbles more deeply into the water column;

(9) Both 2D and 3D simulations show that the presence of bubble can suppress the liquid phase turbulence. As a result, the enstrophy is decreased with

bubbles. The vortex evolution processes are attenuated as well.

8.2 Large Scale Studies

In the surf zone, bubbles generated by breaking waves are subject to the transport by nearshore circulations. In the case of obliquely incident waves, a longshore current develops transporting bubbles in the down-wave direction. On the other hand, if waves are persistently normally incident, the longshore current is mostly absent and instead rip currents develop. The prevailing idea in this case is that bubbles are generated and transported onshore by the breaking waves over the shallow shoals feeding into a rip channel where offshore directed rip currents subsequently transport bubbles outside the surf zone (Reniers et al., 2009). In order to study these processes, a non-hydrostatic wave and bubble model NHWAVE-BUBBLE based on mixture theory has been developed. The model was also validated with the laboratory measurements by Cox and Shin (2003). The following conclusions can be drawn.

(1) The non-hydrostatic wave and bubble model is capable of predicting void fraction evolution under a laboratory surf zone breaking wave. The comparisons between the simulated void fraction and laboratory measurements by Cox and Shin (2003) are fairly good;

(2) The model was successfully applied to study the rip current systems in a real beach. The wave height distributions, rip currents and large-scale eddies inside the surf zone were all captured by the model;

(3) The bubble transport in the surf zone were dominated by the nearshore eddies and rip currents. Bubbles can be transported to the outer surf zone by rip currents.

REFERENCES

Agnon, Y., Madsen, P. A. and Schäffer, H. A., 1999, A new approach to high order Boussinesq models, *J. Fluid Mech.*, 399, 319-333.

Ai C. and Jin S., 2010, Non-hydrostatic finite volume method for non-linear waves interacting with structures, *Comp. Fluids*, 39, 2090-2100

Baldy S., 1993, A generation-dispersion model of ambient and transient bubbles in the close vicinity of breaking waves, *J. Geophy. Res.*, *98*, 18,277-18,293.

Battjes J.A., 1974, Surf similarity, *Proc. 14th Coastal Engrg. Conf.*, ASCE, New York, 466-480

Battjes J.A., 1988, Surf-zone dynamics, *Annual Review of Fluid Mechanics*, 20, 257-293

Becker S., Sokolichin A. and Eigenberger G., 1994, Gas-liquid flow in bubble columns and loop reactors. Part II. Comparison of detailed experiments and flow simulations, *Chem. Engng. Sci.*, *49*, 5747-5762.

Beji S. and Battjes J.A., 1993, Experimental investigation of wave propagation over a bar, *Coastal Engineering*, 19, 151-162

Berkhoff J.C.W., Booy N. and Radder A.C., 1982, Verification of numerical wave propagation models for simple harmonic linear water waves, *Coastal Engineering*, 6, 255-279

Blenkinsopp C. E. and Chaplin J.R., 2007, Void fraction measurements in breaking waves, *Proc. R. Soc. A*, 463, 3151–3170.

Blenkinsopp C. E. and Chaplin J.R., 2010, Bubble size measurements in breaking waves using optical fiber phase detection probes, *IEEE Journal of Oceanic Engineering*, 35, 388–401.

Bradford S.F., 2005, Godunov-based model for nonhydrostatic wave dynamics, *J. Waterway, Port, Coastal and Ocean Engineering*, 131, 226-238

Bradford S.F., 2011, Nonhydrostatic model for surf zone simulation, *J. Waterway, Port, Coastal and Ocean Engineering*, 137(4), 163-174

Brown J., MacMahan J.H., Reniers A.J.H.M. and Thornton E., 2009, Surf zone diffusivity on a rip-channeled beach, *J. Geophys. Res.*, 114, C11015, doi:10.1029/2008JC005158

Buckingham M. J., 1997, Sound speed and void fraction profiles in the sea surface bubble layer, *Applied Acoustics*, 51, 225–250.

Buscaglia G.C., Bombardelli F.A., and Garcia M.H., 2002, Numerical modeling of large-scale bubble plumes accounting for mass transfer effects, *International Journal of Multiphase Flow*, 28, 1763-1785

Cabot W. and Moin P., 2000, Approximate wall boundary conditions in the large-eddy simulation of high Reynolds number flow, *Flow Turb. Combust.*, 63, 269-291

Calhoun R.J. and Street R.L., 2001, Turbulent flow over a wavy surface: Neutral case, *J. Geophys. Res.*, 106, 9277-9293

Carrica P.M., Drew D.A., Bonetto F. and Lahey R.T. Jr., 1999, A polydisperse model for bubbly two-phase flow around a surface ship, *International Journal of Multiphase Flow*, 25, 257-305

Casulli V. and Stelling G.S., 1998, Numerical simulation of 3D quasi-hydrostatic free-surface flows, *J. Hydr. Engnrg.*, 124, 678-686

Casulli V., 1999, A semi-implicit finite difference method for non-hydrostatic, free-surface flow, *Int. J. Numer. Meth. Fluids*, 30, 425-440

Casulli V. and Zanolli P., 2002, Semi-implicit numerical modeling of nonhydrostatic free-surface flows for environmental problems, *Math. Comp. Modeling*, 36, 1131-1149

Chang K.-A. and Liu P.L.-F., 1998, Velocity, acceleration and vorticity under a breaking wave, *Physics of Fluids*, 10, 327-329

Chang K.-A. and Liu P.L.-F., 1999, Experimental investigation of turbulence generated by breaking waves in water of intermediate depth, *Physics of Fluids*, 11, 3390-3400

Chen Q., Madsen P.A. and Basco D.R., 1999, Current effects on nonlinear interactions of shallow-water waves, *Journal of Waterway, Port, Coastal, and Ocean Engineering*, 125(4), 176-186

Chen Q., Kirby J.T., Dalrymple R.A., Shi F. and Thornton E.B., 2003, Boussinesq modeling of longshore currents, *J. Geophys. Res.*, 108, doi:10.1029/2002JC001308

Chen X., 2003, A fully hydrodynamic model for three-dimensional, free-surface flows, *Int. J. Numer. Meth. Fluids*, 42, 929-952

Christensen E.D., 2006, Large eddy simulation of spilling and plunging breakers, *Coastal Engineering*, 53, 463-485

Christensen E.D. and Deigaard R., 2001, Large eddy simulation of breaking waves, *Coastal Engineering*, 42, 53-86

Christensen E.D., Walstra D.J. and Emerat N., 2002, Vertical variation of the flow across the surf zone, *Coastal Engineering*, 45, 169-198

Cipriano R.J. and Blanchard D.C., 1981, Bubble and aerosol spectra produced by a laboratory breaking wave, *J. Geophys. Res.*, 86, 8085-8092

Clift R., Viollet K.R. and Weber M.E., 1978, Bubbles, Drops and Particles, *Academic Press*, New York, USA.

Cowen E.A., Sou I.M., Liu P.L.-F. and Raubenheimer B., 2003, Particle image velocimetry measurements within a laboratory-generated swash zone, *Journal of Engineering Mechanics*, 129, 1119-1129

Cox D.T. and Kobayashi N., 2000, Identification of intensive, intermittent coherent motions under shoaling and breaking waves, *Journal of Geophysical Research*, 105(C6), 14223-14236

Cox D. and Shin S., 2003, Laboratory measurements of void fraction and turbulence in the bore region of surf zone waves, *J. Eng. Mech.*, 129, 1197-1205.

Dalrymple R.A. and Rogers B.D., 2006, Numerical modeling of water waves with the SPH method, *Coastal Engineering*, 53, 141-147

De Leeuw G. and Leifer I., 2002, Bubbles outside the plume during the LUMINY wind wave experiment, *Gas transfer at water surfaces (ed. M. Donelan) Geophysics monograph series*, 127, 295-301, Washington DC: American Geophysical Union

Deane G.B., 1997, Sound generation and air entrainment by breaking waves in the surf zone, *J. Acoust. Soc. Amer.*, 102, 2671-2689

Deane G. B. and Stokes M.D., 1999, Air entrainment processes and bubble size distributions in the surf zone, *J. Phys. Oceanogr.*, 29, 1393–1403

Deane G.B. and Stokes M.D., 2002, Scale dependence of bubble creation mechanisms in breaking waves, *Nature*, 418, 839–844

Deen N.G., Solberg T. and Hjertager B.H., 2001, Large eddy simulation of the gas-liquid flow in a square cross-sectioned bubble column, *Chemical Engineering Science*, 56, 6341-6350

Delnoij E., Lammers F.A., Kuipers J.A.M. and Van Swaaij W.P.M., 1997, Dynamic simulation of dispersed gas-liquid two-phase flow using a discrete bubble model, *Chem. Engng. Sci.*, 52, 1429–1458.

Delnoij E., J. A. M. Kuipers and Van Swaaij W.P.M., 1999, A three-dimensional CFD model for gas-liquid bubble columns, *Chem. Engng. Sci.*, 54, 2217-2226.

Dendy E. D., Padial-Collins N.T. and VanderHeyden W.B., 2002, A general-purpose finite-volume advection scheme for continuous and discontinuous fields on unstructured grids, *J. Comp. Phys.*, 180, 559–583.

Dhotre M.T., Niceno B. and Smith B.L., 2008, Large eddy simulation of a bubble column using dynamic sub-grid scale model, *Chemical Engineering Journal*, 136, 337-348

Drew D. A., 1983, Mathematical modeling of two-phase flow, *Ann. Rev. Fluid Mech.*, 15, 261-291.

Enet F. and Grilli S.T., 2007, Experimental study of tsunami generation by three-dimensional rigid underwater landslides, *J. Waterway, Port, Coast. Ocean Engrng.*, 133, 442-454.

Francois M. M., Cummins S.J., Dendy E. D., Kothe D. B., Sicilian J. M. and Williams M. W., 2006, A balanced-force algorithm for continuous and sharp interfacial surface tension models within a volume tracking framework, *J. Comp. Phys.*, 213, 141-173.

Fringer O.B., Gerritsen M. and Street R.L., 2006, An unstructured-grid, finite-volume, nonhydrostatic, parallel coastal ocean simulator, *Ocean Modelling*, 14, 139-173

Fuhrman, D. R. and Madsen P. A., 2009, Tsunami generation, propagation and run-up with a high-order Boussinesq model, *Coastal Engrng.*, 56, 747-758.

Fulgosi M., Lakehal D., Banerjee S. and De Angelis V., 2003, Direct numerical simulation of turbulence in a sheared air-water flow with a deformable interface, *J. Fluid Mech.*, 482, 319–345.

Garrett C., Li M. and Farmer D., 2000, The connection between bubble size spectra and energy dissipation rates in the upper ocean, *J. Phys. Oceanogr.*, 30, 2163–2170.

Geiman J.D., Kirby J.T., Reniers A.J.H.M. and MacMahan J.H., 2011, Effects of wave averaging on estimates of fluid mixing in the surf zone, *J. Geophys. Res.*, 116, C04006, doi:10.1029/2010JC006678

Gobbi, M. F. and Kirby J. T., 1999, Wave evolution over submerged sills: tests of a high-order Boussinesq model, *Coastal Engrng.*, 37, 57-96.

Gobbi, M. F., Kirby, J. T. and Wei G., 2000, A fully nonlinear Boussinesq model for surface waves. II. Extension to $O(kh^4)$, *J. Fluid Mech.*, 405, 181-210.

Gottlieb S., Shu C.-W. and Tadmor E., 2001, Strong stability-preserving high-order time discretization methods, *SIAM Review*, 43, 89-112

Harlow F.H. and Welch J.E., 1965, Numerical calculation of time-dependent viscous incompressible flow of fluid with free surface, *Phys. Fluids*, 8, 2182-2189

Harten A., Lax P. and van Leer B., 1983, On upstream differencing and Godunov-type schemes for hyperbolic conservation laws, *SIAM Review*, 25, 35

Hirt C.W. and Nichols B.D., 1981, Volume of fluid (VOF) method for the dynamics of free boundaries, *J. Comp. Phys.*, 39, 201-225

Hoque A. and Aoki S., 2005, Distributions of void fraction under breaking waves in the surf zone, *Ocean Engineering*, 32, 1829–1840.

Jeong J. and Hussain F., 1995, On the identification of a vortex, *J. Fluid Mech.*, 285, 69-94

Kataoka I. and Serizawa A., 1989, Basic equations of turbulence in gas-liquid two-phase flow, *International Journal of Multiphase Flow*, 15, 843-855

Kim D.H., Cho Y.-S. and Kim H. J., 2008, Well-balanced scheme between flux and source terms for computation of shallow-water equations over irregular bathymetry, *J. Engnrng. Mech.*, 134, 277-290

Kim, D.H., Lynett P.J. and Socolofsky S.A., 2009, A depth-integrated model for weakly dispersive, turbulent, and rotational fluid flows, *Ocean Modelling*, 27, 198-214.

Kim, D.H. and Lynett P. J., 2011, Turbulent mixing and scalar transport in shallow and wavy flows, *Phys. Fluids*, 23, 016603.

Kubo H. and Sunamura T., 2001, Large-scale turbulent to facilitate sediment motion under spilling breakers, *Proceedings of the 4th Conference on Coastal Dynamics*, Lund, Sweden, 212-221

Lahey Jr. R. T., 2005, The simulation of multidimensional multiphase flows, *Nucl. Eng. Design*, 235, 1043-60.

Lakehal D. and Liovic P., 2006, Large-eddy simulation of steep water waves, *Proceedings of the IUTAM Symposium on Computational Multiphase Flow*, 331-340

Lakehal D. and Liovic P., 2011, Turbulent structure and interaction with surface dynamics in breaking waves, *Journal of Fluid Mechanics*, 674, 522-577

Lai Z., Chen C., Cowles G.W. and Beardsley R.C., 2010, A nonhydrostatic version of FVCOM: 1. Validation experiments, *J. Geophys. Res.*, 115, doi:10.1029/2009JC005525

Lamarre E. and Melville W.K., 1991, Air entrainment and dissipation in breaking waves, *Nature*, 351, 469–472.

Lamarre E. and Melville W.K., 1994, Void-fraction measurements and sound-speed fields in bubble plumes generated by breaking waves, *J. Acoust. Soc. Am.*, 95, 1317–1328.

Larsen J. and Dancy H., 1983, Open boundaries in short-wave simulations – A new approach, *Coast. Engrg.*, 7(3), 285-297

Lasheras J.C. and Choi H., 1988, Three-dimensional instability of a plane free shear layer: an experimental study of formation and evolution of streamwise vortices, *J. Fluid Mech.*, 189, 53-86

Lee J.-J., Skjelbreia E. and Raichlen F., 1982, Measurement of velocities in solitary waves, *J. of Waterway, Port, Coastal and Ocean Div.*, 108, 200-218

Lee J.W., Terbner M.D., Nixon J.B. and Gill P.M., 2006, A 3-D non-hydrostatic pressure model for small amplitude free surface flows, *Int. J. Numer. Meth. Fluids*, 50, 649-672

Leifer I. and de Leeuw G., 2006, Bubbles generated from wind-steepened breaking waves: 1. Bubble plume bubbles, *J. Geophys. Res.*, 111, C06020.

Lemos C., 1992, Wave breaking, A numerical study, Lecture notes in Engineering (V.71), Springer: Berlin

Li B. and Fleming C., 2001, Three-dimensional model of Navier-Stokes equations for water waves, *Journal of Waterway, Port, Coastal, and Ocean Engineering*, 16-25

Li M., L. Zhong and Boicourt W.C., 2005, Simulations of Chesapeake Bay estuary: sensitivity to turbulence mixing parameterizations and comparison with observations, *J. Geophys. Res.*, 110(C12004).

Liang Q. and Marche F., 2009, Numerical resolution of well-balanced shallow water equations with complex source terms, *Advances in Water Resource*, 32, 873-884

Lin P. and Li C.W., 2002, A σ-coordinate three-dimensional numerical model for free surface wave propagation, *Int. J. Numer. Meth. Fluids*, 38, 1045-1068

Lin P. and Liu P.L.-F., 1998, A numerical study of breaking waves in the surf zone, *J. Fluid Mech.*, 359, 239-264

Lin P. and Liu P.L.-F., 1998, Turbulent transport, vorticity dynamics, and solute mixing under plunging breaking waves in surf zone, *J. Geophy. Res.*, 103, 15677-15694

Lin P., Chang K.A. and P.L.-F. Liu, 1999, Runup and rundown of solitary waves on sloping beaches, *J. of Waterway, Port, Coastal and Ocean Division, ASCE*, 125, 247-255

Lin P. and Liu P.L.-F., 1999, Free surface tracking methods and their applications to wave hydrodynamics, *Advances in Coastal and Ocean Engineering*, 5, World Scientific

Liovic P. and Lakehal D., 2007, Multi-physics treatment in the vicinity of arbitrarily deformable gas-liquid interfaces, *J. Comp. Phys.*, 222, 504–535.

Liu P.L.-F. and Lin P., 1997, A numerical model for breaking waves: the volume of fluid method, Research report No. CACR-97-02

Liu P.L.-F., Wu T.-R., Raichlen F., Synolakis C.E. and Borrero J.C., 2005, Runup and rundown generated by three-dimensional sliding masses, *J. Fluid Mech.*, 536, 107-144

Loewen M.R. and Melville W.K., 1991, Microwave backscatter and acoustic radiation from breaking waves, *J. Fluid Mech.*, 224, 601-623

Loewen M.R. and Melville W.K., 1994, An experimental investigation of the collective oscillations of bubble plumes entrained by breaking waves, *J. Acoust. Soc. Amer.*, 95, 1329-1343

Lopez de Bertodano M., Lahey R.T. Jr. and Jones O.C., 1994, Development of a $k-\epsilon$ model for bubbly two-phase flow, *Journal of Fluids Engineering*, 116, 128-134

Lynett, P. and Liu, P. L.-F., 2002, A two-layer approach to wave modelling, *Proc. Roy. Soc. A*, 460, 2637-2669.

Lubin P., Vincent S., Abadie S. and Caltagirone J.-P., 2006, Three-dimensional large eddy simulation of air entrainment under plunging breaking waves, *Coastal Engineering*, 53, 631-655

Ma G., Shi F. and Kirby J.T., 2010, A polydisperse two-fluid model for bubble plumes under breaking waves, *Proceedings of 7th International Conference on Multiphase Flow*, Tampa, Florida, USA

Ma G., Shi F. and Kirby J.T., 2011, A polydisperse two-fluid model for surf zone bubble simulation, *J. Geophys. Res.*, 116, doi:10.1029/2010JC006667

Ma G., Kirby J.T. and Shi F., 2012, Numerical study of turbulence coherent structures and bubble entrainment under surfzone breaking wave, submitted to *J. Fluid Mech.*

Ma G., Shi F. and Kirby J.T., 2012, Shock-capturing non-hydrostatic model for fully dispersive surface wave processes, *Ocean Modelling*, 43-44, 22-35

Ma J., Oberai A.A., Drew D.A., Lahey R.T. Jr and Moraga F.J., 2010, A quantitative sub-grid air entrainment model for bubbly flows - plunging jets, *Computers and Fluids*, 39, 77–86.

MacMahan J.H., Brown J.W., Brown J.A., Thornton E.B., Reniers A., Stanton T., Henriquez M., Gallagher E., Morrison J., Austin M.J., Scott T.M. and Senechal N., 2010, Mean lagrangian flow behavior on an open coast rip-channeled beach: a new perspective, *Marine Geology*, 268, 1-15

Madsen P.A. and Sørensen O.R., 1992, A new form of the Boussinesq equations with improved linear dispersion characteristics. Part A slowly-varying bathymetry, *Coastal Engineering*, 18, 183-204

Martínez-Bazán C., Montañés J.L. and Lasheras J.C., 1999, On the breakup of an air bubble injected into a fully developed turbulent flow. Part 1. Breakup frequency, *J. Fluid Mech.*, 401, 157–182.

Martínez-Bazán C., Montañés J.L. and Lasheras J.C., 1999, On the breakup of an air bubble injected into a fully developed turbulent flow. Part 2. Size PDF of the resulting daughter bubbles, *J. Fluid Mech.*, 401, 183–207.

Martínez-Bazán C., Rodrŕguez-Rodríguez J., Deane G.B., Montañes J.L. and Lasheras J.C., 2010, Considerations on bubble fragmentation models, *J. Fluid Mech.*, 661, 159–177.

Melville W.K., 1996, The role of surface wave breaking in air-sea interaction, *Ann. Rev. Fluid Mech.*, 28, 279-321

Merlivat L. and Memery L., 1983, Gas exchange across and air-water interface: Experimental results and modelling of bubble contribution to transfer, *J. Geophys. Res.*, 88, C1, 707-724

Milelli M., 2002, A numerical analysis of confined turbulent bubble plume, Diss. EH. No. 14799, Swiss Federal Institute of Technology, Zurich.

Moin P. and Kim J., 1985, The structure of the vorticity field in turbulent channel flow. Part 1. Analysis of instantaneous fields and statistical correlations, *J. Fluid Mech.*, 155, 441-464

Moraga F.J., Carrica P.M., Drew D.A. and Lahey R.T. Jr., 2008, A sub-grid air entrainment model for breaking bow waves and naval surface ships, *Computers and Fluids*, 37, 281-298

Mori N., Suzuki T. and Kakuno S., 2007, Experimental study of air bubbles and turbulence characteristics in the surf zone, *J. Geophy. Res.*, 112, C05014.

Mudde R. F. and Simonin O., 1999, Two- and three-dimensional simulations of a bubble plume using a two-fluid model, *Chem. Engng. Sci.*, 54, 5061–5069.

Nadaoka K. and Kondoh T., 1982, Laboratory measurements of velocity field structure in the surf zone by LDV, *Coastal Engineering in Japan*, 25, 125-145

Nadaoka K., Hino M. and Koyano Y., 1989, Structure of the turbulent flow field under breaking waves in the surf zone, *Journal of Fluid Mechanics*, 204, 359-387

Namin M., Lin B. and Falconer R., 2001, An implicit numerical algorithm for solving non-hydrostatic free-surface flow problems, *Int. J. Numer. Meth. Fluids*, 35, 341-356

Nwogu O., 1993, Alternative form of Boussinesq equations for nearshore wave propagation, *Journal of Waterway, Port, Coastal and Ocean Engineering*, 119, 618-638

Osher A. and Sethian J.A., 1988, Fronts propagating with curvature-dependent speed: Algorithms based on Hamilton-Jacobi formulations, *J. Comput. Phys.*, 79, 12-49

Patankar S.V., 1980, Numerical heat transfer and fluid flow, McGraw-Hill, New York

Peregrine D.H., 1983, Breaking waves on beaches, *Annual Review of Fluid Mechanics*, 15, 149-178

Pedersen C., Deigaard R. and Sutherland J., 1998, Measurements of the vertical correlation in turbulence under broken waves, *Coastal Engineering*, 35, 231-249

Phillips N.A., 1957, A coordinate system having some special advantages for numerical forecasting, *J. Meteor.*, 14, 184-185

Reniers A.J.H.M., MacMahan J.H., Thornton E.B., Stanton T.P., Henriquez M., Brown J.W., Brown J.A. and Gallagher E., 2009, Surf zone surface retention on a rip-channeled beach, *J. Geophys. Res.*, 114, C10010, doi:10.1029/2008JC005153

Rider W.J. and Kothe D.B., 1998, Reconstructing volume tracking, *J. Comput. Phys.*, 141, 112-152

Rodi W., 1980, Turbulence models and their application in hydraulics - a state of the art review, In: IAHR, Delft, The Netherlands

Sato Y. and Sekoguchi K., 1975, Liquid velocity distribution in two-phase bubble flow, *Int. J. Multiphase Flow*, 2, 79–95.

Serizawa A. and Kataoka I., 1990, Turbulence suppression in bubbly two-phase flow, *Nuclear Engineering and Design*, 122, 1-16

Shao S. and Ji C., 2006, SPH computation of plunging waves using a 2-D sub-particle scale (SPS) turbulence model, *International Journal of Numerical Method in Fluids*, 51, 913-936

Shi F., Kirby J.T., Haller M.C. and Catalan P., 2008, Modeling of surfzone bubbles using a multiphase VOF model, *Proc. 31st Int. Conf. Coastal Engineering*, Hamburg, 157–169.

Shi F., Kirby J.T. and Ma G., 2010, Modeling quiescent phase transport of air bubbles induced by breaking waves, *Ocean Modelling*. 35, 105-117

Shi F., Kirby J.T., Harris J.C., Geiman J.D. and Grilli S.T., 2012, A high-order adaptive time-stepping TVD solver for Boussinesq modeling of breaking waves and coastal inundation, *Ocean Modelling*, 43-44, 36-51

Smagorinsky J., 1963, General circulation experiments with the primitive equations, *Mon. Weather Rev.*, 91, 99-165.

Sokolichin A. and Eigenberger G., 1999, Applicability of the standard $k - \epsilon$ turbulence model to the dynamic simulation of bubble columns: Part I. Detailed numerical simulations, *Chem. Engng. Sci.*, 54, 2273–2284.

Sou I.M., Cowen E.A. and Liu P.L.-F., 2010, Evolution of the turbulence structure in the surf and swash zones, *Journal of Fluid Mechanics*, 644, 193-216

Sridhar G. and Katz J., 1999, Effect of entrained bubbles on the structure of vortex rings, *Journal of Fluid Mechanics*, 397, 171-202

Stelling G. and Zijlema M., 2003, An accurate and efficient finite-difference algorithm for non-hydrostatic free-surface flow with application to wave propagation, *Int. J. Numer. Meth. Fluids*, 43, 1-23

Stive M.J.F., 1980, Velocity and pressure field of spilling breakers, *Proceedings of 17th International Conference of Coastal Engineering*, Sydney, ASCE, 547-566

Sullivan P. P. and McWilliams J.C., 2010, Dynamics of winds and currents coupled to surface waves, *Ann. Rev. Fluid Mech.*, 42, 19-42

Sussman M., Smereka P. and Osher S., 1994, A level set approach for computing solutions to incompressible two-phase flow, *J. Comp. Phys.*, 114, 146-159

Synolakis C.E., 1987, The runup of solitary waves, *J. Fluid Mech.*, 185, 523-545

Tanaka M., 1986, The stability of solitary waves, *Phys. Fluids*, 29, 650-655

Terrill E. J., Melville W.K. and Stramski D., 2001, Bubble entrainment by breaking waves and their influence on optical scattering in the upper ocean, *J. Geophys. Res.*, 106, 16,815-16,823

Terrill E. J., Lada G. and Melville W.K., 2001, Surf zone bubble populations, *Proceedings-Institute of Acoustics*, 23, 212-219

Thorpe S. A., 1982, On the clouds of bubbles formed by breaking wind-waves in deep water, and their role in air-sea gas transfer, *Phil. Trans. R. Soc. Lond. A*, 304, 155-210

Thuburn J., 1996, Multidimensional flux-limited advection schemes, *J. Comp. Phys.*, 123, 74–83.

Ting F.C.K. and Kirby J.T., 1994, Observation of undertow and turbulence in a laboratory surf zone, *Coastal Engineering*, 24, 52-80

Ting F.C.K. and Kirby J.T., 1995, Dynamics of surf zone turbulence in a strong plunging breaker, *Coastal Engineering*, 24, 177-204

Ting F.C.K. and Kirby J.T., 1996, Dynamics of surf zone turbulence in a spilling breaker, *Coastal Engineering*, 27, 131-160

Ting F.C.K., 2006, Large-scale turbulence under a solitary wave, *Coastal Engineering*, 53, 441-462

Ting F.C.K., 2008, Large-scale turbulence under a solitary wave: Part 2 Forms and evolution of coherent structures, *Coastal Engineering*, 55, 522-536

Ting F.C.K. and Nelson J.R., 2011, Laboratory measurements of large-scale near-bed turbulent flow structures under spilling regular waves, *Coastal Engineering*, 58, 151-172

Troshko A. A. and Hassan Y.A., 2001, A two-equation turbulence model of turbulent bubbly flows, *Int. J. Multiphase Flow*, 27, 1965–2000.

Vagle S., Farmer D.M. and Deane G.B., 2001, Bubble transport in rip currents, *J. Geophys. Res.*, 106, 11,677–11,689.

van den Hengen E.I.V., Deen N.G. and Kuipers J.A.M., 2005, Application of coalescence and breakup models in a discrete bubble model for bubble columns, *Industrial and Engineering Chemistry Research*, 44, 5233-5245

Visser P.J., 1991, Laboratory measurements of uniform longshore currents, *Coastal Engineering*, 15, 563-593

Walters R.A., 2005, A semi-implicit finite element model for non-hydrostatic (dispersive) surface waves, *Int. J. Numer. Meth. Fluids*, 49, 721-737

Wang S.K., Lee S.J., Jones O.C. Jr., and Lahey R.T. Jr., 1987, 3-D turbulence structure and phase distribution measurements in bubbly two-phase flows, *International Journal of Multiphase Flow*, 13, 327-343

Watanabe Y. and Saeki H., 1999, Three-dimensional large eddy simulation of breaking waves, *Coastal Engineering Journal*, 41, 281-301

Watanabe Y., Saeki H. and Hosking R.J., 2005, Three-dimensional vortex structures under breaking waves, *Journal of Fluid Mechanics*, 545, 291-328

Wei G., Kirby J.T., Grilli S.T. and Subramanya R., 1995, A fully nonlinear Boussinesq model for surface waves. Part 1. Highly nonlinear unsteady waves, *J. Fluid Mech.*, 294, 71-92

Wiegel R.L., 1960, A presentation of cnoidal wave theory for practical application, *J. Fluid Mech.*, 7, 273-286

Wilmott C. J., 1981, On the validation of models, *Physical Geography*, 2, 184-194.

Wu C.H., Young C.-C., Chen Q. and Lynett P.J., 2010, Efficient nonhydrostatic modeling of surface waves from deep to shallow water, *J. Waterway, Port, Coastal, and Ocean Engineering*, 136, 104-118

Wu J., 1988, Bubbles in the near-surface ocean: a general description, *J. Geophys. Res.*, 93, 587-590

Wu T.R., 2004, A numerical study of three dimensional breaking waves and turbulence effects, Ph.D dissertation, Cornell University

Yang D. and Shen L., 2009, Characteristics of coherent vortical structures in turbulent flows over progressive surface waves, *Physics of Fluids*, 21, 125106, doi:10.1063/1.3275851

Young C.-C., Wu C.-H., Kuo J.-T. and Liu W.-C., 2007, A higher-order σ-coordinate non-hydrostatic model for nonlinear surface waves, *Ocean Engineering*, 34, 1357-1370

Young C.-C., Wu C.-H., Liu W.-C. and Kuo J.-T., 2009, A higher-order non-hydrostatic σ model for simulating nonlinear refraction-diffraction of water waves, *Coastal Engineering*, 56, 919-930

Young C.-C. and Wu C.-H., 2010, A σ-coordinate non-hydrostatic model with embedded Boussinesq-type-like equations for modeling deep-water waves, *Int. J. Numer. Meth. Fluids*, 63, 1448-1470

Yuan H. and Wu C.-H., 2004, A two-dimensional vertical non-hydrostatic σ model with an implicit method for free-surface flows, *Int. J. Numer. Meth. Fluids*, 44, 811-835

Yuan H. and Wu C.-H., 2004, An implicit three-dimensional fully non-hydrostatic model for free-surface flows, *Int. J. Numer. Meth. Fluids*, 46, 709-733

Zhou J.G., Gauson D.M., Mingham C.G. and Ingram D.M., 2001, The surface gradient method for the treatment of source terms in the shallow-water equations, *J. Comp. Phys.*, 168, 1-25

Zijlema M. and Stelling G.S., 2005, Further experiences with computing non-hydrostatic free-surface flows involving water waves, *Int. J. Numer. Meth. Fluids*, 48, 169-197

Zijlema M. and Stelling G.S., 2008, Efficient computation of surf zone waves using the nonlinear shallow water equations with non-hydrostatic pressure, *Coastal Engineering*, 55, 780-790